The Dissertation Committee for Binghan He
certifies that this is the approved version of the following dissertation:

Towards a Safe and Responsive Control Framework for Human-Centered Robots

Committee:

Luis Sentis, Supervisor

Ufuk Topcu, Co-Supervisor

Farshid Alambeigi

Dongmei Chen

Junmin Wang

Towards a Safe and Responsive Control Framework for Human-Centered Robots

by

Binghan He

DISSERTATION

Presented to the Faculty of the Graduate School of
The University of Texas at Austin
in Partial Fulfillment
of the Requirements
for the Degree of

DOCTOR OF PHILOSOPHY

THE UNIVERSITY OF TEXAS AT AUSTIN
May 2021

Dedicated to my wife Yang.

Acknowledgments

The story of my Ph.D. study starts from seeing a picture of the DREAMER robot on the website of the University of Texas at Austin. Her beautiful face and dexterous hands guided me to find where she belongs to, the Human Centered Robotics Lab. Before I came to Austin for my Ph.D. study, I was told by one of my friends that this would be the starting point of my academic career. Now when I look back on this five-and-a-half-year journey at Austin, I realize that all these research experiences prepared me for my long-term career goal, using human-centered robots to make our lives better. At this end-point of my Ph.D. study, I wish to thank the multitudes of people who helped me toward my research goal.

First, I want to thank my advisors Dr. Luis Sentis and Dr. Ufuk Topcu, and all other members of my dissertation committee. Luis is the person who brings me the philosophy of human-centered robotics: not to replace humans with robots but to use robots to extend our physical and computational capabilities. His enriched ideas of research inspired me a lot during my entire Ph.D. study. Ufuk always uses concise words to disentangle very sophisticated problems. I learned from him to think of many research questions in a very different way. Dr. Farshid Alambeigi, Dr. Dongmei Chen, and Dr. Junmin Wang provided me profound thoughts and suggestions that helped me to improve my works in this dissertation.

Second, I want to thank my former advisors at Purdue University and Cornell University. In my junior year of undergraduate study, Dr. Peter Meckl taught me a lot during my control systems honor course project, which now can be considered as my first taste of robotic research. I learned a lot from the conversations with Dr. Bin Yao during my undergraduate study and every time I met him at conferences. Dr. Andy Ruina reminded me never to be naive about using the linear methods because our physical world is nonlinear and uncertain. Dr. Robert Thorne showed me his humility and patience, which are the qualities of a decent scholar.

Third, I want to thank Dr. Ye Zhao, Dr. Gray C. Thomas, and all other former labmates at the Human Centered Robotics Lab. In the early stage of my Ph.D. study, Ye gave me a lot of very useful advice, which helped me to quickly settle down and start producing my research results at Austin. Gray and I had a lot of collaboration during my Ph.D. study. As a senior colleague in the lab, he guided me into the field of dynamical modeling and control synthesis. Dr. Nicholas A. Paine, Dr. Kenan Isik, Dr. Kwan Suk Kim, Dr. Donghyun Kim, Dr. John W. Hall, and Dr. Steven J. Jorgensen provided me many suggestions for polishing my academic skills.

Forth, I want to thank all other collaborators and friends at the University of Texas at Austin. Huang Huang, Nicolas Brissonneau, and Henry F. Cappel worked with me on human dynamics study. Jaemin Lee and Masha Ghasemi helped me extend my safety control algorithm to multi-joint robotic systems and human-in-the-loop systems. Kunye Chen, Rachel Schlossman, Neal Ormsbee, Mara Altman, Nathan Young, Matt Mangum collaborated with me on using robotic systems to conduct remote teaching and learning. Orion Campbell, Minkyu Kim, Junhyeok Ahn, Mihir Vedantam, Seung Hyeon Bang, Jee-Eun Lee, Ryan Gupta, and all other friends made my Ph.D. study an enjoyable and memorable experience.

Last but not least, I want to thank my family. Ever since my wife Yang Hu and I met at the University of Texas at Austin in 2018, she supported me emotionally with her love and patience. Our parents always encourage us during our study at Austin. My father, Dr. Guilong Zhu, gave me a lot of advice based on the experience of his academic career. He is the image of what I want to be, a professional scholar and upright person.

Thank you all.

Binghan He

May 2021

The works in this dissertation were supported by the Longhorn Innovation Fund for Technology, the U.S. Government, the Office of Naval Research Grant No. N000141512507 and the National Science Foundation Grants No. 1724360, No. 1652113, and No. 1836900.

Towards a Safe and Responsive Control Framework for Human-Centered Robots

Publication No. ____________________

Binghan He, Ph.D.
The University of Texas at Austin, 2021

Supervisors: Luis Sentis
Ufuk Topcu

Human-centered robots are a specific kind of service robot, which interact with humans physically or cognitively and help humans with tasks in uncertain environments. They can be humanoid robots, exoskeletons, or manipulators and mobile platforms that provide us good services. However, human-centered robots are still not perfect enough for us to use nowadays. On the one hand, human-centered robots are still slow and inefficient for their tasks because the human inputs and dynamics that they react to are uncertain, immeasurable, or even completely unknown. On the other hand, human-centered robots face much more complicated safety requirements than other kinds of robots because humans are dynamic and vulnerable during physical human-robot interaction. To resolve these issues of human-centered robots, the work in this dissertation explores new models for reducing human uncertainty and new control algorithms for improving safety warranty.

The first half of this dissertation introduces a complex stiffness model for describing the uncertain human impedance. The discovery of this new model is motivated to explain the observation of a consistent damping ratio of a human versus different environmental dynamics. It replaces the linear damping term in a conventional mass-spring-damping model with a hysteretic damping term, an imaginary value in the frequency domain. Because of the correlation between the stiffness term and the newly discovered hysteretic damping term in the complex stiffness model, we can significantly reduce the human impedance uncertainty. Based on the complex stiffness model, we can adopt nonlinear control strategies for improving the responsiveness and the human-friendliness of human-centered robots.

The second half of this dissertation introduces the concept of a barrier pair, which consists of a barrier function and a controller for the safety verification and warranty of a human-centered robot. We obtain a barrier pair by solving an optimization problem subject to a series of linear matrix inequalities representing the state-space, input, and stability constraints of a human-centered robot. By incorporating sampling-based methods into the synthesis of barrier pairs, human-centered robots can guarantee safe operation with non-convex state-space constraints. The sampling-based barrier pair method helps us construct a control framework of human-robot shared autonomy. A human-centered robot in this control framework uses an inference of a human's objective to figure out how to assist the human and prevent the human from potential accidents.

Table of Contents

List of Tables

List of Figures

Chapter 1

Introduction

1.1 Motivation and Goals

Human-centered robots, whether they are wearable robots that augment the productivity of workers or service robots that improve the quality of lives, react to the inputs from humans [Colgate, Bicchi, Peshkin, and Colgate, 2008]. Different from other types of robots that aim to achieve full autonomy, human-centered robots assist and cooperate with humans. However, human-centered robots are still not perfect enough for us to use in practice nowadays. On the one hand, human-centered robots are still slow and inefficient when attempting to perform practical tasks because of the ambiguous nature of the interaction with humans (either physically or via other communication cues) and the amount of uncertainty existing in human environments. On the other hand, human-centered robots need to provide safety guarantees in ways that make the problem much more complicated than robot operation in simpler industrial setups.

For example, the time-varying nature of human biomechanical impedance makes physical human-robot interactions hard to accomplish with efficiency and safety. Human impedance can be modified by both voluntary muscle contractions or external torques exerted on the human joints [Bennett, Hollerbach, Xu, and Hunter, 1992]. Several studies have shown an approximately linear relationship between the stiffness of the human (found by fitting a linear mass-spring-damper model for a single joint) and an external torque [Agarwal and Gottlieb, 1977; Cannon and Zahalak, 1982; Hunter and Kearney, 1982]. To model the damping behavior exhibited by human joints, other studies have observed that damping behavior also increases with voluntary muscle contractions [Becker and Mote, 1990] or during the application of external torques to the joint [Weiss, Hunter, and Kearney, 1988]. An approximately linear relationship between damping and external torques has also been identified in the human ankle joint, but it is statistically weaker than the strong linear relationship between stiffness and external torques [Agarwal and Gottlieb, 1977; Hunter and Kearney, 1982]. All these studies attempt to reduce the time-varying uncertainty of the models representing human impedance. However, it is unclear from the current literature that a linear relationship between damping and stiffness in human joints represents the general case in a statistically significant sense. Because both human stiffness and damping vary in large amounts, the uncertainty of the parameter space representing human impedance becomes very big. Therefore, employing traditional models of human joint impedance results in very conservative human-robot interactions such as suffering from low control bandwidth.

Adaptive control is a great method for dealing with uncertain dynamical systems. It has been widely applied to robots [Roy and Whitcomb, 2002; Losey, Erwin, McDonald, Sergi, and O'Malley, 2016; Chen, Chen, Yao, Zhu, Zhu, Wang, and Song, 2016] successfully dealing the with partially unknown and uncertain robot parameters by analyzing and estimating them in real-time. The use of electromyography (EMG) signals has enabled the estimation of human impedance [Huang, Cappel, Thomas, He, and Sentis, 2020] and also the estimation of human joint torques [Gui, Liu, and Zhang, 2019] in real-time for improving the bandwidth of physical human-robot interaction. However, the stability of adaptive control given time-varying dynamical processes is not formally proved [Ioannou and Sun, 2012]. It can easily become unstable with quick changes of the human interaction impedance due to for instance abrupt muscle co-contractions. Therefore, from our perspective, adaptive control for physical human-robot interaction requires reliable safety verification and safety guarantees.

Robust frequency domain methods [Buerger and Hogan, 2007] also deal with uncertain human dynamics and can be implemented as output feedback controllers calculated based on human joint positions and human-robot interaction forces. However, to verify safety during human-robot interaction, we need to estimate the internal states related to the human body dynamics. A Luenberger observer [Luenberger, 1964] asymptotically estimates states using only the direct measurement of input and output signals of a linear system. This method can be extended to a nonlinear system by considering the nonlinear dynamics of the system as the modeling error of a linear state space model [Zeitz, 1987]. For bounded modeling errors, the estimation error converges to a residue set instead of converging to zero [Corless and Tu, 1998]. Recently, a sum-of-squares programming method [Pylorof, Bakolas, and Chan, 2019] has been proposed to optimize the convergence rate of robust state estimators for uncertain nonlinear systems. All these methods can help to improve the state estimation related to uncertain human body dynamics. But the state estimates using the previous methods cannot be directly used for safety verification during human-robot interaction until they fully converge to the true states. Therefore the interaction system can violate safety constraints if the state estimation process has not yet finalized.

In dynamical systems such as human-centered robots, the safety of their operation can be verified by a barrier certificate. Similarly to a Lyapunov function for stability verification, a barrier certificate or barrier function provides a sufficient condition for safety verification [Prajna and Jadbabaie, 2004]. But a Lyapunov function needs decrease everywhere in the state space while a barrier function relaxes the global convergence requirement and only needs to be decreasing around the safety bounds. Barrier certificates can be synthesized through sum-of-squares optimization [Prajna, 2006]. Inspired by the idea of a control Lyapunov function [Sontag, 1989], a more ambitious goal is to combine a barrier function and a safety-guaranteeing controller and synthesize them simultaneously [Wieland and Allgöwer, 2007]. The region of attraction of this safety controller is also known as a 'funnel' [Burridge, Rizzi, and Koditschek, 1999], which can be synthesized over a shooting trajectory via the use of multiple local stabilizing controllers [Tedrake, Manchester, Tobenkin, and

Roberts, 2010] or by solving quadratic programs based on control barrier functions [Ames, Xu, Grizzle, and Tabuada, 2016]. These control strategies have been previously proposed to solve closed system problems [Nilsson and Ames, 2018] and two-player game problems [DeCastro and Kress-Gazit, 2015] with safety constraints.

However, all the aforementioned methods focus on problems with convex constraints. If there is an obstacle in the workspace of the robot, the state space control synthesis problem in its general form will necessitate a non-convex motion planning process to avoid the obstacles. In [Reist, Preiswerk, and Tedrake, 2016], a simulation-based method for solving this non-convex motion planning problem is proposed by simulating many controllers and checking constraint satisfaction for each one of them. But simulation-based methods suffer from high computational costs.

For complex robotic systems in dynamic environments, it is important to plan safe workspace trajectories that always satisfy safety and collision avoidance constraints. This type of constrained motion planning problem is often addressed by using sampling-based methods such as a rapidly-exploring random tree (`RRT`) method [Lavalle and Kuffner Jr., 2000]. A kino-dynamic motion planning method [Hauser and Zhou, 2016] can also be considered for trajectory synthesis subject to kinematic and dynamic constraints. This has been previously employed to find asymptotically optimal solutions in a multi-dimensional configuration space using admissible velocity propagation [Pham, Caron, and Nakamura, 2013] and applied to a manipulator robot using visual servoing [Kazemi, Gupta, and Mehrandezh, 2013]. However, it is unproven whether there always exists a stabilizing controller along the planned trajectory.

To resolve the issues mentioned above appearing in the control of human-centered robots, the work of this dissertation explores new models for reducing human model uncertainty and new control algorithms for improving safety.

1.2 Summary of Contributions

The natural impedance of the human body, which corresponds to the dynamic relationship between force and motion, can determine the stability of human-centered robots that rely on interaction-force feedback to assist human operators. In Chapter 2, we consider a class of human-centered robots designed to amplify the strength of operators through the use of feedback of sensed interactions and actuator forces. This type of robotic systems is interesting because they can amplify a human's interaction forces–so long as the human contacts the environment through the robot– and attenuate the operator's perception of the robot's reflected dynamics within the bandwidth limits of the controller. We define an amplification error term based on a reference amplification rate and design a linear feedback compensator to attenuate the error. Since the human operator is an integral part of the system, we design the compensator to be robust to both a realistic variation in human impedance and a large variation in load impedance. We demonstrate that our strategy on a one-degree-of-freedom robot testbed connected to a human arm is successful, using a three-dimensional matrix describing the experimentation choices: slow or fast human motion; light or extreme robot load; and soft or clenched human arm impedances. We demonstrate that a slightly aggressive controller results in a borderline stable system—but only for soft human musculoskeletal behavior when interacting with a heavy load.

While human impedance is typically modelled as a linear system, our experiments performed in Chapter 3 on a single-joint testbed involving 10 human subjects show evidence of nonlinear behavior: a low-frequency asymptotic phase for the dynamic stiffness of the human that is different than the expected zero phase, and an unexpectedly consistent damping ratio as the stiffness and inertia vary. To explain this observation, this chapter considers a new frequency-domain model describing human joint dynamic behavior featuring complex value stiffness comprising a real stiffness term and a hysteretic damping term. Using a statistical F-test, we show that the hysteretic damping term is significant and even more significant than the linear damping term. Further analysis reveals a linear trend linking hysteretic damping and the real part of the stiffness, which allows us to simplify the complex stiffness model down to a 1-parameter system.

Chapter 4 introduces two nonlinear control strategies based on the complex stiffness model mentioned above for improving the responsiveness of human-centered robots. The first nonlinear control strategy is a customizable fractional-order controller that exploits the human complex stiffness behavior to improve strength amplification bandwidth while maintaining stability. We explore a tuning approach that ensures that this stability property is robust to muscle co-contraction for each individual. The second nonlinear control strategy, which we call proportional-and-hysteretic-damping (PHD) control, endows human-like complex stiffness features to robots using a nonlinear realization. We show that this PHD controller has the property of being significantly insensitive to inertia variations.

In Chapter 5, we introduce a safety controller which enforces strict state and input constraints on a robotic system—but only acts when necessary, providing transparent operation of the system within a safe region of the state space. We define this state-space region using a Min-Quadratic Barrier function, which we construct along the equilibrium manifold using Lyapunov functions. This problem can be efficiently formulated using linear matrix inequality controller synthesis for locally valid linearizations. We also introduce the concept of a barrier pair, which consists of a barrier function and a controller to guarantee robot's safety. We demonstrate the efficacy and versatility of our controller and barrier pair synthesis method in simulated examples.

In Chapter 6, we consider the problem of verifying safety constraint satisfaction for single-input single-output systems with uncertain transfer function coefficients. We propose a new type of barrier function based on a vector norm. This type of barrier function guarantees a measurable upper bound without having access to the full state. An identifier-based estimator allows an exact bound for the uncertainty-based barrier function estimate. Assuming that the system is safe at start time, using our method we guarantee an exponentially decreasing bound on the error due to the estimator transient. A method to synthesize the barrier function and the estimator is proposed by formulating two convex sub-problems and by exploiting linear matrix inequalities. The barrier function and the estimator are then used to construct a safety backup controller. We then demonstrate their successful operation in a simulation of a 1 degree-of-freedom human-robot interaction problem.

For a human-centered robot with its workspace space trajectories constrained by obstacles, the synthesis of a safety controller often results in a non-convex optimization problem. Chapter 7 devises a new algorithm to solve this non-convex problem by constructing a rapidly-exploring random tree of barrier pairs. Each barrier pair is composed of a quadratic barrier function and a full state feedback controller. The proposed method constructs a rapidly-exploring random tree to deal with the non-convex constraints and uses barrier pairs to fulfill the local convex constraints. This sampling-based barrier pair method helps us construct a control framework for human-robot shared autonomy. A human-centered robot in this control framework uses an inference of a human's objective to figure out how to assist the human and prevent the human from having potential accidents. We demonstrate this new algorithm using a simulation of a two linkage manipulator robot.

The experimental protocol for the human subject study presented in this dissertation was approved by the Institutional Review Board (IRB) at the University of Texas at Austin under study No. 2017-10-0006. The informed consent forms were signed by all subjects.

The results presented in this dissertation have also appeared in part of the following publications, which are listed in a chronological order.

Peer Reviewed Journal Publications

- N. Brissonneau, B. He, G. C. Thomas, and L. Sentis. Biologically-inspired impedance control with hysteretic damping. *IEEE Control Systems Letters*, 5(5):1717–1722, 2021
- B. He, H. Huang, G. C. Thomas, and L. Sentis. A complex stiffness human impedance model with customizable exoskeleton control. *IEEE Transactions on Neural Systems and Rehabilitation Engineering*, 28(11): 2468–2477, 2020a

Peer Reviewed Conference Publications

- B. He, M. Ghasemi, U. Topcu, and L. Sentis. A barrier pair method for safe human-robot shared autonomy. In *IEEE Conference on Decision and Control (CDC), in review*. IEEE, 2021
- B. He, J. Lee, U. Topcu, and L. Sentis. BP-RRT: Barrier pair synthesis for temporal logic motion planning. In *IEEE Conference on Decision and Control (CDC)*, pages 1404–1409. IEEE, 2020b
- B. He, G. C. Thomas, and L. Sentis. Robust estimator-based safety verification: A vector norm approach. In *2020 American Control Conference (ACC)*. IEEE, 2020c

- B. He, H. Huang, G. C. Thomas, and L. Sentis. Complex stiffness model of physical human-robot interaction: Implications for control of performance augmentation exoskeletons. In *2019 IEEE/RSJ International Conference on Intelligent Robots and Systems (IROS)*, pages 6748–6755. IEEE, 2019
- B. He, G. C. Thomas, N. Paine, and L. Sentis. Modeling and loop shaping of single-joint amplification exoskeleton with contact sensing and series elastic actuation. In *2019 American Control Conference (ACC)*, pages 4580–4587. IEEE, 2019
- G. C. Thomas, B. He, and L. Sentis. Safety control synthesis with input limits: a hybrid approach. In *2018 Annual American Control Conference (ACC)*, pages 792–797. IEEE, 2018

Part I

Responsiveness

Chapter 2

Linear Control for Responsive Human-Centered Robots

In this chapter, we use amplification exoskeletons as examples of human-centered robots to discuss the problems we are facing toward a responsive physical human-robot interaction. Long the purview of science fiction, exoskeletons are quickly becoming a modern reality—augmenting the strength of healthy operators as they walk and interact with the world. A vast literature catalogs the breadth and history of the exoskeleton concept, with survey papers offering disambiguation between such exoskeletons and the orthotic systems designed for medical purposes [Dollar and Herr, 2008], and between "parallel-limb exoskeletons for load transfer" such as our type of system, and several other types that aim to help the human in a different sense [Herr, 2009] (by reducing the metabolic cost of walking, for example [Lee, Kim, Baker, Long, Karavas, Menard, Galiana, and Walsh, 2018]). Amplification exoskeletons, like the concept of a "Human Extender" [Kazerooni, 1990], interact with the

---

The results presented in this chapter have also appeared in part of [He, Thomas, Paine, and Sentis, 2019]. As the primary contributor, Binghan He developed the amplification exoskeleton controller, conducted human subject experiments, and analyzed the experimental data. Gray C. Thomas provided theory supports on frequency domain analysis and controller synthesis. Nicholas A. Paine supported this research with his actuator design and actuator control methods. This research was advised by Luis Sentis.

world and the human operator at the same time, with the world perceiving a strengthened operator, while the operator in feeling a weakened world and a lighter exoskeleton, all through the feedback action of the device in response to force-sensors embedded at the human–robot interface.

With the human maintaining full control over the motion of the amplification exoskeleton, their primary challenge is not so much autonomy as stable feedback control in the presence of the difficult-to-model human and the uncertain environment. Humans possess naturally adjustable compliance properties which depend on muscle activation [Hogan, 1984]. The methodology of interaction controller design [Colgate and Hogan, 1988] has had success modeling humans as active systems which are passive except for non-state-dependent biases. Robust robot impedance [Hogan, 1989] and haptic interface [Colgate and Brown, 1994; Adams and Hannaford, 1999] controller design strategies have supported and used this model to great effect, while acknowledging its conservatism. The task of amplification exoskeletons, however, is to emulate a reduction in mass. This can be achieved stably if the human model is more precisely known [Buerger and Hogan, 2007] than just a passive assumption but is acknowledged to be a challenging problem.

One of the earliest known amplification-oriented exoskeleton is the hulking machine HARDIMAN I [Makinson, Bodine, and Fick, 1969], which introduced the world to the control challenges of exoskeletons, as it was never safe enough to power on both upper and lower body with an operator. Ref. [Kazerooni, 1990], much later, conceived of extenders for industrial use with operators controlling much larger machines through force-sensitive interfaces—acknowledging a tradeoff between stability and performance both in linear and robust-nonlinear models [Kazerooni, 1990]. Ref. [Kazerooni and Guo, 1993] defined a performance criterion for such extenders using a matrix of amplification-levels; a critical frequency, since such amplification cannot be maintained at all frequencies; and introduced a stability filter that allowed the device to ensure robustness to varied operator behavior. However, the later BLEEX exoskeleton from the same lab was not designed in this framework due to practical issues with force sensors [Kazerooni, Racine, Huang, and Steger, 2005] and the discovery of an alternative strategy using high sensitivity cancellation of the natural exoskeleton dynamics—which accomplished an apparent-mass reduction without the force sensors, at the cost of no longer amplifying human-world interaction forces (and extreme sensitivity to the dynamic model) [Kazerooni, 2005].

The strategy of measuring a network of force sensors on the human alone, using them to determine human intent, and then using a simulated ideal reaction to this intent as input to a position controller is known as admittance control, and it represents a slight departure from the human extender ideal: accurate reflection of the environmental forces to the human takes a backseat, since there are no force sensors for the environment. This is a very successful paradigm—at least in the absence of environmental contact—it works for giant gantry robots [Lecours, St-Onge, and Gosselin, 2012], complex upper body robots [Yu and Rosen, 2013], the slow-yet-amplifying (full-) body extender

[Fontana, Vertechy, Marcheschi, Salsedo, and Bergamasco, 2014], and the Sarcos-Ratheon exoskeleton described indirectly in their 2014 Patent [Jacobsen and Olivier, 2014]—which is implied to be hydraulic, admittance based, and capable of walking. However, when admittance robots interact with semi-rigid environments their interaction forces are determined by the position controller, not the human. A modified admittance scheme with position control implemented via inverse dynamics shares these fundamental limitations [Lee, Lee, Kim, Han, Shin, and Han, 2014], and requires either extra force-sensors or modification to the dynamic model to carry load.

A review paper on admittance control [Keemink, van der Kooij, and Stienen, 2017] suggests employing feedback based on acceleration when possible. Acceleration feedback (and the use of accelerometers) dominate the control strategy of BLEEX [Kazerooni, 2005]. And one exoskeleton has used acceleration to reduce the apparent inertia of the operator (rather than merely reducing the apparent mass of the exoskeleton) [Kong and Tomizuka, 2009]. Acceleration has been proposed as a complete framework for exoskeleton control [Boaventura and Buchli, 2016]. But successful as this strategy is, it cannot aid in amplification objectives—since the environment is generally not known in advance.

In one exoskeleton, a simpler strategy was employed which fed contact forces to motor-current through the motion Jacobian transpose [Zanotto, Akiyama, Stegall, and Agrawal, 2015] (a study not on exoskeleton control but on an exoskeleton's effect on human motion). This strategy is able to amplify the human with respect to both interaction forces and exoskeleton dynamic forces, but the researchers only accomplished a modest amplification (around 2) in their study, and did not discuss the tuning of their controller.

In this chapter, we explore the strategies for improving the responsiveness of an amplification exoskeleton using linear human impedance models and linear control methods. Aiming to accomplish higher amplification ratio and faster response, the exoskeleton hardware we use is designed to include high performance force controlled series elastic actuators [Paine, Oh, and Sentis, 2014] (similar to the force controlled actuation in [Kong and Tomizuka, 2009], which used a disturbance observer on motor position based on [Kong, Bae, and Tomizuka, 2009], while ours operates on the spring deflection). Using a series elastic actuator allows us to replicate an amplification error framework reminiscent of [Kazerooni and Guo, 1993], but without a force sensor between the exoskeleton and the environment. Instead, we use the spring deflection of the elastic actuators resulting in our scheme to not only attenuate the load but also the exoskeleton dynamics. As in [Buerger and Hogan, 2007], we need to model the human as an uncertain system and check for complementary stability. However, we design our linear exoskeleton controllers using the uncertain bode plot between desired force (sent to the SEA) and amplification error. Following the arguments laid out in [Buerger and Hogan, 2007], and the additional examples in [Kazerooni and Snyder, 1995; Colgate and Brown, 1994], we employ a single-DOF system to study the simplest possible case of amplification exoskeletons.

2.1 1-DOF Physical Human-Robot Interaction

Fig. 2.1 introduces a 1-DOF model of physical human-robot interaction, where the human is modeled as a mass $\mathbf{M_h}$, a spring $\mathbf{K_h}$, and a damper $\mathbf{B_h}$ and the robot is modeled as a mass $\mathbf{M_e}$. The actuator is modeled as a mass $\mathbf{M_a}$ and a damper $\mathbf{B_a}$. If the human-robot contact is assumed to be rigid, the positions of human and robot are both described as $\theta_\mathbf{e}$. The actuator position is described as $\theta_\mathbf{a}$. An actuator spring $\mathbf{K_s}$ is considered in this model to make the robot compliant for the physical human-robot interaction. This additional actuator spring turns the actuator into a series elastic actuator (SEA) and the control problem of the the robot torque $\tau_\mathbf{s} = \mathbf{K_s} \cdot (\theta_\mathbf{a} - \theta_\mathbf{e})$ into the control problem of an actuator spring deflection control problem. The human-robot contact force $\mathbf{f_c}$, which is measured by a force sensor, and the actuator torque $\tau_\mathbf{a}$, which is generated by the motor current running through the actuator, are the raw output and input of the physical human-robot interaction system. The contact force signal $\mathbf{f_c}$ is cast as a torque $\tau_\mathbf{c}$ using the motion Jacobian $\mathbf{J}$ of the sensor frame ($\tau_\mathbf{c} = \mathbf{J}^\top \mathbf{f_c}$).

2.1.1 Control of Human-Robot Contact Force

Because the human is modeled as a mass-spring-damper, the dynamic stiffness of the human is expressed as

$$\mathbf{S_h} = \tau_\mathbf{c}/\theta_\mathbf{e} = \mathbf{M_h} \cdot \mathbf{s}^2 + \mathbf{B_h} \cdot \mathbf{s} + \mathbf{K_h}. \tag{2.1}$$

The dynamic stiffness of the robot is expressed as

$$\mathbf{S_e} = (\tau_\mathbf{s} - \tau_\mathbf{c})/\theta_\mathbf{e} = \mathbf{M_e} \cdot \mathbf{s}^2, \tag{2.2}$$

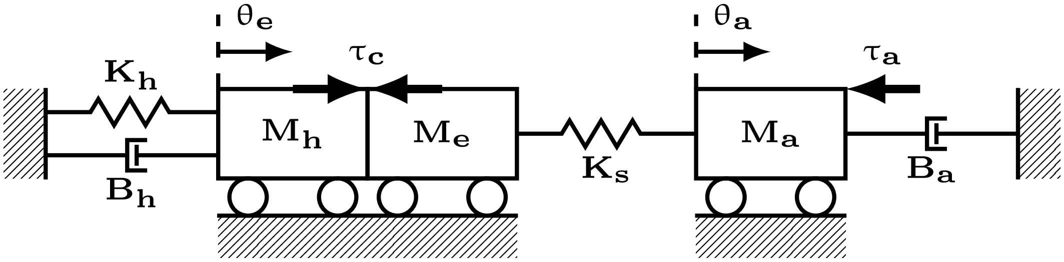

Figure 2.1: A 1-DOF human-robot interaction model includes an uncertain human stiffness $\mathbf{K_h}$, an uncertain human damping $\mathbf{B_h}$, a human mass $\mathbf{M_h}$, and a robot mass $\mathbf{M_e}$. The robot is actuated by a SEA, which is modeled as a spring $\mathbf{K_s}$, a motor damping $\mathbf{B_a}$, and a motor inertia $\mathbf{M_a}$

Together,

$$\mathbf{S_{h\text{-}e}} = \mathbf{S_h} + \mathbf{S_e} = \tau_{\mathbf{s}}/\theta_{\mathbf{e}}, \tag{2.3}$$

represents a sub-system in parallel with the series elastic actuator.

Considering the stiffness of the actuator spring,

$$\mathbf{S_s} = \tau_{\mathbf{s}}/(\theta_{\mathbf{a}} - \theta_{\mathbf{e}}) = \mathbf{K_s}, \tag{2.4}$$

and the dynamic stiffness of the motor,

$$\mathbf{S_a} = (\tau_{\mathbf{a}} - \tau_{\mathbf{s}})/\theta_{\mathbf{a}} = \mathbf{M_a} \cdot \mathbf{s}^2 + \mathbf{B_a} \cdot \mathbf{s}, \tag{2.5}$$

motion of the whole system relates to the required input force,

$$\frac{\tau_{\mathbf{a}}}{\theta_{\mathbf{e}}} = \mathbf{S_{h\text{-}e}} + \frac{(\mathbf{S_{h\text{-}e}} + \mathbf{S_s}) \cdot \mathbf{S_a}}{\mathbf{S_s}}. \tag{2.6}$$

This provides a human-dependent force-control plant,

$$\frac{\tau_{\mathbf{s}}}{\tau_{\mathbf{a}}} = \frac{\mathbf{S_{h\text{-}e}} \cdot \mathbf{S_s}}{\mathbf{S_{h\text{-}e}} \cdot \mathbf{S_s} + (\mathbf{S_{h\text{-}e}} + \mathbf{S_s}) \cdot \mathbf{S_a}}. \tag{2.7}$$

Under the robot force control shown in Fig. 2.2's block diagram bond

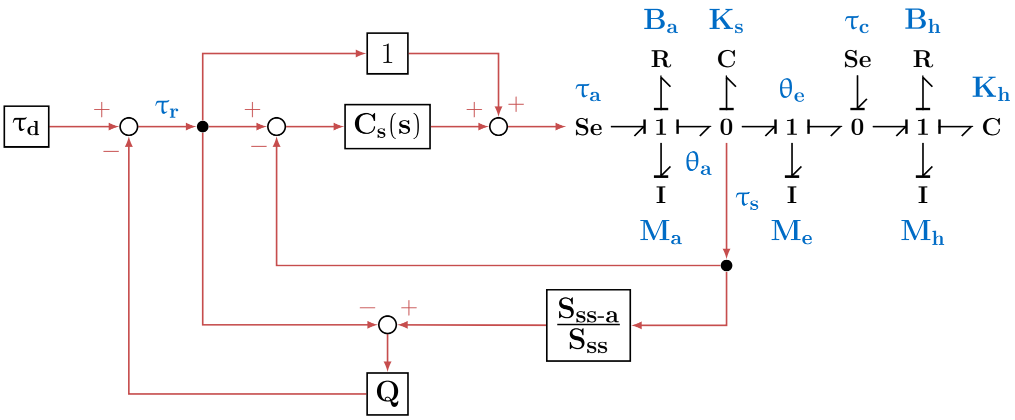

Figure 2.2: A block diagram of robot force control with a disturbance observer. The dynamics of human, robot and actuator are represented as a bond graph with effort sources $\tau_\mathbf{a}$ and $\tau_\mathbf{c}$.

graph,

$$\tau_\mathbf{a} = \tau_\mathbf{r} + \mathbf{C_s}(\mathbf{s}) \cdot (\tau_\mathbf{r} - \tau_\mathbf{s}), \tag{2.8}$$

where $\tau_\mathbf{r}$ is the reference spring force and $\mathbf{C_s}(\mathbf{s})$ is a PD controller. Combining (2.7) and (2.8),

$$\frac{\tau_\mathbf{s}}{\tau_\mathbf{r}} = \frac{\mathbf{S_{h\text{-}e}} \cdot \mathbf{S_{ss}}}{\mathbf{S_{h\text{-}e}} \cdot \mathbf{S_{ss}} + (\mathbf{S_{h\text{-}e}} + \mathbf{S_s}) \cdot \mathbf{S_a}}, \tag{2.9}$$

where $\mathbf{S_{ss}} = \mathbf{S_s} \cdot [1 + \mathbf{C_s}(\mathbf{s})] = \mathbf{b_{ss}} \cdot \mathbf{s} + \mathbf{k_{ss}}$ includes the virtual stiffness and damping of spring. By tuning the PD gains of $\mathbf{C_s}(\mathbf{s})$, the virtual spring stiffness of $\mathbf{k_{ss}}$ and the virtual spring damping $\mathbf{b_{ss}}$ can be modified.

If $\mathbf{S_{h\text{-}e}}$ is infinitely large, (2.9) simplifies to,

$$\frac{\tau_\mathbf{s}}{\tau_\mathbf{r}} = \frac{\mathbf{S_{ss}}}{\mathbf{S_{ss\text{-}a}}}, \tag{2.10}$$

where $\mathbf{S_{ss\text{-}a}} = \mathbf{S_{ss}} + \mathbf{S_a}$ is the combined dynamic stiffness of the virtual spring and the actuator.

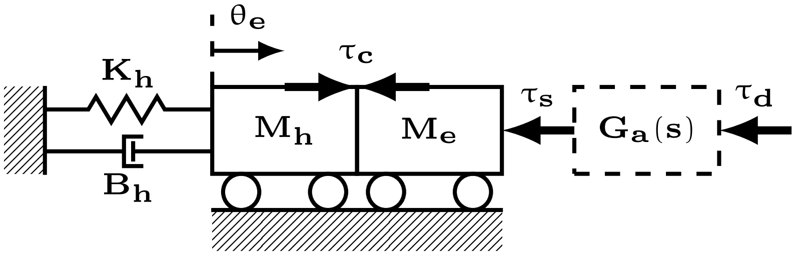

Figure 2.3: A 1-DOF human-robot interaction model includes an uncertain human stiffness $\mathbf{K_h}$, an uncertain human damping $\mathbf{B_h}$, a human mass $\mathbf{M_h}$, and a robot mass $\mathbf{M_e}$. The robot is actuated by a SEA, which is represented by a transfer function $\mathbf{G_a(s)}$.

Under a disturbance observer (DoB) of [Paine, Oh, and Sentis, 2014],

$$\tau_r = \tau_d - [\mathbf{Q} \cdot \frac{\mathbf{S_{ss\text{-}a}}}{\mathbf{S_{ss}}} \cdot \tau_s - \mathbf{Q} \cdot \tau_r], \tag{2.11}$$

where τ_d is the DoB spring torque command and $\mathbf{Q}$ is a low-pass filter of sufficient order to ensure the observer is causal.

Combining (2.9) and (2.11), we obtain a transfer function $\mathbf{G_a(s)}$ from τ_d to τ_s,

$$\mathbf{G_a(s)} = \frac{\tau_s}{\tau_d} = \frac{\mathbf{S_{h\text{-}e}} \cdot \mathbf{S_{ss}}}{\mathbf{S_{h\text{-}e}} \cdot \mathbf{S_{ss}} + [\mathbf{S_{h\text{-}e}} + (1 - \mathbf{Q}) \cdot \mathbf{S_s}] \cdot \mathbf{S_a}}. \tag{2.12}$$

By tuning the cut-off frequency of $\mathbf{Q}$, (2.10) is (approximately) enforced without an infinitely large $\mathbf{S_{h\text{-}e}}$—as explained in [Paine, Oh, and Sentis, 2014], this approximation depends on an inertia lower-bound (in this case, the unloaded robot inertia).

2.1.2 Plant of Physical Human-Robot Interaction

The transfer function $\mathbf{P_c(s)}$ (obtained by combining (2.1), (2.3) and (2.12)) from the desired actuator torque τ_d to the human-robot interaction

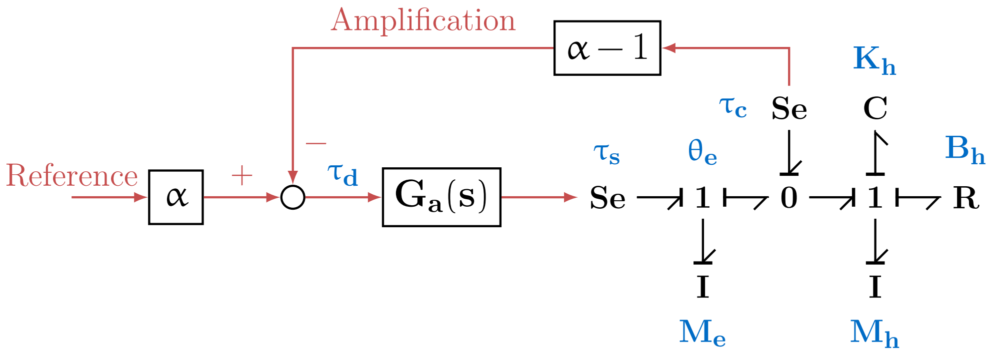

Figure 2.4: A block diagram of amplification control. Dynamics of human with exoskeleton are expressed as a bond graph with effort source of τ_s and τ_c.

torque τ_c is expressed as

$$\mathbf{P_c}(s) = \frac{\tau_c}{\tau_d} = \frac{\mathbf{S_h} \cdot \mathbf{S_{ss}}}{\mathbf{S_{h\text{-}e}} \cdot \mathbf{S_{ss}} + [\mathbf{S_{h\text{-}e}} + (1 - \mathbf{Q}) \cdot \mathbf{S_s}] \cdot \mathbf{S_a}}. \tag{2.13}$$

Let us define α as an amplification factor we want the exoskeleton to achieve. In Fig. 2.4, we show a direct amplification control, which implement a negative feedback of τ_c to τ_d with a gain $\alpha - 1$. It can considered as a proportional control for eliminating τ_c. If a infinitely large value of α can be achieved, we obtain a transparent interaction between the human and the exoskeleton. If a reference torque value is implemented as shown in Fig. 2.4, the direct amplification control will try to eliminate the difference between τ_c and the reference. A more in-depth study of direct amplification is in Chapter 4.

Another way of amplification control is through defining an amplification error signal $\tau_\alpha = (\alpha - 1)\tau_c + \tau_s$, and considering the transfer function $\mathbf{P}_\alpha(s)$ (obtained by combining (2.1), (2.3) and (2.12)) from the desired force τ_d to the error τ_α,

$$\mathbf{P}_\alpha(\mathbf{s}) = \frac{\tau_\alpha}{\tau_\mathbf{d}} = \frac{\mathbf{S}_{\alpha\mathbf{h\text{-}e}} \cdot \mathbf{S}_\mathbf{ss}}{\mathbf{S}_\mathbf{h\text{-}e} \cdot \mathbf{S}_\mathbf{ss} + [\mathbf{S}_\mathbf{h\text{-}e} + (1 - \mathbf{Q}) \cdot \mathbf{S}_\mathbf{s}] \cdot \mathbf{S}_\mathbf{a}}, \tag{2.14}$$

where $\mathbf{S}_{\alpha\mathbf{h\text{-}e}} = \alpha\mathbf{S}_\mathbf{h} + \mathbf{S}_\mathbf{e}$ is the combined dynamic stiffness of the amplified human and exoskeleton.

Because the cut-off frequency of $\mathbf{Q}$ is much larger than the natural frequency of the human system, $\omega_\mathbf{h} = \sqrt{\mathbf{K}_\mathbf{h}/\mathbf{M}_\mathbf{h}}$, and the natural frequency of the force control, $\omega_\mathbf{ss\text{-}a} = \sqrt{\mathbf{k}_\mathbf{ss}/\mathbf{M}_\mathbf{a}}$, $\mathbf{P}_\alpha(\mathbf{s})$ can be approximated:

$$\mathbf{P}_\alpha(\mathbf{s}) \approx \frac{\mathbf{S}_{\alpha\mathbf{h\text{-}e}} \cdot \mathbf{S}_\mathbf{ss}}{\mathbf{S}_\mathbf{h\text{-}e} \cdot \mathbf{S}_\mathbf{ss\text{-}a}}. \tag{2.15}$$

As shown in Fig. 2.5—assuming $\mathbf{k}_\mathbf{ss}/\mathbf{b}_\mathbf{ss}$ is high enough to ignore—$\mathbf{P}_\alpha(\mathbf{s})$ has a pair of conjugate zeros at $\omega_{\alpha\mathbf{h\text{-}e}} = \sqrt{\mathbf{K}_\mathbf{h}/(\mathbf{M}_\mathbf{e}/\alpha + \mathbf{M}_\mathbf{h})}$ and two pairs of conjugate poles at $\omega_\mathbf{h\text{-}e} = \sqrt{\mathbf{K}_\mathbf{h}/(\mathbf{M}_\mathbf{e} + \mathbf{M}_\mathbf{h})}$ and at $\omega_\mathbf{ss\text{-}a}$. $\omega_\mathbf{ss\text{-}a}$ is usually larger than the maximum of $\omega_\mathbf{h}$. However, even if an actuator has a soft serial spring or a huge motor rotor inertia, increasing the gain of $\mathbf{C}_\mathbf{s}(\mathbf{s})$ will result in an $\omega_\mathbf{ss\text{-}a}$ much larger than $\omega_\mathbf{h\text{-}e}$ and $\omega_{\alpha\mathbf{h\text{-}e}}$—which avoids the phase drop below $-180°$ in $\mathbf{P}_\alpha(\mathbf{s})$.

The bode magnitude plot of $\mathbf{P}_\alpha(\mathbf{s})$ starts from $20\log(\alpha)$ dB in steady state. If the loop of $\mathbf{P}_\alpha(\mathbf{s})$ is directly closed, the gain cross-over is decided by the feedback gain—and of course by the shape of $\mathbf{P}_\alpha(\mathbf{s})$, which varies with the value of α, the stiffness and damping of the human, and the environmental impedance.

When α is set very close to 1 the actuator does almost no amplification, and $\mathbf{P}_\alpha(\mathbf{s})$ approaches the closed loop force tracking behavior of the low-level

(a) Magnitude (dB)

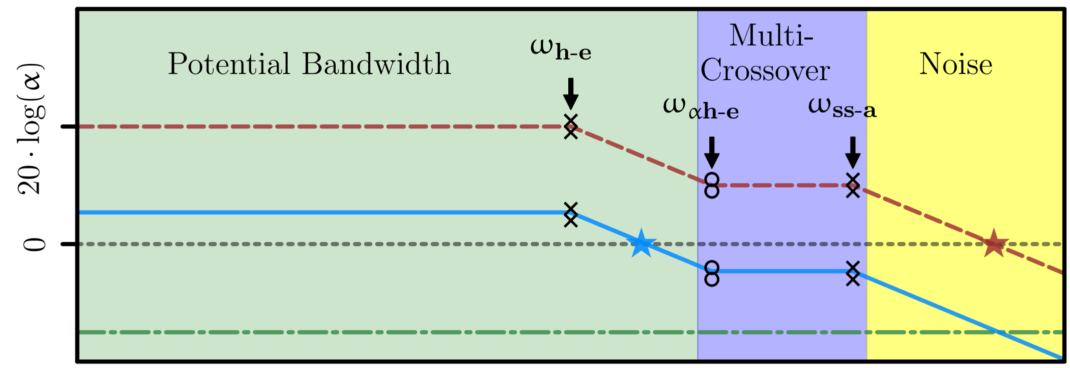

(b) Phase (deg)

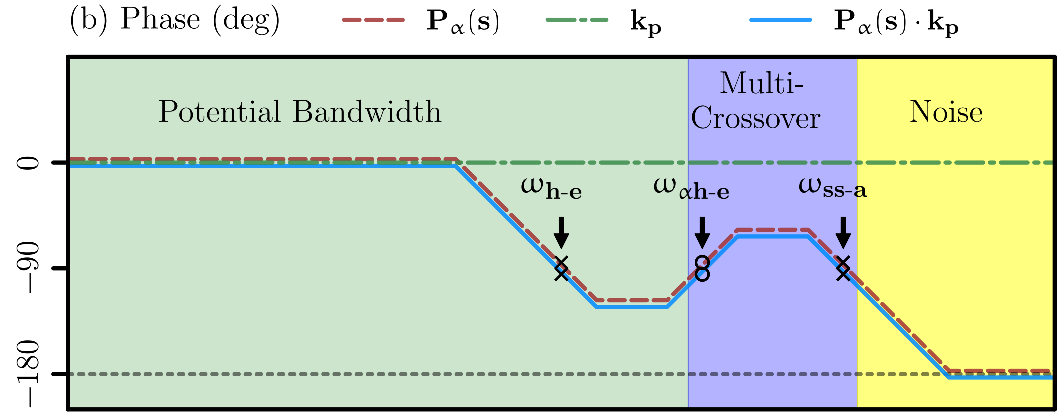

Figure 2.5: Conceptual bode plots with a large $\mathbf{k_{ss}}/\mathbf{b_{ss}}$ show the plant $\mathbf{P}_\alpha(\mathbf{s})$, proportional gain $\mathbf{k_p}$, and compensated open-loop. Regions are color-coded: the green region has practical model-accuracy, the blue region reflects the multi-crossover behavior which makes a compensator design unreliable, and the yellow region is noise dominated in our identification tests, so the model is unreliable. Crosses, circles and stars indicate the poles, zeros and cross-over points.

force controller—in this configuration $\omega_{\alpha\mathbf{h\text{-}e}}$ converges to $\omega_{\mathbf{h\text{-}e}}$ and $\mathbf{P}_{\alpha}(\mathbf{s})$ looks like a second order low pass filter.

On the other hand, as α increases, $\omega_{\alpha\mathbf{h\text{-}e}}$ travels right, and the gap between $\omega_{\mathbf{h\text{-}e}}$ and $\omega_{\alpha\mathbf{h\text{-}e}}$ widens. This gap behaves like a second order lag compensator—and it corresponds to a phase dip that approaches $-180°$ as the gap widens.

When the human stiffness is very low, both $\omega_{\mathbf{h\text{-}e}}$ and $\omega_{\alpha\mathbf{h\text{-}e}}$ shift to lower frequencies together—unless there is an environmental stiffness. If the human becomes stiffer the two shift higher together as well.

Fig. 2.5 highlights three frequency bands. At the highest frequencies, it should be possible to design controllers, but on our hardware the amount of amplified noise makes them to dangerous to try. In the next highest band it is very easy to gain two extra cross-overs, because the zeros at $\omega_{\alpha\mathbf{h\text{-}e}}$ are under damped. The lowest frequency region is where we will attempt to cross over in this chapter.

2.2 Human Mass-Spring-Damper Model

The experiments in this section use the elbow-joint exoskeleton testbed (Fig. 2.6(a)) with a SEA and a contact sensor. The aluminum exoskeleton arm has $\bar{\mathbf{M}}_{\mathbf{e}} = 0.1$ kgm^2.

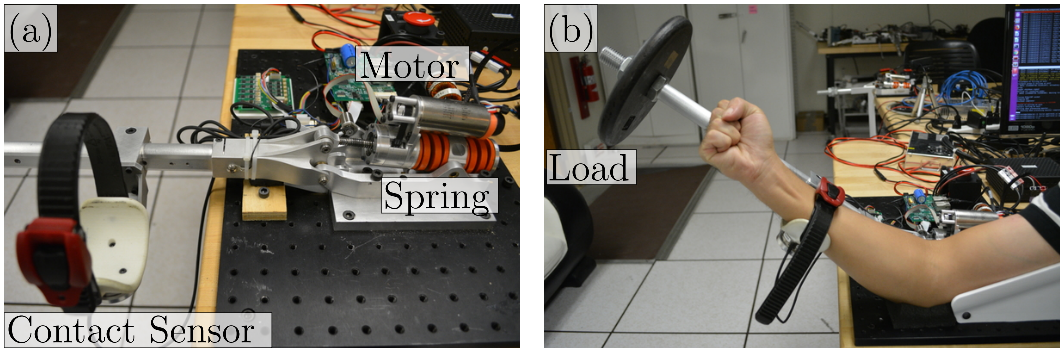

Figure 2.6: P0 elbow-joint exoskeleton testbed (a) is used for a human model identification experiment (b).

Table 2.1: Identified Parameters of Mass-Spring-Damper Model

Experiment	$\mathbf{K_h}$ $(\frac{\text{Nm}}{\text{rad}})$	$\mathbf{B_h}$ $(\frac{\text{Nms}}{\text{rad}})$	$\mathbf{M_h} + \mathbf{M_e}$ (kgm^2)	$\zeta_{\mathbf{h\text{-}e}}$	$\lvert\tau_{\mathbf{d}}\rvert$ (Nm)
1	7.44	0.56	$0.09 + 0.10$	0.24	2.0
2	70.11	1.60	$0.09 + 0.10$	0.22	5.0
3	31.91	1.84	$0.09 + 0.57$	0.20	4.0
4	50.18	4.21	$0.09 + 1.05$	0.28	4.0

2.2.1 Frequency Domain Identification

The human model identification (Fig. 2.6(b)) includes four chirp signal experiments (Exp. 1-4) with a 27-year old male subject. The subject wears the cuff of the contact sensor and straps his upper arm to a fixed mount. A 300 second, exponential chirp signal is provided as a torque command to the low level force controller. The subject tries to hold the exoskeleton still—with various levels of attempted stiffness—as the exoskeleton vibrates. The exoskeleton does not hit its joint safety hard-stops in these experiments, and operator has access to the system emergency stop at all times.

2.2.2 Human Joint Stiffness and Damping

The joint stiffness is decided by contractions in the group of muscles around the joint. By activating a higher level of contractions in flexor and extensor of elbow, the elbow stiffness can be increased [Cannon and Zahalak, 1982]. Exp. 1 and Exp. 2 identify the range of subject's elbow $\mathbf{K_h}$. The muscle around the elbow is as relaxed as possible in Exp. 1-2. The subject clenches his hand into a fist to help him achieve a high stiffness and leaves it open for soft behavior. This is also a convenient way to visually distinguish these two types of human behavior in the rest of this chapter.

Although the stiffness of a human elbow can possibly go up to 400 Nm/rad, such stiffness is only possible with a perturbation of 40 Nm [Lanman, 1980]. The chirp amplitude $|\tau_{\mathbf{d}}|$ is only 2 Nm in Exp. 1 and 5 Nm in Exp. 2 to provide just enough perturbation of torque while the subject can still keep the exoskeleton within the safety joint limits. The results from Exp. 1-2 suggest that $\mathbf{K_h}$ varies within the [7.44, 70.11] Nm/rad range.

Without additional inertia added to the exoskeleton and load, the human is able to maintain an invariant damping ratio of the arm [Perreault, Kirsch, and Crago, 2004]. However, the human is also able to adapt damping and stiffness to compensate the environment dynamics [Milner and Cloutier, 1993]. We added a 5 lb and a 10 lb loads at 18 inches from the joint on the exoskeleton in Exp. 3 and Exp. 4. The results from the four experiments suggest that the human tends to maintain an invariant damping ratio $\zeta_{\mathbf{h\text{-}e}}$ of $\mathbf{S_{h\text{-}e}}$ when wearing the exoskeleton (Tab. 2.1). Therefore, we model the human as a 1-parameter system. With changing values of $\mathbf{K_h}$ and $\mathbf{M_e}$, we predict $\mathbf{B_h}$

$$\mathbf{B_h} = 2\zeta_{\mathbf{h\text{-}e}}\sqrt{\mathbf{K_h}(\mathbf{M_h}+\mathbf{M_e})}. \tag{2.16}$$

The identified values of $\mathbf{K_h}$, $\mathbf{B_h}$ and $\mathbf{M_h}$ (Tab. 2.1) suggest the value of $\zeta_{\mathbf{h\text{-}e}}$ of the subject is around 0.23.

2.3 Proportional-and-Integral Control

2.3.1 Loop Shaping

By adding a proportional gain $\mathbf{k_p}$ less than 1 to $\mathbf{P}_\alpha(\mathbf{s})$, the cross-over shifts below $\omega_{\alpha\mathbf{h\text{-}e}}$. However, It also reduces the low frequency magnitude and increases the closed loop steady state error. An integral term can be added to boost the low frequency magnitude while maintaining the same cross-over below $\omega_{\alpha\mathbf{h\text{-}e}}$. We parameterize a simple PI controller transfer function $\mathbf{C}_\alpha(\mathbf{s})$ (from $-\tau_\mathbf{c}$ to $\tau_\mathbf{d}$ in Fig. 2.4) as

$$\mathbf{C}_\alpha(\mathbf{s}) = \mathbf{k_p}\cdot\frac{\mathbf{s}+\mathbf{z}}{\mathbf{s}}, \tag{2.17}$$

where $\mathbf{z}$ is a zero with $\mathbf{k_p}\cdot\mathbf{z}$ as the integral gain. As a reference, $\mathbf{k_p}=\frac{1}{\alpha}$ starts the compensated open-loop plant at a low frequency gain equal to unity.

The amplification tracking is evaluated by comparing $-\frac{\tau_\mathbf{s}}{\tau_\mathbf{c}}$ to $\alpha-1$. The transfer function from $-(\alpha-1)\tau_\mathbf{c}$ to $\tau_\mathbf{s}$ is equivalent to closing the loop of $\mathbf{C}_\alpha(\mathbf{s})\mathbf{P_s}(\mathbf{s})$. Because the cut-off frequency of $\mathbf{Q}$ is much greater than $\omega_{\mathbf{ss\text{-}a}}$, $\mathbf{C}_\alpha(\mathbf{s})\mathbf{P_s}(\mathbf{s})$ can be simplified as

$$\mathbf{C}_\alpha(\mathbf{s})\mathbf{P_s}(\mathbf{s}) \approx \mathbf{k_p}\cdot\frac{\mathbf{s}+\mathbf{z}}{\mathbf{s}}\cdot\frac{\mathbf{S_{ss}}}{\mathbf{S_{ss\text{-}a}}}. \tag{2.18}$$

Notice that $\frac{\mathbf{S_{ss}}}{\mathbf{S_{ss\text{-}a}}}$ behaves as a low-pass filter with a cut-off frequency at

(a) Magnitude (dB)

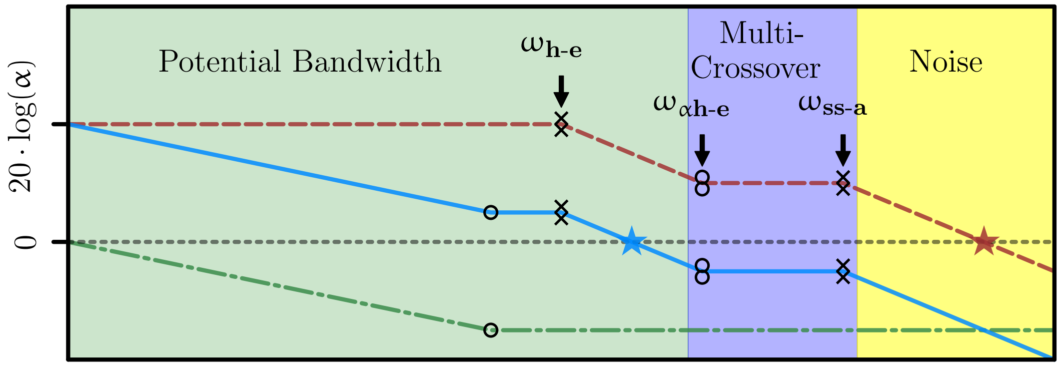

(b) Phase (deg)

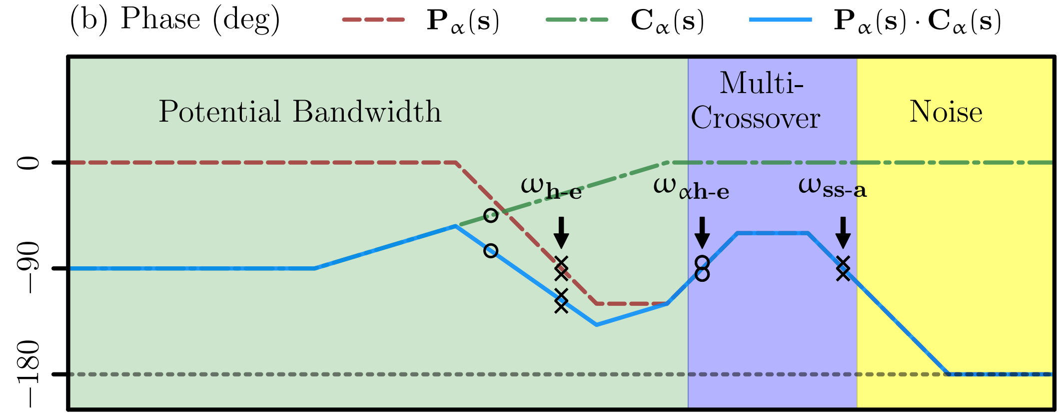

Figure 2.7: Conceptual bode plots with a large $\mathbf{k_{ss}}/\mathbf{b_{ss}}$ show the plant $\mathbf{P}_\alpha(\mathbf{s})$, PI compensator $\mathbf{C}_\alpha(\mathbf{s})$, and compensated open-loop. Regions are color-coded: the green region has practical model-accuracy, the blue region reflects the multi-crossover behavior which makes a compensator design unreliable, and the yellow region is noise dominated in our identification tests, so the model is unreliable. Crosses, circles and stars indicate the poles, zeros and cross-over points.

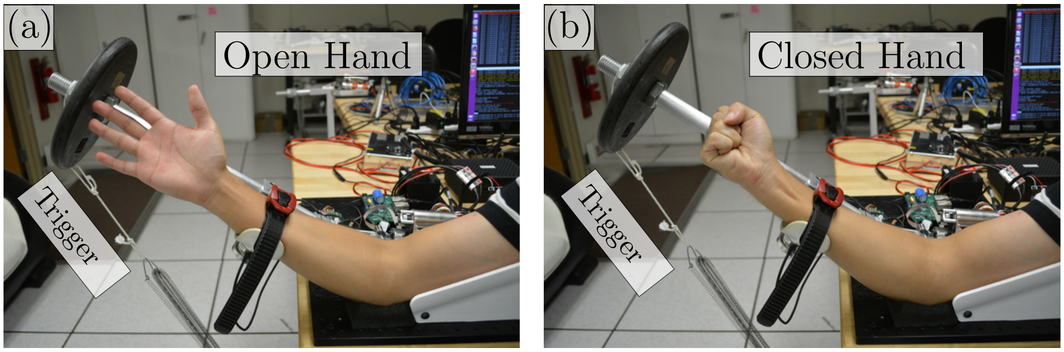

Figure 2.8: Step response with an aggressive controller was triggered by releasing an external spring at the end of the exoskeleton arm. The subject opens (a) and closes (b) his hand to illustrate different levels of muscle co-contraction (and therefore stiffness).

$\omega_{\mathbf{ss\text{-}a}}$. Therefore, $\mathbf{C}_\alpha(\mathbf{s})\mathbf{P}_\mathbf{s}(\mathbf{s})$ is dominated by $\mathbf{C}_\alpha(\mathbf{s})$ at low frequency. This allows the amplification tracking to be deterministic despite the uncertainty from $\mathbf{S}_{\mathbf{h\text{-}e}}$.

The dynamic tracking of amplification depends a lot on the location of $\mathbf{z}$ in $\mathbf{C}_\alpha(\mathbf{s})$ and the magnitude of $\mathbf{C}_\alpha(\mathbf{s})\mathbf{P}_\mathbf{s}(\mathbf{s})$. However, $\mathbf{z}$ cannot be arbitrarily large because it allows $\mathbf{C}_\alpha(\mathbf{s})$ to drop more phase from $\mathbf{P}_\alpha$ between $\omega_{\mathbf{h\text{-}e}}$ and $\omega_{\alpha\mathbf{h\text{-}e}}$.

2.3.2 Examples

Considering the range of $\mathbf{K}_\mathbf{h}$ and $\mathbf{M}_\mathbf{e}$, a model of $\mathbf{P}_\alpha(\mathbf{s})$ with uncertainty can be obtained and used for PI controller design for $\alpha = 10$. In this section, an aggressive controller and a robust controller are implemented to validate the uncertain model and control strategy. The video of all the experiments in this section is available at https://www.youtube.com/watch?v=EUHoAEwCfFY.

Table 2.2: Estimated Model Parameters of Aggressive PI Control

Load (lb)	Hand	$\hat{\mathbf{K}}_{\mathbf{h}}(\frac{\mathrm{Nm}}{\mathrm{rad}})$	$\hat{\mathbf{B}}_{\mathbf{h}}(\frac{\mathrm{Nms}}{\mathrm{rad}})$	$\hat{\zeta}_{\mathbf{h\text{-}e}}$
10	open	27.12	2.34	0.22
10	closed	59.34	3.99	0.25

Aggressive PI Control A controller with $\mathbf{k_p} = 0.1$ and $\mathbf{z} = 30$ is implemented with a load of 10 lb on the exoskeleton, the uncertain model suggests it makes the exoskeleton slightly unstable with a low value of $\mathbf{K_h}$ but fully stable with a high value of $\mathbf{K_h}$ (Fig. 2.9).

To validate this prediction, the subject wearing the exoskeleton with the controller either opens his hand—for low values of $\mathbf{K_h}$—or tightly closes his hand—for high stiffness $\mathbf{K_h}$—in two separate experiments. A spring with one end connected on the ground and the other end hanging on the end of the exoskeleton is released at the beginning of each experiment—a step input in external force (Fig. 2.8).

The experiment results (Fig. 2.10) show that the exoskeleton joint oscillates with a slowly increasing amplitude with open hand and oscillates but settles down in 2 seconds with closed hand. By using the data of $\tau_{\mathbf{c}}$, $\theta_{\mathbf{e}}$ and $\dot{\theta}_{\mathbf{e}}$, a linear regression is built to identify a simplified human model with only damping $\hat{\mathbf{B}}_{\mathbf{h}}$ and stiffness $\hat{\mathbf{K}}_{\mathbf{h}}$ (Tab. 2.2). The value of $\hat{\mathbf{K}}_{\mathbf{h}}$ verifies that human maintains a much higher stiffness with closed hand than open hand. The estimated contact torques $\hat{\tau}_{\mathbf{c}} = \hat{\mathbf{B}}_{\mathbf{h}}\dot{\theta}_{\mathbf{e}} + \hat{\mathbf{K}}_{\mathbf{h}}\theta_{\mathbf{e}}$ are well matched to the measured $\tau_{\mathbf{c}}$ (Fig. 2.10)—which confirms that the system is oscillating despite

(a) Magnitude (dB)

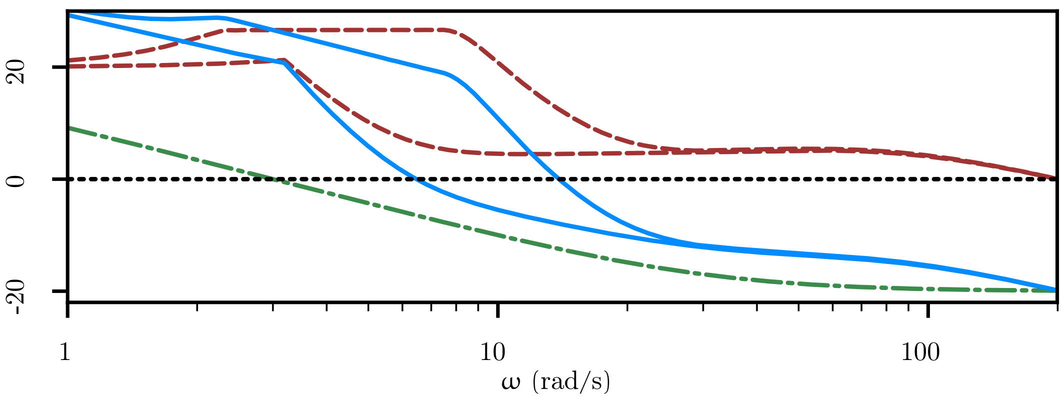

(b) Phase (deg)

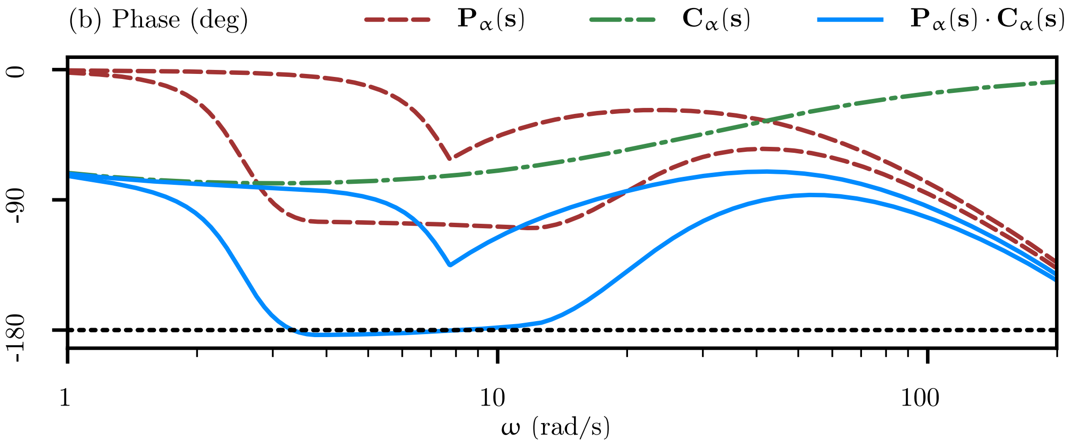

Figure 2.9: Uncertain model of $\mathbf{P}_\alpha(\mathbf{s})$ is made by 20 interpolations of $\mathbf{K_h}$ in the range of [7.44, 70.11] Nm/rad. Time delay is 6 ms.

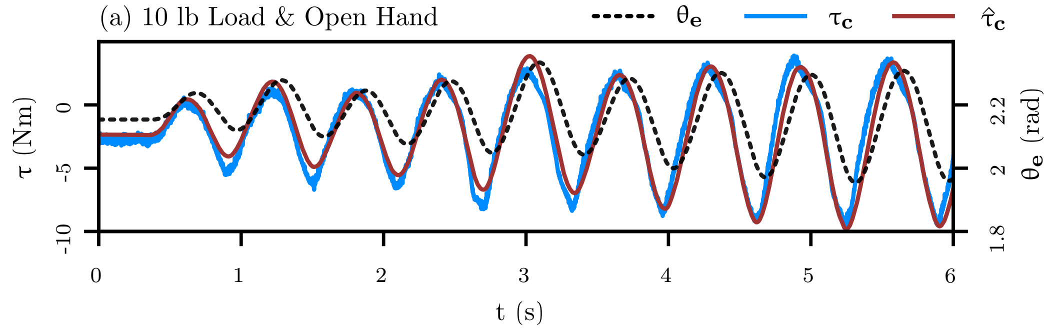

(a) 10 lb Load & Open Hand

(b) 10 lb Load & Closed Hand

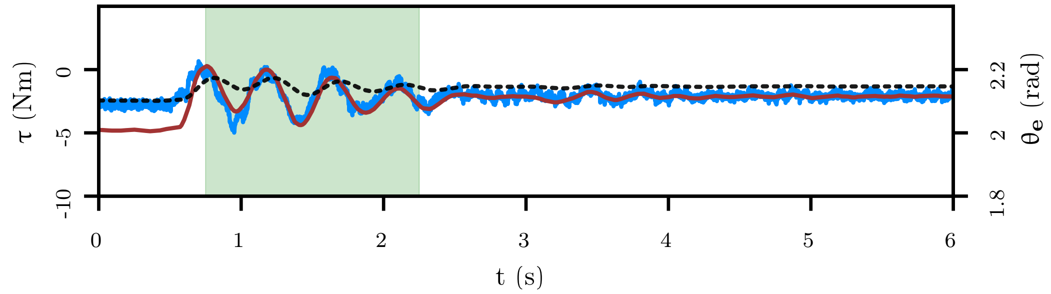

Figure 2.10: Because motion settles down early in (b), only the green highlighted region is used for estimating $\hat{\mathbf{B}}_\mathbf{h}$ and $\hat{\mathbf{K}}_\mathbf{h}$.

Table 2.3: Observed Amplification of Robust PI Control

Load (lb)	Hand	$\lvert -\frac{\tau_{\mathbf{s}}}{\tau_{\mathbf{c}}}\rvert$ (static)	$\lvert -\frac{\tau_{\mathbf{s}}}{\tau_{\mathbf{c}}}\rvert$ (1Hz)	$\angle -\frac{\tau_{\mathbf{s}}}{\tau_{\mathbf{c}}}$ (1Hz)
0	open	8.15	1.48	-53.55°
0	closed	8.05	1.49	-53.68°
10	open	8.13	1.58	-53.39°
10	closed	8.18	1.46	-50.75°

a passive, spring-damper-like, human behavior. The estimated damping ratio $\hat{\zeta}_{\mathbf{h\text{-}e}} = \hat{\mathbf{B}}_{\mathbf{h}}/(2\sqrt{\hat{\mathbf{K}}_{\mathbf{h}}\mathbf{M}_{\mathbf{e}}})$ for open hand is slightly lower than 0.23 and makes the system more unstable than the prediction.

Robust PI Control We also implemented a controller with $\mathbf{k_p} = 0.1$ and $\mathbf{z} = 10$ for improved robustness to parameter variation in the exoskeleton load, and human stiffness (and damping). The uncertain model suggests it maintains a phase margin no less than 10° for permissible values of $\mathbf{K_h}$ and $\mathbf{M_e}$ (Fig. 2.11).

To validate the expectation, the experiments include two different $\mathbf{M_e}$ (with 0 and 10 lb load) and two different $\mathbf{K_h}$ (open and closed hands). The subject generates motion with 0.1 Hz trapezoid-like wave for steady state tests and 1 Hz sinusoid-like wave for dynamic tests.

The integrator in the controller is implemented as a pole $\mathbf{p} = 0.01$ to numerically integrate τ_α. Because the amplification tracking relies mostly on $\mathbf{C}_\alpha(\mathbf{s})$, a static gain of 8.18 and a 1 Hz dynamic gain of 1.42 with phase shift of -56.94° are expected for $-\tau_{\mathbf{s}}/\tau_{\mathbf{c}}$.

The experiment results (Fig. 2.12-2.13) verify that the exoskeleton is stable with all eight settings. The values of gain and phase shift are also close to the expected values (Tab. 2.3). The results show little influence on amplification tracking from the variation of $\mathbf{S_h}$ and $\mathbf{M_e}$, as expected.

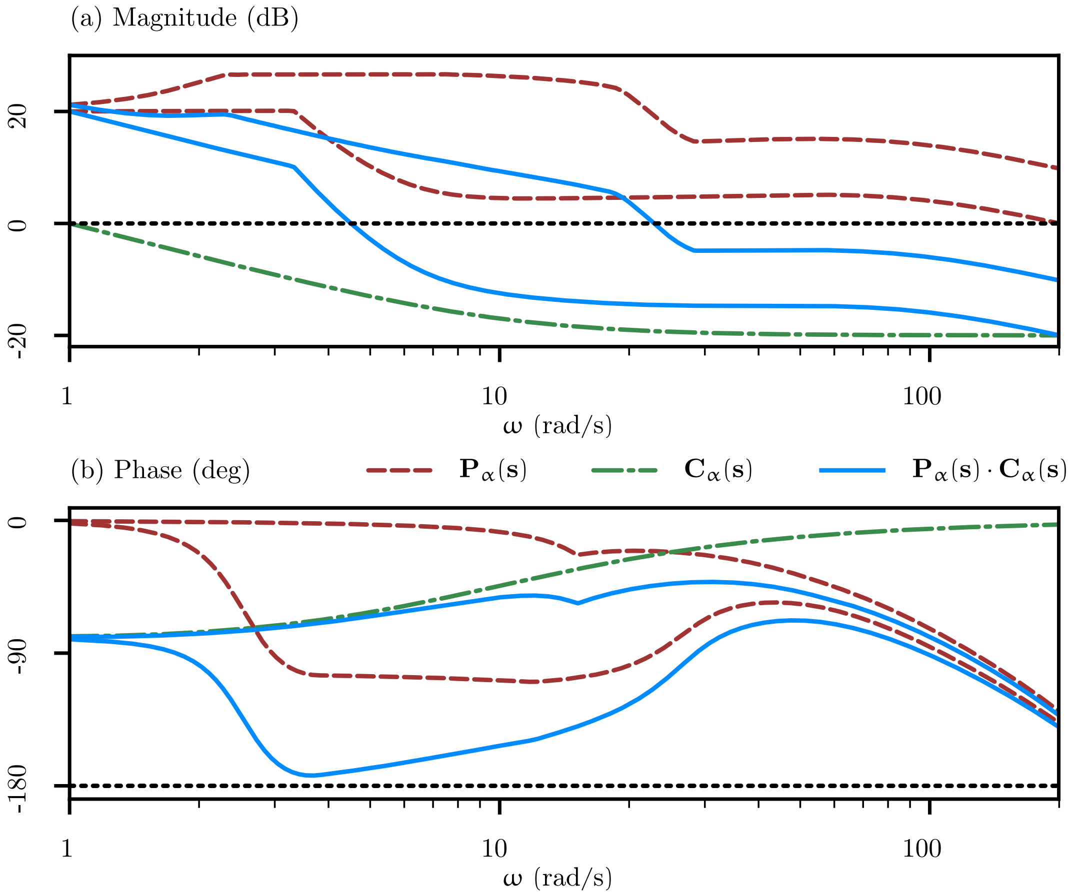

Figure 2.11: Uncertain model of $\mathbf{P}_\alpha(\mathbf{s})$ is made by 20 interpolations of $\mathbf{K_h}$ in the range of [7.44, 70.11] Nm/rad and 20 interpolations of $\mathbf{M_e}$ in the range of [0.1, 1.05] $\text{kg} \cdot \text{m}^2$. Time delay is 6 ms.

(a) 0 Load & Open Hand

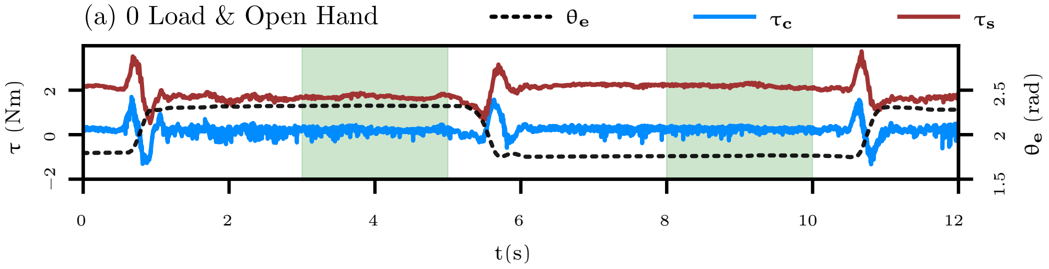

(b) 0 Load & Closed Hand

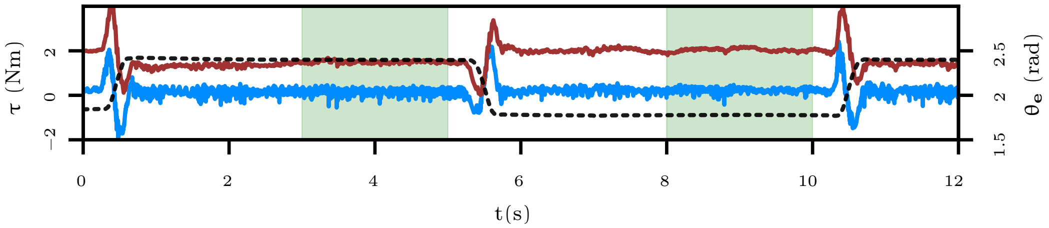

(c) 10 lb Load & Open Hand

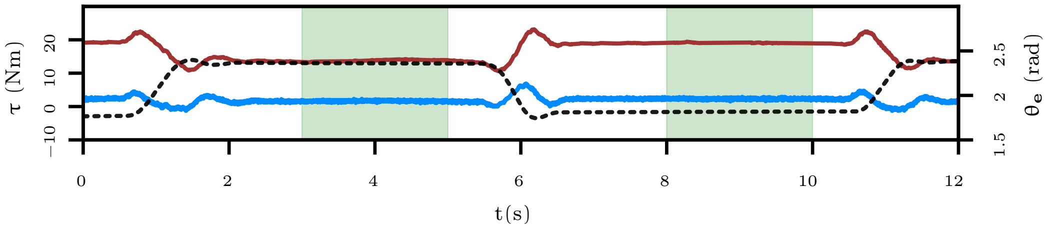

(d) 10 lb Load & Closed Hand

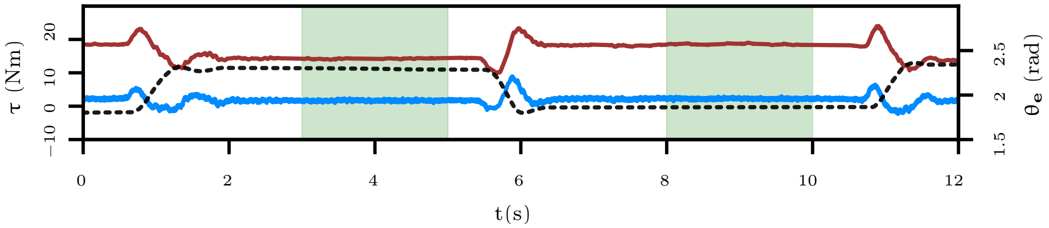

Figure 2.12: Steady state tests (a)-(d) are processed from the subject. Only data in the green highlighted regions are used for calculating the static gain.

(a) 0 Load & Open Hand

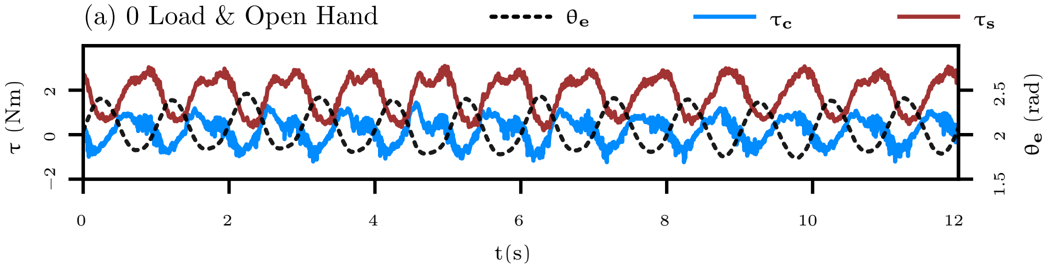

(b) 0 Load & Closed Hand

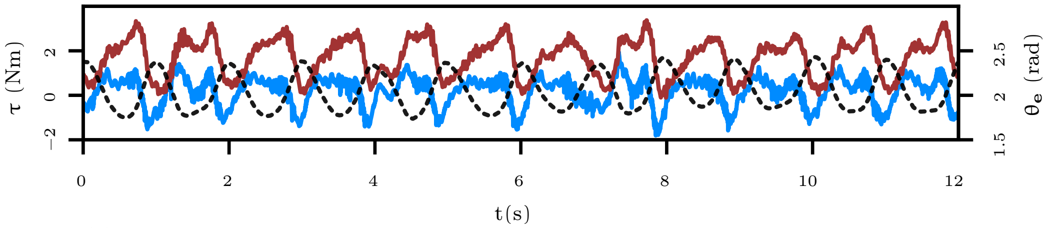

(c) 10 lb Load & Open Hand

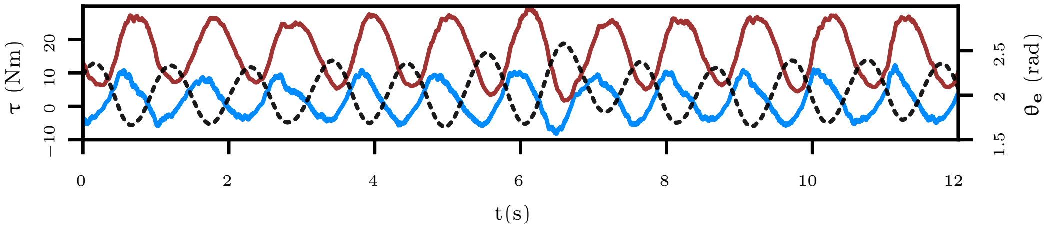

(d) 10 lb Load & Closed Hand

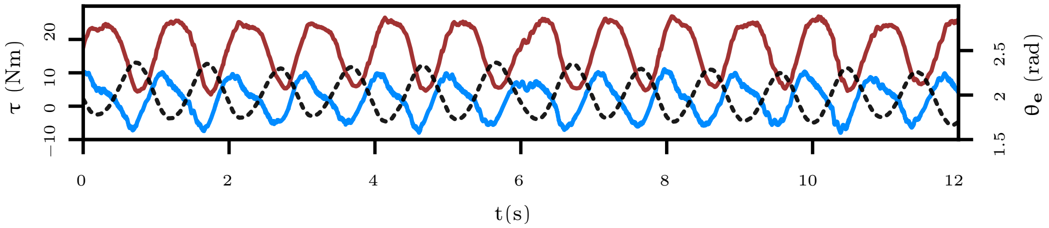

Figure 2.13: 1 Hz dynamic tests (a)-(d) are processed from the subject. All torque data in this figure are used for calculating the gain at 1 Hz.

Chapter 3

Human Complex Stiffness Model

Among all different kinds of dynamic model of an individual human joint, perhaps the most popular one is the mass-spring-damper model—with the additional non-linearity that the spring stiffness of the human joint can be modified by both voluntary muscle contractions or external torques exerted on the joint [Bennett, Hollerbach, Xu, and Hunter, 1992]. Several studies demonstrated a linear relationship between the stiffness of the human (found by fitting a linear mass-spring-damper model for a single joint) and an external torque [Agarwal and Gottlieb, 1977; Cannon and Zahalak, 1982; Hunter and Kearney, 1982]. For modeling the human joint damping, some other studies explored the fact that not only the stiffness but also the damping increases with muscle contractions [Becker and Mote, 1990] and external torques [Weiss, Hunter, and Kearney, 1988]. A linear relationship between the damping and the external torque has also been identified for the human ankle joint, but it is statistically weaker than the strong linear relationship between the stiffness

---

The results presented in this chapter have also appeared in part of [He, Huang, Thomas, and Sentis, 2019] and [He, Huang, Thomas, and Sentis, 2020a]. The human subject study in this work was conducted by Binghan He and Huang Huang. As the primary contributor, Binghan He processed the statistical analysis of experimental data. Gray C. Thomas provided theory supports on statistical analysis. This research was advised by Luis Sentis.

of the ankle and the external torques [Agarwal and Gottlieb, 1977; Hunter and Kearney, 1982]. However, it is not clear from the literature that a linear relationship between the damping and the stiffness of a human joint can be expected in more general cases.

In Chapter 2, we model the damping in the linear mass-spring-damper model through the empirical observation that a relatively consistent damping ratio is maintained by the human elbow across different joint stiffnesses [He, Thomas, Paine, and Sentis, 2019]. Frequency domain identification of the ankle joint impedance [Agarwal and Gottlieb, 1977; Gottlieb and Agarwal, 1978] also showed a consistent damping ratio within the range from 0.22 to 0.49. This damping ratio consistency on the ankle is also supported by the fact that the ankle damping ratio does not have significant change with large variations of mean external torques exerted on the subjects [Weiss, Hunter, and Kearney, 1988]. For upper limbs, a multi-joint impedance study on human arms [Perreault, Kirsch, and Crago, 2004] showed that the damping ratio of the minimally damped mode for the 2-D endpoint impedance in the transverse plane is distributed with a mean of 0.26 and a standard deviation of 0.08. Although this could be explained as the effect of humans adapting their damping to stabilize movement [Milner and Cloutier, 1993], a more detailed explanation of how humans achieve this consistency remains unclear.

Hysteretic damping models have seen success in biomechanical modelling before. In [Agarwal and Gottlieb, 1977], experimental results showed a hysteretic relationship between the applied torque and the ankle angle at very low frequencies. Hysteretic damping is shown indirectly in [Cannon and Zahalak, 1982, Fig. 6], where the human elbow stiffness has a phase shift around 25 degrees in a wide range of low frequencies—contradicting the viscous damping hypothesis. This type of phase behavior is explained (in the field of structural mechanics) by defining a hysteretic damping whose damping coefficient is proportional to the inverse of frequency [Bishop and Johnson, 1960]. Models with hysteretic damping have also been adapted to describe the dynamic properties of the whole body of a seated human [Kitazaki and Griffin, 1997] as well as cockroach legs [Dudek and Full, 2006].

In this chapter, we conduct a more in-depth study about the human stiffness and damping behavior when coupled to an exoskeleton inertia, and test the effectiveness of a hysteretic damping term in the system model. More specifically we compare three models 1) a linear mass, spring, and viscous damper model, 2) a nonlinear complex-stiffness-spring and mass model (that is, a spring, mass, and hysteretic damper model), and 3) a combination model with mass, spring, and both viscous and hysteretic damping. Our results show that there is a statistically significant benefit of the hysteretic damping term (comparing model 1 to model 3 with an F-test), and a less significant benefit for the viscous damping term (comparing model 2 to model 3). This hysteretic damping explains the consistent damping-ratio of the human–exoskeleton resonant peak even as the stiffness and exoskeleton inertia change—which is not well explained by the linear model. And it also explains the low frequency phase lag in human stiffness (previously observed in [Cannon and Zahalak, 1982]). Our elbow joint experiments vary parameters which would result in a differing damping ratio if the linear model were true: we change the inertia of the exoskeleton, and (indirectly, using an adjustable exercise hand grip and a bias torque) the stiffness of the human joint. We also test different exoskeleton strength amplification factors, and it does not appear to elicit a different human behavior than when the inertia is simply reduced.

Similar to Chapter 2, we employed the P0 series elastic elbow-joint exoskeleton from Apptronik Systems (Fig. 3.1) for this study. This exoskeleton has a moment of inertia of 0.1 $\mathrm{kg} \cdot \mathrm{m}^2$ with no load on it, but allows for attaching additional weights to it. A load, attached 0.45 m from the exoskeleton joint, is pictured in Fig. 3.1.b. The contact force $\mathbf{f_c}$ between the human and the exoskeleton is measured by a six-axis force/torque sensor situated below the white 3D printed "cuff" (which includes the adjustable strap which clamps the forearm). This force torque signal is cast as a torque ($\tau_\mathbf{c}$) using the motion Jacobian $\mathbf{J}$ of the sensor frame ($\tau_\mathbf{c} = \mathbf{J}^\top \mathbf{f_c}$). Rubber pads are adhered to the inside surfaces of the cuff and the cuff strap to improve user comfort. Joint position $\theta_\mathbf{e}$ is directly measured by a dedicated encoder at the exoskeleton joint. The series elastic actuator (SEA) has a spring force control bandwidth of 10 Hz and provides high fidelity actuator torque $\tau_\mathbf{s}$ tracking using the force control disturbance observer of [Paine, Oh, and Sentis, 2014].

In parallel with an excitation chirp command (which essentially performs system identification of the human subject), a gravity compensation controller, a human amplification controller, and a bias torque comprise the desired actuator torque signal. The gravity compensation controller takes the measurement of $\theta_\mathbf{e}$ to calculate and compensate the gravity torque $\tau_\mathbf{g}$ acting on the exoskeleton system. The human amplification controller takes the measurement of $\tau_\mathbf{c}$ and multiplies $\tau_\mathbf{c}$ by negative $\alpha - 1$. With the assistance of actuator torques produced from the amplification command, the human's interaction forces with the exoskeleton are amplified by a factor of α. This exoskeleton amplification strategy differs from the one we applied in [He, Thomas, Paine, and Sentis, 2019] in the directness of the amplification feedback.

3.1 Three Human Impedance Models

We use three models describing human-exoskeleton interactions in our statistical tests. As preliminaries, we first define $\mathbf{K_h}$ as the (real-valued) human elbow-joint apparent stiffness, $\mathbf{H_h}$ as the human elbow-joint hysteretic damping, $\mathbf{B_h}$ as the human elbow-joint viscous damping, $\mathbf{M_h}$ as the moment of inertia of the human, and $\mathbf{M_e}$ as the moment of inertia of the exoskeleton. With the amplification control specified by the factor α, the subject feels an attenuated inertia $\mathbf{M_e}/\alpha$ from the interaction with the exoskeleton. Therefore, we also define the perceived inertia $\mathbf{M}_{\mathbf{h\text{-}e}/\alpha} \triangleq \mathbf{M_h} + \mathbf{M_e}/\alpha$ at the elbow joint.

3.1.1 Linear Model Versus Nonlinear Model

The first model is a passive linear model with viscous damping and stiffness:

$$\mathbf{S}_{\mathbf{h\text{-}e}/\alpha}(\mathbf{s}) = \mathbf{M}_{\mathbf{h\text{-}e}/\alpha}\mathbf{s}^2 + \mathbf{B_h}\mathbf{s} + \mathbf{K_h}. \tag{M1}$$

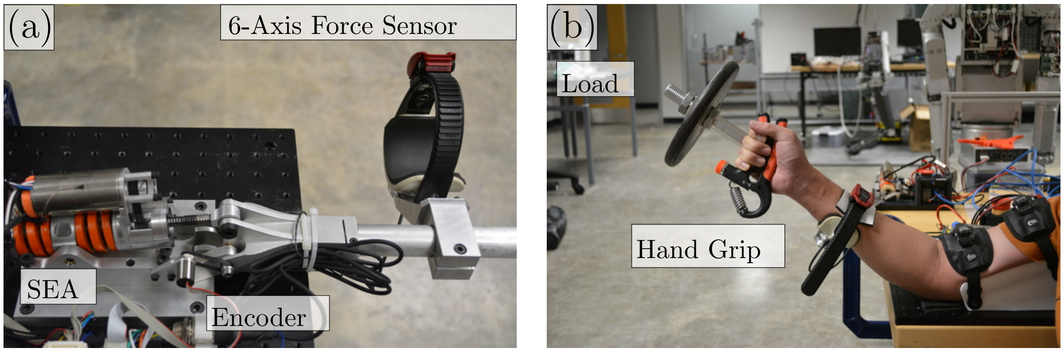

Figure 3.1: Experimental apparatus consisting of a series elastic P0 exoskeleton from Apptronik Systems, featuring an ATI Mini40 force sensitive cuff and a P170 Orion air cooled series elastic actuator module acting through a simple 3 bar linkage.

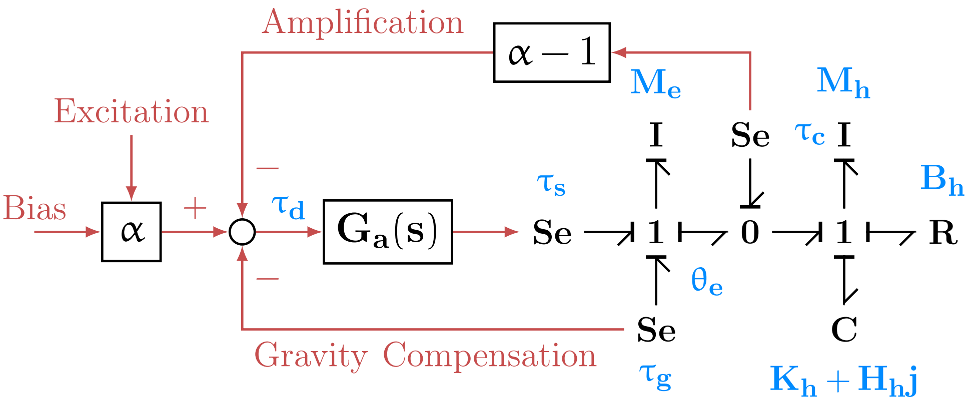

Figure 3.2: Block diagram consisting of amplification, gravity compensation and experiment perturbation. Dynamics of human with exoskeleton are expressed as a bond graph with effort source of τ_s, τ_c and τ_g.

Replacing the viscous damping in (M1) by a hysteretic damping we arrive at our second model:

$$\mathbf{S}_{\mathbf{h\text{-}e}/\alpha}(\mathbf{s}) = \mathbf{M}_{\mathbf{h\text{-}e}/\alpha}\mathbf{s}^2 + \mathbf{H}_\mathbf{h}\mathbf{j} + \mathbf{K}_\mathbf{h}, \tag{M2}$$

where a complex stiffness appears. Finally, to generalize (M1) and (M2), we consider a third model with both viscous and hysteretic damping:

$$\mathbf{S}_{\mathbf{h\text{-}e}/\alpha}(\mathbf{s}) = \mathbf{M}_{\mathbf{h\text{-}e}/\alpha}\mathbf{s}^2 + \mathbf{B}_\mathbf{h}\mathbf{s} + \mathbf{H}_\mathbf{h}\mathbf{j} + \mathbf{K}_\mathbf{h}. \tag{M3}$$

In order to take advantage of the clean human cuff sensor signal, we express these models in terms of the dynamic stiffness of the human alone, $\mathbf{S}_\mathbf{h}(\mathbf{s}) = \tau_\mathbf{c}(\mathbf{s})/\theta_\mathbf{e}(\mathbf{s})$, using the following three equalities to learn the model parameters of (M1)–(M3) respectively:

$$\mathbf{S}_\mathbf{h}(\mathbf{s}) = \mathbf{M}_\mathbf{h}\mathbf{s}^2 + \mathbf{B}_\mathbf{h}\mathbf{s} + \mathbf{K}_\mathbf{h}, \tag{3.1}$$

$$\mathbf{S}_\mathbf{h}(\mathbf{s}) = \mathbf{M}_\mathbf{h}\mathbf{s}^2 + \mathbf{H}_\mathbf{h}\mathbf{j} + \mathbf{K}_\mathbf{h}, \tag{3.2}$$

$$\mathbf{S}_\mathbf{h}(\mathbf{s}) = \mathbf{M}_\mathbf{h}\mathbf{s}^2 + \mathbf{B}_\mathbf{h}\mathbf{s} + \mathbf{H}_\mathbf{h}\mathbf{j} + \mathbf{K}_\mathbf{h}. \tag{3.3}$$

The original transfer function can be recovered by adding in the exoskeleton inertia term $\mathbf{S}_{\mathbf{h\text{-}e}/\alpha}(\mathbf{s}) = \mathbf{S}_\mathbf{h}(\mathbf{s}) + \frac{1}{\alpha}\mathbf{M}_\mathbf{e}\mathbf{s}^2$. By re-casting the parameter estimation problem as the problem of estimating this re-creation of $\mathbf{S}_{\mathbf{h\text{-}e}/\alpha}(\mathbf{s})$, we can take advantage of the clean sensor data and avoid various corrupting effects in the $\tau_\mathbf{s}(\mathbf{s})$ signal. Since the actual exoskeleton's dynamics are bypassed, the potential influence of unmodeled exoskeleton damping on the estimated parameters is eliminated.

3.1.2 Damping Ratio

In order to further explore the relatively consistent damping ratio that we observe from the mass-spring-damper model study in Chapter 2, we also calculate the damping ratio $\zeta_{\mathbf{h\text{-}e}/\alpha}$ of $\mathbf{S}_{\mathbf{h\text{-}e}/\alpha}$. Because M2 and M3 have the $\mathbf{H_h j}$ term which provides a damping effect in addition to $\mathbf{B_h s}$, we define the damping ratio of each model using the imaginary part of the transfer function evaluated at the resonance:

$$\zeta_{\mathbf{h\text{-}e}/\alpha} = \frac{\mathbf{B_h}}{2\sqrt{\mathbf{K_h M}_{\mathbf{h\text{-}e}/\alpha}}} \quad \text{for M1,} \tag{3.4}$$

$$\zeta_{\mathbf{h\text{-}e}/\alpha} = \frac{\mathbf{H_h}\omega^{-1}_{\mathbf{h\text{-}e}/\alpha}}{2\sqrt{\mathbf{K_h M}_{\mathbf{h\text{-}e}/\alpha}}} = \frac{\mathbf{H_h}}{2\mathbf{K_h}} \quad \text{for M2, and} \tag{3.5}$$

$$\zeta_{\mathbf{h\text{-}e}/\alpha} = \frac{\mathbf{B_h}}{2\sqrt{\mathbf{K_h M}_{\mathbf{h\text{-}e}/\alpha}}} + \frac{\mathbf{H_h}}{2\mathbf{K_h}} \quad \text{for M3,} \tag{3.6}$$

where $\omega_{\mathbf{h\text{-}e}/\alpha} = \sqrt{\mathbf{K_h}/\mathbf{M}_{\mathbf{h\text{-}e}/\alpha}}$ is the natural frequency of $\mathbf{S}_{\mathbf{h\text{-}e}/\alpha}$.

3.2 Pilot Study

The experimental protocol was approved by the Institutional Review Board (IRB) at the University of Texas at Austin. The pilot study consists of fifteen perturbation experiments with a 28-year old male subject. The experiments are separated into three groups of five experiments.

Table 3.1: Experimental Setting of Pilot Study

Exp	α	Load (kg)	Grip (kg)	Bias (Nm)	Amplitude (Nm)	Frequency Range (rad/s to rad/s)
1	1	0.6	10	0	2	$2-20$
2	1	2.3				
3	1	4.5				
4	2	4.5				
5	4	4.5				
6	1	0.6	14	4	2	$3-30$
7	1	2.3				
8	1	4.5				
9	2	4.5				
10	4	4.5				
11	1	0.6	27	8	2	$4-40$
12	1	2.3				
13	1	4.5				
14	2	4.5				
15	4	4.5				

3.2.1 Experimental Protocol

The first three experiments in each group are conducted with loads of 0.6 kg, 2.3 kg and 4.5 kg and an α value of 1 (corresponding to a non-amplification controller) while the last two experiment in each group are conducted with a load of 4.5 kg and α values of 2 and 4. The mass of the loads and the mass of the exoskeleton have their gravitational bias torque fully compensated through gravity compensation control, while their inertia is attenuated by a factor of α due to the cuff torque feedback.

The stiffness of the human elbow is influenced by muscle co-contraction as well as by contraction to resist the bias torque. In order to obtain different values of elbow stiffness for the three experiment groups, both the bias torque component of the controller and the co-contraction are varied. The three groups have, respectively, 0 Nm, 4 Nm, and 8 Nm of bias torque. Co-contraction is controlled by having the subject squeeze an adjustable force hand grip. The three groups have a 10-kg, a 14-kg, and a 27-kg gripping force respectively. The amplitude of the perturbation chirp signal is set to be 2 Nm.

To avoid fatigue of the subject, the duration of each perturbation experiment is set to be 100 seconds. The perturbation is set to be an exponential chirp signal, and the results are typically analyzed in the frequency domain. To sufficiently capture the natural frequency for damping feature identification, we set different ranges of frequency for the chirp signal according to the stiffness values the subject achieved from the bias torque and the gripping force. Frequency ranges of 2-20 rad/s, 3-30 rad/s and 4-40 rad/s are set for the chirp signals for the three experiment groups.

After the chirp perturbation experiments, we transfer the time domain data into the frequency domain and identify the dynamic stiffness model of the subject by linear regression. The parameters of the three experiment groups are summarized in Tab. 3.1.

3.2.2 Bode Plots

In the frequency domain results of $\mathbf{S}_{\mathbf{h\text{-}e}/\alpha}$ (Fig. 3.3), the phase starts (at low frequencies) from a value between 25° to 45° instead of zero and changes very little across all the frequencies before it reaches the second order zero at $\omega_{\mathbf{h\text{-}e}/\alpha}$ for each experiment. This type of phase shift is very different from the

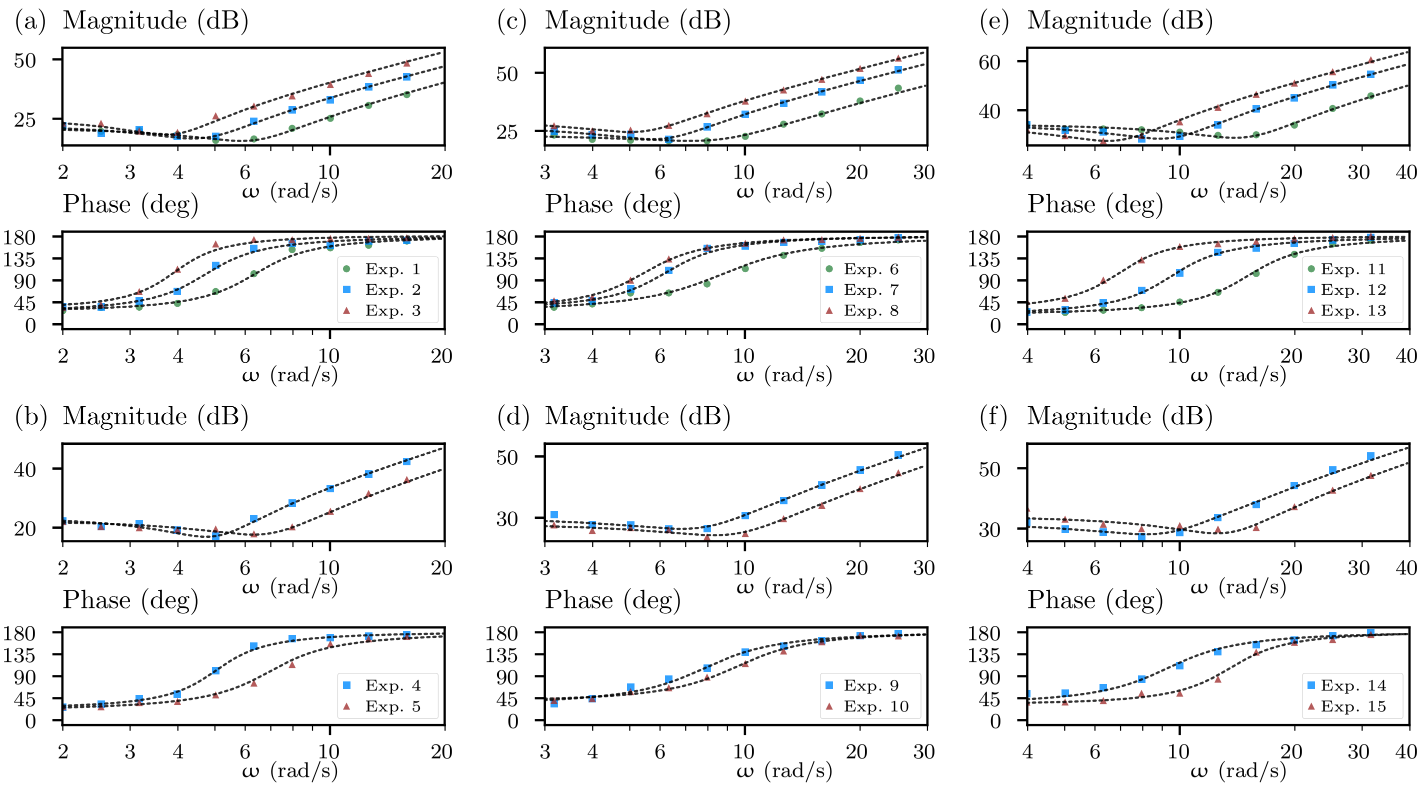

Figure 3.3: Bode plots show frequency domain data of $\mathbf{S}_{\mathbf{h\text{-}e}/\alpha}$ with Exp. 1-5 on (a) and (b), Exp. 6-10 on (c) and (d), and Exp. 11-15 on (e) and (f). The dash lines on each plot show the fitted curves from M3.

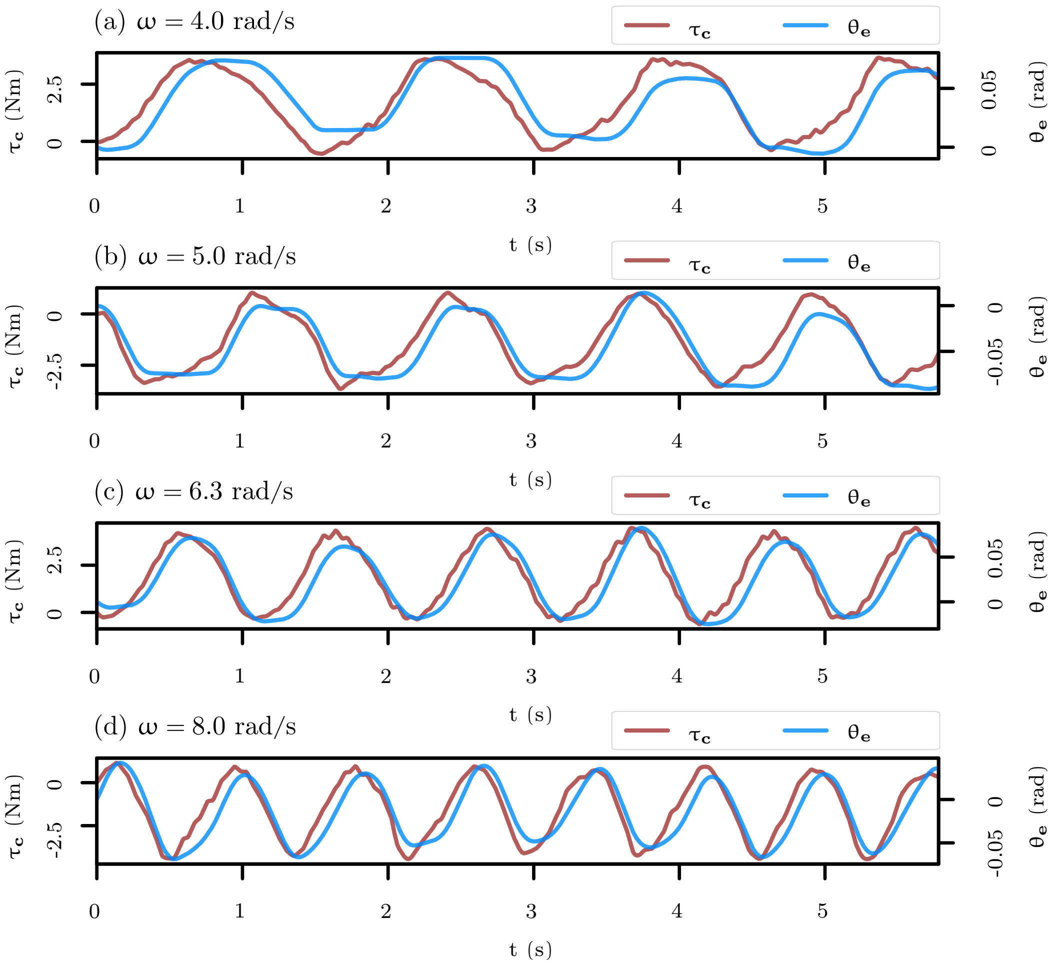

Figure 3.4: Four pieces of time data of $\boldsymbol{\tau_c}$ and $\boldsymbol{\theta_e}$ from Exp.11 used for identifying the frequency data of $\mathbf{S}_{\mathbf{h\text{-}e}/\alpha}$ at the frequencies of 4.0, 5.0, 6.3 and 8.0 rad/s show the phase shift in the time domain.

Table 3.2: Model Parameters of Pilot Study

Exp	Model	$\mathbf{K_h}(\frac{\mathrm{Nm}}{\mathrm{rad}})$	$\mathbf{H_h}(\frac{\mathrm{Nm}}{\mathrm{rad}})$	$\mathbf{B_h}(\frac{\mathrm{Nms}}{\mathrm{rad}})$	$\mathbf{M_{h\text{-}e/\alpha}}$ (kgm^2)	$\omega_{\mathbf{h\text{-}e}/\alpha}(\frac{\mathrm{rad}}{\mathrm{s}})$	$\zeta_{\mathbf{h\text{-}e}/\alpha}$
1	M1	10.05	--	1.03	0.28	5.95	0.31
	M2	10.05	5.89	--	0.28	5.95	0.29
	M3	10.05	4.97	0.18	0.28	5.95	0.30
2	M1	11.80	--	1.51	0.60	4.44	0.28
	M2	11.80	6.68	--	0.60	4.44	0.28
	M3	11.80	5.44	0.31	0.60	4.44	0.29
3	M1	15.74	--	2.09	1.18	3.65	0.24
	M2	15.74	8.33	--	1.18	3.65	0.26
	M3	15.74	10.44	−0.60	1.18	3.65	0.26
4	M1	13.82	--	1.46	0.60	4.78	0.25
	M2	13.82	6.87	--	0.60	4.78	0.25
	M3	13.82	6.01	0.21	0.60	4.78	0.25
5	M1	12.09	--	1.22	0.28	6.59	0.33
	M2	12.09	6.84	--	0.28	6.59	0.28
	M3	12.09	4.26	0.52	0.28	6.59	0.32
6	M1	12.73	--	1.41	0.20	7.94	0.44
	M2	12.73	10.18	--	0.20	7.94	0.40
	M3	12.73	5.86	0.66	0.20	7.94	0.44
7	M1	18.79	--	1.91	0.57	5.72	0.29
	M2	18.79	11.77	--	0.57	5.72	0.31
	M3	18.79	11.54	0.04	0.57	5.72	0.31
8	M1	25.95	--	3.08	1.03	5.02	0.30
	M2	25.95	16.75	--	1.03	5.02	0.32
	M3	25.95	15.48	0.26	1.03	5.02	0.32
9	M1	25.77	--	2.83	0.52	7.02	0.39
	M2	25.77	20.49	--	0.52	7.02	0.40
	M3	25.77	16.60	0.60	0.52	7.02	0.40
10	M1	19.07	--	1.88	0.28	8.32	0.41
	M2	19.07	16.27	--	0.28	8.32	0.43
	M3	19.07	15.72	0.08	0.28	8.32	0.43
11	M1	48.15	--	1.97	0.23	14.4	0.29
	M2	48.15	25.45	--	0.23	14.4	0.26
	M3	48.15	16.66	0.76	0.23	14.4	0.29
12	M1	48.60	--	2.85	0.58	9.13	0.27
	M2	48.60	25.61	--	0.58	9.13	0.26
	M3	48.60	15.19	1.23	0.58	9.13	0.27
13	M1	42.23	--	3.19	1.01	6.47	0.24
	M2	42.23	23.60	--	1.01	6.47	0.28
	M3	42.23	24.08	−0.07	1.01	6.47	0.28
14	M1	32.22	--	2.82	0.46	8.35	0.37
	M2	32.22	25.36	--	0.46	8.35	0.39
	M3	32.22	20.83	0.55	0.46	8.35	0.39
15	M1	42.33	--	2.08	0.27	12.43	0.31
	M2	42.33	26.50	--	0.27	12.43	0.31
	M3	42.33	27.66	−0.11	0.27	12.43	0.31

phase shift usually experienced by a linear system with a constant time delay or a constant damping property in which the phase shift approaches zero in the limit as $\omega \to 0$. As shown in Fig. 3.4, this phase shift is clearly visible even in time domain comparisons of τ_c and θ_e. The data show that the human joint motion θ_e is not perfectly sinusoidal—it stops following the trend of the torque after they both reach their peak values and "waits" before following the torque τ_c in its descent. At low frequencies, these peaks seem especially flat.

3.2.3 Statistical Analysis

In order to compare the significance of $\mathbf{B_h s}$ and $\mathbf{H_h j}$ in the human-exoskeleton interaction model, we calculate the residual square sum (RSS) for all three models, denoted $\mathbf{R_{M1}}$, $\mathbf{R_{M2}}$ and $\mathbf{R_{M3}}$ respectively. For each experiment, we conduct F-tests for each of the two three-parameter models (M1 and M2) against the generalizing four-parameter model (M3). Our F-statistic accounts for complex value data,

$$\mathbf{F_{Mi\text{-}M3}} = \frac{\mathbf{R_{Mi}} - \mathbf{R_{M3}}}{\mathbf{R_{M3}}}(2\mathbf{n} - 4), \quad \text{for } \mathbf{i} = 1, 2 \tag{3.7}$$

where $\mathbf{n}$ is the number of complex value samples at the frequency domain and the real and imaginary parts of each sample are statistically independent. The significance of $\mathbf{B_h s}$ and $\mathbf{H_h j}$ then will be evaluated by comparing this F statistic against a critical F statistic threshold based on a 0.05 false-rejection probability.

We split the 100 seconds of time domain data for each experiment into 10 sequences. For each of the 10 second sequences, only the data from the first 5.78 seconds is used for calculating the frequency domain sample. The remainder period of 4.22 seconds is greater than the 2% settling time for all the 2nd order dynamics of $\mathbf{S_{h\text{-}e/\alpha}}$ identified in the experiments. By this method we can safely assume statistical independence between the 10 single-frequency data points comprising our estimate of the frequency response function for the purposes of statistical testing.

The results of the identified parameters (Tab. 3.2) show that the three models give the same values of $\mathbf{K_h}$, $\mathbf{M_{h\text{-}e/\alpha}}$ and consequently $\omega_{\mathbf{h\text{-}e/\alpha}}$ to two decimal places for each experiment. This is because the difference between the three models is restricted to the imaginary part of $\mathbf{S_{h\text{-}e/\alpha}}$ while $\mathbf{K_h}$ and $\mathbf{M_{h\text{-}e/\alpha}}$ are the coefficients of the real part of $\mathbf{S_{h\text{-}e/\alpha}}$. Although the identified values of $\mathbf{B_h}$ and $\mathbf{H_h}$ are quite different between the three models, the values of $\zeta_{\mathbf{h\text{-}e/\alpha}}$ are still very close for each experiment. This means that the three models give very similar values for the slope of the phase at the resonant frequency $\omega_{\mathbf{h\text{-}e/\alpha}}$.

From M1 to M3, the values of $\mathbf{B_h}$ have been reduced considerably. This means that M3 uses the $\mathbf{H_h j}$ term to replace part of the $\mathbf{B_h}$ term in M1 while maintaining a similar phase behavior at the frequency $\omega_{\mathbf{h\text{-}e/\alpha}}$. From M2 to M3, the values of $\mathbf{H_h}$ have been reduced except for Exp. 3, 13 and 15 in which M3 gives a negative value for $\mathbf{B_h}$. These negative value of $\mathbf{B_h}$ is because there is no lower bound constraint on the value of $\mathbf{B_h}$ during the frequency domain regression for M3. Although a negative value of $\mathbf{B_h}$ brings non-passivity to a linear mass-spring-damper system in the common sense, the $\mathbf{H_h j}$ term in M3 enforces the dynamics of $\mathbf{S_{h\text{-}e/\alpha}}$ to remain passive across the range of frequencies in our experiments.

The results from the F-tests (Fig. 3.5) relate to the significance of $\mathbf{B_h s}$ and $\mathbf{H_h j}$ in M3. Based on the 20 statistically independent data values for each experiment, a critical F-statistic value of 4.49 is calculated for 0.05 false-rejection probability. The results show that values of $\mathbf{F_{M1\text{-}M3}}$ for all the experiments are much higher than the critical F-statistic value, with the values of $\mathbf{F_{M1\text{-}M3}}$ in Exp. 8 and 10 exceeding 100 (c.f. the critical value of 4.49). This proves that the existence of the $\mathbf{H_h j}$ term in M3 significantly improves modeling accuracy of $\mathbf{S_{h\text{-}e/\alpha}}$. The values of $\mathbf{F_{M2\text{-}M3}}$ are mostly below the critical F-statistic value except for Exp. 5, 6, 11 and 12. The other observation is that the value of $\mathbf{F_{M2\text{-}M3}}$ is always much lower than the value of $\mathbf{F_{M2\text{-}M3}}$ for all experiments. Although the effect of the $\mathbf{B_h s}$ term cannot be completely ignored based on the results of these F-tests, we can claim that the $\mathbf{H_h j}$ term is still much more significant than the $\mathbf{B_h s}$ term in M3.

Because the $\mathbf{H_h j}$ term is created to describe the phase shift effect from the complex human stiffness in M2 and M3, we suspect that the identified value of $\mathbf{H_h}$ has a linear relation with the value of $\mathbf{K_h}$. Therefore, we apply linear regression between the values of $\mathbf{H_h}$ and $\mathbf{K_h}$ identified from M2 and M3 (Fig. 3.6). Compared with M3, the linear regression result with M2 shows a stronger linear relationship with a much higher coefficient of determination ($\mathbf{R}^2$). The regression equation identified from the M2 parameters also has a smaller value of bias from the origin of the $\mathbf{H_h}$-$\mathbf{K_h}$ plane compared with the regression equation identified from the M3 parameters. Intuition leads us to expect low bias in the regression equation, since a nonzero value of $\mathbf{H_h}$ when the value of $\mathbf{K_h}$ is zero could not be explained as hysteretic spring behavior.

Based on linear regression equations, we can express the phase shift $\phi_{\mathbf{h\text{-}e}/\alpha}$ (with respect to 0°) at the low frequencies as

$$\phi_{\mathbf{h\text{-}e}/\alpha} = \tan^{-1}(\frac{\mathbf{H_h}}{\mathbf{K_h}}) = \tan^{-1}(\mathbf{c_h} + \frac{\mathbf{d_h}}{\mathbf{K_h}}) \text{ for M2, and} \tag{3.8}$$

$$\phi_{\mathbf{h\text{-}e}/\alpha} = \tan^{-1}(\mathbf{c_h} + \frac{\mathbf{d_h} + \mathbf{B_h}\omega}{\mathbf{K_h}}) \qquad \text{for M3,} \tag{3.9}$$

where $\mathbf{H_h} = \mathbf{c_h}\mathbf{K_h} + \mathbf{d_h}$ is the regression equation identified from the values of $\mathbf{H_h}$ and $\mathbf{K_h}$ in M2 and M3 with $\mathbf{c_h}$ and $\mathbf{d_h}$ being the slope and the bias of the regression equation. By substituting $\mathbf{H_h} = \mathbf{c_h}\mathbf{K_h} + \mathbf{d_h}$ into (3.5) and (3.6), the value of $\zeta_{\mathbf{h\text{-}e}/\alpha}$ for M2 and M3 can be expressed as

$$\zeta_{\mathbf{h\text{-}e}/\alpha} = \frac{\mathbf{H_h}}{2\mathbf{K_h}} = \frac{\mathbf{c_h}}{2} + \frac{\mathbf{d_h}}{2\mathbf{K_h}} \qquad \text{for M2, and} \tag{3.10}$$

$$\zeta_{\mathbf{h\text{-}e}/\alpha} = \frac{\mathbf{c_h}}{2} + \frac{\mathbf{d_h}}{2\mathbf{K_h}} + \frac{\mathbf{B_h}}{2\sqrt{\mathbf{K_h}\mathbf{M}_{\mathbf{h\text{-}e}/\alpha}}} \qquad \text{for M3.} \tag{3.11}$$

Because the values of $\mathbf{d_h}$ of the regression equations for M2 and M3 and the values of $\mathbf{B_h}$ for M3 are relatively small, the phase shift at the low frequencies is dominated by the value of $\tan^{-1}(\mathbf{c_h})$ and the value of $\zeta_{\mathbf{h\text{-}e}/\alpha}$ is dominated by the constant $\mathbf{c_h}/2$ term. This explains the fact that the phase shift is non-zero at low frequencies and the fact that the value of $\zeta_{\mathbf{h\text{-}e}/\alpha}$ changes very little compared to the changes of $\mathbf{K_h}$ and $\mathbf{M}_{\mathbf{h\text{-}e}/\alpha}$ across all our experiments.

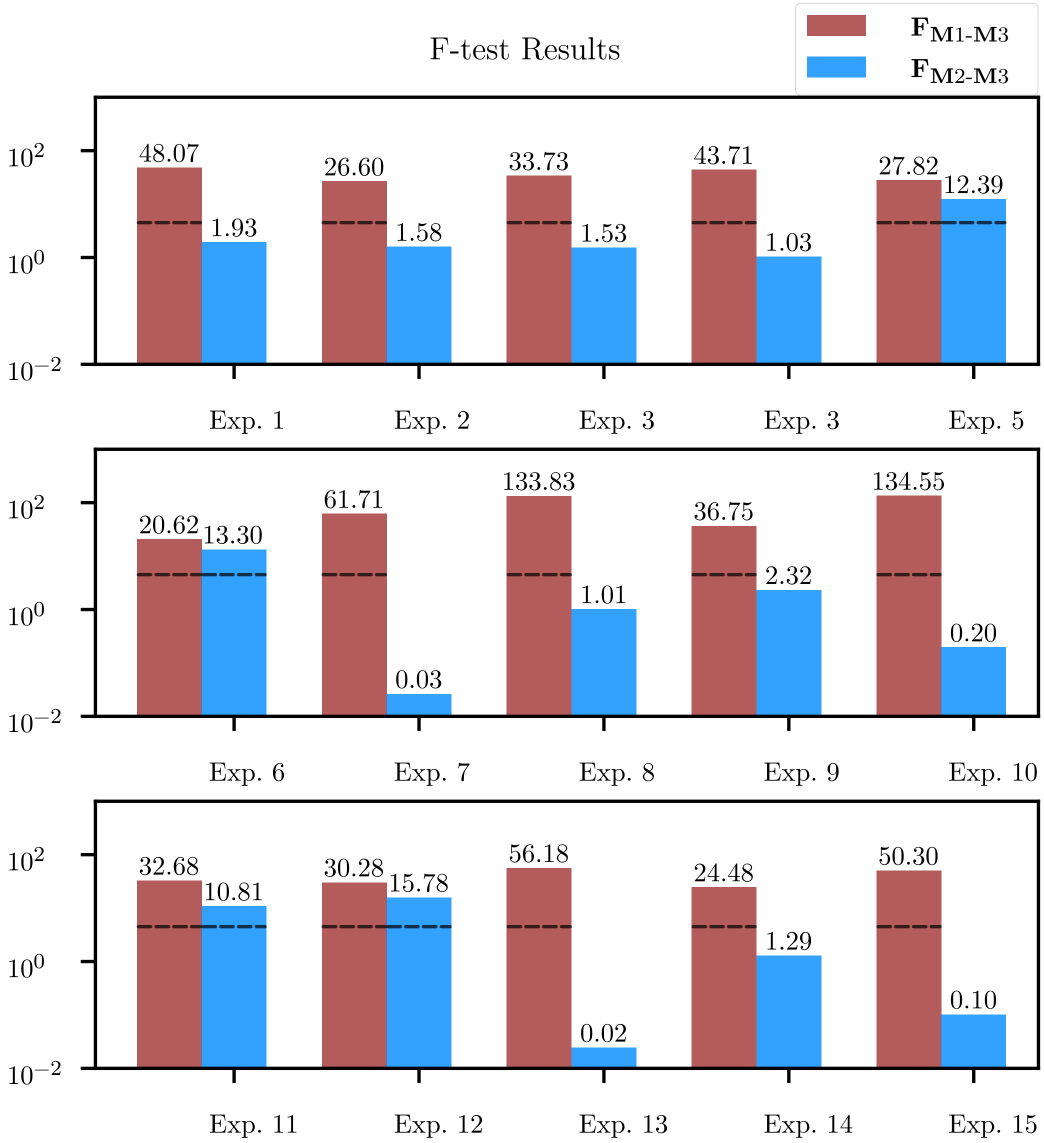

Figure 3.5: F-statistics on log scale for all experiments show the significant improvement on modeling accuracy from M1 to M3 and a partial improvement from M2 to M3. The dashed line appears on a bar if the F-statistic value is over the critical F-statistic value of 4.49 (false-rejection probability of 0.05).

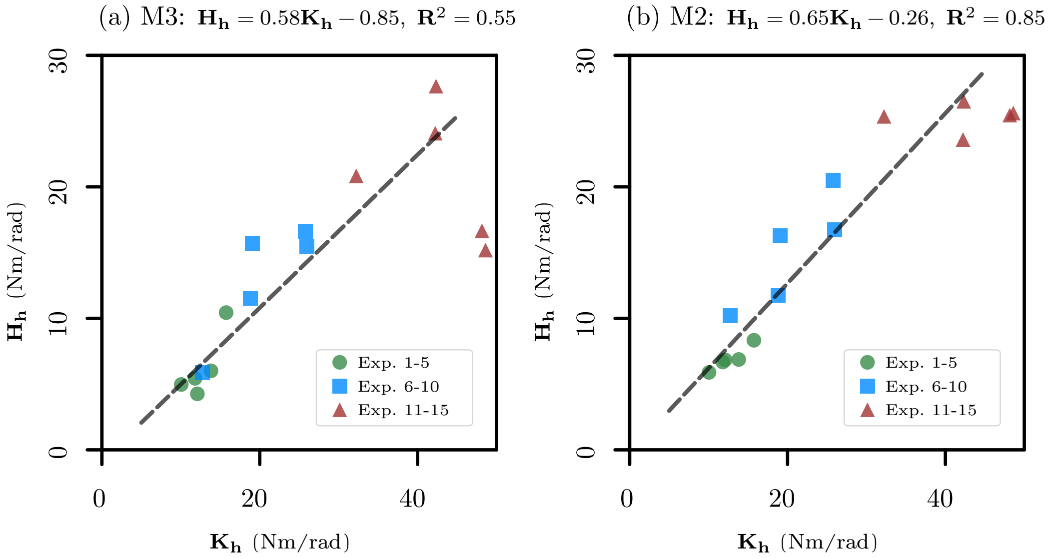

Figure 3.6: Linear Regressions between $\mathbf{H_h}$ and $\mathbf{K_h}$ for M3 (a) and M2 (b) show that the parameters of M2 have a stronger linear relationship (that is, a higher $\mathbf{R}^2$ value).

3.3 Full Study

The full study consists of nine perturbation experiments with 10 healthy subjects between the ages of 21-29, where subjects A-E are females and subjects F-J are males.

3.3.1 Experimental Protocol

The nine experiments are separated into three groups of three experiments. The three experiments in each group are conducted with a 4.5 kg load and an α value of 1 (corresponding to no amplification), 2, and 4. The gravity torque of the load and the exoskeleton itself are cancelled out by the gravity compensation feature of the controller, while the total inertia is attenuated by

Table 3.3: Experimental Setting of Full Study

Exp	α	Load (kg)	Grip (kg)	Bias (Nm)	Amplitude (Nm)	Frequency Range (rad/s to rad/s)
1	1	4.5	10	0	2	2×10^0 to $2 \times 10^{0.9}$
2	2					
3	4					
4	1	4.5	14	4	2	3×10^0 to $3 \times 10^{0.9}$
5	2					
6	4					
7	1	4.5	27	8	2	4×10^0 to $4 \times 10^{0.9}$
8	2					
9	4					

a factor of α due to the amplification feature.

Each of the three experimental groups are differently perturbed to achieve variation in elbow stiffnesses. Because the stiffness is determined by both muscle co-contraction and contraction to resist an external torque, we induce variation in stiffness by having each subject squeeze an adjustable force hand grip and by applying a bias torque from the actuator. The three experimental groups are divided into pairs of gripping forces and bias torques. The first group uses a 10 kg gripping force and a 0 Nm bias torque. The second group uses 14 kg and 4 Nm. And the third group uses 27 kg and 8 Nm.

Each of the nine perturbation experiments includes ten 60-sec periods. The bias torque is gradually added during the first 5 sec of each period while the subject raises the forearm to around a 45° angle from the resting position and starts to squeeze the hand grip. Then, a sinusoidal perturbation signal is added for the next 10 sec. After the sinusoidal perturbation signal finishes, the

Table 3.4: Observed Phase Shifts of Full Study

Subject	Exp. 1-3 (deg)		Exp. 4-6 (deg)		Exp. 7-9 (deg)	
	Mean	S.E.	Mean	S.E.	Mean	S.E.
A	27.8	3.1	25.4	2.8	18.1	2.5
B	27.2	2.4	34.8	2.5	35.2	2.0
C	16.7	2.6	21.6	3.3	22.8	2.7
D	34.7	2.7	38.5	2.4	33.3	3.0
E	17.6	2.5	10.7	2.8	11.1	2.2
F	33.7	2.1	33.4	2.2	27.5	3.0
G	23.9	3.2	16.7	3.2	15.2	2.6
H	19.3	3.1	23.4	4.4	25.3	2.2
I	18.3	2.5	14.5	3.7	10.4	2.4
J	19.9	3.2	20.0	3.6	14.6	4.1
Cuff	6.0	0.6	6.5	0.9	7.6	1.2

bias torque is gradually subtracted for another 5 sec with the subject bringing the arm back to the resting position and relaxing the hand. To avoid fatigue, the subject rests for the next 40 sec in each period.

In order to capture the natural frequency of the human elbow joint wearing the exoskeleton, we set different values of the perturbation frequency for the different groups of experiments previously described. The three experimental groups use 2 rad/s, 3 rad/s, and 4 rad/s for perturbation in the first time period. For other time periods, we set the perturbation frequencies to be $10^{0.1}$ times the frequency of the previous perturbation.

The amplitude of the sinusoidal perturbation signal is set to 2 Nm. However, after the perturbation frequency is higher than the natural frequency of $\mathbf{S}_{\mathbf{h\text{-}e}/\alpha}(\mathbf{s})$, the inertia effect $\mathbf{M}_{\mathbf{h\text{-}e}/\alpha}$ starts dominating the dynamic response and therefore the angle of displacement $\theta_{\mathbf{e}}$ becomes less and less sensitive to

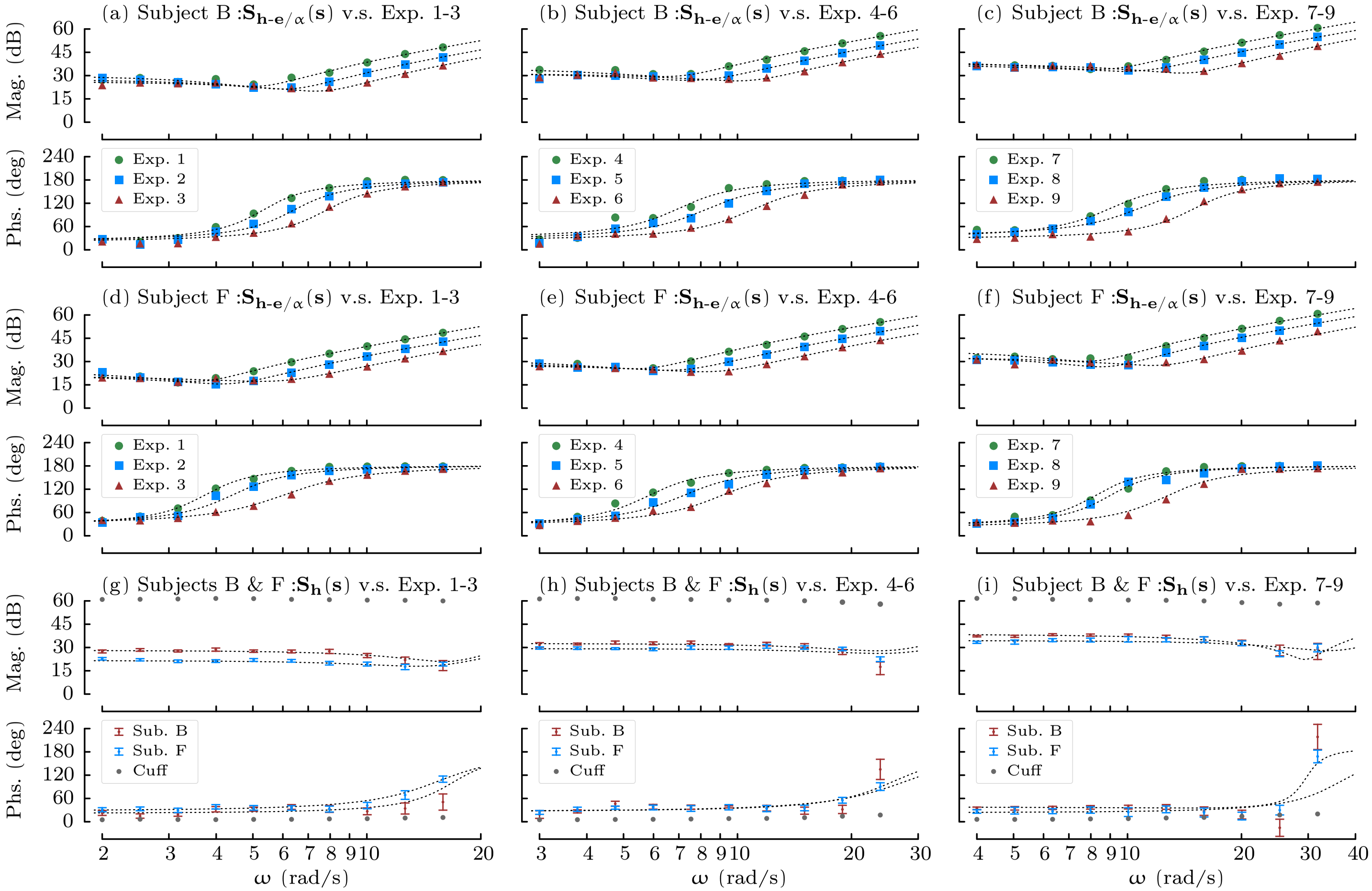

Figure 3.7: Bode plots for $\mathbf{S_{h\text{-}e/\alpha}(s)}$ showing all experiments for subject B in (a)-(c) and for subject F in (d)-(f). Bode plots for $\mathbf{S_h(s)}$ in (g)-(i) showing the mean and standard error across each experimental group for subjects B and F. The gray dots in (g)-(i) show the dynamic stiffness of the cuff identified through a superposition test. The dash lines show the fitted curves using M3 and (3.3).

the torque excitation. Thus, starting at the 8th perturbation time period for each experiment, we increase the amplitude of the perturbation signal by $10^{0.2}$ times in order to increase the sensitivity to the torque excitation.

In the end, we identify the three models of $\mathbf{S}_{\mathbf{h}\text{-}\mathbf{e}/\alpha}$ for all 90 subject experiments using linear regression in the frequency domain obtained from time domain data. The parameters of all nine experimental settings are summarized in Tab. 3.3.

3.3.2 Bode Plots

The frequency data for the two most representative subjects are shown in Fig. 3.7. Fig. 3.7.(a)-(f) shows the Bode plots of $\mathbf{S}_{\mathbf{h}\text{-}\mathbf{e}/\alpha}(\mathbf{s})$. Similarly to [Agarwal and Gottlieb, 1977, Fig. 4], [Gottlieb and Agarwal, 1978, Fig. 3], [Zahalak and Heyman, 1979, Fig. 2], the phase for each experiment shows a non-zero value (near 30° for subjects B and F) at low frequencies. This type of phase shift is very different from the phase shift values usually described by linear systems with viscous damping where the phase shift approaches zero as $\omega \to 0$.

Since $\mathbf{S}_{\mathbf{h}}(\mathbf{s})$ is unaffected by changes of $\mathbf{M}_{\mathbf{h}\text{-}\mathbf{e}/\alpha}$, we compute the statistics for all three experiments in each experimental group. Fig. 3.7.(g)-(i) shows the mean and standard error for each experimental group. Similarly to [Cannon and Zahalak, 1982, Fig. 6], the phase shift in each experimental group changes very little across a wide range of frequencies before it reaches the second order zero at the natural frequency $\omega_{\mathbf{h}}$ of $\mathbf{S}_{\mathbf{h}}(\mathbf{s})$.

Tab. 3.4 shows the mean and standard error for the phase shift of $\mathbf{S_h(s)}$ in each experimental group across different frequencies. The data for the last three frequencies is excluded from the calculation due to the effect of the second order zero at $\omega_{\mathbf{h}}$.

The sensor configuration for this experiment measures the deflection at the exoskeleton's hinge joint as well as the human torque using the cuff's six-axis force/torque sensor. Using this setup, we conduct a test of superposition for differentiating between the human elbow and cuff impedances. Fig. 3.7.(g)-(i) and Tab. 3.4 show the frequency data and phase shift values of the cuff attached to a rigid object. The phase of the cuff is lower than the phases of all human subjects. Furthermore, the magnitude of the cuff stiffness is above 60 dB (1000 Nm/rad), which is significantly higher than the stiffness values of all human subjects as shown in Tab. 3.4. We conclude that the human impedance becomes the dominant factor measured in our experiments.

3.3.3 Statistical Analysis

Since we split each experiment into ten 60-sec periods with 40-sec resting time within each period, the response of $\mathbf{S}_{\mathbf{h\text{-}e}/\alpha}\mathbf{(s)}$ to the sinusoidal perturbation in each period completely dies out before the next period. Therefore, for the purposes of statistical testing, we can safely assume statistical independence between any two single-frequency data points in each experiment.

Regarding the 10-sec sinusoidal perturbation within each period, only the data from the second 5-sec part of the perturbation is used for calculating each frequency domain sample. Because the first 5-sec perturbation time is greater than the 2% settling time for all $\mathbf{S_{h\text{-}e/\alpha}(s)}$ identified in our experiments, the output response reaches sinusoidal steady-state before entering the second 5-sec perturbation time period.

For each experiment on each subject, we calculate the residual square sum for all three models, denoted as $\mathbf{R_{M1}^{sub\text{-}exp}}$, $\mathbf{R_{M2}^{sub\text{-}exp}}$ and $\mathbf{R_{M3}^{sub\text{-}exp}}$ respectively, where $\mathbf{sub} = \text{A, B,} \cdots \text{, J}$ and $\mathbf{exp} = 1, 2, \cdots, 9$ are the indices of subjects and experiments. For $\mathbf{i} = 1, 2, 3$, let us define

$$\mathbf{R_{Mi}^{sub}} \triangleq \sum_{\mathbf{exp}=1}^{9} \mathbf{R_{Mi}^{sub\text{-}exp}}, \quad \mathbf{R_{Mi}^{exp}} \triangleq \sum_{\mathbf{sub}=\text{A}}^{\text{J}} \mathbf{R_{Mi}^{sub\text{-}exp}}, \tag{3.12}$$

$$\mathbf{R_{Mi}^{all}} \triangleq \sum_{\mathbf{exp}=1}^{9} \sum_{\mathbf{sub}=\text{A}}^{\text{J}} \mathbf{R_{Mi}^{sub\text{-}exp}}. \tag{3.13}$$

In order to compare the significance of $\mathbf{B_h s}$ and $\mathbf{H_h j}$ in the human-exoskeleton interaction model, we conduct F-tests for each of the two three-parameter models (M1 and M2) against the generalizing four-parameter model (M3). Our F-statistic accounts for frequency domain data. For $\mathbf{i} = 1, 2$,

$$\mathbf{F_{Mi\text{-}M3}^{sub}} = \frac{\mathbf{R_{Mi}^{sub}} - \mathbf{R_{M3}^{sub}}}{\mathbf{R_{M3}^{sub}}} \cdot \frac{(2\mathbf{n}-4)\cdot \mathbf{n_{exp}}}{(4-3)\cdot \mathbf{n_{exp}}}, \tag{3.14}$$

$$\mathbf{F_{Mi\text{-}M3}^{exp}} = \frac{\mathbf{R_{Mi}^{exp}} - \mathbf{R_{M3}^{exp}}}{\mathbf{R_{M3}^{exp}}} \cdot \frac{(2\mathbf{n}-4)\cdot \mathbf{n_{sub}}}{(4-3)\cdot \mathbf{n_{sub}}}, \tag{3.15}$$

$$\mathbf{F_{Mi\text{-}M3}^{all}} = \frac{\mathbf{R_{Mi}^{all}} - \mathbf{R_{M3}^{all}}}{\mathbf{R_{M3}^{all}}} \cdot \frac{(2\mathbf{n}-4)\cdot \mathbf{n_{exp}} \cdot \mathbf{n_{sub}}}{(4-3)\cdot \mathbf{n_{exp}} \cdot \mathbf{n_{sub}}}, \tag{3.16}$$

where $\mathbf{n_{sub}} = 10$ is the number of subjects, $\mathbf{n_{exp}} = 9$ is the number of experiments per subject, $\mathbf{n} = 10$ is the number of complex value samples in the frequency domain, and the factor of two represents statistical independence between the real and imaginary parts of each sample.

We now focus on the statistical significance analysis presented in Fig. 3.8. Fig. 3.8.(a) shows a subject-wise comparison of the significance of the terms $\mathbf{B_h s}$ and $\mathbf{H_h j}$ that we use in M3. A critical F-statistic value of 1.95 is calculated for 0.05 false-rejection probability with $(9, 144)$ degrees of freedom. The results show that the values of $\mathbf{F^{sub}_{M1\text{-}M3}}$ for all subjects are higher than the critical F-statistic value. In particular, the values of $\mathbf{F^{sub}_{M1\text{-}M3}}$ for subjects B, D, and F exceed 20. These results prove that the existence of $\mathbf{H_h j}$ in M3 significantly improves modeling accuracy of $\mathbf{S_{h\text{-}e/\alpha}}$ for all subjects. The values of $\mathbf{F^{sub}_{M2\text{-}M3}}$ are mostly below the critical F-statistic value except for subjects A and C. Another observation is that the value of $\mathbf{F^{sub}_{M2\text{-}M3}}$ is lower than the value of $\mathbf{F^{sub}_{M1\text{-}M3}}$ for most of the subjects except for subject A.

Fig. 3.8.(b) shows an experiment-wise comparison of the models. A critical F-statistic value of 1.89 is calculated for 0.05 false-rejection probability with $(10, 160)$ degrees of freedom. The results show that the values of $\mathbf{F^{exp}_{M1\text{-}M3}}$ for all subjects are much higher than the critical F-statistic value. These results prove that the existence of $\mathbf{H_h j}$ in M3 significantly improves modeling accuracy of $\mathbf{S_{h\text{-}e/\alpha}}$ for all stiffness and inertia settings. The values of $\mathbf{F^{exp}_{M2\text{-}M3}}$ are mostly lower than the critical F-statistic value except for the three experiments with amplification factor $\alpha = 4$ (Exp. 3, 6, 9). Also, we can see a clear increment of the values of $\mathbf{F^{exp}_{M2\text{-}M3}}$ (i.e. the significance of $\mathbf{B_h s}$ in M3) as α gets higher.

Regarding the significance of the terms $\mathbf{B_h s}$ and $\mathbf{H_h j}$ used in M3 over all subjects and all experiments, a critical F-statistic value of 1.27 is calculated

(a) F-test v.s. Subject

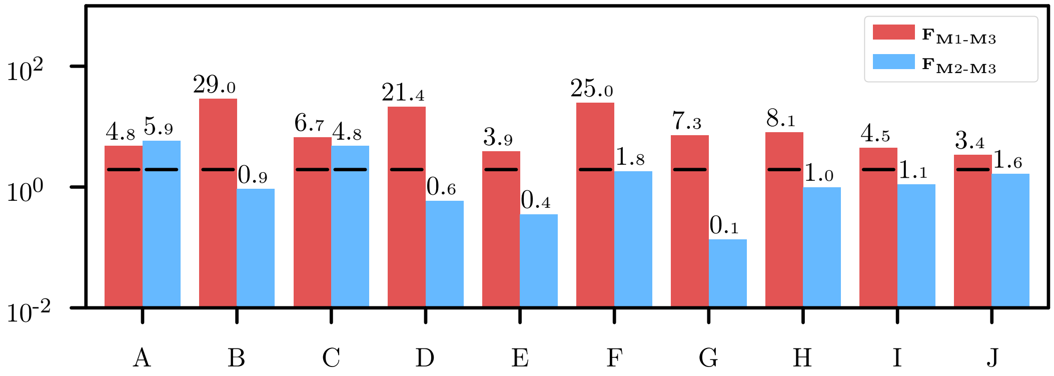

(b) F-test v.s. Experiment

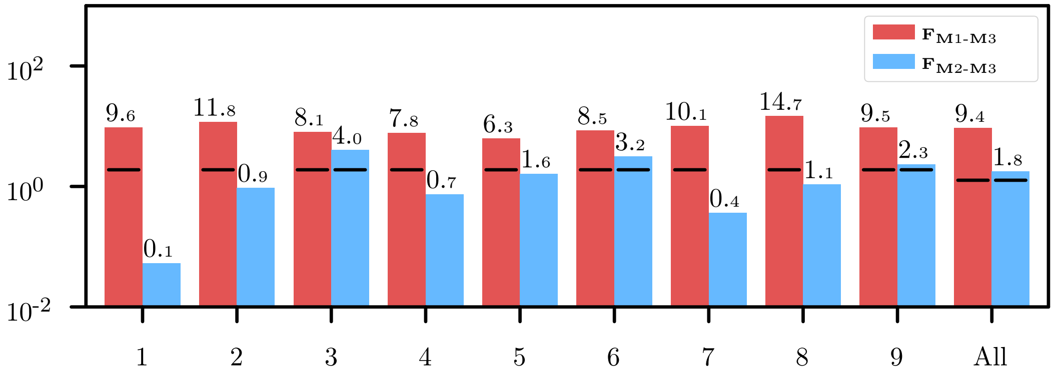

Figure 3.8: Bar charts on log scale show first, all $\mathbf{F}^{\mathbf{sub}}_{\mathbf{Mi\text{-}M3}}$ in (a), second all $\mathbf{F}^{\mathbf{exp}}_{\mathbf{Mi\text{-}M3}}$ in the first nine columns of (b), and third $\mathbf{F}^{\mathbf{all}}_{\mathbf{Mi\text{-}M3}}$ in the last column of (b), for $\mathrm{i} = 1, 2$. The solid line appears on a bar if the F-statistic value is over the critical F-statistic value with a false-rejection probability of 0.05.

for a 0.05 false-rejection probability with $(90, 1440)$ degrees of freedom. The value of $\mathbf{F}^{\mathbf{all}}_{\mathbf{M1\text{-}M3}}$ is much larger than 1.27 while the value of $\mathbf{F}^{\mathbf{all}}_{\mathbf{M2\text{-}M3}}$ is only slightly above 1.27. Although the effect of $\mathbf{B_h s}$ cannot be completely ignored based on the results of these F-tests, we can claim that the term $\mathbf{H_h j}$ has much more significance than the term $\mathbf{B_h s}$ as used in M3.

In our single-subject pilot study [He, Huang, Thomas, and Sentis, 2019], a linear regression is applied to describe the relationship between $\mathbf{H_h}$ and $\mathbf{K_h}$ identified from M2 and M3. However, based on our frequency domain results, the phase shifts of $\mathbf{S}_{\mathbf{h\text{-}e}/\alpha}(\mathbf{s})$ for some subjects are not consistent over different stiffness values. Therefore, a linear relationship between $\mathbf{H_h}$ and $\mathbf{K_h}$ is not always ensured for all subjects. Instead, we apply linear regression between the base 10 logarithms of $\mathbf{H_h}$ and $\mathbf{K_h}$ and use it to identify a power law between these two parameters. Since the value of $\mathbf{H_h}$ is not guaranteed to be positive from the parameter identification of M3, we only calculate the power law between $\mathbf{H_h}$ and $\mathbf{K_h}$ of M2.

Tab. 3.5 shows the identified parameter values of $\mathbf{H_h}$ and $\mathbf{K_h}$ using M2, with a coefficient of determination ($\mathbf{R}^2$) in the range of $0.88 \sim 1.00$. We define β_0 and β_1 as the intercept and slope of the linear regression equation between the base 10 logarithms of $\mathbf{H_h}$ and $\mathbf{K_h}$. From the parameter identification results using M2, a very strong linear relationship between logarithms is observable across all subjects, with an $\mathbf{R}^2$ value in the range of $0.73 \sim 0.96$. Fig. 3.9.(a)-(b) show the regression results of subjects B and F.

The last three rows of Tab. 3.5 show the identified power law parameters. The damping ratio and low-frequency phase shift of M2 can be expressed as

$$\zeta_{\mathbf{h\text{-}e}/\alpha} = \mathbf{c_h}/2, \quad \phi_{\mathbf{h\text{-}e}/\alpha} = \tan^{-1}(\mathbf{c_h}), \tag{3.17}$$

where $\mathbf{c_h}$ is a hysteretic damping loss factor [Bishop and Johnson, 1960] expressed as

$$\mathbf{c_h} \triangleq \mathbf{H_h}/\mathbf{K_h} = 10^{\beta_0} \cdot \mathbf{K_h}^{\beta_1 - 1} \tag{3.18}$$

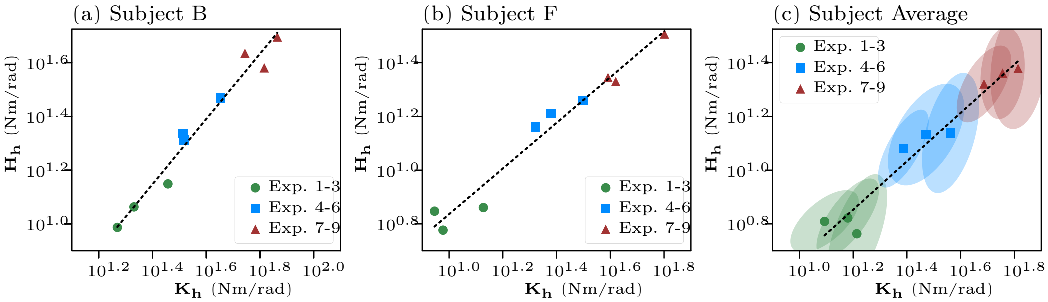

Figure 3.9: Here we show plots of $\mathbf{H_h}$ versus $\mathbf{K_h}$ for M2 on a log scale, with the results for subjects B and F in (a)-(b) and the geometric average across all subjects in (c). The dash lines and the ellipsoids show the linear regression results and the co-variances on the log scale.

obtained by substituting the power law $\mathbf{H_h} = 10^{\beta_0} \cdot \mathbf{K_h}^{\beta_1}$.

The last column of Tab. 3.5 shows the geometric average (i.e. arithmetic average of the logarithms) of the complex stiffness parameters across all subjects. We apply a linear regression to the logarithms of these average values and identify a power law of $\beta_0 = -0.23$, $\beta_1 = 0.90$, and $\mathbf{R}^2 = 0.95$ (Fig. 3.9.(c)). As the subject average stiffness increases from 12.40 to 65.12 Nm/rad, the value of $\zeta_{\mathbf{h\text{-}e}/\alpha}$ decreases from 0.23 to 0.19 as calculated using (3.17) and is within a 1-standard deviation range of the damping ratio of the minimally damped mode of the human arm (0.26 ± 0.08) described in [Perreault, Kirsch, and Crago, 2004].

As in [He, Huang, Thomas, and Sentis, 2019], the correlation between $\mathbf{H_h}$ and $\mathbf{K_h}$ can be introduced into M2 to reduce it to a 1-parameter complex stiffness model. Adopting this reduced model allows simplifying (3.2) to

$$\mathbf{S_h}(\mathbf{s}) = \tau_\mathbf{c}/\theta_\mathbf{e} = \mathbf{M_h}\mathbf{s}^2 + \mathbf{K_h}(1 + \mathbf{c_h}\mathbf{j}), \tag{3.19}$$

and the dynamic stiffness of the human coupled with the exoskeleton $\mathbf{S_{h\text{-}e}}(\mathbf{s})$

Table 3.5: M2 Model Parameters of Full Study

Exp	Parameter	Subject										
		A	B	C	D	E	F	G	H	I	J	Average
1	$\mathbf{K_h}$ (Nm/rad)	12.68	28.67	17.76	16.88	11.55	13.41	17.95	17.37	18.85	13.77	16.35
	$\mathbf{H_h}$ (Nm/rad)	5.26	14.09	5.22	12.38	3.92	7.26	4.48	5.22	5.30	2.56	5.80
	$\mathbf{R}^2$	0.99	0.98	0.97	0.98	0.96	1.00	0.97	0.95	0.95	0.96	-
2	$\mathbf{K_h}$ (Nm/rad)	16.05	21.43	12.62	16.85	14.72	9.49	19.39	14.62	20.16	10.78	15.13
	$\mathbf{H_h}$ (Nm/rad)	8.08	11.57	4.79	9.58	4.59	5.98	8.98	5.42	6.55	4.43	6.64
	$\mathbf{R}^2$	0.95	0.99	0.96	0.98	0.97	0.98	0.97	0.96	0.97	0.96	-
3	$\mathbf{K_h}$ (Nm/rad)	10.16	18.59	10.88	10.60	12.87	8.83	12.33	12.41	22.70	10.03	12.40
	$\mathbf{H_h}$ (Nm/rad)	6.60	9.70	4.63	7.19	5.72	7.04	7.05	5.14	9.14	4.35	6.44
	$\mathbf{R}^2$	0.97	0.98	0.88	0.90	0.90	0.99	0.96	0.95	0.96	0.97	-
4	$\mathbf{K_h}$ (Nm/rad)	28.69	45.01	30.81	39.08	35.16	31.57	41.56	34.24	62.06	27.66	36.52
	$\mathbf{H_h}$ (Nm/rad)	9.95	29.42	14.01	30.98	7.13	18.18	13.72	7.97	15.69	8.57	13.75
	$\mathbf{R}^2$	0.96	0.96	0.94	0.98	0.97	0.98	0.91	0.96	0.96	0.96	-
5	$\mathbf{K_h}$ (Nm/rad)	26.97	32.64	18.81	27.25	36.50	23.94	41.65	47.88	36.65	17.92	29.60
	$\mathbf{H_h}$ (Nm/rad)	15.25	21.69	7.51	21.78	9.74	16.28	13.54	23.64	10.60	7.26	13.57
	$\mathbf{R}^2$	0.93	0.96	0.95	0.96	0.93	0.99	0.89	0.94	0.93	0.97	-
6	$\mathbf{K_h}$ (Nm/rad)	24.23	32.94	25.85	29.05	26.09	20.93	24.41	24.21	26.29	14.55	24.37
	$\mathbf{H_h}$ (Nm/rad)	14.23	20.52	11.31	18.23	8.48	14.48	9.93	10.15	12.11	7.01	12.03
	$\mathbf{R}^2$	0.90	0.97	0.97	0.98	0.95	0.99	0.92	0.97	0.88	0.95	-
7	$\mathbf{K_h}$ (Nm/rad)	45.12	73.23	66.65	54.75	63.99	63.31	78.08	55.26	108.33	60.11	65.12
	$\mathbf{H_h}$ (Nm/rad)	13.52	49.62	34.33	45.87	11.70	32.12	20.20	25.01	23.61	12.83	23.90
	$\mathbf{R}^2$	0.94	0.98	0.96	0.94	0.92	0.97	0.97	0.97	0.98	0.95	-
8	$\mathbf{K_h}$ (Nm/rad)	52.45	55.48	63.19	59.58	59.37	41.71	67.47	69.80	68.61	41.52	57.03
	$\mathbf{H_h}$ (Nm/rad)	17.52	43.15	31.05	39.03	16.03	21.37	19.20	28.97	14.61	15.99	22.97
	$\mathbf{R}^2$	0.91	0.98	0.97	0.98	0.95	0.99	0.97	0.97	0.94	0.97	-
9	$\mathbf{K_h}$ (Nm/rad)	40.87	65.45	45.33	46.37	46.67	39.03	49.83	63.44	67.79	33.68	48.63
	$\mathbf{H_h}$ (Nm/rad)	20.08	38.08	17.76	24.44	14.52	22.11	17.62	33.32	18.52	13.92	20.93
	$\mathbf{R}^2$	0.93	0.98	0.96	0.98	0.92	0.95	0.92	0.97	0.95	0.93	-
Power Law	β_0	0.03	-0.55	-0.55	-0.21	-0.11	-0.01	0.00	-0.56	-0.10	-0.26	-0.23
	β_1	0.73	1.21	1.12	1.03	0.70	0.85	0.70	1.10	0.73	0.84	0.90
	$\mathbf{R}^2$	0.77	0.97	0.97	0.94	0.86	0.96	0.83	0.91	0.87	0.73	0.95

becomes,

$$\mathbf{S_{h\text{-}e}}(\mathbf{s}) = \tau_\mathbf{s}/\theta_\mathbf{e} = \mathbf{M_{h\text{-}e}}\mathbf{s}^2 + \mathbf{K_h}(1 + \mathbf{c_h}\mathbf{j}), \tag{3.20}$$

where $\mathbf{M_{h\text{-}e}} = \mathbf{M_h} + \mathbf{M_e}$ is the combined inertia between the human and the exoskeleton. Similarly to (3.17), the damping ratio and low-frequency phase shift of $\mathbf{S_h}(\mathbf{s})$ and $\mathbf{S_{h\text{-}e}}(\mathbf{s})$ can also be expressed as $\mathbf{c_h}/2$ and $\tan^{-1}(\mathbf{c_h})$.

3.4 Historical Review

While the noticeable phase shift values observed in this study are consistent with the ankle and elbow joint phase values reported in [Agarwal and Gottlieb, 1977; Gottlieb and Agarwal, 1978; Zahalak and Heyman, 1979; Cannon and Zahalak, 1982], some research studies also report very small phase shift values for other human joints. Yet, our proposed complex stiffness model still holds for those results. For example, the damping ratio for the human knee joint reported in [Pope et al., 1976, Fig. 5] is 0.02, which results in a phase shift of 2.34° using equation (3.17). This kind of small hysteretic damping characteristic can be easily overlooked.

Low-frequency phase shifts are found in muscle spindles [Poppele and Bowman, 1970] and arteries [Westerhof and Noordergraaf, 1970] of mammals, suggesting that joint hysteretic damping could be due to the bio-mechanical properties of the human tissue. Therefore, we suspect that the human neuromuscular system, either through muscle and tendon hysteresis or through neural hysteretic behavior, is the mechanism behind our hysteretic damping hypothesis.

Because Fig. 3.7.(g)-(i) shows a consistent phase shift across a wide range of low frequencies, it is natural to consider that the phase behavior of $\mathbf{S_h(s)}$ has already reached a low-frequency asymptote at the lowest tested frequency and it will not change much at lower frequencies than that. This is difficult to experimentally verify because lower frequencies require longer experimental times making it harder for the subjects. Nonetheless, our lowest tested frequency, 2 rad/s ($\approx$ 0.3 Hz), is below the frequencies reported in references [Agarwal and Gottlieb, 1977; Gottlieb and Agarwal, 1978; Zahalak and Heyman, 1979; Cannon and Zahalak, 1982; Hunter and Kearney, 1982]. In addition, our tested frequency range covers the frequencies that are important for practical control system design.

Chapter 4

Nonlinear Control for Responsive Human-Centered Robots

In Chapter 2, we introduce the amplification exoskeletons, which is a specific type of human centered robots. While the concept of an amplification exoskeleton is an old idea [Yagn, 1890; Makinson, Bodine, and Fick, 1969; Kazerooni and Guo, 1993], a system which delivers on the dream of transparent interaction, of "feeling like the system is not there," through augmentation of sensed human interaction forces is still an ambitious goal of force control technology today [Kazerooni, 2005; Dollar and Herr, 2008; Jacobsen and Olivier, 2014; Fontana, Vertechy, Marcheschi, Salsedo, and Bergamasco, 2014]. Unlike assistive exoskeletons which help complete predictable behaviors [Zhang, Fiers, Witte, Jackson, Poggensee, Atkeson, and Collins, 2017; Lee, Kim, Baker, Long, Karavas, Menard, Galiana, and Walsh, 2018] or rehabilitation exoskeletons

---

The results presented in this chapter have also appeared in part of [He, Huang, Thomas, and Sentis, 2019] and [Brissonneau, He, Thomas, and Sentis, 2021]. The human subject experiments in [He, Huang, Thomas, and Sentis, 2019] were conducted by Binghan He and Huang Huang. As the primary contributor, Binghan He developed the fractional-order control method for amplification exoskeletons. Gray C. Thomas provided theory supports on frequency domain analysis. In the work of [Brissonneau, He, Thomas, and Sentis, 2021], Nicolas Brissonneau is the primary contributor in developing algorithm and conducting experiments. Binghan He provided supports on programming the algorithm in the early stage and assisting the data analysis. Gray C. Thomas provided theory supports on frequency and time domain analysis. These works were advised by Luis Sentis.

[Kong, Moon, Jeon, and Tomizuka, 2010; Kim and Deshpande, 2017] which simulate rehabilitation therapy, human augmentation exoskeletons [Kazerooni, 2005; Lee, Lee, Kim, Han, Shin, and Han, 2014] use non-passive feedback control to amplify the user's strength. But this type of feedback control brings the system closer to instability. And since the robot is in a feedback interconnection with the human, a model of the human's dynamic behavior plays a critical role in determining the stability of a human-centered robot [Buerger and Hogan, 2007; He, Thomas, Paine, and Sentis, 2019].

In Chapter 3, we validate a complex stiffness model for human elbow joint dynamics. The primary model validation experiment uses statistical F-tests to compare three dynamic stiffness models: a linear mass, spring, and viscous damper model, a nonlinear complex-stiffness-spring and mass model (that is, a spring, mass, and hysteretic damper model), and a combined model with mass, spring, and both viscous and hysteretic damping. This hysteretic damping explains the consistent damping ratio of the human–exoskeleton resonant peak even as the stiffness and exoskeleton inertia change—which is not well explained by the linear model. And it also explains the low frequency phase lag in human stiffness (previously observed in [Agarwal and Gottlieb, 1977; Gottlieb and Agarwal, 1978; Zahalak and Heyman, 1979; Cannon and Zahalak, 1982]).

Based on this new model, we introduce two nonlinear control methods in this chapter for improving the responsiveness of human-centered robots. First, we develop a customizable fractional-order control strategy to take full advantage of the low-frequency phase lag for each individual. Based on results from the previous test, a customized fractional order is chosen for each of three subjects such that the behavior is nearly oscillatory (marginally stable). The subjects then change their co-contraction level to illustrate the phenomenon of co-contraction induced instability and subject dependent co-contraction relationships with stability. The three subjects span the range of observed co-contraction–stability relationships. Compared to the PI control strategy in Chapter 2, this fractional-order control strategy improves dynamical amplification (at 10 rad/s) by $81 \sim 88\%$.

Then, we investigates how to transfer human-like complex stiffness feature to human-centered robots. The challenge of this problem is that the time-domain representation of a complex stiffness is non-causal and therefore cannot be realized in practice. Based on a causal approximation of complex stiffness proposed in [Reid, 1956], we develop a proportional-and-hysteretic-damping (PHD) control method. We show that the step response of our PHD controller maintains a percentage overshoot, which is insensitive to inertia.

4.1 Fractional-Order Control

The amplification feedback we discuss in this section is the same as the direct amplification feedback shown in Fig. 3.2 in which the amplification command is $-\tau_c$ multiplied by $\alpha - 1$. But instead of a constant value of α across all frequencies, we introduce a frequency dependent amplification transfer function $\alpha(\mathbf{s}) = \mathbf{k_p} \cdot \mathbf{F}(\mathbf{s}) + 1$, where $\mathbf{k_p}$ is a proportional gain and $\mathbf{F}(\mathbf{s})$

is a fractional order controller customized according to the complex stiffness behavior displayed by users.

4.1.1 Loop Shaping

Based on (3.19) and (3.20), the plant transfer function $\mathbf{P(s)}$ from $\tau_{\mathbf{d}}$ to $\tau_{\mathbf{c}}$ can be expressed as

$$\mathbf{P(s)} = \frac{\mathbf{S_h(s)}}{\mathbf{S_{h\text{-}e}(s)}} \cdot \mathbf{G_a(s)} = \frac{\mathbf{M_h s^2 + K_h(1 + c_h j)}}{\mathbf{M_{h\text{-}e} s^2 + K_h(1 + c_h j)}} \cdot \mathbf{G_a(s)} \tag{4.1}$$

where the SEA transfer function $\mathbf{G_a(s)} = \tau_{\mathbf{s}}/\tau_{\mathbf{d}}$ acts as a 2nd order low-pass filter. Because of the high bandwidth of the SEA force controller, the natural frequency $\omega_{\mathbf{a}}$ of $\mathbf{G_a(s)}$ is much greater than the natural frequencies $\omega_{\mathbf{h\text{-}e}} = \sqrt{\mathbf{K_h/M_{h\text{-}e}}}$ and $\omega_{\mathbf{h}} = \sqrt{\mathbf{K_h/M_h}}$ of $\mathbf{S_{h\text{-}e}(s)}$ and $\mathbf{S_h(s)}$.

Considering the frequency domain properties from low to high frequencies, $\mathbf{P(s)}$ has a pair of conjugate poles at $\omega_{\mathbf{h\text{-}e}}$, then a pair of conjugate zeros at $\omega_{\mathbf{h}}$ and then another pair of conjugate poles at $\omega_{\mathbf{a}}$ (Fig. 4.1). Between $\omega_{\mathbf{h\text{-}e}}$ and $\omega_{\mathbf{h}}$, $\mathbf{S_{h\text{-}e}(s)}$ is dominated by its inertia effect and the magnitude of $\mathbf{P(s)}$ decreases while the phase decreases from 0°. On the other hand, $\mathbf{S_h(s)}$ is still dominated by the complex stiffness and prevents the phase moving below $\tan^{-1}(\mathbf{c_h}) - 180^\circ$.

If we apply a very large value of $\mathbf{k_p}$, the gain crossover of $\mathbf{P(s)}$ falls beyond $\omega_{\mathbf{a}}$. The phase margin with such crossover is very close to zero because of the 2nd order SEA dynamics. Also, the closed loop behavior amplifies the high frequency sensor noise from the actual signal from $\tau_{\mathbf{c}}$ (which is usually de-noised by a low-pass filter beyond the frequency of $\omega_{\mathbf{a}}$ that makes the closed loop even more likely to be unstable). Similarly to [He, Thomas, Paine, and Sentis, 2019], the crossover frequency cannot be placed between $\omega_\mathbf{h}$ and $\omega_\mathbf{a}$ because multiple crossovers could easily occur. Besides the multiple crossovers, this frequency range is also outside of the tested frequency ranges in Chapter 3. The unmodeled dynamics from the human and cuff will cause additional stability issues if a crossover is placed there. Instead, a new crossover can be safely placed at the frequency between $\omega_\mathbf{h\text{-}e}$ and $\omega_\mathbf{h}$ using a smaller $\mathbf{k_p}$ (Fig. 4.1). As a rule of thumb, $\mathbf{k_p}$ can be set as

$$\begin{aligned} \mathbf{k_p} &= (\omega_\mathbf{gc}/\omega_\mathbf{h})^2 = (\mathbf{M_{h\text{-}e}}/\mathbf{M_h})^{\frac{1}{2}}, \\ \omega_\mathbf{gc} &\triangleq \sqrt{\mathbf{K_h}/(\mathbf{M_{h\text{-}e}}\cdot\mathbf{M_h})^{\frac{1}{2}}}, \end{aligned} \tag{4.2}$$

where the crossover $\omega_\mathbf{gc}$ of $\mathbf{k_p}\cdot\mathbf{P(s)}$ is exactly in the middle between $\omega_\mathbf{h\text{-}e}$ to $\omega_\mathbf{h}$ in the log scale.

In Chapter 2, an additional integral term is added to the proportional gain $\mathbf{k_p}$ to boost the amplification at low frequencies while maintaining the same crossover frequency between $\omega_\mathbf{h\text{-}e}$ and $\omega_\mathbf{h}$. However, a PI controller has a -90° phase at low frequency, which can result in loss of stability if the zero of the PI controller is too close to the crossover.

Therefore, we propose a fractional order controller to take advantage of the complex stiffness model,

$$\mathbf{F(s)} = \mathbf{k_f}\cdot\mathbf{s}^{-\mathbf{f}}, \tag{4.3}$$

where $\mathbf{f}$ is the fractional order (that is, a non-integer power of $\mathbf{s}$) of $\mathbf{F(s)}$ and $\mathbf{k_f}$ is a gain which allows tuning the magnitude of $\mathbf{F(s)}$ in the frequency domain. The fractional order controller in (4.3) has its magnitude decreasing $-20\cdot\mathbf{f}$ dB

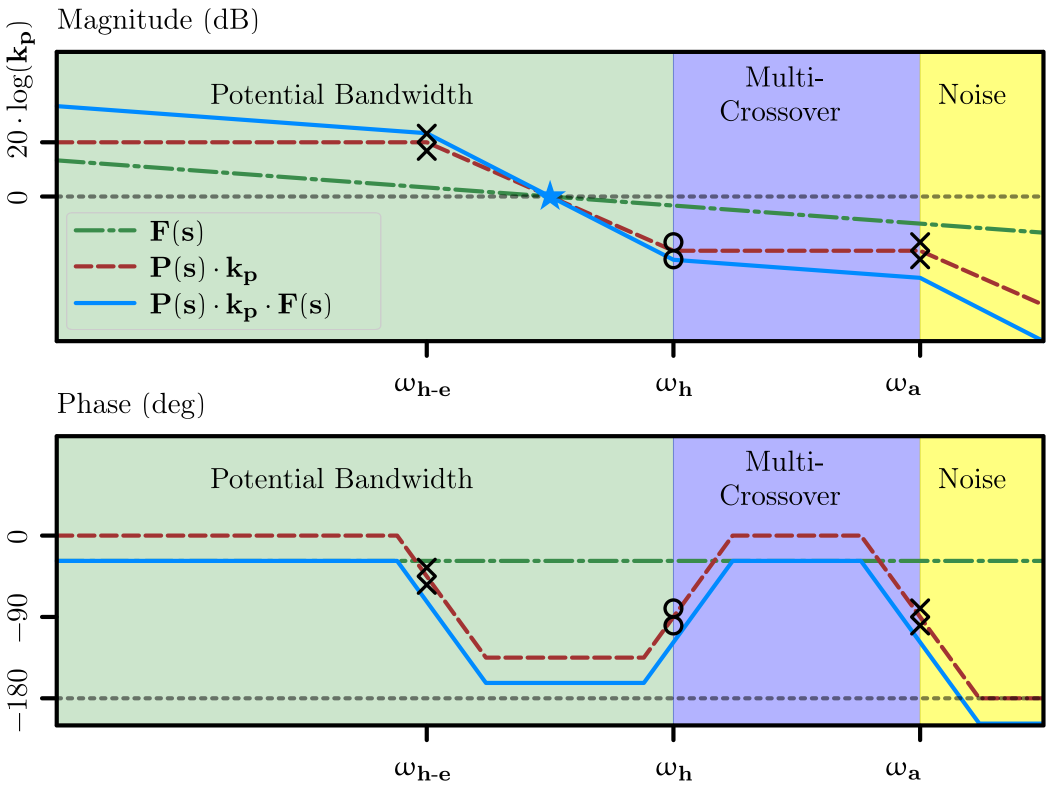

Figure 4.1: These conceptual bode plots show $\mathbf{P}(\mathbf{s})$ with its poles (crosses) and zeros (circles). The various regions are color-coded: the model is trustworthy in the green region, the blue region reflects the multi-crossover behavior which makes an amplification controller design unreliable, and the yellow region is dominated by sensor noise from $\tau_{\mathbf{c}}$. A fractional-order controller $\mathbf{F}(\mathbf{s})$ complements a proportional controller $\mathbf{k_p}$ by boosting the low-frequency amplification.

per decade and its phase staying at $-90 \cdot \mathbf{f}$ degrees at all frequencies.

By multiplying (4.3) by the proportional gain $\mathbf{k_p}$, the gain of the controller is increased at low frequency and reduced at high frequency (for further de-noising the measurement of $\tau_{\mathbf{c}}$). If $\mathbf{k_f}$ is tuned to make $\mathbf{F}(\mathbf{s})$ have the exact same crossover frequency as $\mathbf{k_p} \cdot \mathbf{P}(\mathbf{s})$, we will obtain the magnitude bode plot $\mathbf{k_p} \cdot \mathbf{P}(\mathbf{s}) \cdot \mathbf{F}(\mathbf{s})$ rotated from $\mathbf{k_p} \cdot \mathbf{P}(\mathbf{s})$ with pivot at the point of the gain crossover frequency (Fig. 4.1). Since the exact crossover frequency of $\mathbf{k_p} \cdot \mathbf{P}(\mathbf{s})$ varies with the value of $\mathbf{K_h}$, $\mathbf{k_f}$ can be set as

$$\mathbf{k_f} = \hat{\omega}_{\mathbf{gc}}^{\mathbf{f}}, \quad \hat{\omega}_{\mathbf{gc}} \triangleq \sqrt{\hat{\mathbf{K}}_{\mathbf{h}}/(\mathbf{M_{h\text{-}e}} \cdot \mathbf{M_h})^{\frac{1}{2}}}, \tag{4.4}$$

where $\hat{\omega}_{\mathbf{gc}}$ is chosen as a nominal crossover frequency of $\mathbf{k_p} \cdot \mathbf{P}(\mathbf{s})$ with $\hat{\mathbf{K}}_{\mathbf{h}} \triangleq (\underline{\mathbf{K}}_{\mathbf{h}} \cdot \bar{\mathbf{K}}_{\mathbf{h}})^{1/2}$ being the geometric mean between the lower bound $\underline{\mathbf{K}}_{\mathbf{h}}$ and the upper bound $\bar{\mathbf{K}}_{\mathbf{h}}$.

Because of the non zero phase shift associated with the complex stiffness behavior, a positive phase margin can be guaranteed if $0 < \mathbf{f} < \tan^{-1}(\mathbf{c_h})/90$. The fractional order controller can be precisely designed for all subjects based on the values of β_0 and β_1 shown in Tab. 3.5 through the settings

$$\mathbf{f} = \begin{cases} \tan^{-1}(10^{\beta_0} \cdot \bar{\mathbf{K}}_{\mathbf{h}}^{\beta_1 - 1})/90 - \phi/90, & \text{if } \beta_1 < 1, \\ \tan^{-1}(10^{\beta_0} \cdot \underline{\mathbf{K}}_{\mathbf{h}}^{\beta_1 - 1})/90 - \phi/90, & \text{if } \beta_1 \geqslant 1, \end{cases} \tag{4.5}$$

where $\phi > 0$ is a user-defined guaranteed phase margin. Differently from [He, Huang, Thomas, and Sentis, 2019] where a constant $\mathbf{c_h}$ is assumed, (4.5) considers the lowest value of $\mathbf{c_h}$ of a subject in the stiffness range $[\underline{\mathbf{K}}_{\mathbf{h}}, \bar{\mathbf{K}}_{\mathbf{h}}]$.

As a fractional-order controller, $\mathbf{F}(\mathbf{s})$ cannot be implemented directly into a computational control process. However, from [He, Huang, Thomas, and Sentis, 2019], we can approximate it as the product of many 1st order lag filters,

$$\mathbf{F}(\mathbf{s}) = \frac{\mathbf{k_f}}{\mathbf{p}_1^{\mathbf{f}}} \cdot \prod_{\mathbf{i}=1}^{\mathbf{n}} \frac{1 + \mathbf{s}/\mathbf{z_i}}{1 + \mathbf{s}/\mathbf{p_i}}, \tag{4.6}$$

$$\mathbf{z_i}/\mathbf{p_i} = \mathbf{r_{zp}}, \quad \text{for } \mathbf{i} = 1, 2, \cdots, \mathbf{n} \tag{4.7}$$

$$\mathbf{p_i}/\mathbf{p_{i-1}} = \mathbf{r_{pp}}, \quad \text{for } \mathbf{i} = 2, 3, \cdots, \mathbf{n}, \tag{4.8}$$

where $\mathbf{n}$ is the number of lag filters and the pole and the zero for each lag filter are $-\mathbf{p_i}$ and $-\mathbf{z_i}$. We define $\mathbf{r_{zp}}$ such that all lag filters have an equal distance between the pole and the zero, and we define $\mathbf{r_{pp}}$ such that there is a constant distance between adjacent lag filters (in log frequency space). The amplification controller in (4.6) functions as a fractional-order filter in the frequency range of $[\mathbf{p_1},\ \mathbf{z_n}]$ rad/s. The fractional order can be approximated as $\mathbf{f} \approx \log(\mathbf{r_{zp}})/\log(\mathbf{r_{pp}})$.

4.1.2 Examples

In Chapter 3, we presented the results of a 10-subject study, where subjects A-E are females and subjects F-J are males. Based on (4.5), we conducted loop shaping experiments on subjects B, D and G who, respectively, had the highest value, the closest value to 1, and the lowest value of β_1 across all subjects. Our loop shaping study consists of two tuning experiments and two amplification experiments.

The value of $\mathbf{M_e}$ is 1.01 $\mathrm{kg} \cdot \mathrm{m}^2$, which includes a 4.5 kg load at the end of the exoskeleton arm. Although we do not measure the value of $\mathbf{M_h}$ directly from our subjects, an average $\mathbf{M_h}$ of 0.11 $\mathrm{kg} \cdot \mathrm{m}^2$ can be obtained from a 10-subject measurement study presented in [Cannon and Zahalak, 1982]. Based on these inertia values and (4.2), we set $\mathbf{k_p} = 3.2$.

As shown in Tab. 3.5, the human stiffness changes from 10.03 to 108.33 Nm/rad across all subjects and all experiments, which gives us a nominal value of $\hat{\mathbf{K}}_\mathbf{h} = 32.96$ Nm/rad. Based on (4.4) and (4.6), we compute $\hat{\omega}_{gc} \approx 10$ rad/s and implement an approximate fractional-order controller using 5 lag filters with $\mathbf{p}_1 = 1$ and $\mathbf{r_{pp}} = 10^{0.5}$ such that $\hat{\omega}_{gc}$ is located at the center of the frequency range defined by $[\mathbf{p}_1, \mathbf{p}_5]$ rad/s.

The two tuning experiments we perform aim to find out the fractional order of a subject where the minimum phase margin ϕ is near zero. From (4.5), we gradually increase the fractional order, f, from low value to higher values until the exoskeleton starts to oscillate. We do that with subjects employing low and high human stiffness behaviors. The maximum stable value of **f** will be the lower value between the two stiffness cases. An important advantage is that this tuning strategy does not require prior knowledge of the human complex stiffness. Similarly to the modeling experiments previously presented, we regulate the low and high stiffness of a subject by setting the gripping force as 10 and 27 kg and the bias torque as 0 and 8 Nm.

After the tuning experiments outlined above, we subtract 0.12 from the marginally stable fractional order, which provides a minimum phase margin $\phi = 10.8°$. Then, we conduct two amplification experiments both with a gripping force of 14 kg and a bias torque of 4 Nm. These two experiments are conducted using sinusoidal voluntary movements performed by the subjects with frequencies of 1 and 10 rad/s. The voluntary sinusoidal movements are guided by showing the subject a visual signal of the actual joint position $\theta_{\mathbf{e}}$ and the desired sinusoidal wave on a screen. The amplification factor α for these sinusoidal voluntary movements can be calculated from the experimental data after the experiments.

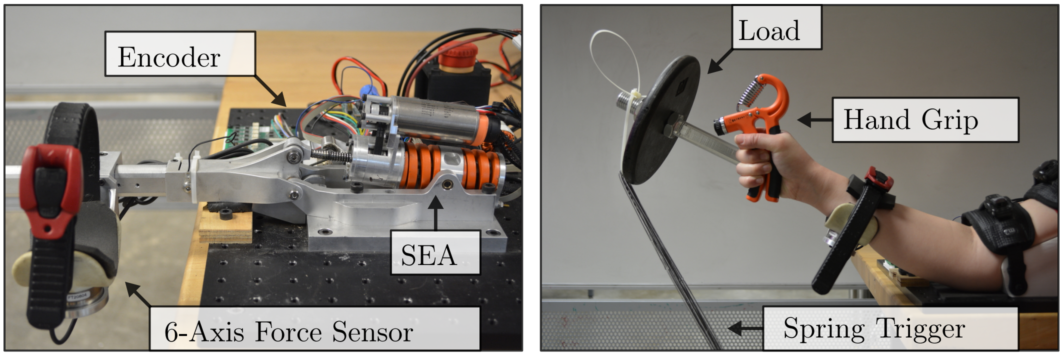

(a) Apparatus (b) Experimental Setup

Figure 4.2: Experimental apparatus: the series elastic P0 exoskeleton featuring an ATI Mini40 force sensitive cuff and a P170 Orion air cooled series elastic actuator module acting through a simple 3 bar linkage. During all experiments, subjects apply forces to a adjustable hand grip to regulate their elbow stiffness. A spring trigger is used for perturbation during the post-tuning tests.

In order to study the performance of the tuned amplification controllers for various subjects, we define $\tilde{\tau}_{\mathbf{s}} \triangleq \tau_{\mathbf{s}} + \tau_{\mathbf{g}} - \mathbf{bias}$ and $\tilde{\tau}_{\mathbf{c}} \triangleq \tau_{\mathbf{c}} - \mathbf{bias}$. The real-time amplification factor for the proposed amplification controller can be expressed as $\alpha(\mathbf{t}) = \tilde{\tau}_{\mathbf{s}}(\mathbf{t})/\tilde{\tau}_{\mathbf{c}}(\mathbf{t}) + 1$.

After gradually increasing the fractional order for low and high human stiffness behaviors until the exoskeleton starts to oscillate continuously, we obtain the values f = 0.72, 0.56, 0.22 for subjects B, D, G. In order to display the tuning results concisely, we conduct two post-tuning tests involving low and high human stiffness setups. We attach a set of mechanical springs to the tip of the exoskeleton arm (Fig. 4.2.(b)) and quickly detach it to test the dynamic response of the controller. The response of $\theta_{\mathbf{e}}$ and $\tilde{\tau}_{\mathbf{c}}$ for the post-tuning tests are shown in Fig. 4.3.

In Tab. 3.5, we had identified that β_1 for subject B was greater than 1.

(a) Subject B : $\mathbf{f} = 0.72$

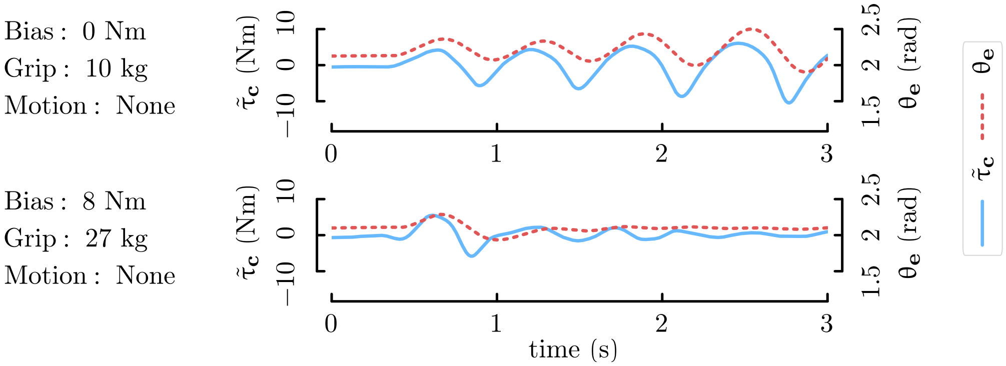

(b) Subject D : $\mathbf{f} = 0.56$

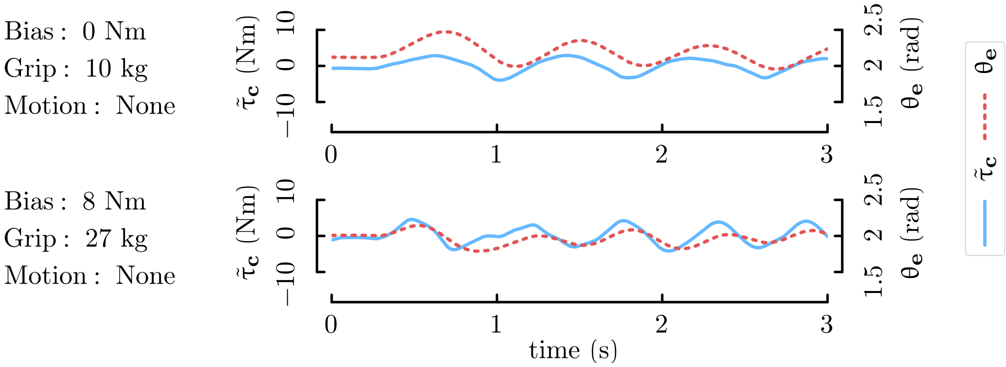

(c) Subject G : $\mathbf{f} = 0.22$

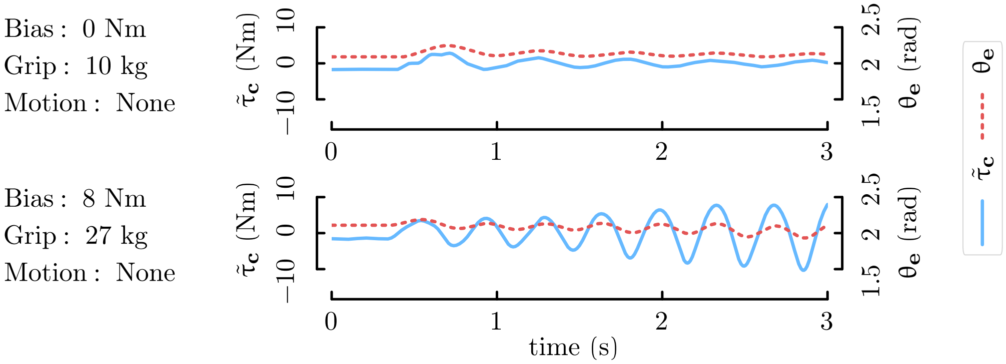

Figure 4.3: (a)-(c) show the responses of θ_e (dash red) and $\tilde{\tau}_c$ (solid blue) for the post-tuning tests on subjects B, D and G.

(a) Subject B : $\mathbf{f} = 0.60$

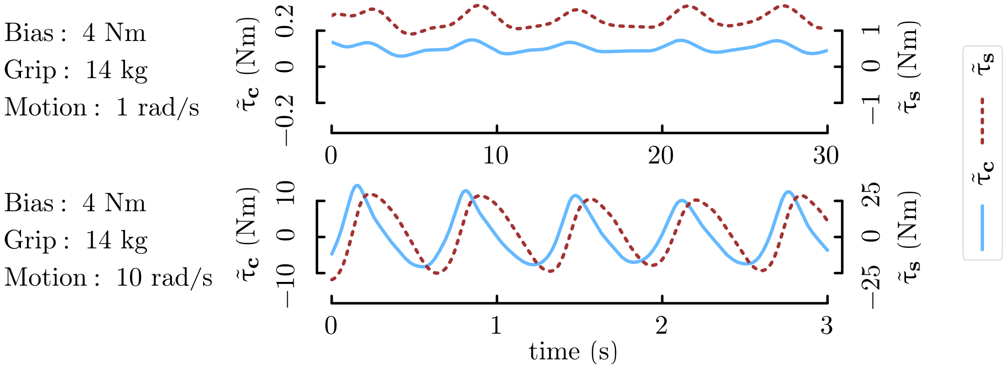

(b) Subject D : $\mathbf{f} = 0.44$

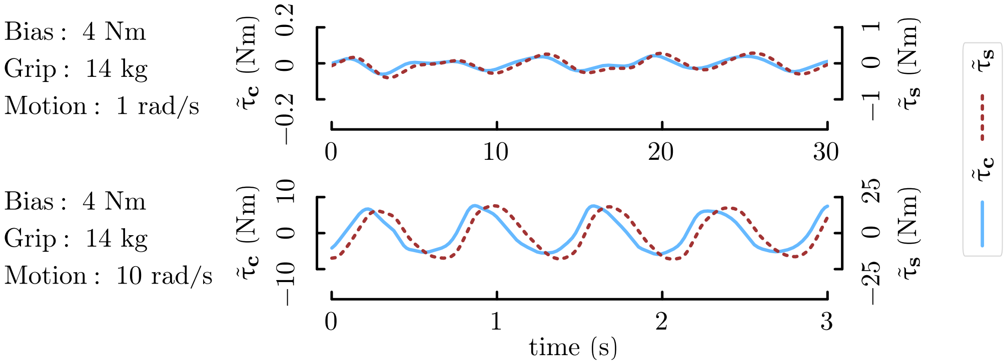

(c) Subject G : $\mathbf{f} = 0.10$

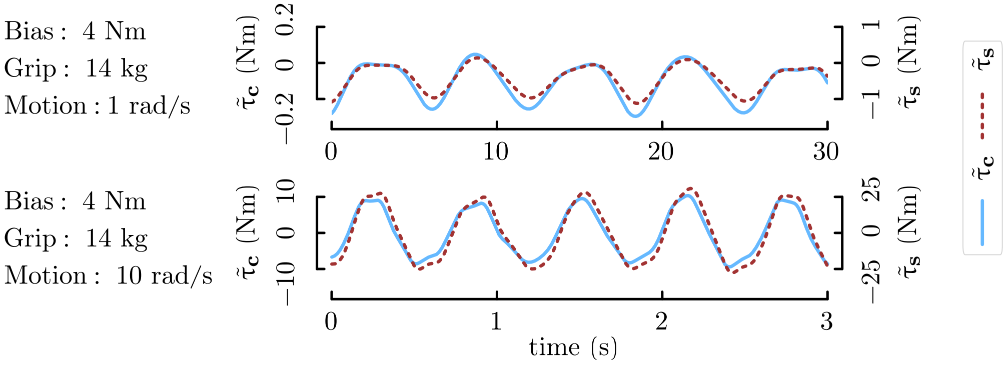

Figure 4.4: (a)-(c) show the responses of $\tilde{\tau}_{\mathbf{s}}$ (dash red) and $\tilde{\tau}_{\mathbf{c}}$ (solid blue) for the amplification tests on subjects B, D and G.

Table 4.1: Observed Amplification of Fractional-Order Control

Subject	f	$\lvert\frac{\tilde{\tau}_s}{\tilde{\tau}_c}\rvert$ (1 rad/s)	$\angle\frac{\tilde{\tau}_s}{\tilde{\tau}_c}$ (1 rad/s)	$\lvert\frac{\tilde{\tau}_s}{\tilde{\tau}_c}\rvert$ (10 rad/s)	$\angle\frac{\tilde{\tau}_s}{\tilde{\tau}_c}$ (10 rad/s)
B	0.60	10.86	−25.2°	2.83	−54.9°
D	0.44	6.74	−28.2°	2.84	−42.5°
G	0.10	3.70	−8.8°	2.99	−12.6°

This explains why the post-tuning test for subject B applying high stiffness is less oscillatory than the post-tuning test applying low stiffness. Because the value of β_1 is very close to 1 for subject D, the results for both post-tuning tests are very similar. Similarly, the high stiffness post-tuning test for subject G is more oscillatory than the low stiffness post-tuning test because $\beta_1 < 1$.

When we subtract 0.12 from **f** for subjects B, D and G, we get the values 0.60, 0.44 and 0.10. The behaviors of $\tilde{\tau}_s$ and $\tilde{\tau}_c$ for sinusoidal voluntary movements between 1 and 10 rad/s demonstrate that the exoskeleton is stable for all subjects using our proposed custom robust amplification controllers (Fig. 4.4). The values for the gain and the phase shift for $\tilde{\tau}_s$ and $\tilde{\tau}_c$ during the amplification tests are shown in Tab. 4.1.

Notice that the subjects are able to maintain values between $\lvert\frac{\tilde{\tau}_s}{\tilde{\tau}_c}\rvert =$ 2.83 ~ 2.99 with a voluntary motion of 10 rad/s. In Chapter 2 which did not incorporate the proposed complex stiffness model [He, Thomas, Paine, and Sentis, 2019], the value of $\lvert\frac{\tilde{\tau}_s}{\tilde{\tau}_c}\rvert$ was between 1.46 ~ 1.58 at 6.3 rad/s (experimentally validated), and a value of 1.12 at 10 rad/s (theoretically estimated). Therefore, the fractional-order control strategy shows a 81 ~ 88% improvement in the magnitude when using a dynamical amplification factor

$\alpha(\mathbf{s}) = \tilde{\tau}_{\mathbf{s}}(\mathbf{s})/\tilde{\tau}_{\mathbf{c}}(\mathbf{s}) + 1$.

4.2 Proportional-and-Hysteretic-Damping Control

In (3.17), we use the complex stiffness model to explain how humans maintain the consistency of their damping ratios versus different stiffness and inertia values. If a robot has a similar complex stiffness feature to a human, the dynamical behavior of the robot will be more consistent while interacting with different uncertain environments. Therefore, the next question for us to study is how to build a control system which reproduces a virtual complex stiffness on a robot.

4.2.1 Hilbert Transformation

For a linear mass-spring-damper system

$$\mathbf{S_r}(\mathbf{s}) = \mathbf{m} \cdot \mathbf{s}^2 + \mathbf{b} \cdot \mathbf{s} + \mathbf{k}, \tag{4.9}$$

the most direct way for changing it into a complex stiffness system is to let we let $\mathbf{b} = \frac{\mathbf{h}}{\omega}$. Then, we obtain

$$\mathbf{S_r}(\mathbf{s}) = \mathbf{m} \cdot \mathbf{s}^2 + \mathbf{h} \cdot \mathbf{j} + \mathbf{k}. \tag{4.10}$$

However, the frequency ω at the current moment is not available if we do not know the robot's motion in the future moment. This observation shows that (4.10) is non-causal and cannot be realized in time domain.

While complex stiffness $\mathbf{F}(\mathbf{s}) = \mathbf{h} \cdot \mathbf{j} + \mathbf{k}$ is a frequency-domain equation,

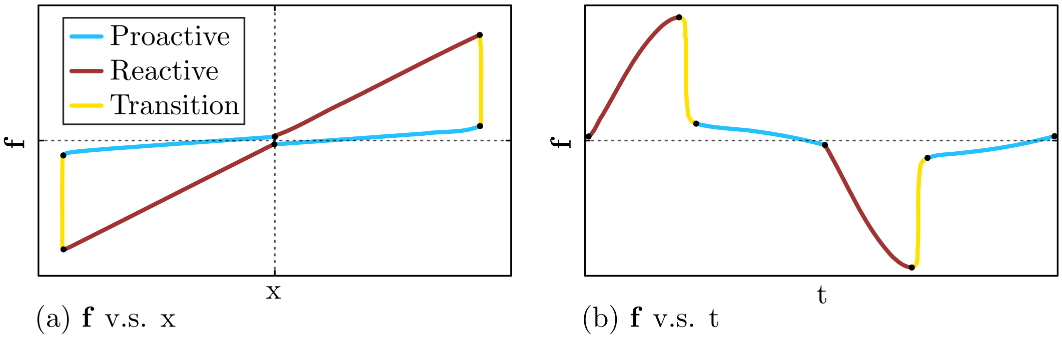

(a) **f** v.s. x (b) **f** v.s. t

Figure 4.5: (a) shows the phases and transitions describing the dynamics of the PHD controller in the force to position plane while following a sinusoidal desired position input over one period, while (b) shows the associated time response of **f** to a sinusoidal position input.

its time-domain representation can be expressed as

$$\mathbf{f}(\mathbf{t}) = \mathbf{h} \cdot \hat{\mathbf{x}}(\mathbf{t}) + \mathbf{k} \cdot \mathbf{x}(\mathbf{t}), \tag{4.11}$$

where $\mathbf{x}(\mathbf{t})$ is the robot position variable and $\hat{\mathbf{x}}(\mathbf{t})$ is the Hilbert transform of $\mathbf{x}(\mathbf{t})$ [Inaudi and Kelly, 1995] defined as

$$\hat{\mathbf{x}}(\mathbf{t}) = -\frac{1}{\pi} \int_{-\infty}^{\infty} \frac{\mathbf{x}(\mathbf{t})}{\mathbf{t} - \tau} \mathbf{d}\tau. \tag{4.12}$$

Based on (4.12), it is also obvious that the time-domain representation of complex stiffness is non-casual.

4.2.2 Reid Model

In [Reid, 1956], a causal approximation of the time-domain representation of complex stiffness is expressed as

$$\mathbf{f}(\mathbf{t}) = \frac{\pi}{2} \cdot \mathbf{h} \cdot \operatorname{sgn}(\mathbf{x}(\mathbf{t}) \cdot \dot{\mathbf{x}}(\mathbf{t})) \cdot \mathbf{x}(\mathbf{t}) + \mathbf{k} \cdot \mathbf{x}(\mathbf{t}). \tag{4.13}$$

Based on the idea of Reid model, we propose our proportional-and-hysteretic-damping (PHD) control method [Brissonneau, He, Thomas, and Sentis, 2021]. A PHD controller switches between two linear virtual springs (Fig. 4.5.a) as

$$\mathbf{f}(\mathbf{t}) = \begin{cases} \mathbf{k}_1 \cdot \mathbf{x}(\mathbf{t}), & \text{if } \operatorname{sgn}(\mathbf{x}(\mathbf{t}) \cdot \dot{\mathbf{x}}(\mathbf{t})) < 0, \\ \mathbf{k}_2 \cdot \mathbf{x}(\mathbf{t}), & \text{if } \operatorname{sgn}(\mathbf{x}(\mathbf{t}) \cdot \dot{\mathbf{x}}(\mathbf{t})) \geqslant 0, \end{cases} \tag{4.14}$$

where $\mathbf{k}_1 \triangleq (1-\beta) \cdot \mathbf{k}_{\mathbf{PHD}}$ and $\mathbf{k}_2 \triangleq (1+\beta) \cdot \mathbf{k}_{\mathbf{PHD}}$ are the stiffness values of the two virtual springs and β decides how much these two stiffness values deviate from a nominal stiffness value $\mathbf{k}_{\mathbf{PHD}}$. If the position and velocity of the virtual spring deflection are in opposite directions, the PHD controller is in its proactive phase and switches to virtual spring $\mathbf{k}_1 \cdot \mathbf{x}(\mathbf{t})$. Otherwise, if the position and velocity of the virtual spring deflection are in the same direction, the PHD controller is in its reactive phase and switches to virtual spring $\mathbf{k}_2 \cdot \mathbf{x}(\mathbf{t})$. If we input a sinusoidal perturbation of $\mathbf{x}(\mathbf{t})$ into the PHD controller, the force output $\mathbf{f}(\mathbf{t})$ (Fig. 4.5.b) will also switch between the sinusoidal response of virtual spring $\mathbf{k}_1 \cdot \mathbf{x}(\mathbf{t})$ and the sinusoidal response of virtual spring $\mathbf{k}_2 \cdot \mathbf{x}(\mathbf{t})$ based on whether the PHD controller is in a proactive phase or a reactive phase.

Percentage Overshoot Notice that the PHD controller switches between two marginally stable sub-systems if we implement it to a robot with inertia $\mathbf{m}$. For a 2nd order system that is marginally stable, its step response is sinusoidal. We can analytically calculate the amount of overshoot using conservation of energy. The potential energy equality $\frac{1}{2} \cdot \mathbf{k}_1 \cdot {\mathbf{x}_1}^2 = \frac{1}{2} \cdot \mathbf{k}_2 \cdot {\mathbf{x}_2}^2$ holds between

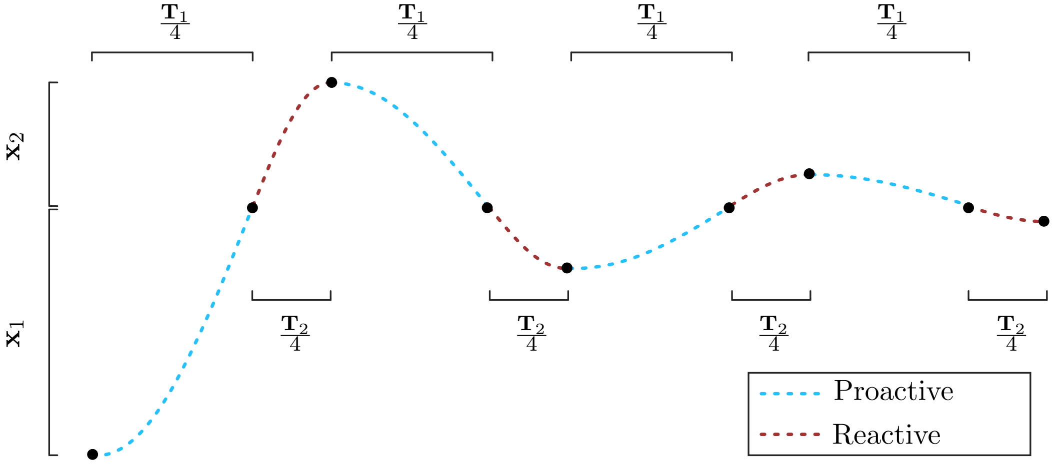

Figure 4.6: This figure illustrates the contribution of each stiffness due to a step input in the time-domain.

subsequent peaks in amplitude, $\mathbf{x}_1$ and $\mathbf{x}_2$ (see Fig. 4.6). And therefore,

$$\frac{|\mathbf{x}_2|}{|\mathbf{x}_1|} = \sqrt{\frac{\mathbf{k}_1}{\mathbf{k}_2}}. \tag{4.15}$$

Substituting $\mathbf{k}_1 \triangleq (1-\beta) \cdot \mathbf{k}_{\mathbf{PHD}}$ and $\mathbf{k}_2 \triangleq (1+\beta) \cdot \mathbf{k}_{\mathbf{PHD}}$, the percentage overshoot $\%\mathrm{OS}_{\mathbf{PHD}}$ of controlling the inertia $\mathbf{m}$ using the proposed PHD controller can be expressed as

$$\%\mathrm{OS}_{\mathbf{PHD}} = 100 \cdot \frac{|\mathbf{x}_2|}{|\mathbf{x}_1|} = 100 \cdot \sqrt{\frac{1-\beta}{1+\beta}}, \tag{4.16}$$

which is irrelevant to both the robot inertia $\mathbf{m}$ and the nominal stiffness $\mathbf{k}_{\mathbf{PHD}}$.

Damped Natural Frequency Considering again the step response behavior in Fig. 4.6, the response of a PHD controller is defined by the consecutive switch between two stiffness $\mathbf{k}_1$ and $\mathbf{k}_2$. The switching happens when $\mathbf{q}$ or $\dot{\mathbf{q}}$ crosses zero. We can split the full period into four quadrants, such that each quadrant

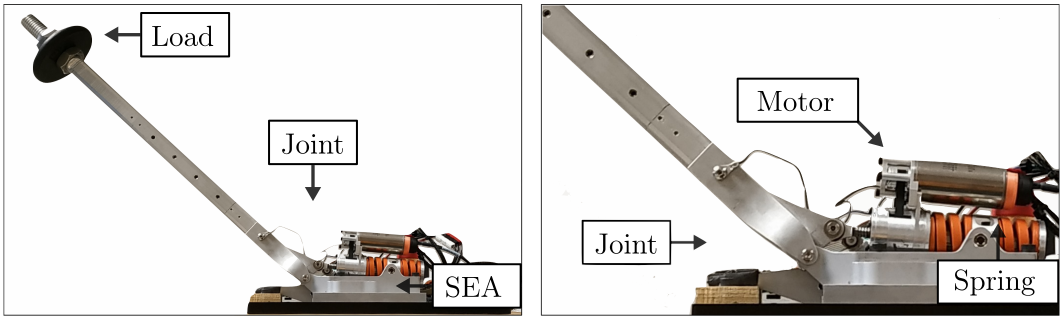

(a) Experimetal Setup (b) Apparatus

Figure 4.7: A modified Taurus Testing System with a P-170 Orion actuator

is the result of a single linear spring behavior:

$$\mathbf{T_{PHD}} = 2 \cdot \frac{\mathbf{T}_1}{4} + 2 \cdot \frac{\mathbf{T}_2}{4}, \tag{4.17}$$

where $\mathbf{T}_1$ and $\mathbf{T}_2$ are the duration of the full periods of the mass-spring dynamics solely dominated by $\mathbf{k}_1$ and $\mathbf{k}_2$. Let us define ω_1 and ω_2 as the natural frequencies of the inertia $\mathbf{m}$ with virtual springs $\mathbf{k}_1$ and $\mathbf{k}_2$. By substituting $\mathbf{T}_1 = \frac{2\pi}{\omega_1}$, $\mathbf{T}_2 = \frac{2\pi}{\omega_2}$, and $\mathbf{T_{PHD}} = \frac{2\pi}{\omega^{\mathbf{d}}_{\mathbf{PHD}}}$ into (4.17), we can express the damped natural frequency $\omega^{\mathbf{d}}_{\mathbf{PHD}}$ as

$$\omega^{\mathbf{d}}_{\mathbf{PHD}} = \frac{2 \cdot \omega_1 \cdot \omega_2}{\omega_1 + \omega_2}, \tag{4.18}$$

Substituting $\omega_1 = \sqrt{\mathbf{k}_1/\mathbf{m}}$ and $\omega_2 = \sqrt{\mathbf{k}_2/\mathbf{m}}$ into (4.18), we obtain

$$\omega^{\mathbf{d}}_{\mathbf{PHD}} = \frac{2 \cdot \sqrt{\mathbf{k}_1 \cdot \mathbf{k}_2}}{\sqrt{\mathbf{k}_1 \cdot \mathbf{m}} + \sqrt{\mathbf{k}_2 \cdot \mathbf{m}}}. \tag{4.19}$$

Substituting $\mathbf{k}_1 \triangleq (1-\beta) \cdot \mathbf{k_{PHD}}$ and $\mathbf{k}_2 \triangleq (1+\beta) \cdot \mathbf{k_{PHD}}$, we get

$$\omega^{\mathbf{d}}_{\mathbf{PHD}} = \sqrt{\frac{\mathbf{k_{PHD}}}{\mathbf{m}} \cdot \frac{2 \cdot (1-\beta^2)}{1 + \sqrt{1-\beta^2}}}. \tag{4.20}$$

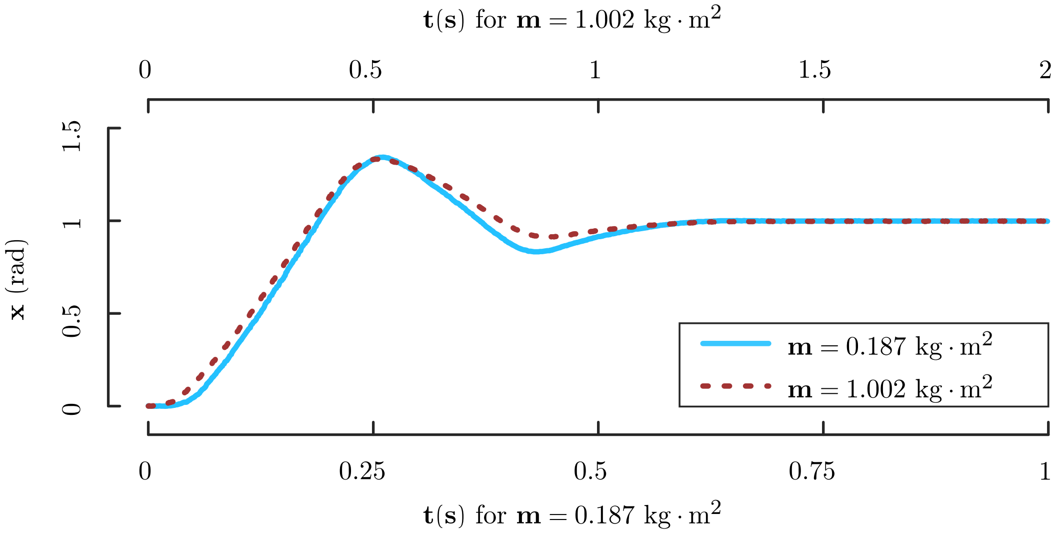

Figure 4.8: Two step responses overlaid with different time-scales demonstrate the nearly-identical step response shape even as inertia increases by a factor of 5.36. Both responses use the same PHD controller with parameters $\mathbf{k_{PHD}} = 52.79$ and $\beta = 0.76$.

4.2.3 Series Elastic Actuator Example

To confirm the performance of our PHD controller, we perform experiments in the hardware testbed shown in Fig. 4.7. Fig. 4.8 shows the PHD controller's performance in two step-responses verified in hardware with differing load inertia. The two step responses are overlaid, but plotted on different time axes, to highlight their similar shapes and nearly identical overshoot behaviors.

Part II

Safety

Chapter 5

State Feedback Control for Safe Human-Centered Robots

Safe human-robot interaction is mission-critical for human-centered robots. For a dynamical system like a human-centered robot, the safety of its operation can be verified by a barrier certificate. Similar to a Lyapunov function for stability verification, a barrier certificate or barrier function provides a sufficient condition for safety verification [Prajna and Jadbabaie, 2004]. But a Lyapunov function needs to be decreasing everywhere in the state space while a barrier function relaxes the global convergence requirement and only needs to be decreasing at the safety bounds. Barrier certificates can be synthesized through sum-of-squares optimization [Prajna, 2006]. Inspired by the idea of a control Lyapunov function [Sontag, 1989], a more ambitious goal is to combine the barrier function and the safety guarantee controller through a control barrier function and synthesize them simultaneously [Wieland and Allgöwer, 2007].

Controllers which ensure safe operation of dynamic systems despite un-

---

The results presented in this chapter have also appeared in part of [Thomas, He, and Sentis, 2018]. As the primary contributor, Gray C. Thomas developed the control theory and did the mathematical proofs of this work. Binghan He programmed the control algorithms and conducted simulations for the proof of concept. This research was advised by Luis Sentis.

trusted inputs are widely appreciated for their straightforward safety verification. They find application where safety is critical, and also where input foresight is unavailable. These systems must first guarantee future satisfaction of both state and input constraints on the dynamic system—with input limits being a critical complicating factor. As was famously argued in the first Bode lecture, input limits on the fuel rod controller explain the signal behavior minutes before the Chernobyl reactor's nuclear melt-down [Stein, 2003]. A natural secondary goal is to maximize the region of the state space that the controller certifies as safe to use.

Unlike the reference governor [Bemporad, 1998], which enforces state constraints by way of constrained model predictive control [Mayne, Rawlings, Rao, and Scokaert, 2000], safety controllers for nonlinear systems use the sub-level sets of a scalar function—a Lyapunov function, or one of several relaxations—to encode information about the safe region boundary.

Several barrier Lyapunov nonlinear approaches start by building a Lyapunov function which is infinite within the unsafe region. Backstepping [Tee, Ge, and Tay, 2009] and adaptive control techniques [Liu and Tong, 2016] can then guarantee safety, if not input limits. Less restrictive barrier functions and barrier certificates must decrease only at the boundary [Prajna and Jadbabaie, 2004]—the sub-level set of zero. Barrier Lyapunov functions can be constructed from a Lyapunov function and a barrier function [Ames, Xu, Grizzle, and Tabuada, 2016], but finding such functions is the classical art of nonlinear control practitioners.

A control Lyapunov function [Sontag, 1989] merely needs to be capable of decreasing everywhere, and control barrier functions [Wieland and Allgöwer, 2007] relax limitations on the choice of scalar function to the utmost—but still leaves the construction of such functions, and the bounding of the input, as an art. The secondary, or non-safety control objectives can be combined into a composite function [Romdlony and Jayawardhana, 2016], or added to the optimization which determines the input [Ames, Xu, Grizzle, and Tabuada, 2016], [Nguyen and Sreenath, 2016a], [Nguyen and Sreenath, 2016b], but doing so alters the original controller's behavior everywhere. In particular, [Nguyen and Sreenath, 2016a] and [Nguyen and Sreenath, 2016b] emphasize that high relative order constraints require careful adjustments to the boundary function to avoid large inputs.

Automatic synthesis of barrier certificates through sum of squares (SoS) optimization [Prajna, 2006] has emerged as the standard solution to this design-burden issue, and has been adopted in safety verification [Barry, Majumdar, and Tedrake, 2012], and region of attraction estimation [Glassman, Desbiens, Tobenkin, Cutkosky, and Tedrake, 2012] for already designed controllers in the presence of constraints. Most ambitiously, the LQR-Tree algorithm [Tedrake, 2009], [Tedrake, Manchester, Tobenkin, and Roberts, 2010] attempts to map out the entire backwards-reachable state space using the union of funnels—the sub-level sets of trajectory tracking LQR Lyapunov functions. The LQR-Tree strategy could potentially be adapted to safety control, but remains structurally plagued by the non-conservative polynomial approximation of the dynamics, inability to exploit choices available during controller design, and—despite efforts to improve the speed by sacrificing guarantees [Reist and Tedrake, 2010]—dimensional explosion of the SoS sub-problem, trajectory optimization sub-problem, and the tree structure in the full state space [Tedrake, Manchester, Tobenkin, and Roberts, 2010].

Linear matrix inequality (LMI) controller synthesis problems (c.f. [Boyd, El Ghaoui, Feron, and Balakrishnan, 1994]) offer a conservative way to certify invariant ellipsoids as safe—and design controllers to maximize their area. Such invariant ellipsoids have been applied to input and state constrained linear systems [Hu and Lin, 2003], and it has been shown that under these conditions the convex hull of the regions is also invariant. But the these ellipsoids must share the same center. The less-explored, non-convex min-quadratic function mentioned in [Hu, Ma, and Lin, 2006] for same-center ellipsoids—which bears similarity to the minimization over quadratics that runs once to select the starting funnel in [Reist and Tedrake, 2010]—is more easily adapted to our purpose.

In this chapter, we propose to use linear differential inclusions to approximate a nonlinear system at a grid of equilibriums—each a conservative approximation of the nonlinear model within some region of validity. For each equilibrium we use an LMI to find the linear feedback and quadratic Lyapunov function such that the function's unity-sublevel set satisfies all state and input constraints while certifying the largest volume region. Our min-quadratic barrier function is the minimum over all of these quadratic Lyapunov functions—minus one so that the 0-sub-level set is an approximation of the safe region. This produces an approximate safe region which is the union of ellipsoids, region e in Fig. 5.1-5.2.

The ideal safety controller, in our view, would adhere exactly to Fig. 5.1-5.2's region (a), applying either no input, or limit-saturated input as soon as the state hits the boundary of the safe region. This strategy relies on being able to compute this region, but this is only feasible in SISO systems of order less than 2, in which case the safety boundary can be found by a series of integrations [Bobrow, Dubowsky, and Gibson, 1985; Thomas and Sentis, 2016; Pham, Caron, Lertkultanon, and Nakamura, 2017].

We use two slightly negative "threshold" level sets of the min-quadratic barrier function to engage and disengage the safety controller—which applies the equilibrium-centered linear feedback law associated with the current minimum over the Lyapunov functions when active. When the state reaches the first (greater) threshold, the controller activates, applies a control input guaranteed to reduce the active Lyapunov function, and thus reduces the min-quadratic barrier function itself. This continues until the min-quadratic barrier function falls below the second (lower) threshold, and the system returns to transparent operation. Trajectories which stay within the larger of the two threshold level sets are thus unaffected by the safety control.

We demonstrate our technique by constructing the region in which an inverted pendulum can balance, subject to speed and tight input limits—demonstrating the natural emergence of an exponential deceleration limit near the point where the force of gravity overwhelms the pendulum. We also simulate the high relative order behavior of a series elastic actuator under position and motor effort constraints.

5.1 Barrier Pairs

Various methods create control barrier functions to ensure safety constraint satisfaction. A reciprocal control barrier function which is infinite within the unsafe region can be obtained through back-stepping methods [Tee, Ge, and Tay, 2009; Liu and Tong, 2016]. The non-safety control objectives can be combined into a composite function [Romdlony and Jayawardhana, 2016], or added to the optimization of quadratic programming which determines the input [Ames, Xu, Grizzle, and Tabuada, 2016; Nguyen and Sreenath, 2016b], but doing so alters the original controller's behavior everywhere. In particular, Ref. [Nguyen and Sreenath, 2016b] emphasizes that high relative order constraints require careful adjustments to the boundary function to avoid large inputs. To solve this issue, a semi-definite programming method in [Pylorof and Bakolas, 2016] is proposed for enforcing the safety input constraints.

The synthesis of a control barrier function can be considered a problem of finding an invariant set of the system which is also a subset of the safe region in the state space. Based on this idea, a barrier pair is defined.

Definition 5.1 ([Thomas, He, and Sentis, 2018]) A *barrier pair* is a pair of functions $(\mathbf{B}(\mathbf{x}), \mathbf{k}(\mathbf{x}))$ with two following properties:

(a) $-1 < \mathbf{B}(\mathbf{x}) \leqslant 0, \quad \mathbf{u} = \mathbf{k}(\mathbf{x}) \implies \dot{\mathbf{B}}(\mathbf{x}) < 0,$

(b) $\mathbf{B}(\mathbf{x}) \leqslant 0 \implies \mathbf{x} \in \mathcal{X},\ \mathbf{k}(\mathbf{x}) \in \mathcal{U},$

where $\mathbf{x} \in \mathcal{X}$ and $\mathbf{u} \in \mathcal{U}$ are the safety constraints, $\mathbf{B}(\mathbf{x})$ is a barrier function and $\mathbf{k}(\mathbf{x})$ is a feedback controller.

The sub-level set of $\mathbf{B}(\mathbf{x})$ corresponding to zero value becomes a safe region under the operation of controller $\mathbf{u} = \mathbf{k}(\mathbf{x})$. If a barrier pair is specified as

$$\mathbf{B}(\mathbf{x}) = \mathbf{x}^\top \mathbf{Q}^{-1}\mathbf{x} - 1, \quad \mathbf{k}(\mathbf{x}) = \mathbf{K}\mathbf{x} \tag{5.1}$$

where $\mathbf{B}(\mathbf{x})$ is a quadratic barrier function with a positive definite matrix $\mathbf{Q}$ and $\mathbf{k}(\mathbf{x})$ is a full state feedback controller, the barrier pair synthesis problem becomes a convex optimization with a series of linear matrix inequalities (LMIs) [Boyd, El Ghaoui, Feron, and Balakrishnan, 1994] for enforcing state and input constraint satisfaction.

5.1.1 Barrier Pair Synthesis for Polytopic LDIs

For a strictly causal n-input-m-output system, whether it is linear or non-linear and whether it is time-invariant or time-varying, we can model it as a polytopic linear differential inclusion (LDI) [Boyd, El Ghaoui, Feron, and Balakrishnan, 1994]

$$\begin{aligned} \dot{\mathbf{x}} &= \mathbf{A}(\mathbf{t})\mathbf{x} + \mathbf{B}(\mathbf{t})\mathbf{u}, \\ \mathbf{y} &= \mathbf{C}(\mathbf{t})\mathbf{x}, \end{aligned} \tag{5.2}$$

where $\mathbf{A}(\mathbf{t}) \in \mathrm{Co}\{\mathbf{A}_1, \mathbf{A}_2, \ldots, \mathbf{A}_{\mathbf{n_a}}\}$, $\mathbf{B}(\mathbf{t}) \in \mathrm{Co}\{\mathbf{B}_1, \mathbf{B}_2, \ldots, \mathbf{B}_{\mathbf{n_b}}\}$, $\mathbf{C}(\mathbf{t}) \in \mathrm{Co}\{\mathbf{C}_1, \mathbf{C}_2, \ldots, \mathbf{C}_{\mathbf{n_c}}\}$, $\mathbf{x} \triangleq [x_1, \cdots, x_{\mathbf{n}}]^\top$ is the vector of state, $\mathbf{y} \triangleq [y_1, \cdots, y_{\mathbf{m}}]^\top$ is the vector of output, and $\mathbf{u} \triangleq [u_1, \cdots, u_{\mathbf{n}}]^\top$ is the vector of input. Its input and state constraints (Fig. 5.1-5.2) are expressed as

$$\mathcal{U} \triangleq \{\mathbf{u} : |\mathbf{b}_{\mathbf{n}\text{-}\mathbf{i}}\mathbf{u}| \leqslant \bar{u}_{\mathbf{i}},\ \mathbf{i} = 1, \cdots, \mathbf{n}\}, \tag{5.3}$$

$$\mathcal{X} \triangleq \{\mathbf{x} : |\mathbf{b}_{\mathbf{m}\text{-}\mathbf{i}}\mathbf{C}_{\mathbf{j}}\mathbf{x}| \leqslant \bar{y}_{\mathbf{i}},\ \mathbf{i} = 1, \cdots, \mathbf{m},\ \mathbf{j} = 1, \cdots, \mathbf{n_c}\}, \tag{5.4}$$

where $\mathbf{b}_{\mathbf{n}\text{-}\mathbf{i}} \in \mathbf{R}^{1\times\mathbf{n}}$ for $\mathbf{i} = 1, \cdots, \mathbf{n}$ is the standard basis (row) vectors of $\mathbf{n}$-dimensional Euclidean space and $\mathbf{b}_{\mathbf{m}\text{-}\mathbf{i}} \in \mathbf{R}^{1\times\mathbf{m}}$ for $\mathbf{i} = 1, \cdots, \mathbf{m}$ is the standard basis (row) vectors of $\mathbf{m}$-dimensional Euclidean space.

The input constraint LMIs can be expressed as

$$\begin{bmatrix} \mathbf{Q} & \star \\ \mathbf{b}_{\mathbf{n}\text{-}\mathbf{i}}\mathbf{Y} & \bar{u}_{\mathbf{i}}^2 \end{bmatrix} \succeq 0, \quad \forall\, \mathbf{i} = 1, \ldots, \mathbf{n} \tag{5.5}$$

where $\mathbf{Y} \triangleq \mathbf{K}\mathbf{Q}$. The state constraint LMIs can be expressed as

$$\begin{bmatrix} \mathbf{Q} & \star \\ \mathbf{b}_{\mathbf{m}\text{-}\mathbf{i}}\mathbf{C}_{\mathbf{j}}\mathbf{Q} & \bar{y}_{\mathbf{i}}^2 \end{bmatrix} \succeq 0, \quad \forall\, \mathbf{i} = 1, \ldots, \mathbf{m} \atop \mathbf{j} = 1, \ldots, \mathbf{n}. \tag{5.6}$$

To guarantee the invariance of the barrier function, a Lyapunov stability LMI in [Boyd, El Ghaoui, Feron, and Balakrishnan, 1994] for the norm-bound LDI model is expressed as

$$\mathbf{A}_{\mathbf{i}}\mathbf{Q} + \mathbf{Q}\mathbf{A}_{\mathbf{i}}^\top + \mathbf{B}_{\mathbf{j}}\mathbf{Y} + \mathbf{Y}^\top\mathbf{B}_{\mathbf{j}}^\top \preceq 0, \quad \forall\, \mathbf{i} = 1, \ldots, \mathbf{n_a} \atop \mathbf{j} = 1, \ldots, \mathbf{n_b}. \tag{5.7}$$

where $\mu_{\mathbf{x}}$ and $\mu_{\mathbf{u}}$ are positive real scalar variables. A LMI problem for maximizing the volume of the ellipsoidal region of attraction $\{\mathbf{x} : \mathbf{x}^\top\mathbf{Q}^{-1}\mathbf{x} \leqslant 1\}$ can be expressed as

$$\begin{aligned} \underset{\mathbf{Q},\mathbf{Y}}{\mathsf{maximize}} \quad & \mathsf{log}(\mathsf{det}(\mathbf{Q})) \\ \mathsf{subject\ to} \quad & \mathbf{Q} \succ 0,\ (5.5),\ (5.6),\ (5.7) \end{aligned} \tag{5.8}$$

which automatically generates a barrier pair $(\mathbf{B}(\mathbf{x}), \mathbf{k}(\mathbf{x}))$ if the problem is feasible.

5.1.2 Barrier Pair Synthesis for Norm-Bound LDIs

Similarly, we can also model a strictly causal n-input-m-output system as a norm-bound linear differential inclusion (LDI) [Boyd, El Ghaoui, Feron, and Balakrishnan, 1994]

$$\begin{aligned} \dot{\mathbf{x}} &= (\mathbf{A_a} + \mathbf{A_b}\Delta\mathbf{A_c})\mathbf{x} + (\mathbf{B_a} + \mathbf{B_b}\Delta\mathbf{B_c})\mathbf{u}, \\ \mathbf{y} &= (\mathbf{C_a} + \mathbf{C_b}\Delta\mathbf{C_c})\mathbf{x}, \end{aligned} \tag{5.9}$$

where $\|\Delta\| \leqslant 1$, $\mathbf{x} \triangleq [x_1, \cdots, x_\mathbf{n}]^\top$ is the vector of state, $\mathbf{y} \triangleq [y_1, \cdots, y_\mathbf{m}]^\top$ is the vector of output, and $\mathbf{u} \triangleq [u_1, \cdots, u_\mathbf{n}]^\top$ is the vector of input. Its input and state constraints (Fig. 5.1-5.2) are expressed as

$$\mathcal{U} \triangleq \{\mathbf{u} : |\mathbf{b_{n\text{-}i}}\mathbf{u}| \leqslant \bar{u}_\mathbf{i},\ \mathbf{i} = 1, \cdots, \mathbf{n}\}, \tag{5.10}$$

$$\mathcal{X} \triangleq \{\mathbf{x} : |\mathbf{b_{m\text{-}i}}(\mathbf{C_a} + \mathbf{C_b}\Delta\mathbf{C_c})\mathbf{x}| \leqslant \bar{y}_\mathbf{i},\ \|\Delta\| \leqslant 1,\ \mathbf{i} = 1, \cdots, \mathbf{m}\}, \tag{5.11}$$

where $\mathbf{b_{n\text{-}i}} \in \mathbf{R}^{1\times\mathbf{n}}$ for $\mathbf{i} = 1, \cdots, \mathbf{n}$ is the standard basis (row) vectors of $\mathbf{n}$-dimensional Euclidean space and $\mathbf{b_{m\text{-}i}} \in \mathbf{R}^{1\times\mathbf{m}}$ for $\mathbf{i} = 1, \cdots, \mathbf{m}$ is the standard basis (row) vectors of $\mathbf{m}$-dimensional Euclidean space.

The input constraint LMIs can be expressed as

$$\begin{bmatrix} \mathbf{Q} & \star \\ \mathbf{b_{n\text{-}i}}\mathbf{Y} & \bar{u}_\mathbf{i}^2 \end{bmatrix} \succeq 0, \quad \forall\, \mathbf{i} = 1, \ldots, \mathbf{n} \tag{5.12}$$

where $\mathbf{Y} \triangleq \mathbf{KQ}$. The state constraint LMIs derived using the S-procedure [Ma and Chen, 2006] can be expressed as

$$\begin{bmatrix} \bar{y}_{\mathbf{j}}^2\mathbf{Q} & \star & \star & \star \\ \mathbf{0} & \mu_{\mathbf{j}}\mathbf{I} & \star & \star \\ \mathbf{b_{m\text{-}j}C_aQ} & \mu_{\mathbf{j}}\mathbf{b_{m\text{-}j}C_b} & 1 & \star \\ \mathbf{C_cQ} & \mathbf{0} & \vec{0} & \mu_{\mathbf{j}}\mathbf{I} \end{bmatrix} \succeq 0, \quad \forall\, \mathbf{j} = 1, \ldots, \mathbf{m} \tag{5.13}$$

where $\mu_{\mathbf{j}}$ for $\mathbf{j} = 1, \ldots, \mathbf{m}$ are positive real scalar variables. To guarantee the invariance of the barrier function, a Lyapunov stability LMI in [Boyd, El Ghaoui, Feron, and Balakrishnan, 1994] for the norm-bound LDI model is expressed as

$$\begin{bmatrix} \mathbf{A_aQ} + \mathbf{QA_a^\top} + \mathbf{B_aY} + \mathbf{Y^\top B_a^\top} + \mu_{\mathbf{x}}\mathbf{A_bA_b^\top} + \mu_{\mathbf{u}}\mathbf{B_bB_b^\top} & \star & \star \\ \mathbf{A_cQ} & -\mu_{\mathbf{x}}\mathbf{I} & \star \\ \mathbf{B_cY} & \mathbf{0} & -\mu_{\mathbf{u}}\mathbf{I} \end{bmatrix} \preceq 0, \tag{5.14}$$

where $\mu_{\mathbf{x}}$ and $\mu_{\mathbf{u}}$ are positive real scalar variables. A LMI problem for maximizing the volume of the ellipsoidal region of attraction $\{\mathbf{x} : \mathbf{x}^\top\mathbf{Q}^{-1}\mathbf{x} \leqslant 1\}$ can be expressed as

$$\begin{aligned} &\underset{\mathbf{Q},\,\mathbf{Y}}{\mathsf{maximize}} && \mathsf{log}(\mathsf{det}(\mathbf{Q})) \\ &\mathsf{subject\ to} && \mathbf{Q} \succ 0,\ (5.12),\ (5.13),\ (5.14) \end{aligned} \tag{5.15}$$

which automatically generates a barrier pair $(\mathbf{B}(\mathbf{x}), \mathbf{k}(\mathbf{x}))$ if the problem is feasible.

5.1.3 Composite Barrier Pairs

To certify a larger region of attraction, composite quadratic barrier functions (Fig. 5.1-5.2) can combine multiple existing quadratic barrier functions, either centered at the origin [Hu and Lin, 2003; He, Thomas, and Sentis, 2020c] or with multiple equilibrium points [Thomas, He, and Sentis, 2018]. The LQR-tree strategy [Tedrake, Manchester, Tobenkin, and Roberts, 2010], which

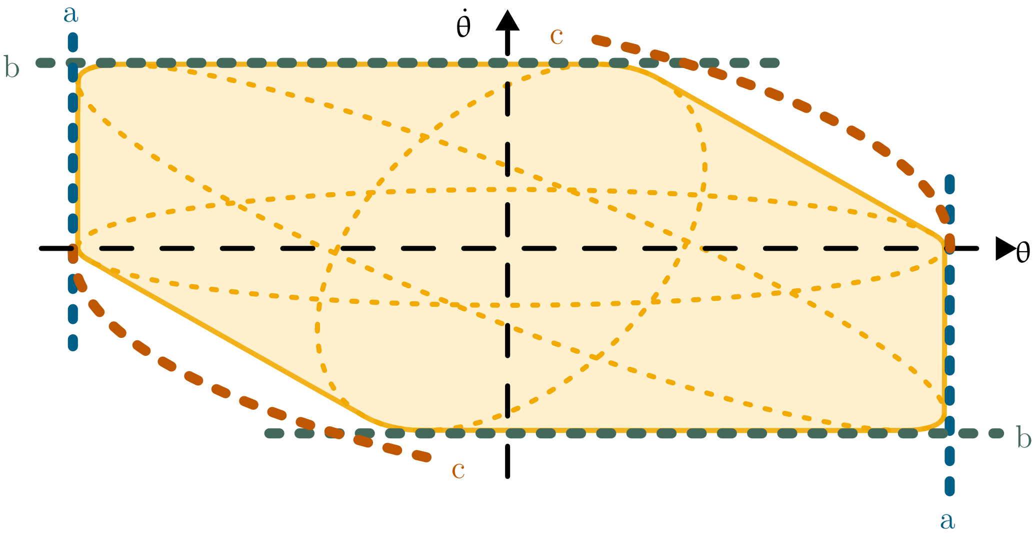

Figure 5.1: Single-Equilibrium Composition [Hu and Lin, 2003]

could potentially be applied to the barrier pair synthesis problem, creates a series of connected regions of attraction using quadratic Lyapunov functions for mapping the reachable state space. In [Hannaford and Ryu, 2002], a strategy was proposed to observe the safety of a system through its passivity which can be considered as a more conservative safety constraint than quadratic Lyapunov stability.

Proposition 5.1 ([Thomas, He, and Sentis, 2018]) For any list of barrier pairs $(\mathbf{B}_1, \mathbf{k}_1)$, $(\mathbf{B}_2, \mathbf{k}_2)$, $\ldots$, $(\mathbf{B}_\mathbf{N}, \mathbf{k}_\mathbf{N})$, the pair comprising the min-barrier function

$$\mathbf{B}(\mathbf{x}) \triangleq \min_{\mathbf{n}=1,\ldots,\mathbf{N}} \mathbf{B}_\mathbf{n}(\mathbf{x}) \tag{5.16}$$

and control input

$$\mathbf{k}(\mathbf{x}) \triangleq \mathbf{k}_\mathbf{n}(\mathbf{x}) \mid \mathbf{n} \in \arg\min_{\mathbf{n}=1,\ldots,\mathbf{N}} \mathbf{B}_\mathbf{n}(\mathbf{x}), \tag{5.17}$$

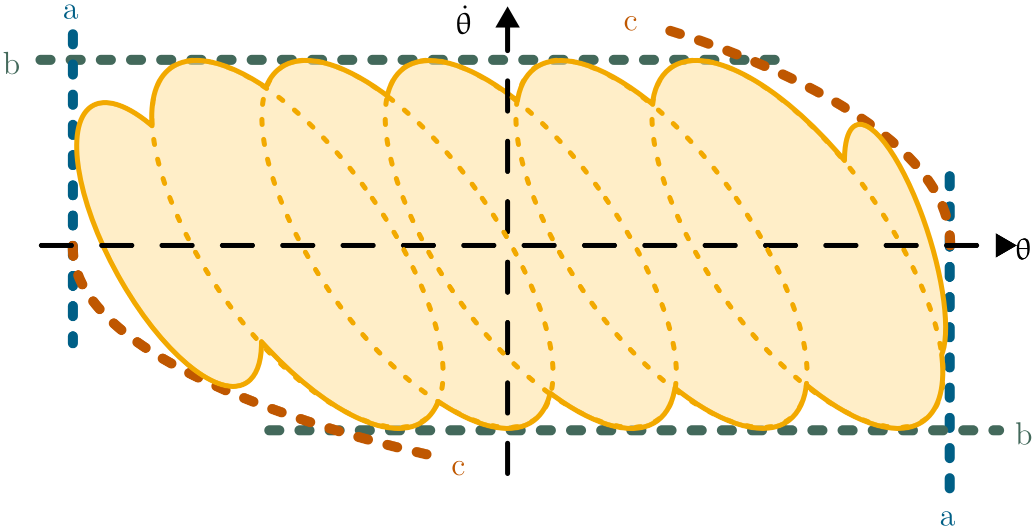

Figure 5.2: Multi-Equilibrium Composition [Thomas, He, and Sentis, 2018]

$(\mathbf{B}, \mathbf{k})$, is also a barrier pair.

Proof Consider the set

$$\mathcal{N} = \underset{\mathbf{n}=1,\ldots,\mathbf{N}}{\arg\min} \mathbf{B}_{\mathbf{n}}(\mathbf{x}), \tag{5.18}$$

and in particular an $\mathbf{n} \in \mathcal{N} : \mathbf{k}(\mathbf{x}) = \mathbf{k}_{\mathbf{n}}(\mathbf{x})$. Assuming first that $-1 < \mathbf{B}(\mathbf{x}) \leqslant 0$ and $\mathbf{u} = \mathbf{k}(\mathbf{x})$,

$$\dot{\mathbf{B}}(\mathbf{x}) \leqslant \dot{\mathbf{B}}_{\mathbf{n}}(\mathbf{x}) < 0, \tag{5.19}$$

since $(\mathbf{B}_{\mathbf{n}}, \mathbf{k}_{\mathbf{n}})$ is a barrier pair, $\mathbf{u} = \mathbf{k}(\mathbf{x}) = \mathbf{k}_{\mathbf{n}}(\mathbf{x})$, and $-1 < \mathbf{B}(\mathbf{x}) = \mathbf{B}_{\mathbf{n}}(\mathbf{x}) \leqslant 0$. This demonstrates property (a) in Definition 5.1. As for property (b) in Definition 5.1, using the same choice of $\mathbf{n}$,

$$0 \geqslant \mathbf{B}(\mathbf{x}) = \mathbf{B}_{\mathbf{n}}(\mathbf{x}) \implies \mathbf{x} \in \mathcal{X},\ \mathbf{k}(\mathbf{x}) = \mathbf{k}_{\mathbf{n}}(\mathbf{x}) \in \mathcal{U} \tag{5.20}$$

□

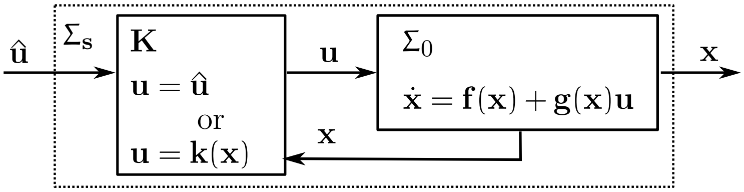

Figure 5.3: Block diagram, re-purposed from [Wieland and Allgöwer, 2007], showing a safety controller $\mathbf{K}$ in feedback with the original system Σ_0 to produce a safe system $\Sigma_{\mathbf{s}}$. The safety controller chooses either to be completely transparent ($\mathbf{u} = \hat{\mathbf{u}}$) or apply the known-to-be-safe input $\mathbf{u} = \mathbf{k}(\mathbf{x})$.

5.2 Examples

Equipped with barrier pair $(\mathbf{B}, \mathbf{k})$, with its potentially non-smooth $\mathbf{k}$, we opt for an explicitly discontinuous safety controller (Fig. 5.3) with a simple state machine (Fig. 5.4) to produce hysteretic behavior—reminiscent of [Prajna and Jadbabaie, 2004]'s second example of a safe hybrid system.

Behavior is tuned by two near-zero thresholds $\bar{\epsilon}$ and $\underline{\epsilon}$, $0 \geqslant \bar{\epsilon} > \underline{\epsilon} > -1$. As $\underline{\epsilon} \to \bar{\epsilon}$, the safety controller enforces the inequality constraint $\mathbf{B} \leqslant \bar{\epsilon}$, and as $\underline{\epsilon} \to -1$ it returns the system to the nearest equilibrium after each run-in with the safety limits. Detuning $\bar{\epsilon}$ from the ideal of zero can only reduce $\mathcal{X}_0$, but offers a hedge against real-world noisy signals in the computation of $\mathbf{B}(\mathbf{x})$. The gap between $\bar{\epsilon}$ and $\underline{\epsilon}$ indirectly sets the rate of back and forth switching when the system is up against the limit.

In the examples, we use a min-quadratic barrier pair—simply the combination of those barrier pairs resulting from the LMI sub-problem. We therefore expect that applying the control $\mathbf{k}(\mathbf{x})$ guarantees exponential convergence to one of the equilibriums—though which one, and whether the system will

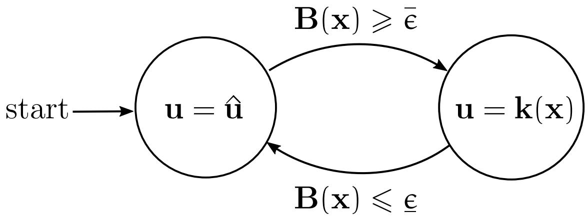

Figure 5.4: Hybrid Control System

transition between local control laws as it settles is not clear before hand. (This behavior is later visualized in Figs. 5.6 and 5.9.) The original equilibriums now represent the multiple minima of $\mathbf{B}$, all of them sharing the minimum value -1.

In this section, we provide two simulation examples demonstrating the operation of the hybrid safety controller. The first example is a second order unstable nonlinear system, an inverted pendulum[1] (Fig. 5.5). The second example is a spring-mass system with 1 input and 4 states—which we use to explore the behavior near high relative-order constraints. In both examples, we use only equilibrium-centered barrier pairs—generated using our example LMI subproblem.

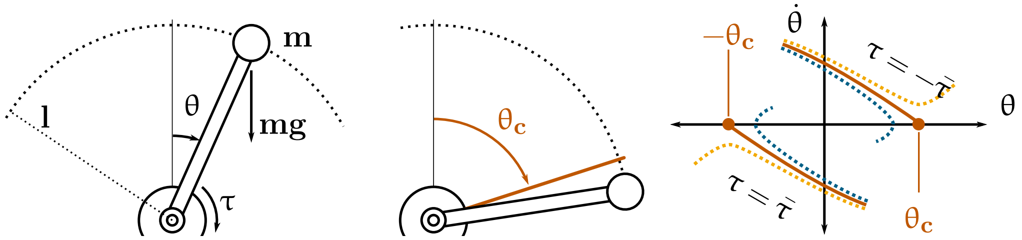

Figure 5.5: Inverted pendulum model with natural position limit θ_c—a "point of no return"—due to input limit $-\bar{\tau} \leqslant \tau \leqslant \bar{\tau}$, which causes θ_c to be a critical point in the flow field for $\tau = -\bar{\tau}$ and $-\theta_c$ to be one in the flow field for $\tau = \bar{\tau}$. In our approach such points are implicitly treated as on the boundary of the unsafe set.

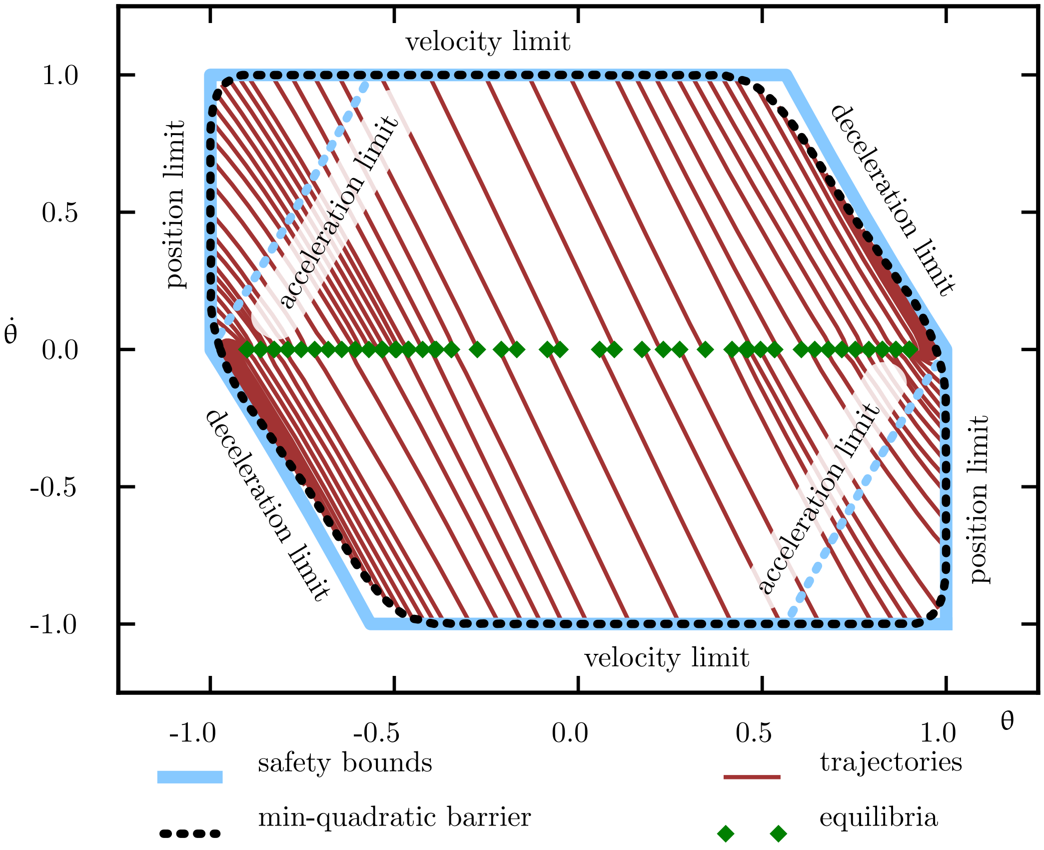

Figure 5.6: Visualizing the min-quadratic approximation of the safe region with 50 ellipsoids. Acceleration limits bound reachable region, but non-reachable region can still be safe, (as starting points, for example). Simulated trajectories at the bound demonstrate behavior of under $\mathbf{k}(\mathbf{x})$ control.

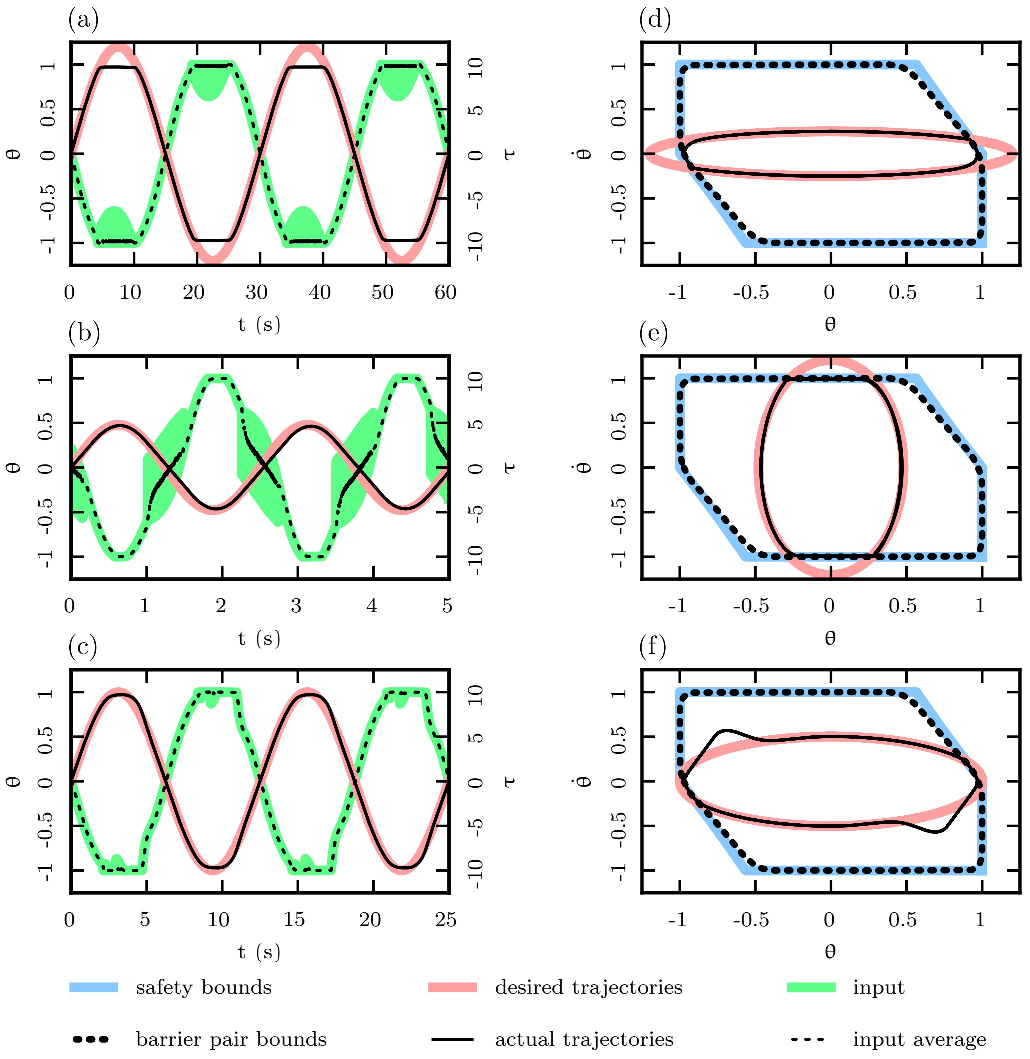

Figure 5.7: The inverted pendulum system protected by the safety controller, with a low priority reference tracking task for three references—one which exceeds position bounds (a,b), one which exceeds velocity bounds (c,d) and one which would just barely push this input limited unstable system past the point of no return (e,f). Each test shown both in the time domain (a,c,e), and in the phase space (b,d,f). Chattering input signal visualized raw and with low-pass filter. Input signal in low speed (a) and (e) examples dominated by gravity bias, hence behavior mostly opposite the position. 50 equilibrium point resolution. Signal tracking after leaving $\mathbf{B}(\mathbf{x}) = \underline{\epsilon}$ implemented with a simple feedback linearizing controller.

5.2.1 Inverted Pendulum Example

We consider an inverted pendulum (Fig. 5.5, $\mathbf{m} = 1$ kg, $\mathbf{l} = 1.213$ m, $\mathbf{g} = 9.8$ m/s/s), with safe region

$$\begin{aligned} \mathcal{X} &= \left\{ \begin{bmatrix}\theta\\ \dot\theta\end{bmatrix} \ :\ |\theta| \leqslant \theta_{\mathbf{c}} = 1 \text{ rad},\ |\dot\theta| \leqslant 1 \text{ rad/s} \right\}, \\ \mathcal{U} &= \{\tau :\ |\tau| \leqslant \bar\tau = 10 \text{ N}\cdot\text{m}\}, \end{aligned} \tag{5.21}$$

and dynamics

$$\mathbf{ml}^2\ddot\theta = \tau + \mathbf{mgl}\cdot\sin(\theta). \tag{5.22}$$

Linearizing around equilibrium $\theta_{\mathbf{e}}, \tau_{\mathbf{e}}$, with a validity region[2] $|\theta - \theta_{\mathbf{e}}| < \alpha = \min(0.25, \theta_{\mathbf{c}} - |\theta_{\mathbf{e}}|)$

$$\begin{aligned} \begin{bmatrix}\dot\theta\\ \ddot\theta\end{bmatrix} &\in \operatorname{Co}\left\{ \begin{bmatrix} 0 & 1 \\ \frac{\mathbf{g}}{\mathbf{l}}\mathbf{cos}(\theta_{\mathbf{e}}) \pm \bar\zeta & 0 \end{bmatrix} \begin{bmatrix}\theta - \theta_{\mathbf{e}} \\ \dot\theta - \dot\theta_{\mathbf{e}}\end{bmatrix} + \begin{bmatrix} 0 \\ \frac{1}{\mathbf{ml}^2}\end{bmatrix} (\tau - \tau_{\mathbf{e}}) \right\}, \\ \forall \quad \begin{bmatrix}\theta\\ \dot\theta\end{bmatrix} &\in \left\{ \begin{bmatrix}\theta\\ \dot\theta\end{bmatrix} \ :\ |\theta - \theta_{\mathbf{e}}| \leqslant \alpha,\ |\dot\theta| \leqslant 1\, \mathbf{rad}\cdot\mathbf{s}^{-1} \right\} \subseteq \mathcal{X}, \\ \tau &\in \mathcal{U}, \end{aligned}$$

where $\bar\zeta = \max\limits_{\theta : |\theta - \theta_{\mathbf{e}}| < \alpha} \zeta(\theta)$ represents a bound on linearization error,

$$\zeta(\theta) = \frac{\mathbf{g}}{\mathbf{l}} \left[\frac{\mathbf{sin}(\theta) - \mathbf{sin}(\theta_{\mathbf{e}})}{\theta - \theta_{\mathbf{e}}} - \mathbf{cos}(\theta_{\mathbf{e}}) \right]. \tag{5.23}$$

While it is possible to analytically calculate this bound, it is also simple to compute via one dimensional brute force search.[3]

---

[1] Though others have focused on the inverted pendulum for its interesting swing-up dynamics, we imagine a pendulum for which falling is a catastrophic failure.

[2] This validity region could potentially be iteratively tuned to match the extent of the ellipse, but such concerns are of lesser importance than verifying safety. Indeed, few systems will even have a readily available function for mapping these tuned regions to trustworthy models.

[3] This is not a conservative strategy in general, but it is an extremely accurate approximation relative to the numerical tolerances in the LMI subproblem.

This brings us to the LMI subproblems: we construct 50 barrier pairs to approximate the safe region using ellipsoids (Fig. 5.6), and then combine them—forming a barrier pair with a min-quadratic barrier function.

In the simulation (Fig. 5.7), the inverted pendulum system is protected by the safety controller, with the safe system $\mathbf{\Sigma_s}$ itself in a feedback configuration with a reference tracking controller. We demonstrate the behavior using three references. For a reference exceeding position bounds (Fig. 5.7 a,b), the pendulum stops very close to the position bound and returns to tracking after the reference returns to $\mathcal{X}_0$. In the mean time, constraints are enforced by high speed switching. For a reference exceeding velocity bounds (Fig. 5.7 c,d), the pendulum stalls at the maximum allowable velocity. For a reference which would just barely push this input-limited unstable system past the point of no return (Fig. 5.7 e,f), the pendulum begins to rail the deceleration in advance of impact, and comes to a full stop in the safe region. When the reference returns to $\mathcal{X}_0$ it is moving relatively fast, and the reference-tracker has to exceed this speed to catch up. While this last-second deceleration behavior is not as perfect as is possible with second order systems, it is close—and this is encouraging for the higher order systems for which no equally simple policy exists.

The time plots (Fig. 5.7 a,c,d) show the pendulum never violates any state or input limits during the tasks. By comparing the time plots between positions and inputs, the safety controller only applies $\mathbf{k}(\mathbf{x})$ when it is necessary. The chattering (fast switching) of the input happens because our $\bar{\epsilon} \approx \underline{\epsilon} \approx 0$. When the pendulum is in the safety region, the performance of the reference

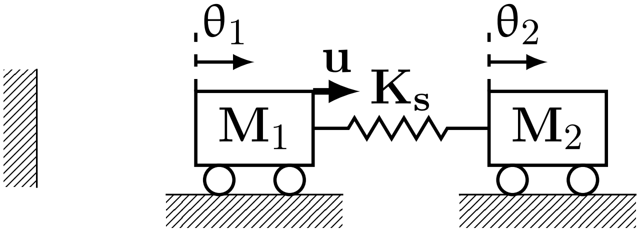

Figure 5.8: A conceptual series elastic actuator model, with higher relative order constraints.

tracking controller is preserved.

5.2.2 Series Elastic Actuator Example

A series elastic actuator can be conceptually modeled as a dual spring-mass system (Fig 5.8) with $\mathbf{M_1}$ as the motor, $\mathbf{M_2}$ as the output inertia, and $\mathbf{u}$ as the motor effort ($\mathbf{M_1} = \mathbf{M_2} = 1$, $\mathbf{K_s} = 1$). The safe constraints includes position limits, velocity limits, motor effort limits, and spring deflection limits:

$$\mathcal{X} = \{(\theta_1,\ \dot{\theta}_1,\ \theta_2,\ \dot{\theta}_2)^\top :\ |\theta_1 - \theta_2| \leqslant 1,\ |\theta_\mathbf{i}| \leqslant 1,\ |\dot{\theta}_\mathbf{i}| \leqslant 1,\ \mathbf{i} = 1, 2\},$$
$$\mathcal{U} = \{\mathbf{u} :\ |\mathbf{u}| \leqslant 10\}. \tag{5.24}$$

A linear state equation

$$\mathbf{M_1}\ddot{\theta}_1 = \mathbf{K_s}(\theta_2 - \theta_1) + \mathbf{u} \tag{5.25}$$

$$\mathbf{M_2}\ddot{\theta}_2 = \mathbf{K_s}(\theta_1 - \theta_2) \tag{5.26}$$

is valid in any point of the safe region. We use 50 barrier pairs to approximate the safe state space region.

30 trajectories are simulated on each of the 6 2-D projections (Fig. 5.9) of the state space. These trajectories start from the edge of the min-

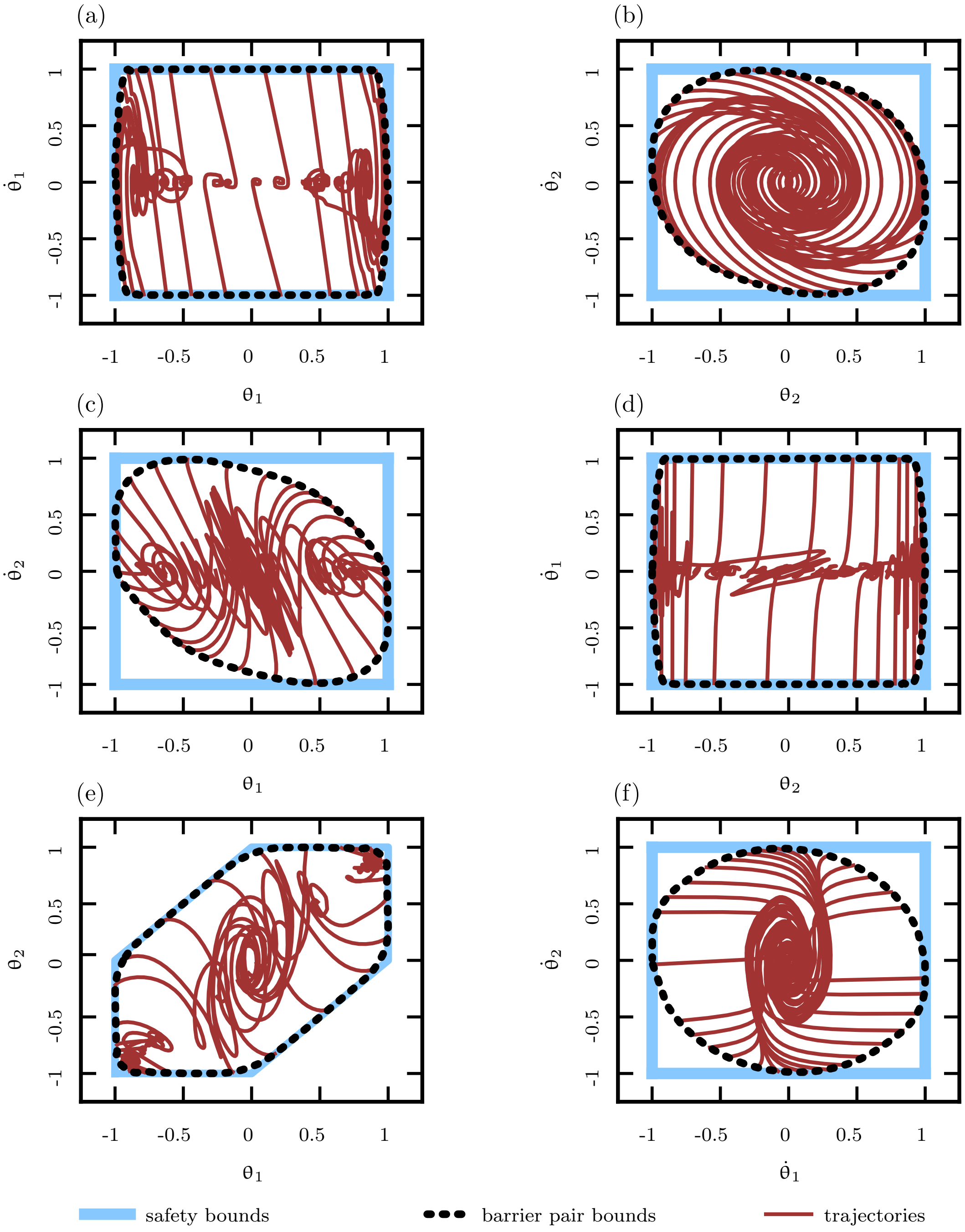

Figure 5.9: Visualizing multi-equilibrium composition in the SEA example.

quadratic barrier and converge to one of its 50 minima, and these projections offer a glimpse into the approximation performance of our strategy in this four dimensional space—which notably allows very tight adherence to the position limits in input, output, and spring deflection states.

Chapter 6

Output Feedback Control for Safe Human-Centered Robots

Safe control is mission critical for robotic systems with humans in the loop. Uncertain robot model parameters and the lack of direct human state knowledge bring extra difficulty to the stabilization of human–robot systems. Methods such as robust loop shaping [Buerger and Hogan, 2007; He, Thomas, Paine, and Sentis, 2019; Thomas, Coholich, and Sentis, 2019], model reference adaptive control [Chen, Chen, Yao, Zhu, Zhu, Wang, and Song, 2016] and energy shaping control [Lv and Gregg, 2017] aim to balance the closed loop stability and performance of physical human robot interaction systems. However, there is no backup controller if these systems fail to maintain safety, because backup safety controllers require full state availability.

For systems with direct state measurements, safety is usually verified by a barrier certificate. Similar to a Lyapunov function, a barrier function or barrier certificate decreases at the boundary of its zero level set [Prajna and

---

The results presented in this chapter have also appeared in part of [He, Thomas, and Sentis, 2020c]. As the primary contributor, Binghan He developed the control theory, did the mathematical proofs, programmed the control algorithms, and conducted simulations for the proof of concept. Gray C. Thomas provided theory supports on linear matrix inequality methods. This research was advised by Luis Sentis.

Jadbabaie, 2004]. While barrier certificate can be synthesized automatically through sum-of-squares (SoS) optimization [Prajna, 2006], a more ambitious goal is to combine the synthesis of the barrier function and the controller together through a control barrier function [Wieland and Allgöwer, 2007]. Various methods such as backstepping [Tee, Ge, and Tay, 2009] and quadratic programming [Ames, Xu, Grizzle, and Tabuada, 2016; Nguyen and Sreenath, 2016b] create control barrier functions to ensure output and state constraint satisfaction while other methods such as semidefinite programming [Pylorof and Bakolas, 2016] aimed to also include input saturation.

Safety warranties can also be considered a problem of finding an invariant set of the system which is also a subset the safe region in the state space. This allows us to consider using the synthesis of a quadratic Lyapunov function subject to the state and input constraints in a series of linear matrix inequalities (LMIs) [Boyd, El Ghaoui, Feron, and Balakrishnan, 1994]. To certify a larger safe region, composite quadratic Lyapunov functions can combine multiple existing certificates, either centered at the origin [Hu and Lin, 2003] or with multiple equilibrium points [Thomas, He, and Sentis, 2018]. The LQR-Tree strategy [Tedrake, Manchester, Tobenkin, and Roberts, 2010], which could potentially be applied to safety control, creates a series of connected regions of attraction (also known as funnels) using quadratic Lyapunov functions for mapping the reachable state space. In [Hannaford and Ryu, 2002], a strategy was proposed to observe the safety of a system through its passivity which can be considered as a more conservative safety constraint than quadratic Lyapunov stability.

A state space realization models a physical process if it correctly reproduces the corresponding output for each admissible input [Morse, 1974]. A Luenberger observer [Luenberger, 1964] asymptotically estimates the state of such a model of a linear system with only the direct measurement of input and output. This idea has also been extended for system with nonlinear modeling error [Zeitz, 1987]. For bounded modeling errors, the estimation error converges to a residue set instead of zero [Corless and Tu, 1998]. Recently, a method of using sum-of-squares programming [Pylorof, Bakolas, and Chan, 2019] aims to optimize the converging rate of a robust state estimation for uncertain nonlinear systems. But the estimated state still cannot be directly used for evaluation of barrier functions until it fully converges. The system could possibly violate the safety constraints before the barrier function estimation becomes valid.

In this chapter, we aim to close the gap between state estimation and safety assurance for uncertain systems. In order to address the barrier function estimation, we start with an identifier-based state estimator [Morse, 1996] which provides us a state estimate that is linear with the uncertain transfer function coefficients. Then, we define a vector norm based on a quadratic Lyapunov function such that a triangle inequality can be applied to decompose it into estimated state and estimation error. A convex polytopic bound on the estimated state is availiable through the estimator structure, and an upper bound on the estimation error arises from the convergence rate of the estimator and initial error. To obtain a larger safe (state-space) region, we extend this upper bound searching strategy to another vector norm defined based on a composite quadratic Lyapunov function [Hu and Lin, 2003], whose unit level set is a convex hull of the unit level sets of multiple quadratic Lyapunov functions. Using these vector norms, we derive our proposed barrier functions for uncertain systems with stable static output feedback. The synthesis of an estimator for the proposed barrier functions can be done in a two-step convex optimization using linear matrix inequalities, first optimizing the barrier function and then optimizing the estimator. This establishes a barrier pair [Thomas, He, and Sentis, 2018], which can be used with a hybrid safety controller to guarantee safety even for arbitrary inputs. In the end, our hybrid safety controller is demonstrated in a simulation of a simple human-exoskeleton interaction model with human stiffness uncertainty and velocity and force limits.

Let us consider an $\mathbf{n}$-th order strictly proper uncertain SISO system $\Sigma_{\mathbf{p}}$ with transfer function

$$\mathbf{P}(\mathbf{s}) = \frac{\mathbf{y}(\mathbf{s})}{\mathbf{u}(\mathbf{s})} = \frac{b_1\mathbf{s}^{\mathbf{n}-1} + \cdots + b_{\mathbf{n}-1}\mathbf{s} + b_{\mathbf{n}}}{\mathbf{s}^{\mathbf{n}} + a_1\mathbf{s}^{\mathbf{n}-1} + \cdots + a_{\mathbf{n}-1}\mathbf{s} + a_{\mathbf{n}}}, \tag{6.1}$$

$$\mathbf{a_i} \in [\underline{a}_{\mathbf{i}},\ \bar{a}_{\mathbf{i}}],\ \ \mathbf{i} \in \{1,\ 2,\ \cdots,\ \mathbf{n}\}, \tag{6.2}$$

$$\mathbf{b_j} \in [\underline{b}_{\mathbf{j}},\ \bar{b}_{\mathbf{j}}],\ \ \mathbf{j} \in \{1,\ 2,\ \cdots,\ \mathbf{n}\}, \tag{6.3}$$

where $\mathbf{u}$ and $\mathbf{y}$ are the input and output of $\Sigma_{\mathbf{p}}$ and $\mathbf{i}$ and $\mathbf{j}$ are the indices of the polynomial coefficients.

A state space realization of (6.1) can be expressed as

$$\dot{\mathbf{x}} = \mathbf{A}\mathbf{x} + \mathbf{b_u}\mathbf{u}, \tag{6.4}$$

$$\mathbf{y} = \mathbf{c}_0\mathbf{x}, \tag{6.5}$$

where $\mathbf{x}$ is the state vector. We specify $(\mathbf{A}, \mathbf{b_u}, \mathbf{c}_0)$ as an n-dimensional observable canonical form with $\mathbf{c}_0 \overset{\Delta}{=} [1, 0, \cdots, 0]$. With the state space realization in the form of (6.4), the problem we consider is defined as follows.

Suppose there exists a stable controller for the parameter uncertain system $\Sigma_\mathbf{p}$ which can satisfy constraints $\mathbf{x} \in \mathcal{X}$ and $\mathbf{u} \in \mathcal{U}$ indefinitely for all initial states in $\mathcal{X}_\mathbf{s} \subseteq \mathcal{X}$, find an estimator $\Sigma_\mathbf{e}$ that can observe whether the system is inside the safe region $\mathcal{X}_\mathbf{s}$ with direct measurement of only the input $\mathbf{u}$ and output $\mathbf{y}$ even when this controller is not necessarily active.

6.1 Vector Norm Functions

In order to upper bound the barrier function proposed later in this chapter, we recall the following two properties of a vector norm function.

Lemma 6.1 For every vector $\mathbf{x}$ in some vector space within $\mathbf{R^n}$, let $\|\cdot\|$ be a scalar function of $\mathbf{x}$ with the following properties.

(a) $0 < \|\mathbf{x}\| < \infty$ except for $\|\mathbf{x}\| = 0$ at the origin.

(b) $\|\lambda\mathbf{x}\| = |\lambda|\|\mathbf{x}\|$ for all $\lambda \in \mathbf{R}$.

Then $\|\cdot\|$ satisfies

(c) $\|\mathbf{x}+\mathbf{y}\| \leqslant \|\mathbf{x}\| + \|\mathbf{y}\|$

if and only if $\Omega \overset{\Delta}{=} \{\mathbf{x} \mid \|\mathbf{x}\| \leqslant 1\}$ is convex.

These properties (a), (b) and (c) in Lemma 6.1 are also called the three characteristic properties of a vector norm.

Lemma 6.2 Let $\|\cdot\|$ be a vector norm function satisfying (a), (b) and (c) in Lemma 6.1. Suppose there is a vector $\mathbf{x}_0 = \sum_{\mathbf{j}=1}^{\mathbf{N}} \gamma_{\mathbf{j}} \mathbf{x}_{\mathbf{j}}$ with $\sum_{\mathbf{j}=1}^{\mathbf{N}} \gamma_{\mathbf{j}} = 1$, $0 \leqslant \gamma_{\mathbf{j}} < 1$ for all $\mathbf{j} = 1, 2, \cdots, \mathbf{N}$ and $\|\mathbf{x}_0\| = \lambda$. Then there exists an index $\mathbf{j}$ such that $\|\mathbf{x}_{\mathbf{j}}\| \geqslant \lambda$.

Proof Suppose that $\|\mathbf{x}_{\mathbf{j}}\| < \lambda$ for all $\mathbf{j} = 1, 2, \cdots, \mathbf{N}$. Based on (b) in Lemma 6.1, we have $\|\gamma_{\mathbf{j}}\mathbf{x}\| = |\gamma_{\mathbf{j}}|\|\mathbf{x}\|$ for all $\mathbf{j} = 1, 2, \cdots, \mathbf{N}$.

Applying (c) in Lemma 6.1 to $\|\mathbf{x}_0\|$ we get

$$\|\mathbf{x}_0\| = \Big\| \sum_{\mathbf{j}=1}^{\mathbf{N}} \gamma_{\mathbf{j}} \mathbf{x}_{\mathbf{j}} \Big\| \leqslant \sum_{\mathbf{j}=1}^{\mathbf{N}} \gamma_{\mathbf{j}} \|\mathbf{x}_{\mathbf{j}}\| < \sum_{\mathbf{j}=1}^{\mathbf{N}} \gamma_{\mathbf{j}} \lambda = \lambda, \tag{6.6}$$

which contradicts $\|\mathbf{x}_0\| = \lambda$. □

The triangle inequality of vector norms allows us to decompose the state $\mathbf{x}$ into the estimated state $\hat{\mathbf{x}}$ and estimation error ϵ. While we do not know $\mathbf{x}$, we know $\hat{\mathbf{x}}$ and can bound ϵ within a decaying window—allowing us to extend barrier pairs [Thomas, He, and Sentis, 2018] to systems without full state availability.

6.1.1 Norm of Quadratic Lyapunov Function

Let us define a quadratic Lyapunov function as $\mathbf{V}_{\mathbf{q}}(\mathbf{x}) = \mathbf{x}^\top \mathbf{Q}^{-1} \mathbf{x}$ where $\mathbf{Q}$ is a positive definite matrix. We can form a vector norm using its square root,

$$\|\mathbf{x}\|_{\mathbf{q}} \triangleq \mathbf{V}_{\mathbf{q}}^{\frac{1}{2}}(\mathbf{x}), \tag{6.7}$$

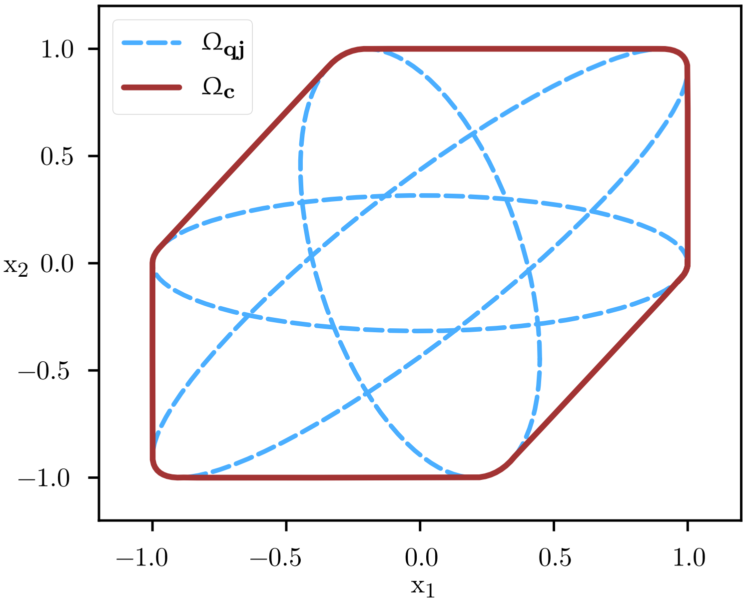

Figure 6.1: A unit ball $\Omega_{\mathbf{c}}$ of $\|\mathbf{x}\|_{\mathbf{c}}$ equivalent to the convex hull of the ellipsoidal unit balls $\Omega_{\mathbf{qj}}$ of three different $\|\mathbf{x}\|_{\mathbf{qj}}$.

because $\mathbf{V_q}(\mathbf{x})$ is positive definite, $\mathbf{V_q}(\lambda\mathbf{x}) = \lambda^2\mathbf{V_q}(\mathbf{x})$ and the unit level set of $\mathbf{V}(\mathbf{x})$ is convex.

6.1.2 Norm of Composite Quadratic Lyapunov Function

In order to obtain a larger safe region $\mathcal{X}_{\mathbf{s}}$, a composite quadratic Lyapunov function is considered. For multiple different quadratic Lyapunov functions defined with positive-definite matrices $\mathbf{Q}_1, \mathbf{Q}_2, \cdots, \mathbf{Q}_{\mathbf{n_q}}$, a composite quadratic Lyapunov function [Hu and Lin, 2003] is defined as

$$\mathbf{V_c}(\mathbf{x}) \triangleq \min_{\gamma} \mathbf{x}^\top \mathbf{Q}^{-1}(\gamma)\mathbf{x}, \tag{6.8}$$

$$\mathbf{Q}(\gamma) \triangleq \sum_{\mathbf{j}=1}^{\mathbf{n_q}} \gamma_{\mathbf{j}} \mathbf{Q_j}, \tag{6.9}$$

where $\sum_{\mathbf{j}=1}^{\mathbf{n_q}} \gamma_{\mathbf{j}} = 1$ and $\gamma_{\mathbf{j}} \geqslant 0$ for all $\mathbf{j} = 1, 2, \cdots, \mathbf{n_q}$.

The unit level set of $\mathbf{V_c}(\mathbf{x})$ is the convex hull of all the unit level sets of $\mathbf{V_{qj}}(\mathbf{x}) = \mathbf{x}^\top \mathbf{Q_j^{-1}} \mathbf{x}$ for $\mathbf{j} = 1, 2, \cdots, \mathbf{n_q}$ and is therefore also a convex shape (see Fig. 6.1). Since $\mathbf{V_c}(\mathbf{x})$ is positive definite and $\mathbf{V_c}(\lambda \mathbf{x}) = \lambda^2 \mathbf{V_c}(\mathbf{x})$, we can use Lemma 6.1 to define the "composite" vector norm,

$$\|\mathbf{x}\|_\mathbf{c} \triangleq \mathbf{V_c^{\frac{1}{2}}}(\mathbf{x}). \tag{6.10}$$

6.2 Estimator-Based Barrier Pairs

6.2.1 Robust State Estimator

Since only $\mathbf{u}$ and $\mathbf{y}$ are directly measured, we need to estimate $\mathbf{x}$ in (6.4) to verify safety. According to Lemma 1 in [Morse, 1980], we can select a strictly stable $\mathbf{A}_0$ in observable canonical form such that (6.4) becomes

$$\dot{\mathbf{x}} = \mathbf{A}_0 \mathbf{x} + \mathbf{b_y} \mathbf{y} + \mathbf{b_u} \mathbf{u}, \tag{6.11}$$

where $\mathbf{A}$ in (6.4) is replaced by $\mathbf{A}_0 + \mathbf{b_y} \mathbf{c}_0$. Let the characteristic equation of $\mathbf{A}_0$ be $\mathbf{s^n} + \hat{a}_1 \mathbf{s^{n-1}} + \cdots + \hat{a}_{\mathbf{n}-1} \mathbf{s} + \hat{a}_\mathbf{n}$. Since $(\mathbf{c}_0, \mathbf{A}_0)$ is also a pair in the observable canonical form, $\mathbf{b_y}$ and $\mathbf{b_u}$ are

$$\mathbf{b_y} = [\hat{a}_1 - a_1,\ \hat{a}_2 - a_2,\ \cdots,\ \hat{a}_\mathbf{n} - a_\mathbf{n}]^\top, \tag{6.12}$$

$$\mathbf{b_u} = [b_1,\ b_2,\ \cdots,\ b_\mathbf{n}]^\top, \tag{6.13}$$

which are either linear with or affine to the coefficients of the polynomials of $\mathbf{P}(\mathbf{s})$ in (6.1).

We estimate $\mathbf{x}$ through an identifier-based estimator which includes a pair of sensitivity function filters expressed as

$$\begin{aligned}\dot{\theta}_{\mathbf{y}} &= \mathbf{A}_0^\top \theta_{\mathbf{y}} + \mathbf{c}_0^\top \mathbf{y},\\ \dot{\theta}_{\mathbf{u}} &= \mathbf{A}_0^\top \theta_{\mathbf{u}} + \mathbf{c}_0^\top \mathbf{u},\end{aligned} \tag{6.14}$$

where $(\mathbf{A}_0^\top, \mathbf{c}_0^\top)$ is a controllable pair in the canonical form.

Lemma 6.3 Suppose $\mathbf{E}_{\mathbf{y}} = \mathbf{C}_0^{-1}\Theta_{\mathbf{y}}^\top$ and $\mathbf{E}_{\mathbf{u}} = \mathbf{C}_0^{-1}\Theta_{\mathbf{u}}^\top$ where $\mathbf{C}_0$ is the observability matrix of $(\mathbf{c}_0, \mathbf{A}_0)$, and $\Theta_{\mathbf{y}}$ and $\Theta_{\mathbf{u}}$ are the controllability matrices of $(\mathbf{A}_0^\top, \theta_{\mathbf{y}})$ and $(\mathbf{A}_0^\top, \theta_{\mathbf{u}})$. $\mathbf{E}_{\mathbf{y}}\mathbf{b}_{\mathbf{y}} + \mathbf{E}_{\mathbf{u}}\mathbf{b}_{\mathbf{u}}$ converges to $\mathbf{x}$ exponentially.

Proof This is similar to Lemma 2 in [Morse, 1980]. Notice that $\mathbf{C}_0$ is also the transpose of the controllability matrix of $(\mathbf{A}_0^\top, \mathbf{c}_0^\top)$. We can derive from (6.14) that

$$\begin{aligned}\dot{\mathbf{E}}_{\mathbf{y}}^\top &= \mathbf{A}_0^\top \mathbf{E}_{\mathbf{y}}^\top + \mathbf{I}\mathbf{y},\\ \dot{\mathbf{E}}_{\mathbf{u}}^\top &= \mathbf{A}_0^\top \mathbf{E}_{\mathbf{u}}^\top + \mathbf{I}\mathbf{u}.\end{aligned} \tag{6.15}$$

Because $\mathbf{A}_0$ is in a canonical form, it is easy to show that $\mathbf{E}_{\mathbf{y}}\mathbf{A}_0 = \mathbf{A}_0\mathbf{E}_{\mathbf{y}}$ and $\mathbf{E}_{\mathbf{u}}\mathbf{A}_0 = \mathbf{A}_0\mathbf{E}_{\mathbf{u}}$. Therefore, by taking the transpose of (6.15), we obtain $\dot{\mathbf{E}}_{\mathbf{y}} = \mathbf{A}_0\mathbf{E}_{\mathbf{y}} + \mathbf{I}\mathbf{y}$ and $\dot{\mathbf{E}}_{\mathbf{u}} = \mathbf{A}_0\mathbf{E}_{\mathbf{u}} + \mathbf{I}\mathbf{u}$.

If we define $\hat{\mathbf{x}} \triangleq \mathbf{E}_{\mathbf{y}}\mathbf{b}_{\mathbf{y}} + \mathbf{E}_{\mathbf{u}}\mathbf{b}_{\mathbf{u}}$, then $\dot{\hat{\mathbf{x}}} = \mathbf{A}_0\hat{\mathbf{x}} + \mathbf{b}_{\mathbf{y}}\mathbf{y} + \mathbf{b}_{\mathbf{u}}\mathbf{u}$. Since $\mathbf{A}_0$ is strictly stable, we have $\mathbf{x} = \hat{\mathbf{x}} + \epsilon$ where $\epsilon = \mathbf{e}^{\mathbf{A}_0\mathbf{t}}(\mathbf{x}(0) - \hat{\mathbf{x}}(0))$. □

Notice that the dynamics of $\hat{\mathbf{x}}$ can also be expressed as

$$\dot{\hat{\mathbf{x}}} = \mathbf{A}\hat{\mathbf{x}} + \mathbf{b}_{\mathbf{y}}(\mathbf{y} - \mathbf{c}_0\hat{\mathbf{x}}) + \mathbf{b}_{\mathbf{u}}\mathbf{u}, \tag{6.16}$$

which is a Luenberger observer of (6.4). However (6.16) cannot be directly implemented because of the uncertainty in $\mathbf{b}_{\mathbf{y}}$ and $\mathbf{b}_{\mathbf{u}}$. The identifier-based estimator in (6.14) provides us a convex hull containing the estimated state vector $\hat{\mathbf{x}}$,

$$\begin{aligned} &\hat{\mathbf{x}}(\mathbf{b_y},\,\mathbf{b_u}) \in \mathrm{Co}\Bigg\{ \mathbf{E_y}\begin{bmatrix}\hat{a}_1-a_1\\ \hat{a}_2-a_2\\ \vdots\\ \hat{a}_\mathbf{n}-a_\mathbf{n}\end{bmatrix} + \mathbf{E_u}\begin{bmatrix}b_1\\ b_2\\ \vdots\\ b_\mathbf{n}\end{bmatrix}, \\ &\qquad\qquad\qquad \mathbf{a_i}\in\{\underline{a}_\mathbf{i},\ \bar{a}_\mathbf{i}\},\ \mathbf{b_j}\in\{\underline{b}_\mathbf{j},\ \bar{b}_\mathbf{j}\}, \\ &\qquad\qquad\qquad \text{for } \mathbf{i},\,\mathbf{j}=1,\,2,\,\cdots,\,\mathbf{n}\ \Bigg\}. \end{aligned} \tag{6.17}$$

Because of the initial estimation error $\epsilon_0 \overset{\Delta}{=} \mathbf{x}(0)-\hat{\mathbf{x}}(0)$, any barrier function $\mathbf{B}(\mathbf{x})$ aiming to constrain the system inside the safe region $\mathcal{X}_\mathbf{s}$ cannot be directly bounded using $\hat{\mathbf{x}}(\mathbf{b_y},\,\mathbf{b_u})$. Instead, our goal is to find an upper bound for the barrier function using both $\hat{\mathbf{x}}(\mathbf{b_y},\,\mathbf{b_u})$ and ϵ_0.

For a given pair of $\mathbf{E_y}$ and $\mathbf{E_u}$, we can derive from Lemma 6.2 that the maximum values of $\|\hat{\mathbf{x}}\|_\mathbf{q}$ and $\|\hat{\mathbf{x}}\|_\mathbf{c}$ occur at one of vertices of the convex hull in (6.17).

Theorem 6.1 If a strictly stable matrix $\mathbf{A}_0$ in (6.11) and (6.14) satisfies

$$\mathbf{A}_0\mathbf{Q}+\mathbf{Q}\mathbf{A}_0^\top+2\alpha\mathbf{Q}\preceq 0, \tag{6.18}$$

then for all $\mathbf{t}\geqslant 0$ there exists an $\mathbf{i}\in\{1,\,\cdots,\,\mathbf{N}\}$ such that

$$\|\mathbf{x}\|_\mathbf{q}\leqslant\|\hat{\mathbf{x}}(\mathbf{b_{yi}},\,\mathbf{b_{ui}})\|_\mathbf{q}+\mathbf{e}^{-\alpha\mathbf{t}}\|\epsilon_0\|_\mathbf{q}, \tag{6.19}$$

where $\hat{\mathbf{x}}(\mathbf{b_{yi}},\,\mathbf{b_{ui}})$ for $\mathbf{i}=1,\,2,\,\cdots,\,\mathbf{N}$ are the all vertices of (6.17).

Proof From Lemma 6.1, we have $\|\mathbf{x}\|_\mathbf{q}\leqslant\|\hat{\mathbf{x}}\|_\mathbf{q}+\|\epsilon\|_\mathbf{q}$. The time derivative of $\mathbf{V_q}(\epsilon)$ can be expressed as

$$\dot{\mathbf{V}}_\mathbf{q}(\epsilon)=\epsilon^\top(\mathbf{Q}^{-1}\mathbf{A}_0+\mathbf{A}_0^\top\mathbf{Q}^{-1})\epsilon=\epsilon^\top\mathbf{Q}^{-1}(\mathbf{A}_0\mathbf{Q}+\mathbf{Q}\mathbf{A}_0^\top)\mathbf{Q}^{-1}\epsilon. \tag{6.20}$$

By substituting (6.18), $\dot{\mathbf{V}}_{\mathbf{q}}(\epsilon) \leqslant -2\alpha \mathbf{V}_{\mathbf{q}}(\epsilon)$ which guarantees that $\mathbf{V}_{\mathbf{q}}(\epsilon) \leqslant \mathbf{e}^{-2\alpha \mathbf{t}} \mathbf{V}_{\mathbf{q}}(\epsilon_0)$. Therefore, $\|\epsilon\|_{\mathbf{q}} \leqslant \mathbf{e}^{-\alpha \mathbf{t}} \|\epsilon_0\|_{\mathbf{q}}$. Together with Lemma 6.2, we have (6.19). □

This Theorem 6.1 provides an upper bound on $\|\mathbf{x}\|_{\mathbf{q}}$ which is available in that it be calculated from $\hat{\mathbf{x}}$ and ϵ_0 for all $\mathbf{t} \geqslant 0$.

Theorem 6.2 For all $\mathbf{j} = 1, 2, \cdots, \mathbf{n}_{\mathbf{q}}$, if a strictly stable matrix $\mathbf{A}_0$ in (6.11) and (6.14) satisfies

$$\mathbf{A}_0 \mathbf{Q}_{\mathbf{j}} + \mathbf{Q}_{\mathbf{j}} \mathbf{A}_0^{\top} + 2\alpha \mathbf{Q}_{\mathbf{j}} \preceq 0, \tag{6.21}$$

then for all $\mathbf{t} \geqslant 0$ there exists an $\mathbf{i} \in \{1, \cdots, \mathbf{N}\}$ such that

$$\|\mathbf{x}\|_{\mathbf{c}} \leqslant \|\hat{\mathbf{x}}(\mathbf{b}_{\mathbf{yi}}, \mathbf{b}_{\mathbf{ui}})\|_{\mathbf{c}} + \mathbf{e}^{-\alpha \mathbf{t}} \|\epsilon_0\|_{\mathbf{c}} \tag{6.22}$$

where $\hat{\mathbf{x}}(\mathbf{b}_{\mathbf{yi}}, \mathbf{b}_{\mathbf{ui}})$ for $\mathbf{i} = 1, 2, \cdots, \mathbf{N}$ are the all vertices of (6.17).

Proof As in Theorem 6.1. □

Therefore, an upper bound on $\|\mathbf{x}\|_{\mathbf{c}}$ can be calculated using $\hat{\mathbf{x}}$ and ϵ_0 for all $\mathbf{t} \geqslant 0$.

6.2.2 Output Feedback Safety Controller

We can now introduce two barrier pairs using our vector norms and static output feedback controller.

Proposition 6.1 Suppose $\mathbf{V}_{\mathbf{q}}$ is a quadratic Lyapunov function for system of (6.4) and (6.5) with a static output feedback $\mathbf{u} = \mathbf{k}\mathbf{y}$ and $\Omega_{\mathbf{q}}$ is a unit ball of $\|\mathbf{x}\|_{\mathbf{q}}$ defined as (6.7). If

$$\Omega_{\mathbf{q}} \subseteq \mathcal{X} \cap \{\mathbf{x} \mid \mathbf{c}_0 \mathbf{x} \in \mathbf{k}^{-1} \mathcal{U}\}, \tag{6.23}$$

then $(\|\mathbf{x}\|_{\mathbf{q}} - 1,\ \mathbf{ky})$ is a barrier pair.

Proof Let $\mathbf{B_q}(\mathbf{x}) = \|\mathbf{x}\|_{\mathbf{q}} - 1$. Its time derivative is

$$\dot{\mathbf{B}}_{\mathbf{q}}(\mathbf{x}) = \frac{1}{2}\|\mathbf{x}\|_{\mathbf{q}}^{-1}\dot{\mathbf{V}}_{\mathbf{q}}. \tag{6.24}$$

Since $\|\mathbf{x}\|_{\mathbf{q}}^{-1} > 0$ and $\dot{\mathbf{V}}_{\mathbf{q}} < 0$ when $-1 < \mathbf{B_q}(\mathbf{x}) \leqslant 0$, $(\mathbf{B_q}(\mathbf{x}),\ \mathbf{ky})$ satisfies (a) in Definition 5.1. From (6.23), we also have (b) in Definition 5.1 satisfied. □

Proposition 6.2 Suppose $\mathbf{V_c}$ is a composite quadratic Lyapunov function defined as (6.8) and (6.9) for the system of (6.4) and (6.5), with static output feedback $\mathbf{u} = \mathbf{ky}$ and that $\Omega_{\mathbf{c}}$ is a unit ball of $\|\mathbf{x}\|_{\mathbf{c}}$ defined as in (6.10). If we have

$$\Omega_{\mathbf{c}} \subseteq \mathcal{X} \cap \{\mathbf{x} \mid \mathbf{c}_0\mathbf{x} \in \mathbf{k}^{-1}\mathcal{U}\}, \tag{6.25}$$

then $(\|\mathbf{x}\|_{\mathbf{c}} - 1,\ \mathbf{ky})$ is a barrier pair.

Proof As in Proposition 6.1. □

As in (6.19) and (6.22), upper bounds of the barrier functions of these two barrier pairs can be calculated using $\hat{\mathbf{x}}$ and ϵ_0 for all $\mathbf{t} \geqslant 0$.

6.2.3 Barrier Pair Synthesis Sub-Problems

Both barrier functions $\mathbf{B_c}(\mathbf{x}) \triangleq \|\mathbf{x}\|_{\mathbf{c}} - 1$ and their identifier-based estimators can be synthesized with LMIs, through the sub-problem of synthesizing $\mathbf{B_q}(\mathbf{x}) \triangleq \|\mathbf{x}\|_{\mathbf{q}} - 1$.

Barrier Function Synthesis With static output feedback, the closed loop system of (6.4) is still a polytopic linear differential inclusion (PLDI) model

[Boyd, El Ghaoui, Feron, and Balakrishnan, 1994] $\dot{\mathbf{x}} \in \mathbf{A_c x}$ with

$$\mathbf{A_c} = \mathrm{Co}\left\{ \begin{bmatrix} 0 & 1 & & 0 \\ \vdots & & \ddots & \\ 0 & 0 & & 1 \\ 0 & 0 & \cdots & 0 \end{bmatrix} - \begin{bmatrix} a_1 \\ a_2 \\ \vdots \\ a_\mathbf{n} \end{bmatrix} \mathbf{c}_0 + \begin{bmatrix} b_1 \\ b_2 \\ \vdots \\ b_\mathbf{n} \end{bmatrix} \mathbf{k c}_0, \right.$$
$$\mathbf{a_i} \in \{\underline{a}_\mathbf{i},\ \bar{a}_\mathbf{i}\},\ \mathbf{b_j} \in \{\underline{b}_\mathbf{j},\ \bar{b}_\mathbf{j}\},$$
$$\left. \text{for } \mathbf{i},\ \mathbf{j} = 1,\ 2,\ \cdots,\ \mathbf{n} \right\}. \tag{6.26}$$

Supposing that $\mathcal{X}$ and $\mathcal{U}$ can be described (perhaps conservatively) as

$$\mathcal{X} = \{\mathbf{x} : |\mathbf{f_i x}| \leqslant 1,\ \ \mathbf{i} = 1,\ 2,\ \cdots,\ \mathbf{n_f}\}, \tag{6.27}$$

$$\mathcal{U} = \{\mathbf{u} : \quad |\mathbf{u}| \leqslant \bar{\mathbf{u}}\}, \tag{6.28}$$

they can be enforced by LMIs

$$\mathbf{f_i Q_j f_i^\top} \leqslant 1, \quad \forall\ \mathbf{i} = 1,\ 2,\ \cdots,\ \mathbf{n_f}, \tag{6.29}$$

$$\mathbf{c}_0 \mathbf{Q_j} \mathbf{c}_0^\top \leqslant \frac{\bar{\mathbf{u}}^2}{\mathbf{k}^2}. \tag{6.30}$$

To synthesize $\mathbf{Q_j}$, we maximize the width of the unit ball of $\mathbf{x}^\top \mathbf{Q_j}^{-1} \mathbf{x}$ along some state space direction $\mathbf{x_j}$ by minimizing $\rho_\mathbf{j}$ subject to the following LMI

$$\begin{bmatrix} \rho_\mathbf{j} & \mathbf{x_j^\top} \\ \mathbf{x_j} & \mathbf{Q_j} \end{bmatrix} \succeq 0, \tag{6.31}$$

such that the optimization sub-problem becomes

$$\begin{aligned} \underset{\mathbf{Q_j}}{\text{minimize}} \quad & \rho_\mathbf{j} \\ \text{subject to} \quad & (6.29),\ (6.30),\ (6.31),\ \mathbf{Q_j} \succ 0, \\ & \mathbf{A_{ci} Q_j} + \mathbf{Q_j A_{ci}^T} + 2\alpha_0 \mathbf{Q_j} \preceq 0, \\ & \forall\ \mathbf{i} = 1,\ 2,\ \cdots,\ \mathbf{N}. \end{aligned} \tag{6.32}$$

where $\mathbf{A_{ci}}$ for $\mathbf{i} = 1,\ 2,\ \cdots,\ \mathbf{N}$ are the all vertices of (6.26). A positive value of α_0 is used to guarantee a minimum exponential decay rate for $\|\mathbf{x}\|_\mathbf{c}$.

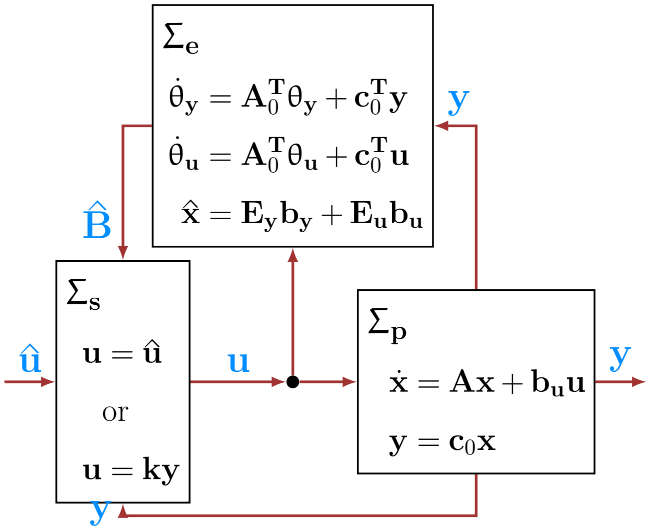

Figure 6.2: Block diagram consisting of plant $\Sigma_{\mathbf{p}}$, estimator $\Sigma_{\mathbf{e}}$ and hybrid safety controller $\Sigma_{\mathbf{s}}$.

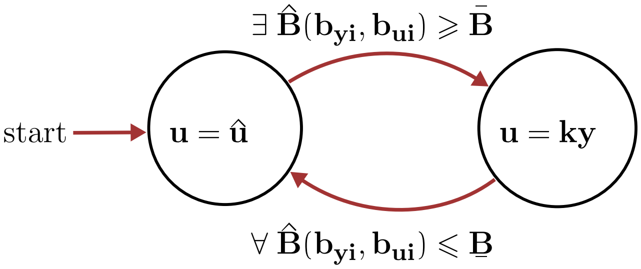

Figure 6.3: Switching logic of hybrid safety controller $\Sigma_{\mathbf{s}}$.

Estimator Synthesis While it is simple to specify an $\mathbf{A}_0$ in (6.11) with a fast decay rate of ϵ (choosing big negative-real-part eigenvalues), this does not necessarily improve the value of α in (6.22). To synthesize an $\mathbf{A}_0$ in the set of matrices in observable canonical form $\mathcal{O} \subset \mathbf{R}^{\mathbf{n}\times\mathbf{n}}$ we directly optimize for α:

$$\begin{aligned} \underset{\mathbf{A}_0\in\mathcal{O}}{\text{maximize}} \quad & \alpha \\ \text{subject to} \quad & \mathbf{A}_0\mathbf{Q_j} + \mathbf{Q_j}\mathbf{A}_0^\top + 2\alpha\mathbf{Q_j} \preceq 0, \\ & \forall\, \mathbf{j} = 1,\, 2,\, \cdots,\, \mathbf{n_q}, \end{aligned} \tag{6.33}$$

knowing that a solution $\alpha \geqslant \alpha_0$ will exist. (Any $\mathbf{A}_0$ in the convex hull of (6.26) is guaranteed to satisfy the constraints in (6.33) with a decay rate of α_0.)

6.3 A Human-Robot Interaction Example

To enforce safety satisfaction on a potentially unsafe input $\hat{\mathbf{u}}$, we can estimate the barrier function as

$$\hat{\mathbf{B}}_\mathbf{c}(\mathbf{b_y},\, \mathbf{b_u}) \triangleq \|\hat{\mathbf{x}}(\mathbf{b_y},\, \mathbf{b_u})\|_\mathbf{c} + \mathbf{e}^{-\alpha\mathbf{t}}\|\epsilon_0\|_\mathbf{c} - 1. \tag{6.34}$$

With this estimate, we can design a hybrid safety controller $\Sigma_\mathbf{s}$ which decides whether to apply either $\hat{\mathbf{u}}$ or $\mathbf{ky}$ (that is, the safety backup control law) as the input in order to keep $\mathbf{B_c} \leqslant 0$ (see Fig. 6.2) and therefore guarantee safety.

According to Theorem 6.2, system $\Sigma_\mathbf{p}$ is guaranteed to be safe if $\hat{\mathbf{B}}_\mathbf{c}(\mathbf{b_{yi}},\, \mathbf{b_{ui}}) \leqslant 0$ for all vertices $\hat{\mathbf{x}}(\mathbf{b_{yi}},\, \mathbf{b_{ui}})$ of convex hull (6.17). Therefore, the switching logic for $\Sigma_\mathbf{s}$ defined in Fig. 6.3, which introduces two near-zero thresholds $\underline{\mathbf{B}}$ and $\bar{\mathbf{B}}$ (with $-1 < \underline{\mathbf{B}} < \bar{\mathbf{B}} \leqslant 0$), will result in robust safety.

To illustrate robust barrier function estimation and hybrid safety control,

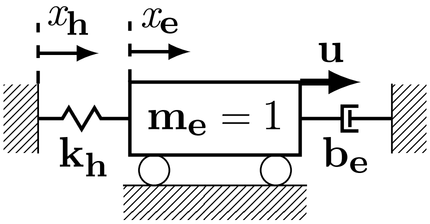

Figure 6.4: Our simplified human-human interaction model, a mass-spring-damper system, includes an uncertain human stiffness $\mathbf{k_h}$, an exoskeleton damping $\mathbf{b_e}$, and an exoskeleton inertia $\mathbf{m_e}$.

we introduce a simplified human-exoskeleton interaction model. As shown in Fig. 6.4, this model is a mass-spring-damper with uncertain human stiffness $\mathbf{k_h}$, the exoskeleton damping $\mathbf{b_e}$, and exoskeleton inertia $\mathbf{m_e}$.

6.3.1 Barrier Pair Synthesis

The exoskeleton plant can be expressed as a transfer function

$$\mathbf{P}(\mathbf{s}) = \frac{\mathbf{y}(\mathbf{s})}{\mathbf{u}(\mathbf{s})} = \frac{\mathbf{k_h}}{\mathbf{m_e}\mathbf{s}^2 + \mathbf{b_e}\mathbf{s} + \mathbf{k_h}} \tag{6.35}$$

where the input $\mathbf{u}$ is the actuator force exerted and the output $\mathbf{y} \triangleq \mathbf{k_h}(x_\mathbf{e} - x_\mathbf{h})$ is the contact force between human and exoskeleton. Although the contact force and the exoskeleton position, $x_\mathbf{e}$, can be measured, the reference position, $x_\mathbf{h}$, of the human spring is not available because of the unknown stiffness.

Suppose that the uncertain value of $\mathbf{k_h}$ is in the range from 4 to 12 and that the value of $\mathbf{b_e}$ is 12. We can express the closed loop $\mathbf{A_c}$ matrix set with static output feedback as a convex hull

$$\mathbf{A_c} = \mathrm{Co}\left\{ \begin{bmatrix} -12 & 1 \\ -\mathbf{k_h} & 0 \end{bmatrix} + \begin{bmatrix} 0 \\ \mathbf{k_h} \end{bmatrix} \mathbf{kc}_0, \quad \mathbf{k_h} = 4,\ 12 \right\}. \tag{6.36}$$

And the safety constraints can be defined via the sets

$$\begin{aligned}\mathcal{X} &= \{[x_1,\ x_2]^\top :\ |-x_1 + x_2/12| \leqslant 1\},\\ \mathcal{U} &= \{\mathbf{u}:\ |\mathbf{u}| \leqslant 1.2\},\end{aligned} \tag{6.37}$$

where the output $\mathbf{y} = x_1$ and $\dot{\mathbf{y}} = -12x_1 + x_2$, so $\mathcal{X}$ is constraining the output derivative $|\dot{\mathbf{y}}| \leqslant 12$.

We choose the static output feedback gain $\mathbf{k} = -1.2$ which is stable, and leads to a human amplification factor of 2.2 and the output constraint $|\mathbf{y}| \leqslant 1$. In Fig. 6.5, we construct a barrier function $\mathbf{B_c}$ from two different quadratic Lyapunov functions (optimized along directions $\mathbf{x_j} = [1,\ 0]^\top$ and $\mathbf{x_j} = [1,\ 12]^\top$) generated by synthesis (6.32) with a shared decay rate of $\alpha_0 = 0.50$. Then, an $\mathbf{A}_0$ matrix with a characteristic polynomial $\mathbf{s}^2 + \hat{a}_1\mathbf{s} + \hat{a}_2$ (with $\hat{a}_1 = 13.60$ and $\hat{a}_2 = 18.68$) and a higher decay rate ($\alpha = 0.68$) is generated from synthesis (6.33). Notice that the optimal $\mathbf{A}_0$ matrix is not exactly inside the convex hull of (6.36).

6.3.2 Simulation

In the numerical simulation, human stiffness $\mathbf{k_h} = 8$. In our first simulation, we release the system near the boundary of $\Omega_\mathbf{c}$ with zero nominal input. In the second simulation the system starts at the origin and we apply a nominal input $\hat{\mathbf{u}}$ which tracks an unsafe reference $\mathbf{y}$ trajectory: $\mathbf{y}(\mathbf{t}) = 1.2 \cdot \sin(0.05 \cdot 2\pi\mathbf{t})$. In the first test (Fig. 6.5.a) the static output feedback is always on, to demonstrate the slower decay of $\hat{\mathbf{B}}_\mathbf{c}(\mathbf{k_h})$. In the second (Fig. 6.5.b), the static output feedback is turned on when $\max(\hat{\mathbf{B}}_\mathbf{c}(\mathbf{k_h})) \geqslant \bar{\mathbf{B}} = -0.01$ and is

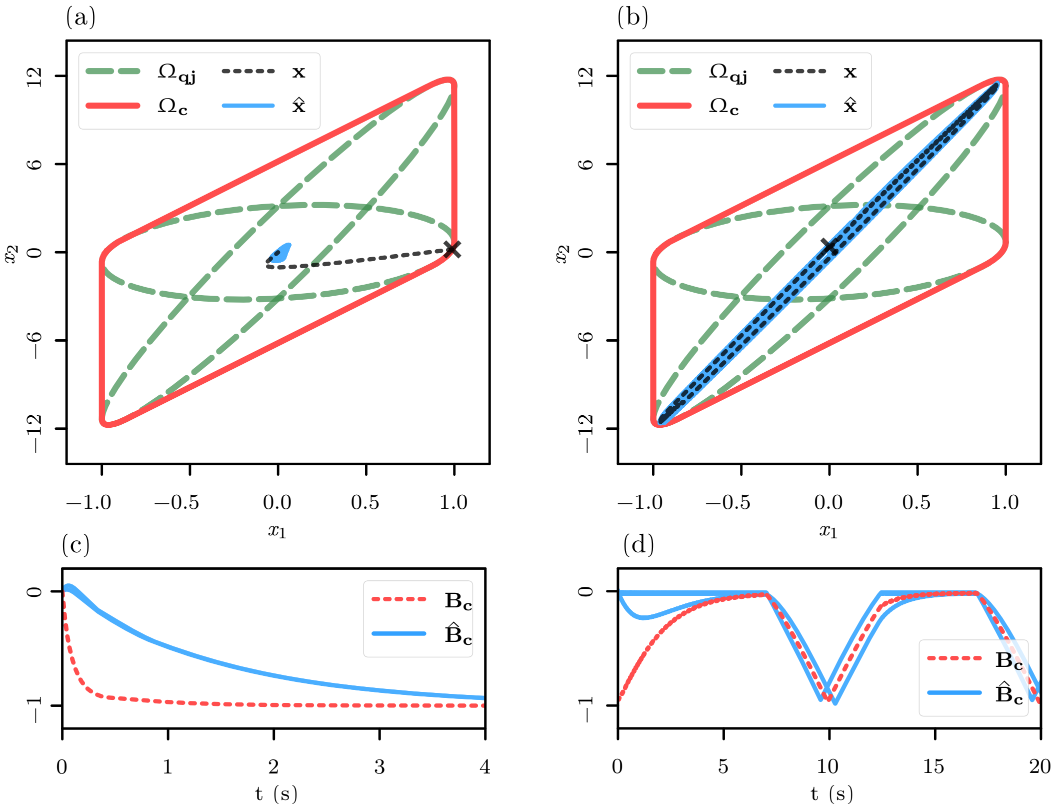

Figure 6.5: In the first simulation, the system state is initialized near the boundary of $\Omega_{\mathbf{c}}$ (phase plot in (a)). The maximum $\hat{\mathbf{B}}_{\mathbf{c}}(\mathbf{k_h})$ converges slower than $\mathbf{B_c}$ (in (c)). In the second simulation, an unsafe sinusoidal input $\hat{\mathbf{u}}$ is forced to be safely inside $\Omega_{\mathbf{c}}$ by a hybrid safety controller (phase plot in (b)). This safety controller activates only when $\max(\hat{\mathbf{B}}_{\mathbf{c}}(\mathbf{k_h})) \approxeq 0$ (see (d)).

turned off when all values of $\max(\hat{\mathbf{B}}_{\mathbf{c}}(\mathbf{k_h})) \leqslant \underline{\mathbf{B}} = -0.02$. This switching logic forces the system to stop near the boundary of $\Omega_{\mathbf{c}}$—deviating from the unsafe trajectory to produce a safe output. In both tests, the largest element of $\hat{\mathbf{B}}_{\mathbf{c}}(\mathbf{k_h})$ converges to zero slower than the value of $\mathbf{B_c}$ such that $\max(\hat{\mathbf{B}}_{\mathbf{c}}(\mathbf{k_h})) \geqslant \mathbf{B_c}$, as shown in Fig. 6.5.c and Fig. 6.5.d respectively.

Chapter 7

Sampling-Based Safety Control

Unlike full robot autonomy, shared autonomy allows a robot to leverage the perceptual and decision making capabilities of operators while helping them to work more efficiently and accurately [Colgate, Bicchi, Peshkin, and Colgate, 2008]. Across different fields, such as brain-computer interfaces [Carlson and Millán, 2013], autonomous driving [Fridman, 2018], and teleoperation [Javdani, Admoni, Pellegrinelli, Srinivasa, and Bagnell, 2018], shared autonomy helps us to improve our productivity without completely removing the human from the task at hand. However, safety becomes critical with shared autonomy, especially when operators and robots interact through physical contact. On the one hand, the human's objective is not directly measurable but can be inferred based on the robot's sensing of human inputs such as contact forces. The robot needs this inference of the human's objective to figure out how to assist the human and prevent them from potential accidents. On the other

---

The results presented in this chapter have also appeared in part of [He, Lee, Topcu, and Sentis, 2020b] and [He, Ghasemi, Topcu, and Sentis, 2021]. As the primary contributor, Binghan He developed the control theory, did the mathematical proofs, programmed the control algorithms, and conducted simulations for the proof of concept. Jaemin Lee provided theory supports on multi-body robot dynamics in the work of [He, Lee, Topcu, and Sentis, 2020b]. Mahsa Ghasemi provided theory supports on human intention inference in the work of [He, Ghasemi, Topcu, and Sentis, 2021]. These works were co-advised by Luis Sentis and Ufuk Topcu.

hand, human inputs can alter the robot's current path resulting in additional safety concerns. Therefore in a shared autonomy task, the robot faces a conflict between inferring the human's objectives and maintaining safety under the interaction with human inputs.

For a nonlinear dynamical system such as a robot, safety is usually verified through barrier functions [Prajna and Jadbabaie, 2004]. Just like Lyapunov functions for stability verification, barrier functions provide sufficient conditions for safety verification. But barrier functions relax the global convergence requirement of Lyapunov functions and only need to be decreasing at the safety bounds. Various methods create barrier functions with controllers to enforce safety constraint satisfaction. For state-space constraints, controllers can be synthesized simultaneously with barrier functions using back-stepping [Tee, Ge, and Tay, 2009] or quadratic programming methods [Ames, Xu, Grizzle, and Tabuada, 2016; Nguyen and Sreenath, 2016b]. Input constraints can also be enforced using semi-definite programming methods [Pylorof and Bakolas, 2016; Thomas, He, and Sentis, 2018].

While the above methods aim to resolve the safety problem for a robot alone, it is a more challenging problem to guarantee safety for a robot that has physical contact with a person. This is because humans represent an uncertain dynamical sub-system when physically interacting with robots. The internal states of the human dynamics are usually immeasurable. In Chapter 2-4, we use robust control strategies [He, Thomas, Paine, and Sentis, 2019; He, Huang, Thomas, and Sentis, 2019] to address the uncertain human dynamics and achieve complementary stability for human-robot coupled system. However, the control problems we study in those chapters only consider the robot as a strict follower of the human's trajectory and hence, relies on the human to obey safety constraints. In human-robot shared autonomy, the robot needs to enforce safety constraints in relation to the human's objective such that it can prevent them from potential accidents.

In this chapter, we consider a robot operating around multiple different polytopic regions defined in the workspace of its end-effector and a human operator that applies a norm-bound interaction force to the robot's end-effector intermittently. During real-time human-robot shared autonomy operation, we aim to infer the operator's target region from a time series of intermittent human force measurements and create a sequence of barrier pairs such that the robot's end-effector can safely move to the target region without passing through all other regions.

In order to address the safety problem during shared autonomy operation, we develop a barrier pair rapidly-exploring random tree method to generate sequences of barrier pairs given different human objectives. Each barrier pair comprises a quadratic barrier function and a state feedback controller. We synthesize the state feedback controllers in these barrier pairs using a robust control strategy so that the robot can satisfy the safety constraints for different human objectives and reject the human input interventions. Based on the human intention inference formulated from the human input measurements, the robot can execute these barrier pair sequences accordingly and help the human to safely accomplish the objective. We demonstrate this control method on a simulation of a two-linkage manipulator robot, where a human operator uses a keyboard to control a simulated human force exerted on the end-effector of the manipulator robot.

7.1 Multi-Body Robot Dynamics

In this section, we recall the basics of multi-body robot dynamics. For convenience, $\mathbf{x}_{\mathsf{a}_\mathrm{i}}$ is defined as the geometric center for the region of a_i and $\bar{\mathsf{a}}_\mathrm{i} \triangleq \mathbf{R}^\mathrm{n} \setminus \mathsf{a}_\mathrm{i}$ is defined as a workspace region excluding the set for a_i.

7.1.1 Lagrangian Equation

The Lagrangian dynamics of an n-DOF robot can be expressed as

$$\mathbf{M}(\mathbf{q}) \cdot \ddot{\mathbf{q}} + \mathbf{C}(\mathbf{q},\, \dot{\mathbf{q}}) \cdot \dot{\mathbf{q}} = \mathbf{u} + \mathbf{J}^\top(\mathbf{q}) \cdot \mathbf{w} \tag{7.1}$$

where $\mathbf{M}(\mathbf{q})$ is the matrix of inertia, $\mathbf{C}(\mathbf{q},\, \dot{\mathbf{q}})$ is the coefficient matrix of Coriolis and centrifugal effects, $\mathbf{J}(\mathbf{q})$ is the matrix of Jacobian, $\mathbf{q} \triangleq [q_1,\, \cdots,\, q_\mathrm{n}]^\top$ is the vector of joint positions with $\dot{\mathbf{q}}$ and $\ddot{\mathbf{q}}$ defined as its first and second order time derivatives, $\mathbf{u} \triangleq [u_1,\, \cdots,\, u_\mathrm{n}]^\top$ is the vector of joint torques and $\mathbf{w} \triangleq [w_1,\, \cdots,\, w_\mathrm{n}]^\top$ is the vector of external forces exerted by the human. An n-dimensional workspace position vector $\mathbf{x} \triangleq [x_1,\, \cdots,\, x_\mathrm{n}]^\top$ can be calculated from the joint position vector using

$$\mathbf{x} = \mathbf{F}(\mathbf{q}) \tag{7.2}$$

where $\mathbf{F}(\cdot)$ represents the forward kinematics. By linearizing (7.1) and (7.2) around an equilibrium point $[\mathbf{q}_\mathbf{e}^\top,\, \vec{0}^\top]^\top$, we obtain the state-space form

$$\begin{bmatrix}\dot{\tilde{\mathbf{q}}}\\ \ddot{\tilde{\mathbf{q}}}\end{bmatrix} = \begin{bmatrix}\mathbf{0} & \mathbf{I}\\ \mathbf{0} & \mathbf{M}^{-1}(\mathbf{q}_\mathbf{e})\mathbf{C}(\mathbf{q}_\mathbf{e},\, \vec{0})\end{bmatrix}\begin{bmatrix}\tilde{\mathbf{q}}\\ \dot{\tilde{\mathbf{q}}}\end{bmatrix} + \begin{bmatrix}\mathbf{0}\\ \mathbf{M}^{-1}(\mathbf{q}_\mathbf{e})\end{bmatrix}\mathbf{u} + \begin{bmatrix}\mathbf{0}\\ \mathbf{M}^{-1}(\mathbf{q}_\mathbf{e})\mathbf{J}^\top(\mathbf{q}_\mathbf{e})\end{bmatrix}\mathbf{w} \tag{7.3}$$

$$\tilde{\mathbf{x}} = \begin{bmatrix}\mathbf{J}(\mathbf{q}_\mathbf{e}) & \mathbf{0}\end{bmatrix}\begin{bmatrix}\tilde{\mathbf{q}}\\ \dot{\tilde{\mathbf{q}}}\end{bmatrix} \tag{7.4}$$

where $\tilde{\mathbf{q}} \triangleq \mathbf{q} - \mathbf{q}_\mathbf{e}$ and $\tilde{\mathbf{x}} \triangleq \mathbf{x} - \mathbf{x}_\mathbf{e}$ with $\mathbf{x}_\mathbf{e} = \mathbf{F}(\mathbf{q}_\mathbf{e})$. The partial derivative of $\mathbf{F}(\mathbf{q})$ with respect to $\mathbf{q}$ is the Jacobian matrix $\mathbf{J}(\mathbf{q})$.

7.1.2 Norm-Bound LDI Model

Our proposed method relies on formulating an LMI problem to synthesize the barrier pairs subject to local convex constraints. However, the linearized state space equations (7.3) and (7.4) become inaccurate if the state $[\mathbf{q}^\top,\, \dot{\mathbf{q}}^\top]^\top$ deviates from the equilibrium. Before employing barrier pair synthesis, we need to ensure that the linear model is valid for all states in the constrained state space $\mathcal{Z}$ of the barrier pair.

If we express the norm-bound uncertainties of the linearized robot dynamical model in (7.3) and (7.4) as

$$\mathbf{M}^{-1}(\mathbf{q}) \cdot \mathbf{C}(\mathbf{q},\, \dot{\mathbf{q}}) \in \{\mathbf{A}_1 + \mathbf{A}_2\Delta\mathbf{A}_3 : \|\Delta\| \leqslant 1\} \tag{7.5}$$

$$\mathbf{M}^{-1}(\mathbf{q}) \cdot \mathbf{J}^\top(\mathbf{q}) \in \{\,\mathbf{B}_1^\mathbf{w} + \mathbf{B}_2^\mathbf{w}\Delta\mathbf{B}_3^\mathbf{w} : \|\Delta\| \leqslant 1\} \tag{7.6}$$

$$\mathbf{M}^{-1}(\mathbf{q}) \in \{\mathbf{B}_1^\mathbf{u} + \mathbf{B}_2^\mathbf{u}\Delta\mathbf{B}_3^\mathbf{u} : \|\Delta\| \leqslant 1\} \tag{7.7}$$

$$\mathbf{J}(\mathbf{q}) \in \{\ \mathbf{J}_1 + \mathbf{J}_2\Delta\mathbf{J}_3 : \|\Delta\| \leqslant 1\} \tag{7.8}$$

for all state $[\mathbf{q}^\top,\, \dot{\mathbf{q}}^\top]^\top$ in the constrained state space $\mathcal{Z}$ around the equilibrium, a norm-bound linear differential inclusion (LDI)

$$\begin{bmatrix} \dot{\tilde{\mathrm{q}}} \\ \ddot{\tilde{\mathrm{q}}} \end{bmatrix} = \begin{bmatrix} \mathbf{0} & \mathbf{I} \\ \mathbf{0} & \mathbf{A}_1 + \mathbf{A}_2 \Delta \mathbf{A}_3 \end{bmatrix} \begin{bmatrix} \tilde{\mathrm{q}} \\ \dot{\tilde{\mathrm{q}}} \end{bmatrix} + \begin{bmatrix} \mathbf{0} \\ \mathbf{B}_1^{\mathbf{u}} + \mathbf{B}_2^{\mathbf{u}} \Delta \mathbf{B}_3^{\mathbf{u}} \end{bmatrix} \mathbf{u} + \begin{bmatrix} \mathbf{0} \\ \mathbf{B}_1^{\mathbf{w}} + \mathbf{B}_2^{\mathbf{w}} \Delta \mathbf{B}_3^{\mathbf{w}} \end{bmatrix} \mathbf{w} \tag{7.9}$$

$$\tilde{\mathbf{x}} = \begin{bmatrix} \mathbf{J}_1 + \mathbf{J}_2 \Delta \mathbf{J}_3 & \mathbf{0} \end{bmatrix} \begin{bmatrix} \tilde{\mathrm{q}} \\ \dot{\tilde{\mathrm{q}}} \end{bmatrix}. \tag{7.10}$$

We can formulate a norm-bound LDI by calculating $\mathbf{M}^{-1}(\mathbf{q}) \cdot \mathbf{C}(\mathbf{q}, \dot{\mathbf{q}})$, $\mathbf{M}^{-1}(\mathbf{q}) \cdot \mathbf{J}^\top(\mathbf{q}, \dot{\mathbf{q}})$, $\mathbf{M}^{-1}(\mathbf{q})$ and $\mathbf{J}(\mathbf{q})$ from a number of sample states in $\mathcal{Z}$ and using quadric inclusion programs [Thomas and Sentis, 2019] to fit an inclusion model.

Since we assume the polytopic regions are polytopic, each edge of an polytopic region can be transformed into an inequality constraint. To exclude the undesirable regions of a transition, only one of these inequality constraints need to be considered for each undesirable region. Otherwise, the state space can be over-constrained. If the workspace position x_e of an equilibrium satisfies multiple inequality constraints associated with an undesirable region, we can select the edge which has the maximal distance to $\mathbf{x}_\mathbf{e}$ to avoid being over-constrained. Based on the selected inequality constraints $|\mathbf{a}_\mathbf{i}\tilde{\mathbf{x}}| < \bar{a}_\mathrm{i}$ associated with all undesirable regions $\mathsf{a}_1, \mathsf{a}_2, \cdots, \mathsf{a}_{\mathsf{n}_\mathsf{o}}$, a local convex state space region $\mathcal{Z}_{\mathbf{safe}}$ can be defined as

$$\begin{aligned} \mathcal{Z}_{\mathbf{safe}} \triangleq \{[\tilde{\mathbf{q}}^\top, \dot{\tilde{\mathbf{q}}}^\top]^\top : |\mathbf{a}_\mathrm{i}(\mathbf{J}_1 + \mathbf{J}_2 \Delta \mathbf{J}_3)\ \tilde{\mathbf{q}}| < \bar{a}_\mathrm{i}, \\ \|\Delta\| \leqslant 1,\ \mathrm{i} = 1, \cdots, \mathrm{n}_\mathrm{o}\}, \end{aligned} \tag{7.11}$$

where a_i for $\mathrm{i} = 1, \cdots, \mathrm{n}_\mathrm{o}$ are row vectors with n_o as the number of undesirable polytopic regions.

However, $\mathcal{Z}_{\mathbf{safe}}$ cannot be directly used as the constrained state space region $\mathcal{Z}$ for barrier pair synthesis because it has no joint velocity state constraints. In some cases, a selected edge of an undesirable region has a very long distance to $\mathrm{x_e}$ and result in a very large uncertainty of the norm-bound LDI model. Therefore, we need some additional state space constraints for defining $\mathcal{Z}$. Let us first define another constrained state space $\mathcal{Z}_0$ as

$$\begin{aligned}\mathcal{Z}_0 \triangleq \{[\tilde{\mathbf{q}}^\top, \dot{\tilde{\mathbf{q}}}^\top]^\top : |\mathbf{b}_\mathrm{i}(\mathbf{J}_1 + \mathbf{J}_2\Delta\mathbf{J}_3)\ \tilde{\mathbf{q}}| < \bar{x}_\mathrm{i},\ |\mathbf{b}_\mathrm{i}\dot{\tilde{\mathbf{q}}}| < \bar{\dot{q}}_\mathrm{i}, \\ \|\Delta\| \leqslant 1,\ \mathrm{i} = 1, \cdots, \mathrm{n}\},\end{aligned} \tag{7.12}$$

where $\mathrm{b_i}$ for $\mathrm{i} = 1, \cdots, \mathrm{n}$ are the standard basis (row) vectors of n-dimensional Euclidean space. Then, the constrained state space region for the valid norm-bound LDI model is defined as $\mathcal{Z} \triangleq \mathcal{Z}_{\mathbf{safe}} \cap \mathcal{Z}_0$.

Similar to (7.11) and (7.12), a constrained input space region $\mathcal{U}$ and a constrained external input space region $\mathcal{W}$ can be formulated as

$$\mathcal{U} \triangleq \{\mathbf{u} : |\mathbf{b}_\mathrm{i}\mathbf{u}| < \bar{u}_\mathrm{i},\ \mathrm{i} = 1, \cdots, \mathrm{n}\}. \tag{7.13}$$

$$\mathcal{W} \triangleq \{\mathbf{w} : \|\mathbf{w}\| < \bar{w}\}. \tag{7.14}$$

7.2 Barrier Pair Rapidly-Exploring Random Trees

The robot controller needs to guarantee that the transitions for all continuous states in one polytopic region to another polytopic region following the high-level discrete controller. It can be considered as a trajectory planning problem with uncertain initial state conditions corresponding to the regions defined by the atomic propositions. The region of attraction of the generated robust trajectory planner is also known as a ‘funnel’ [Burridge, Rizzi, and Koditschek, 1999]. A ‘funnel’ can be synthesized over a shooting trajectory via multiple local stabilizing controllers [Tedrake, Manchester, Tobenkin, and

Roberts, 2010] or by solving quadratic programs based on control barrier functions [Ames, Xu, Grizzle, and Tabuada, 2016]. These strategies have been proposed to solve closed system problems [Nilsson and Ames, 2018] and reactive synthesis problems [DeCastro and Kress-Gazit, 2015] with temporal logic constraints. The real challenge is that the trajectory planning problem in its general form is a non-convex problem, for instance, when there are polytopic regions located between the initial and goal polytopic regions. In [Reist, Preiswerk, and Tedrake, 2016], a simulation-based method to solve the non-convex problem is proposed by simulating a number of 'funnels' and checking constraint satisfaction for each funnel. However, simulation-based methods suffer from high computational costs.

For robotic systems, this type of non-convex motion planning problem is usually addressed using sampling-based methods such as the rapidly-exploring random tree (RRT) method [Lavalle and Kuffner Jr., 2000]. In an RRT algorithm, a random position $\mathbf{x}_{\mathsf{rand}}$ is sampled from the reachable space in every iteration. An RRT graph expands toward the sampled position from its closest vertex $\mathbf{x}_{\mathsf{near}}$ by a predefined distance δ. The trajectory that connects an initial position $\mathbf{x}_0$ and a desired position $\mathbf{x}_{\mathsf{f}}$ can be extracted from the graph in the end. By incorporating optimal control theory in the sampled trajectory of RRT, the convergence rate of the motion planning problem is greatly improved [Karaman and Frazzoli, 2011]. To improve the exploration of the RRT graph, a sampling strategy based on the estimated feasibility set of a robot is proposed in [Shkolnik, Walter, and Tedrake, 2009]. However, the transitions between

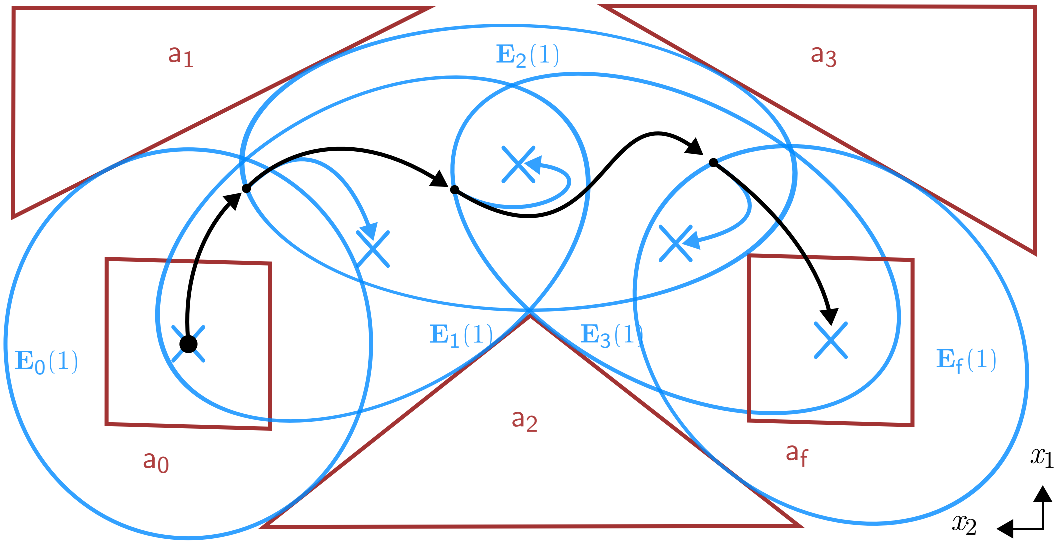

Figure 7.1: Atomic proposition a_0, a_1, a_2, a_3, a_f represent the polytopic regions (red) in workspace. The proposed BP-RRT consists of a sequence of barrier pairs with their sub-level sets $\mathbf{E}(1)$ (blue) interconnected to guarantee the transition between a_0 and a_f. An example trajectory (black) switches to a different barrier pair controller as it enters the sub-level set of another barrier pair.

the vertices of the RRT trajectory are not guaranteed to avoid collisions with the undesirable state-space regions without having barrier certificates [Prajna, 2006] along the RRT trajectory.

In order to solve the non-convex robot motion planning problem for the shared-autonomy operation, we propose a new approach consisting of a rapidly-exploring random tree of barrier pairs [Thomas, He, and Sentis, 2018]. Our method employs RRT to deal with non-convex constraints while employing barrier pairs equipped with sub-optimal stabilizing controllers to fulfill local convex constraints. Let us recall the definition of a barrier pair.

Definition 7.1 [Thomas, He, and Sentis, 2018]: A *barrier pair* for a robot with dynamics in form of (7.1) is a pair consisting of a barrier function and a controller $(\mathbf{B},\ \mathbf{k})$ with the following properties

(a) $-1 < \mathbf{B}(\tilde{\mathbf{q}},\ \dot{\tilde{\mathbf{q}}}) \leqslant 0, \mathbf{u} = \mathbf{k}(\tilde{\mathbf{q}},\ \dot{\tilde{\mathbf{q}}}) \implies \dot{\mathbf{B}}(\tilde{\mathbf{q}},\ \dot{\tilde{\mathbf{q}}}) < 0,$

(b) $\mathbf{B}(\tilde{\mathbf{q}},\ \dot{\tilde{\mathbf{q}}}) \leqslant 0 \implies [\tilde{\mathbf{q}}^\top,\ \dot{\tilde{\mathbf{q}}}^\top]^\top \in \mathcal{Z},\ \mathbf{k}(\tilde{\mathbf{q}},\ \dot{\tilde{\mathbf{q}}}) \in \mathcal{U},$

where $[\tilde{\mathbf{q}}^\top,\ \dot{\tilde{\mathbf{q}}}^\top]^\top \in \mathcal{Z}$ and $\mathbf{u} \in \mathcal{U}$ are the state and input constraints.

Similar to Chapter 5, we define a barrier pair as

$$\mathbf{B} = \begin{bmatrix} \tilde{\mathbf{q}} \\ \dot{\tilde{\mathbf{q}}} \end{bmatrix}^\top \mathbf{Q}^{-1} \begin{bmatrix} \tilde{\mathbf{q}} \\ \dot{\tilde{\mathbf{q}}} \end{bmatrix} - 1, \quad \mathbf{k} = \mathbf{K} \begin{bmatrix} \tilde{\mathbf{q}} \\ \dot{\tilde{\mathbf{q}}} \end{bmatrix} \tag{7.15}$$

where $\mathbf{B}$ is a quadratic barrier function with a positive definite matrix $\mathbf{Q}$ and $\mathbf{k}$ is a full state feedback controller, the barrier pair synthesis becomes a linear matrix inequality (LMI) optimization problem [Thomas, He, and Sentis, 2018].

For convenience, we use $(\mathbf{Q}, \mathbf{K})$ to represent a barrier pair $(\mathbf{B}, \mathbf{k})$ in the form of (7.15) and define $\mathbf{E}(\varepsilon) \triangleq \{[\tilde{\mathbf{q}}^\top,\ \dot{\tilde{\mathbf{q}}}^\top]^\top \mid [\tilde{\mathbf{q}}^\top,\ \dot{\tilde{\mathbf{q}}}^\top]\mathbf{Q}^{-1}[\tilde{\mathbf{q}}^\top,\ \dot{\tilde{\mathbf{q}}}^\top]^\top \leqslant \varepsilon^2\}$ as the sub-level set of $\mathbf{B}$ corresponding to a value $\varepsilon^2 - 1$. Based on Definition 1, the zero sub-level set $\mathbf{E}(1)$ of the barrier function $\mathbf{B}$ needs to satisfy all constraints defined by $\mathcal{Z}$ and $\mathcal{U}$.

The proposed approach is illustrated in Fig. 7.1. It starts with finding an equilibrium point inside the goal polytopic region $\mathsf{a_f}$ and synthesizing a barrier pair in the form of (7.15), subject to local convex state constraints (e.g. surrounding undesirable polytopic regions) for this equilibrium. We then sample a new equilibrium point inside the sub-level set $\mathbf{E}_\mathbf{f}(1)$ for the first barrier pair and synthesize a new barrier pair subject again to local convex state constraints for the new equilibrium. Inside the sub-level sets of the existing barrier pairs, another equilibrium is sampled, followed by a barrier pair synthesis. This barrier pair sampling process is iterated until the sub-level set of a barrier pair contains the equilibrium of a barrier pair whose sub-level set $\mathbf{E}_0(1)$ contains the entire initial polytopic region a_0. In the end, we obtain a sequence of interconnected barrier pairs between a_0 and a_f without passing through undesirable polytopic regions.

7.2.1 Barrier Pair Synthesis Sub-Problems

The barrier pair synthesis problem includes a series of LMI constraints and generates a quadratic barrier function $\mathbf{B}$ with a full state controller $\mathbf{k}$ in the form of (7.15). First, the sequence of barrier pairs needs to contain the two desired polytopic regions a_0 and a_f defining the automaton transitions and exclude all undesirable polytopic regions $\mathsf{a}_1, \cdots, \mathsf{a}_{\mathsf{n}_\mathsf{o}}$.

Although a desired polytopic region a_d is assumed to be polytopic in the Cartesian workspace, its joint space projection is not guaranteed to be polytopic. In order to ensure that the ellipsoidal sub-level set $\mathbf{E}(1)$ of a barrier pair contains a_d, we sample a number of points from all edges of a_d and let $\mathbf{E}(1)$ contain the joint space projections of these Cartesian space samples using the following set of LMIs

$$\begin{bmatrix} 1 & \star \\ \mathbf{R}(\mathbf{x}_\mathrm{i}) - \mathbf{q}_\mathbf{e} & \mathbf{S}_1\mathbf{Q}\mathbf{S}_1^\top \end{bmatrix} \succeq 0, \quad \forall\, \mathrm{i} = 1, \ldots, \mathrm{n_p} \tag{7.16}$$

where $\mathrm{n_p}$ is the number of sampled workspace points at the edge of a_d with $\mathsf{a}_\mathsf{d} =$

$\mathsf{Co}\{\mathbf{x}_1, \cdots, \mathbf{x_p}\}$, $\mathbf{R}(\cdot)$ is an inverse kinematics operator and $\mathbf{S}_1 \triangleq [\mathbf{I_{n\times n}}, \mathbf{0_{n\times n}}]$.

Using the S-procedure [Ma and Chen, 2006], the inequality constraints $|\mathbf{a_i}\tilde{\mathbf{x}}| < \bar{a}_\mathrm{i}$ of $\mathcal{Z}_\mathbf{safe}$ in (7.11) can be transformed into a set of LMIs

$$\begin{bmatrix} \bar{a}_\mathrm{i}^2\mathbf{Q} & \star & \star & \star \\ \mathbf{0} & \gamma_\mathrm{i}\mathbf{I} & \star & \star \\ \mathbf{a}_\mathrm{i}\mathbf{J}_1\mathbf{S}_1\mathbf{Q} & \gamma_\mathrm{i}\mathbf{a}_\mathrm{i}\mathbf{J}_2 & 1 & \star \\ \mathbf{J}_3\mathbf{S}_1\mathbf{Q} & \mathbf{0} & \vec{0} & \gamma_\mathrm{i}\mathbf{I} \end{bmatrix} \succeq 0,\ \forall\,\mathrm{i} = 1, \ldots, \mathrm{n_o} \tag{7.17}$$

where γ_i for $\mathrm{i} = 1, \ldots, \mathrm{n_o}$ are positive real scalar variables.

Similar to (7.17), the workspace position constraints $|\mathbf{b_i}\tilde{\mathbf{x}}| < \bar{x}_\mathrm{i}$ of $\mathcal{Z}_0$ defined in (7.12) can be transformed into a set of LMIs

$$\begin{bmatrix} \bar{x}_\mathrm{i}^2\mathbf{Q} & \star & \star & \star \\ \mathbf{0} & \mu_\mathrm{i}\mathbf{I} & \star & \star \\ \mathbf{b}_\mathrm{i}\mathbf{J}_1\mathbf{S}_1\mathbf{Q} & \mu_\mathrm{i}\mathbf{b}_\mathrm{i}\mathbf{J}_2 & 1 & \star \\ \mathbf{J}_3\mathbf{S}_1\mathbf{Q} & \mathbf{0} & \vec{0} & \mu_\mathrm{i}\mathbf{I} \end{bmatrix} \succeq 0,\ \forall\,\mathrm{i} = 1, \ldots, \mathrm{n} \tag{7.18}$$

where μ_i for $\mathrm{i} = 1, \ldots, \mathrm{n}$ are positive real scalar variables. The joint velocity constraint LMIs of $\mathcal{Z}_0$ are expressed as

$$\begin{bmatrix} \mathbf{Q} & \star \\ \mathbf{b}_\mathrm{i}\mathbf{S}_2\mathbf{Q} & \bar{\dot{q}}_\mathrm{i}^2 \end{bmatrix} \succeq 0,\ \forall\,\mathrm{i} = 1, \ldots, \mathrm{n} \tag{7.19}$$

where $\mathbf{S}_2 \triangleq [\mathbf{0_{n\times n}}, \mathbf{I_{n\times n}}]$.

Although the full state feedback controller $\mathbf{k}$ in (7.15) turns the input constraints into state constraints, $\mathbf{K}$ is also a variable to be solved. In [Boyd, El Ghaoui, Feron, and Balakrishnan, 1994], a new variable $\mathbf{Y} \triangleq \mathbf{KQ}$ is introduced to express the input constraints into LMIs. After the barrier pair synthesis problem is solved, $\mathbf{K}$ can be extracted by multiplying $\mathbf{Y}$ by $\mathbf{Q}^{-1}$ on the right hand side. The input constraint LMIs can be expressed as

$$\begin{bmatrix} \mathbf{Q} & \star \\ \mathbf{b}_\mathrm{i}\mathbf{Y} & \bar{u}_\mathrm{i}^2 \end{bmatrix} \succeq 0,\ \forall\,\mathrm{i} = 1, \ldots, \mathrm{n} \tag{7.20}$$

for enforcing the input constraints $|\mathbf{b_i u}| \leqslant \bar{u}_i$ of $\mathcal{U}$ defined in (7.13).

Let us first consider a simpler case in which there is no human force input $\mathbf{w}$ exerted to the robot. To guarantee the invariance of the barrier function, we include a Lyapunov stability LMI in [Boyd, El Ghaoui, Feron, and Balakrishnan, 1994] for the norm-bound LDI model

$$\begin{bmatrix} \mathbf{X}_0 & \star & \star \\ \bar{\mathbf{A}}_3\mathbf{Q} & -\mu_{\mathbf{x}}\mathbf{I} & \star \\ \mathbf{B}_3^{\mathbf{u}}\mathbf{Y} & \mathbf{0} & -\mu_{\mathbf{u}}\mathbf{I} \end{bmatrix} \preceq 0, \tag{7.21}$$

where

$$\begin{aligned} \mathbf{X}_0 = {} & \bar{\mathbf{A}}_1\mathbf{Q} + \mathbf{Q}\bar{\mathbf{A}}_1^\top + \bar{\mathbf{B}}_1^{\mathbf{u}}\mathbf{Y} + \mathbf{Y}^\top\bar{\mathbf{B}}_1^{\mathbf{u}\top} + \mu_{\mathbf{x}}\bar{\mathbf{A}}_2\bar{\mathbf{A}}_2^\top + \mu_{\mathbf{u}}\bar{\mathbf{B}}_2^{\mathbf{u}}\bar{\mathbf{B}}_2^{\mathbf{u}\top} \\ & + \alpha\mathbf{Q} \end{aligned} \tag{7.22}$$

$$\bar{\mathbf{A}}_1 = \mathbf{S}_1^\top\mathbf{S}_2 + \mathbf{S}_2^\top\mathbf{A}_1\mathbf{S}_2,\ \bar{\mathbf{A}}_2 = \mathbf{S}_2^\top\mathbf{A}_2,\ \bar{\mathbf{A}}_3 = \mathbf{A}_3\mathbf{S}_2, \tag{7.23}$$

$$\bar{\mathbf{B}}_1^{\mathbf{u}} = \mathbf{S}_2^\top\mathbf{B}_1^{\mathbf{u}},\ \bar{\mathbf{B}}_2^{\mathbf{u}} = \mathbf{S}_2^\top\mathbf{B}_2^{\mathbf{u}}, \tag{7.24}$$

and $\mu_{\mathbf{x}}$ and μ_{u} are positive real scalar variables.

Then, the volume of the ellipsoid $\mathbf{E}(1)$ is maximized through the cost function of the log of the determinant of $\mathbf{Q}$ [Boyd, El Ghaoui, Feron, and Balakrishnan, 1994]. A barrier pair synthesis sub-problem $(\mathbf{B}, \mathbf{k}) = \mathsf{BP}(\mathbf{x_e}, \mathsf{a_d}, \bar{\mathsf{a}}_1, \cdots, \bar{\mathsf{a}}_{n_o}, \mathcal{Z}_0, \mathcal{U})$ for $\mathcal{W} = \varnothing$ can be expressed as

$$\begin{aligned} & \underset{\mathbf{Q},\,\mathbf{Y}}{\text{maximize}} && \log(\det(\mathbf{Q})) \\ & \text{subject to} && \mathbf{Q} \succ 0, \\ & && (7.16),\ (7.17),\ (7.18),\ (7.19),\ (7.20),\ (7.21) \end{aligned} \tag{7.25}$$

for finding a sub-level set $\mathbf{E}(1)$ that contains the desired region $\mathsf{a_d}$ and excludes the undesirable regions $\mathsf{a}_1, \mathsf{a}_2, \cdots, \mathsf{a}_{n_o}$.

By the following proposition, the robot's Lyapunov stability can also be enforced under the impact of norm-bound human input $\mathbf{w}$.

Proposition 7.1 For a robot starting from a state in the zero sub-level set $\mathbf{E}(1)$ of the barrier pair $(\mathbf{B}, \mathbf{K})$, the robot state converges to a residue set $\mathbf{E}(\varepsilon_0)$ with an exponential convergence rate no less than $\frac{\alpha}{2}$ if

$$\begin{bmatrix} \mathbf{X}_{11} & \star \\ \mathbf{X}_{21} & \mathbf{X}_{22} \end{bmatrix} \preceq 0, \tag{7.26}$$

where

$$\begin{aligned} \mathbf{X}_{11} = & \begin{bmatrix} \bar{\mathbf{A}}_1\mathbf{Q} + \mathbf{Q}\bar{\mathbf{A}}_1^\top + \bar{\mathbf{B}}_1^{\mathbf{u}}\mathbf{Y} + \mathbf{Y}^\top\bar{\mathbf{B}}_1^{\mathbf{u}\top} + \alpha\mathbf{Q} & \bar{\mathbf{B}}_1^{\mathbf{w}} \\ \bar{\mathbf{B}}_1^{\mathbf{w}\top} & -\alpha\frac{\varepsilon_0^2}{\bar{w}^2}\mathbf{I} \end{bmatrix} \\ & + \begin{bmatrix} \bar{\mathbf{A}}_2 & \bar{\mathbf{B}}_2^{\mathbf{u}} & \bar{\mathbf{B}}_2^{\mathbf{w}} \\ \mathbf{0} & \mathbf{0} & \mathbf{0} \end{bmatrix} \begin{bmatrix} \mu_{\mathbf{x}}\mathbf{I} & \mathbf{0} & \mathbf{0} \\ \mathbf{0} & \mu_{\mathbf{u}}\mathbf{I} & \mathbf{0} \\ \mathbf{0} & \mathbf{0} & \mu_{\mathbf{w}}\mathbf{I} \end{bmatrix} \begin{bmatrix} \bar{\mathbf{A}}_2 & \bar{\mathbf{B}}_2^{\mathbf{u}} & \bar{\mathbf{B}}_2^{\mathbf{w}} \\ \mathbf{0} & \mathbf{0} & \mathbf{0} \end{bmatrix}^\top \end{aligned} \tag{7.27}$$

$$\mathbf{X}_{21} = \begin{bmatrix} \bar{\mathbf{A}}_3\mathbf{Q} & \mathbf{0} \\ \mathbf{B}_3^{\mathbf{u}}\mathbf{Y} & \mathbf{0} \\ \mathbf{0} & \mathbf{B}_3^{\mathbf{w}} \end{bmatrix} \tag{7.28}$$

$$\mathbf{X}_{22} = \begin{bmatrix} -\mu_{\mathbf{x}}\mathbf{I} & \mathbf{0} & \mathbf{0} \\ \mathbf{0} & -\mu_{\mathbf{u}}\mathbf{I} & \mathbf{0} \\ \mathbf{0} & \mathbf{0} & -\mu_{\mathbf{w}}\mathbf{I} \end{bmatrix} \tag{7.29}$$

$$\bar{\mathbf{B}}_1^{\mathbf{w}} = \mathbf{S}_2^\top\mathbf{B}_1^{\mathbf{w}}, \ \bar{\mathbf{B}}_2^{\mathbf{w}} = \mathbf{S}_2^\top\mathbf{B}_2^{\mathbf{w}}, \tag{7.30}$$

and $\mu_{\mathbf{x}}$, $\mu_{\mathbf{u}}$ and $\mu_{\mathbf{w}}$ are positive real scalar variables.

Proof Let us define $\mathbf{z} \triangleq [\tilde{\mathbf{q}}^\top, \dot{\tilde{\mathbf{q}}}^\top]^\top$. Based on the matrices defined in (7.23), (7.24) and (7.30), (7.9) can be expressed as

$$\dot{\mathbf{z}} = \bar{\mathbf{A}}_1\mathbf{z} + \bar{\mathbf{B}}_1^{\mathbf{u}}\mathbf{u} + \bar{\mathbf{B}}_1^{\mathbf{w}}\mathbf{w} + \bar{\mathbf{A}}_2\mathbf{p}_{\mathbf{z}} + \bar{\mathbf{B}}_2^{\mathbf{u}}\mathbf{p}_{\mathbf{u}} + \bar{\mathbf{B}}_2^{\mathbf{w}}\mathbf{p}_{\mathbf{w}} \tag{7.31}$$

where

$$\mathbf{p_z} = \Delta \mathbf{q_z}, \quad \mathbf{q_z} = \bar{\mathbf{A}}_3 \mathbf{z}, \tag{7.32}$$

$$\mathbf{p_u} = \Delta \mathbf{q_u}, \quad \mathbf{q_u} = \mathbf{B}_3^{\mathbf{u}} \mathbf{u}, \tag{7.33}$$

$$\mathbf{p_w} = \Delta \mathbf{q_w}, \quad \mathbf{q_w} = \mathbf{B}_3^{\mathbf{w}} \mathbf{w}. \tag{7.34}$$

For barrier function $\mathbf{B} = \mathbf{z}^\top \mathbf{P} \mathbf{z} - 1$ with controller $\mathbf{u} = \mathbf{K}\mathbf{z}$, the time derivative of $\mathbf{B}$ is

$$\dot{\mathbf{B}} = \begin{bmatrix} \mathbf{z} \\ \mathbf{w} \\ \mathbf{p_z} \\ \mathbf{p_u} \\ \mathbf{p_w} \end{bmatrix}^\top \begin{bmatrix} (\bar{\mathbf{A}}_1 + \bar{\mathbf{B}}_1^{\mathbf{u}} \mathbf{K})^\top \mathbf{P} + \mathbf{P}(\bar{\mathbf{A}}_1 + \bar{\mathbf{B}}_1^{\mathbf{u}} \mathbf{K}) & \star & \star & \star & \star \\ \bar{\mathbf{B}}_1^{\mathbf{w}\top} \mathbf{P} & \mathbf{0} & \star & \star & \star \\ \bar{\mathbf{A}}_2^\top \mathbf{P} & \mathbf{0} & \mathbf{0} & \star & \star \\ \bar{\mathbf{B}}_2^{\mathbf{u}\top} \mathbf{P} & \mathbf{0} & \mathbf{0} & \mathbf{0} & \star \\ \bar{\mathbf{B}}_2^{\mathbf{w}\top} \mathbf{P} & \mathbf{0} & \mathbf{0} & \mathbf{0} & \mathbf{0} \end{bmatrix} \begin{bmatrix} \mathbf{z} \\ \mathbf{w} \\ \mathbf{p_z} \\ \mathbf{p_u} \\ \mathbf{p_w} \end{bmatrix}. \tag{7.35}$$

In addition, we have

$$\mathbf{w}^\top \mathbf{w} \leqslant \bar{w}^2, \tag{7.36}$$

$$\mathbf{z}^\top \mathbf{P} \mathbf{z} \leqslant \varepsilon_0^2, \tag{7.37}$$

for the norm-bound human input $\mathbf{w}$ and the residue set $\{\mathbf{z} \mid \mathbf{B} \leqslant \varepsilon_0^2 - 1\}$ of the barrier function.

Using the S-procedure, we can combine (7.32), (7.33), (7.34), (7.36), (7.37), and $\dot{\mathbf{B}} \leqslant 0$ into

$$\begin{bmatrix} \tilde{\mathbf{X}}_{11} & \star & \star \\ \tilde{\mathbf{X}}_{21} & \tilde{\mathbf{X}}_{22} & \star \\ \mathbf{0} & \mathbf{0} & -\alpha\varepsilon_0^2 + \alpha_{\mathbf{w}} \bar{w}^2 \end{bmatrix} \preceq 0. \tag{7.38}$$

where

$$\tilde{\mathbf{X}}_{11} = \begin{bmatrix} (\bar{\mathbf{A}}_1 + \bar{\mathbf{B}}_1^{\mathbf{u}}\mathbf{K})^\top \mathbf{P} + \mathbf{P}(\bar{\mathbf{A}}_1 + \bar{\mathbf{B}}_1^{\mathbf{u}}\mathbf{K}) + \alpha\mathbf{P} & \mathbf{P}\bar{\mathbf{B}}_1^{\mathbf{w}} \\ \bar{\mathbf{B}}_1^{\mathbf{w}\top}\mathbf{P} & -\alpha_{\mathbf{w}}\mathbf{I} \end{bmatrix}$$

$$+ \begin{bmatrix} \bar{\mathbf{A}}_3 & \mathbf{0} \\ \mathbf{B}_3^{\mathbf{u}}\mathbf{K} & \mathbf{0} \\ \mathbf{0} & \mathbf{B}_3^{\mathbf{w}} \end{bmatrix}^\top \begin{bmatrix} \lambda_{\mathbf{x}}\mathbf{I} & \mathbf{0} & \mathbf{0} \\ \mathbf{0} & \lambda_{\mathbf{u}}\mathbf{I} & \mathbf{0} \\ \mathbf{0} & \mathbf{0} & \lambda_{\mathbf{w}}\mathbf{I} \end{bmatrix} \begin{bmatrix} \bar{\mathbf{A}}_3 & \mathbf{0} \\ \mathbf{B}_3^{\mathbf{u}}\mathbf{K} & \mathbf{0} \\ \mathbf{0} & \mathbf{B}_3^{\mathbf{w}} \end{bmatrix} \tag{7.39}$$

$$\tilde{\mathbf{X}}_{21} = \begin{bmatrix} \bar{\mathbf{A}}_2^\top\mathbf{P} & \mathbf{0} \\ \bar{\mathbf{B}}_2^{\mathbf{u}\top}\mathbf{P} & \mathbf{0} \\ \bar{\mathbf{B}}_2^{\mathbf{w}\top}\mathbf{P} & \mathbf{0} \end{bmatrix} \tag{7.40}$$

$$\tilde{\mathbf{X}}_{22} = \begin{bmatrix} -\lambda_{\mathbf{x}}\mathbf{I} & \mathbf{0} & \mathbf{0} \\ \mathbf{0} & -\lambda_{\mathbf{u}}\mathbf{I} & \mathbf{0} \\ \mathbf{0} & \mathbf{0} & -\lambda_{\mathbf{w}}\mathbf{I} \end{bmatrix} \tag{7.41}$$

Without loss of generality, we can let $\alpha_{\mathbf{w}} = \alpha\frac{\varepsilon_0^2}{\bar{w}^2}$ such that (7.38) becomes

$$\begin{bmatrix} \tilde{\mathbf{X}}_{11} & \star \\ \tilde{\mathbf{X}}_{21} & \tilde{\mathbf{X}}_{22} \end{bmatrix} \preceq 0 \tag{7.42}$$

which is equivalent to (7.26) for $\mu_{\mathbf{x}} = \frac{1}{\lambda_{\mathbf{x}}}$, $\mu_{\mathbf{u}} = \frac{1}{\lambda_{\mathbf{u}}}$, $\mu_{\mathbf{w}} = \frac{1}{\lambda_{\mathbf{w}}}$, and $\mathbf{Q} = \mathbf{P}^{-1}$. $\square$

Finally, we can express our barrier pair synthesis sub-problem $(\mathbf{B}, \mathbf{k}) = \mathsf{BP}(\mathbf{x_e}, \mathsf{a_d}, \bar{\mathsf{a}}_1, \cdots, \bar{\mathsf{a}}_{\mathsf{n_o}}, \mathcal{Z}_0, \mathcal{U}, \mathcal{W}, \epsilon_0)$ for a robot with a norm-bound human force input $\mathbf{w}$ as

$$\begin{aligned} \underset{\mathbf{Q},\mathbf{Y}}{\mathsf{maximize}} \quad & \mathsf{log}(\mathsf{det}(\mathbf{Q})) \\ \mathsf{subject\ to} \quad & \mathbf{Q} \succ 0, \\ & (7.16), (7.17), (7.18), (7.19), (7.20), (7.26) \end{aligned} \tag{7.43}$$

for finding a sub-level set $\mathbf{E}(1)$ that contains the desired region $\mathsf{a_d}$ and excludes the undesirable regions $\mathsf{a}_1, \mathsf{a}_2, \cdots, \mathsf{a}_{\mathsf{n_o}}$.

(7.25) can be considered as a special case of (7.43) where $\mathcal{W} = \varnothing$ and $\epsilon_0 = 0$.

```
Algorithm 1 $\mathbf{G} \leftarrow$ RRT($\mathbf{x}_0$, $\mathbf{x}_f$, $\delta$, $\bar{a}_1, \cdots, \bar{a}_{n_o}$)
Require: Initial state $\mathbf{x}_0$, goal state $\mathbf{x}_f$, incremental distance $\delta$, state constraints $\bar{a}_1, \cdots, \bar{a}_{n_o}$
Ensure: RRT graph $\mathbf{G}$
 1: $\delta_0 \leftarrow$ GetDistance($\mathbf{x}_f$, $\mathbf{x}_0$)
 2: $\mathbf{G}$.AddVertex($\mathbf{x}_f$)
 3: $\mathbf{x}_{new} \leftarrow \mathbf{x}_f$
 4: while $\delta_0 > \delta$ do
 5:     $\mathbf{x}_{rand} \leftarrow$ RandomState($\bigcap_{i=1}^{n_o} \bar{a}_i$)
 6:     $\mathbf{x}_{near} \leftarrow$ NearestVertex($\mathbf{x}_{rand}$, $\mathbf{G}$)
 7:     $\mathbf{x}_{new} \leftarrow$ NewState($\mathbf{x}_{near}$, $\mathbf{x}_{rand}$, $\delta$)
 8:     if $\mathbf{x}_{new} \in \bigcap_{i=1}^{n_o} \bar{a}_i$ then
 9:         $\delta_0 \leftarrow$ GetDistance($\mathbf{x}_{new}$, $\mathbf{x}_0$)
10:         $\mathbf{G}$.AddVertex($\mathbf{x}_{new}$), $\mathbf{G}$.AddEdge(($\mathbf{x}_{near}, \mathbf{x}_{new}$))
11:     end if
12: end while
13: $\mathbf{G}$.AddVertex($\mathbf{x}_0$), $\mathbf{G}$.AddEdge(($\mathbf{x}_{new}, \mathbf{x}_0$))
```

7.2.2 Barrier Pair Sampling Algorithm

Let us recall the algorithm of RRT that generates trajectories from $\mathbf{x}_0$ to $\mathbf{x}_f$ subject to workspace constraints $\mathbf{x} \in \bigcap_{i=1}^{n_o} \bar{a}_i$ where n_o is the number of undesirable regions. In Algorithm 1, a random state $\mathbf{x}_{rand}$ is sampled from the reachable space in line 5. In line 6-7, the graph extends toward the sampled state from its closest vertex by a constant distance δ. The algorithm terminates when distance to the initial state $\mathbf{x}_0$ is smaller than δ. The trajectory that connects $\mathbf{x}_0$ and $\mathbf{x}_f$ can be generated from the graph.

In Algorithm 1, line 5-7 can be considered as the essential steps of building a RRT trajectory with the rest of the algorithm checking the state constraint satisfaction and the distance to $\mathbf{x}_0$. We leverage these essential steps

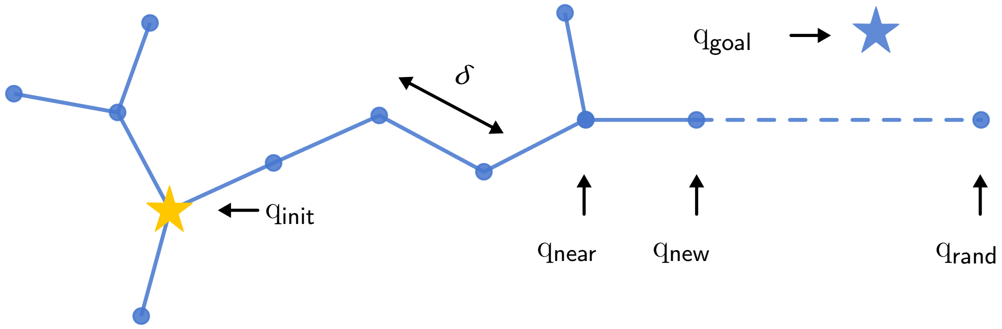

Figure 7.2: RRT Graph Expansion

of RRT to combine the barrier pair into a sequence that connects two polytopic regions in the reachable workspace.

BP-RRT Without Human Force Input Algorithm 2 describes our BP-RRT method for a robot without human force input $\mathbf{w}$. Line 1-3 in Algorithm 2 initialize the graph by creating a barrier pairs which contain workspace region a_f, where the graph starts from. In order to build the graph, a joint position $\mathbf{q}_{\mathsf{rand}}$ is sampled in line 5. If a sample of $\mathbf{q}_{\mathsf{rand}}$ is not reachable because of the undesirable polytopic regions, it will be excluded.

Line 5-7 in Algorithm 2 is similar to line 5-7 in Algorithm 1. However, instead of applying a constant incremental distance δ as RRT, the new equilibrium $\mathbf{q}_{\mathsf{new}}$ is obtained by projecting the random equilibrium $\mathbf{q}_{\mathsf{rand}}$ to the hyper-surface of level set $\mathbf{E}_{\mathsf{near}}(\varepsilon_1)$ of the nearest barrier pair with $-1 < \epsilon_1 \leqslant 0$ (Fig. 7.3). Therefore, $\mathbf{q}_{\mathsf{new}}$ is always inside the boundaries of the previously created barrier pairs and there is no need to check if $\mathbf{q}_{\mathsf{new}}$ satisfies the polytopic constraints.

Algorithm 2 $\mathbf{G} \leftarrow \texttt{BPRRT}(\mathsf{a}_0, \mathsf{a}_\mathsf{f}, \bar{\mathsf{a}}_1, \cdots, \bar{\mathsf{a}}_{n_o}, \mathcal{Z}_0, \mathcal{U}, \varepsilon_1)$

```
Require: Initial region $\mathsf{a}_0$, goal region $\mathsf{a}_\mathsf{f}$, constraints associated with undesirable regions $\bar{\mathsf{a}}_1, \cdots, \bar{\mathsf{a}}_{n_o}$, state space constraint $\mathcal{Z}_0$, input constraint $\mathcal{U}$, scalar $\varepsilon_1$ $(0 < \varepsilon_1 \leqslant 1)$
Ensure: BP-RRT graph $\mathbf{G}$
 1: $(\mathbf{Q}_\mathsf{f}, \mathbf{K}_\mathsf{f}) \leftarrow \texttt{BP}(\mathbf{x}_{\mathsf{a}_\mathsf{f}}, \mathsf{a}_\mathsf{f}, \bar{\mathsf{a}}_1, \cdots, \bar{\mathsf{a}}_{n_o}, \mathcal{Z}_0, \mathcal{U}, \varnothing, 0)$
 2: $\mathbf{G}.\texttt{AddVertex}(\mathbf{x}_\mathsf{f})$, $\mathbf{G}.\texttt{AddBP}((\mathbf{Q}_\mathsf{f}, \mathbf{K}_\mathsf{f}))$
 3: $(\mathbf{Q}_\mathsf{new}, \mathbf{K}_\mathsf{new}) \leftarrow (\mathbf{Q}_\mathsf{f}, \mathbf{K}_\mathsf{f})$, $\mathbf{x}_\mathsf{new} \leftarrow \mathbf{x}_\mathsf{f}$
 4: while $\mathbf{x}_0 \notin \mathbf{E}_\mathsf{new}(\varepsilon_1)$ do
 5:     $\mathbf{q}_\mathsf{rand} \leftarrow \texttt{RandomConfiguration}(\bigcap_{i=1}^{n_o} \bar{\mathsf{a}}_i)$
 6:     $\mathbf{E}_\mathsf{near}(\varepsilon_1) \leftarrow \texttt{NearestBP}(\mathbf{q}_\mathsf{rand}, \mathbf{G}, \varepsilon_1)$
 7:     $\mathbf{q}_\mathsf{att} \leftarrow \texttt{NewEquilibrium}(\mathbf{q}_\mathsf{rand}, \mathbf{E}_\mathsf{near}(\varepsilon_1))$
 8:     $\mathbf{x}_\mathsf{att} \leftarrow \mathbf{F}(\mathbf{q}_\mathsf{att})$
 9:     $(\mathbf{Q}_\mathsf{att}, \mathbf{K}_\mathsf{att}) \leftarrow \texttt{BP}(\mathbf{x}_\mathsf{att}, \varnothing, \bar{\mathsf{a}}_1, \cdots, \bar{\mathsf{a}}_{n_o}, \mathcal{Z}_0, \mathcal{U}, \varnothing, 0)$
10:     $\varepsilon_2 \leftarrow \sqrt{[\mathbf{q}_\mathsf{near}^\top - \mathbf{q}_\mathsf{att}^\top, \vec{0}^\top]^\top \, \mathbf{Q}_\mathsf{att}^{-1} \, [\mathbf{q}_\mathsf{near}^\top - \mathbf{q}_\mathsf{att}^\top, \vec{0}^\top]}$
11:     if $\varepsilon_2 \leqslant 1$ then
12:         $(\mathbf{Q}_\mathsf{new}, \mathbf{K}_\mathsf{new}) \leftarrow (\mathbf{Q}_\mathsf{att}, \mathbf{K}_\mathsf{att})$, $\mathbf{x}_\mathsf{new} \leftarrow \mathbf{x}_\mathsf{att}$
13:         $\mathbf{G}.\texttt{AddVertex}(\mathbf{x}_\mathsf{new})$, $\mathbf{G}.\texttt{AddBP}((\mathbf{Q}_\mathsf{new}, \mathbf{K}_\mathsf{new}))$, $\mathbf{G}.\texttt{AddEdge}((\mathbf{x}_\mathsf{near}, \mathbf{x}_\mathsf{new}))$
14:     end if
15: end while
16: $(\mathbf{Q}_0, \mathbf{K}_0) \leftarrow \texttt{BP}(\mathbf{x}_{\mathsf{a}_0}, \mathsf{a}_0, \bar{\mathsf{a}}_1, \cdots, \bar{\mathsf{a}}_{n_o}, \mathcal{Z}_0, \mathcal{U}, \varnothing, 0)$
17: $\mathbf{G}.\texttt{AddVertex}(\mathbf{x}_0)$, $\mathbf{G}.\texttt{AddBP}((\mathbf{Q}_0, \mathbf{K}_0))$, $\mathbf{G}.\texttt{AddEdge}((\mathbf{x}_\mathsf{new}, \mathbf{x}_0))$
```

The algorithm terminates if there exists a sub-level set $\mathbf{E}_\mathsf{new}(\varepsilon)$ of a new barrier pair $(\mathbf{Q}_\mathsf{new}, \mathbf{K}_\mathsf{new})$ that contains the equilibrium of the barrier pair of a_0. Then, the branch that connects a_0 and a_f can be extracted from the BP-RRT graph. The barrier pair sequence is executed in reverse order for barrier pair synthesis to achieve the transition from a_0 to a_f.

The robot's safe transition from $(\mathbf{Q}_\mathsf{new}, \mathbf{K}_\mathsf{new})$ to $(\mathbf{Q}_\mathsf{near}, \mathbf{K}_\mathsf{near})$ is guaranteed because $\mathbf{q}_\mathsf{new}$ is inside $\mathbf{E}_\mathsf{near}(1)$. By checking the condition in line 11, we can also enforce the safe transition from $(\mathbf{Q}_\mathsf{near}, \mathbf{K}_\mathsf{near})$ to $(\mathbf{Q}_\mathsf{new}, \mathbf{K}_\mathsf{new})$.

Algorithm 3 $\mathbf{G} \leftarrow \mathtt{BPRRT}(\mathsf{a}_0, \mathsf{a}_\mathsf{f}, \bar{\mathsf{a}}_1, \cdots, \bar{\mathsf{a}}_{n_o}, \mathcal{Z}_0, \mathcal{U}, \mathcal{W}, \varepsilon_0, \varepsilon_1)$

```
Require: Initial region $\mathsf{a}_0$, goal region $\mathsf{a}_\mathsf{f}$, constraints associated with undesirable regions $\bar{\mathsf{a}}_1, \cdots, \bar{\mathsf{a}}_{n_o}$, state space constraint $\mathcal{Z}_0$, robot input constraint $\mathcal{U}$, human input constraint $\mathcal{W}$, scalar $\varepsilon_0$ $(0 < \varepsilon_0 \leqslant 1)$, scalar $\varepsilon_1$ $(0 < \varepsilon_1 \leqslant 1)$
Ensure: BP-RRT graph $\mathbf{G}$
 1: $(\mathbf{Q}_\mathsf{f}, \mathbf{K}_\mathsf{f}) \leftarrow \mathtt{BP}(\mathbf{x}_{\mathsf{a}_\mathsf{f}}, \mathsf{a}_\mathsf{f}, \bar{\mathsf{a}}_1, \cdots, \bar{\mathsf{a}}_{n_o}, \mathcal{Z}_0, \mathcal{U}, \mathcal{W}, \varepsilon_0)$
 2: $\mathbf{G}.\mathtt{AddVertex}(\mathbf{x}_\mathsf{f})$, $\mathbf{G}.\mathtt{AddBP}((\mathbf{Q}_\mathsf{f}, \mathbf{K}_\mathsf{f}))$
 3: $(\mathbf{Q}_\mathsf{new}, \mathbf{K}_\mathsf{new}) \leftarrow (\mathbf{Q}_\mathsf{f}, \mathbf{K}_\mathsf{f})$, $\mathbf{x}_\mathsf{new} \leftarrow \mathbf{x}_\mathsf{f}$
 4: while $\mathbf{x}_0 \notin \mathbf{E}_\mathsf{new}(\varepsilon_1)$ do
 5:     $\mathbf{q}_\mathsf{rand} \leftarrow \mathtt{RandomConfiguration}(\bigcap_{i=1}^{n_o} \bar{\mathsf{a}}_i)$
 6:     $\mathbf{E}_\mathsf{near}(\varepsilon_1) \leftarrow \mathtt{NearestBP}(\mathbf{q}_\mathsf{rand}, \mathbf{G}, \varepsilon_1)$
 7:     $\mathbf{q}_\mathsf{att} \leftarrow \mathtt{NewEquilibrium}(\mathbf{q}_\mathsf{rand}, \mathbf{E}_\mathsf{near}(\varepsilon_1))$
 8:     $\mathbf{x}_\mathsf{att} \leftarrow \mathbf{F}(\mathbf{q}_\mathsf{att})$
 9:     $(\mathbf{Q}_\mathsf{att}, \mathbf{K}_\mathsf{att}) \leftarrow \mathtt{BP}(\mathbf{x}_\mathsf{att}, \varnothing, \bar{\mathsf{a}}_1, \cdots, \bar{\mathsf{a}}_{n_o}, \mathcal{Z}_0, \mathcal{U}, \mathcal{W}, \varepsilon_0)$
10:     $\varepsilon_2 \leftarrow \sqrt{[\mathbf{q}_\mathsf{near}^\top - \mathbf{q}_\mathsf{att}^\top, \vec{0}^\top]^\top \, \mathbf{Q}_\mathsf{att}^{-1} \, [\mathbf{q}_\mathsf{near}^\top - \mathbf{q}_\mathsf{att}^\top, \vec{0}^\top]}$
11:     if $\mathbf{Q}_\mathsf{att} \preceq \frac{(1-\varepsilon_1)^2}{\varepsilon_0^2} \cdot \mathbf{Q}_\mathsf{near}$ and $\mathbf{Q}_\mathsf{near} \preceq \frac{(1-\varepsilon_2)^2}{\varepsilon_0^2} \cdot \mathbf{Q}_\mathsf{att}$ then
12:         $(\mathbf{Q}_\mathsf{new}, \mathbf{K}_\mathsf{new}) \leftarrow (\mathbf{Q}_\mathsf{att}, \mathbf{K}_\mathsf{att})$, $\mathbf{x}_\mathsf{new} \leftarrow \mathbf{x}_\mathsf{att}$
13:         $\mathbf{G}.\mathtt{AddVertex}(\mathbf{x}_\mathsf{new})$, $\mathbf{G}.\mathtt{AddBP}((\mathbf{Q}_\mathsf{new}, \mathbf{K}_\mathsf{new}))$, $\mathbf{G}.\mathtt{AddEdge}((\mathbf{x}_\mathsf{near}, \mathbf{x}_\mathsf{new}))$
14:     end if
15: end while
16: $(\mathbf{Q}_0, \mathbf{K}_0) \leftarrow \mathtt{BP}(\mathbf{x}_{\mathsf{a}_0}, \mathsf{a}_0, \bar{\mathsf{a}}_1, \cdots, \bar{\mathsf{a}}_{n_o}, \mathcal{Z}_0, \mathcal{U}, \mathcal{W}, \varepsilon_0)$
17: $\mathbf{G}.\mathtt{AddVertex}(\mathbf{x}_0)$, $\mathbf{G}.\mathtt{AddBP}((\mathbf{Q}_0, \mathbf{K}_0))$, $\mathbf{G}.\mathtt{AddEdge}((\mathbf{x}_\mathsf{new}, \mathbf{x}_0))$
```

Therefore, the barrier pair sequence we obtain is bidirectional. Notice that the condition in line 11 checks if $\mathbf{q}_\mathsf{near}$ is also inside $\mathbf{E}_\mathsf{new}(1)$. This condition can also be expressed as an LMI similar to (7.16) and potentially included in the convex optimization problem defined in (7.25).

BP-RRT With Norm-Bound Human Force Input Although Algorithm 2 provides us the steps for creating a BP-RRT graph, it cannot be used directly to solve the interaction problem because of the additional human input $\mathbf{w}$. Therefore, we need to formulate a new barrier pair sampling algorithm for creating a barrier pair sequence that moves the robot's end-effector safely to a human desired region $\mathsf{a_d}$ under the human input intervention.

We extend our BP-RRT method to a robot under a human force input $\mathbf{w}$, as outlined in Algorithm 3. The algorithm initializes the BP-RRT graph by creating a barrier pair at $\mathsf{a_f}$ in line 1-3, expands it by sampling new barrier pairs in line 4-14, and completes it by creating a barrier pair at $\mathsf{a_0}$ in line 15-16.

Different from Algorithm 2, Algorithm 3 considers two scalar inputs ε_0 and ε_1 (Fig. 7.4). The first scalar input ε_0, previously introduced in (7.27), defines the residue set $\mathbf{E}(\varepsilon_0)$ of a barrier pair. Similar to the scalar input ε_1 in Algorithm 2, the second scalar input ε_1 defines a hyper-surface of sub-level set $\mathbf{E}_{\mathsf{near}}(\varepsilon_1)$ of the nearest barrier pair found in line 6 such that a new equilibrium $\mathbf{q}_{\mathsf{att}}$ can be obtained by projecting a random configuration $\mathbf{q}_{\mathsf{rand}}$ sampled in line 5 to this hyper-surface.

In order to enforce the robot's safe transition between two barrier pairs of an edge in the graph, the residue set $\mathbf{E}_{\mathsf{att}}(\varepsilon_0)$ of the newly sampled barrier pair created in line 9 needs to be completely inside the zero sub-level set $\mathbf{E}_{\mathsf{near}}(1)$ of the nearest barrier pair found in line 6. We can check this safety requirement through the condition stated in the following proposition.

Proposition 7.2 Suppose $(\mathbf{Q}_1, \mathbf{K}_1)$ and $(\mathbf{Q}_2, \mathbf{K}_2)$ represent two barrier pairs forming an edge in a BP-RRT graph. Let $\mathbf{z}_1 \triangleq [\mathbf{q}_1^\top, \vec{0}^\top]^\top$ and $\mathbf{z}_2 \triangleq [\mathbf{q}_2^\top, \vec{0}^\top]^\top$ be the equilibrium points of $(\mathbf{Q}_1, \mathbf{K}_1)$ and $(\mathbf{Q}_2, \mathbf{K}_2)$ located at the hyper-surface

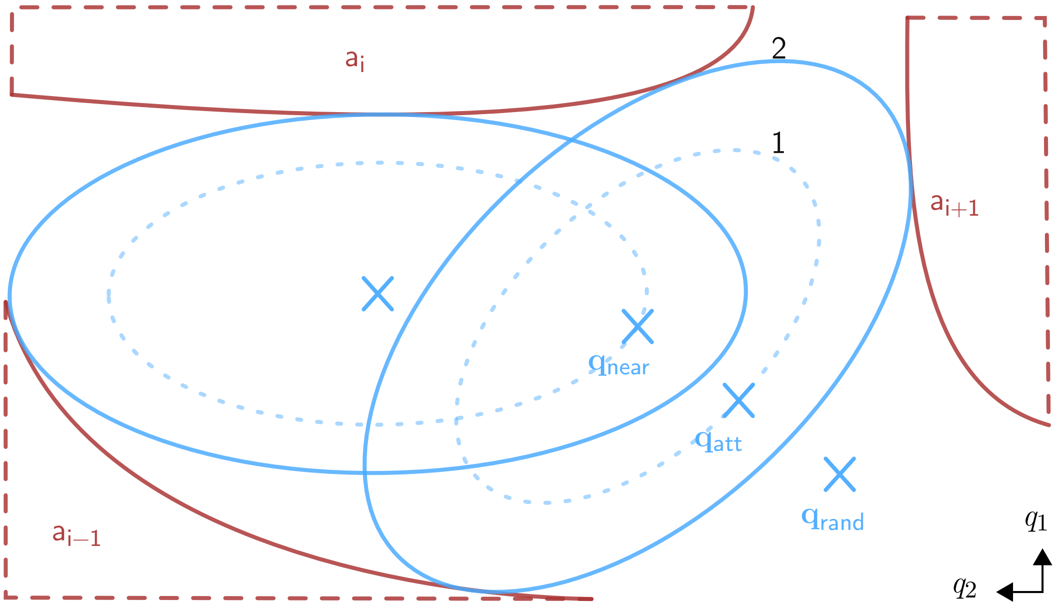

Figure 7.3: By projecting a random joint space position $\mathbf{q}_{\mathsf{rand}}$ to the hyper-surface of $\mathbf{E}_{\mathsf{near}}(\epsilon)$ of the nearest barrier pair, a new equilibrium $\mathbf{q}_{\mathsf{att}}$ of BP-RRT is created. Notice that even if the workspace undesirable regions are polytopic, their joint space projections are not guaranteed to be also polytopic. The numbers indicate ^{1} the hyper-surface of $\mathbf{E}_{\mathsf{near}}(\epsilon_1)$, and ^{2} the zero sub-level set $\mathbf{E}_{\mathsf{near}}(1)$.

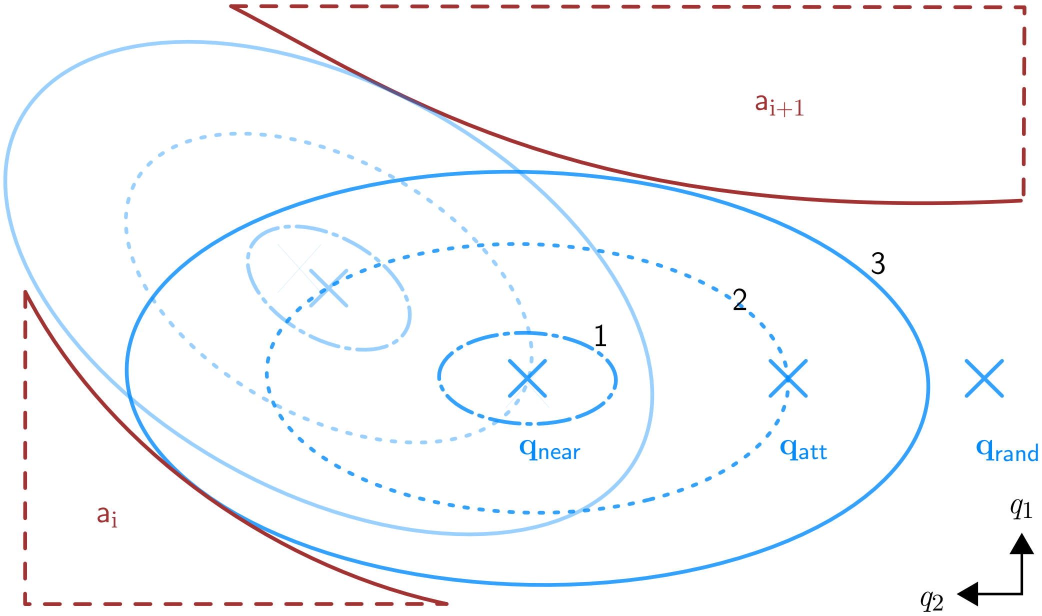

Figure 7.4: By projecting a random joint space position q_{rand} to the hyper-surface of $\mathbf{E}_{\mathsf{near}}(\epsilon_1)$ of the nearest barrier pair, a new equilibrium $\mathbf{q}_{\mathsf{att}}$ of BP-RRT is created. The residue set $\mathbf{E}_{\mathsf{new}}(\epsilon_0)$ of the new barrier pair is designed to be strictly inside the zero sub-level set $\mathbf{E}_{\mathsf{near}}(1)$ of the nearest barrier pair. Notice that even if the undesirable regions of the workspace are polytopic, their joint space projections are not guaranteed to be also polytopic. The numbers indicate ^{1} the residue set $\mathbf{E}_{\mathsf{near}}(\epsilon_0)$, ^{2} the hyper-surface of $\mathbf{E}_{\mathsf{near}}(\epsilon_1)$, and ^{3} the zero sub-level set $\mathbf{E}_{\mathsf{near}}(1)$.

of $\mathbf{E}_2(\varepsilon_2)$ and $\mathbf{E}_1(\varepsilon_1)$, respectively. Let $\mathbf{E}_1(\varepsilon_0)$ and $\mathbf{E}_2(\varepsilon_0)$ be the residue sets of $(\mathbf{Q}_1, \mathbf{K}_1)$ and $(\mathbf{Q}_2, \mathbf{K}_2)$. The robot can safely transit between the zero sub-level sets $\mathbf{E}_1(1)$ and $\mathbf{E}_2(1)$ of these two barrier pairs if $\mathbf{Q}_1 \preceq \frac{(1-\varepsilon_2)^2}{\varepsilon_0^2} \cdot \mathbf{Q}_2$ and $\mathbf{Q}_2 \preceq \frac{(1-\varepsilon_1)^2}{\varepsilon_0^2} \cdot \mathbf{Q}_1$.

Proof Let us define a vector norm function

$$\|\star\|_{\mathbf{Q}_1} \triangleq \sqrt{\star^\top \mathbf{Q}_1^{-1} \star} \tag{7.44}$$

based on the quadratic part in the barrier function of $(\mathbf{Q}_1, \mathbf{K}_1)$. Because equilibrium $\mathbf{z}_2$ of $(\mathbf{Q}_2, \mathbf{K}_2)$ is on hyper-surface of $\mathbf{E}_1(\varepsilon_1)$, we have

$$\|\mathbf{z}_2 - \mathbf{z}_1\|_{\mathbf{Q}_1} = \varepsilon_1. \tag{7.45}$$

Suppose $\mathbf{z}_1'$ is a point on the hyper-surface of $\mathbf{E}_1(1)$, we have

$$\|\mathbf{z}_1' - \mathbf{z}_2\|_{\mathbf{Q}_1} + \|\mathbf{z}_2 - \mathbf{z}_1\|_{\mathbf{Q}_1} \geqslant \|\mathbf{z}_1' - \mathbf{z}_1\|_{\mathbf{Q}_1} = 1 \tag{7.46}$$

because of the triangle inequality of $\|\star\|_{\mathbf{Q}_1}$. Based on (7.45) and (7.46), we have

$$\|\mathbf{z}_1' - \mathbf{z}_2\|_{\mathbf{Q}_1} \geqslant 1 - \varepsilon_1 \tag{7.47}$$

which is equivalent to

$$\{\mathbf{z} \mid (\mathbf{z} - \mathbf{z}_2)^\top \mathbf{Q}_1^{-1} (\mathbf{z} - \mathbf{z}_2) \leqslant (1 - \varepsilon_1)^2\} \subseteq \mathbf{E}_1(1). \tag{7.48}$$

If $\mathbf{Q}_1 \preceq \frac{(1-\varepsilon_2)^2}{\varepsilon_0^2} \cdot \mathbf{Q}_2$, we have

$$\mathbf{E}_2(\varepsilon_0) \subseteq \{\mathbf{z} \mid (\mathbf{z} - \mathbf{z}_2)^\top \mathbf{Q}_1^{-1} (\mathbf{z} - \mathbf{z}_2) \leqslant (1 - \varepsilon_1)^2\}. \tag{7.49}$$

Combining (7.48) and (7.49), we have $\mathbf{E}_2(\varepsilon_0) \subseteq \mathbf{E}_1(1)$. If the robot starts from any states in $\mathbf{E}_2(1)$, it safely converges to a subset in $\mathbf{E}_1(1)$ using barrier pair $(\mathbf{Q}_2, \mathbf{K}_2)$.

Similarly, we have $\mathbf{E}_1(\varepsilon_0) \subseteq \mathbf{E}_2(1)$ if $\mathbf{Q}_2 \preceq \frac{(1-\varepsilon_1)^2}{\varepsilon_0^2} \cdot \mathbf{Q}_1$. $\square$

Line 11 in Algorithm 3 checks the condition in Proposition 2. Notice that this condition guarantees the safe transition between $(\mathbf{Q}_{\mathsf{near}}, \mathbf{K}_{\mathsf{near}})$ and $(\mathbf{Q}_{\mathsf{att}}, \mathbf{K}_{\mathsf{att}})$ in both directions. Therefore, although the graph is initialized from a_f and expanded toward a_0, we can finally extract a sequence of barrier pairs which plan safe robot trajectories from a_0 to a_f and from a_f to a_0.

Notice that we check the condition in Proposition 2 after the barrier pair synthesis because $\mathbf{Q}_{\mathsf{near}} \preceq \frac{(1-\varepsilon_2)^2}{\varepsilon_0^2} \cdot \mathbf{Q}_{\mathsf{att}}$ in line 11 of Algorithm 3 is a non-convex LMI constraint and cannot be included in the convex optimization problem defined in (7.43). However, this also means $\mathbf{Q}_{\mathsf{att}} \preceq \frac{(1-\varepsilon_1)^2}{\varepsilon_0^2} \cdot \mathbf{Q}_{\mathsf{near}}$ in line 11 of Algorithm 3 is a convex LMI constraint which can be potentially added to our barrier pair synthesis problem.

7.3 A Human-Robot Shared Autonomy Example

Our BP-RRT algorithm is demonstrated through a simulation of a 2-link manipulator robot with an equal length of 0.75 m for each link, a mass of 2.5 kg located at the distal end of each link, and a torque limit of 25 N · m for each joint. Fig. 7.5 shows the definition of polytopics in the workspace of the robot end effector, where a_1, a_2, a_3 represent the desired task regions, a_4, a_5, a_6 represent obstacle regions, and a_7 represents the region where the robot's base is located.

The manipulator robot starts from an end-effector position in a_1. A human operator decides whether to apply a 1 N force to the end-effector during the simulation. The human operator chooses the direction of the 1 N force from 8 different possible directions through a keyboard. The robot uses the measurement of human force input to infer which task region in a_1, a_2 and a_3 the human wants its end-effector to move to. Then, a barrier pair sequence synthesized using in advance our BP-RRT algorithm is executed based on the inference of the human's objective.

7.3.1 Human Intention Inference

Based on the concept of Boltzmann rationality [Baker, Tenenbaum, and Saxe, 2007; Morgenstern and Von Neumann, 1953], we propose our human intent inference method for interpreting the human input $\mathbf{w}$ in the shared autonomy. Boltzmann rationality formalizes intent according to a variable that quantifies the value of the human's actions. In particular, it states that a rational human takes an action with probability proportional to the exponentiated value of that human action. Therefore, an action with higher value is more probable to be chosen by the human.

In the setting of robotic manipulation considered in this chapter, we define the value of the human's action based on how well the human force $\mathbf{w}$ aligns with the direction toward the human's goal. Let a denote the human's goal, $\mathbf{x}_\mathbf{t}$ denote the position of the robot's end-effector at time $\mathbf{t}$, and $\mathbf{w}_\mathbf{t}$ denote the human force exerted at time $\mathbf{t}$. Recall that $\mathbf{x}_{\mathsf{a}_\mathsf{i}}$ is the center of a polytopic region a_i in the workspace. We define the likelihood function of exerting the

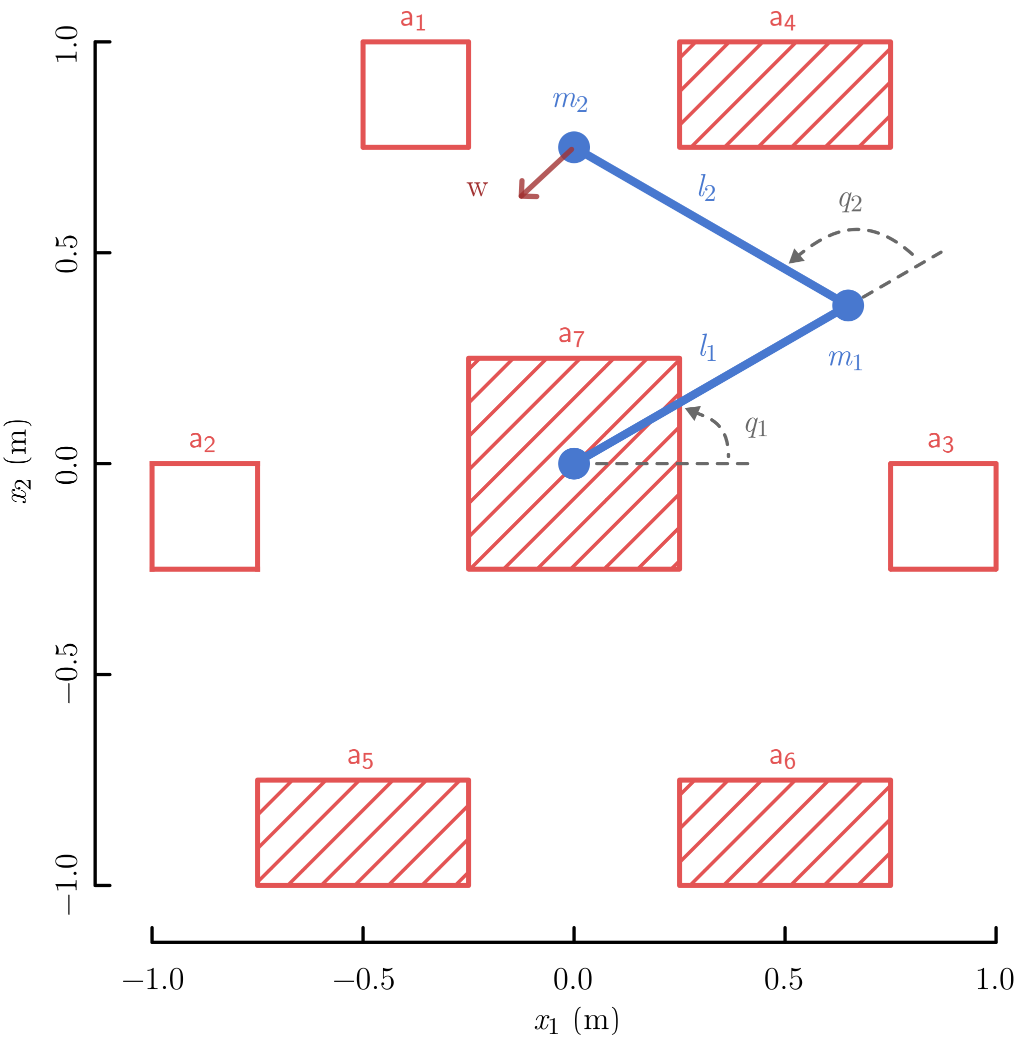

Figure 7.5: A 2-link manipulator robot moves its end effector in a workspace with different polyoptic regions. a_1, a_2, and a_3 represent the desired task regions, a_4, a_5, and a_6 represent obstacle regions, and a_7 represents the region where the robot's base is located.

force $\mathbf{w_t}$ conditioned on the true human's goal a as

$$\mathsf{p}(\mathbf{w_t} \mid \mathsf{a} = \mathsf{a_i}) = \beta_0^{-1} \cdot \exp(\beta_1 \cdot \langle \mathbf{w_t}, \mathbf{x}_{\mathsf{a_i}} - \mathbf{x_t} \rangle), \tag{7.50}$$

where $\beta_0 > 0$, $\beta_1 > 0$, and the value of the human's action is captured by the inner product of $\mathbf{w_t}$ and the direction toward the target region $\mathbf{x}_{\mathsf{a_i}} - \mathbf{x_t}$. The value of this inner product indicates how well the exerted force is correlated with the direction toward the target region. β_0 is a partition function defined as

$$\beta_0 = \int_{\mathbf{w} \in \mathcal{W}} \exp(\beta_1 \cdot \langle \mathbf{w_t}, \mathbf{x}_{\mathsf{a_i}} - \mathbf{x_t} \rangle) \, \mathrm{d}\mathbf{w}, \tag{7.51}$$

where $\mathcal{W}$ is the domain of feasible human force input defined in (7.14). β_1 is the rationality parameter representing the degree of human's rationality.

Now, using the likelihood function, we can compute and update the robot's belief over the human's intended target region. Let us define the robot's belief as

$$\mathsf{b}_t(\mathsf{a_i}) = \mathsf{p}(\mathsf{a} = \mathsf{a_i} \mid \mathbf{w}_0, \ldots, \mathbf{w_t}) \tag{7.52}$$

which denotes the probability of the target region being $\mathsf{a_i}$ given the history of human's inputs. Initially, the system starts with a uniform belief, i.e., $\mathsf{b}_0 \sim \texttt{unif}\{1, n_o\}$. Then, we can update the belief using the Bayes' theorem

$$\mathsf{b}_t(\mathsf{a_i}) = \frac{\mathsf{b}_{t-1}(\mathsf{a_i}) \cdot \mathsf{p}(\mathbf{w_t} \mid \mathsf{a} = \mathsf{a_i})}{\sum_{j=1}^{n_o} \mathsf{b}_{t-1}(\mathsf{a_j}) \cdot \mathsf{p}(\mathbf{w_t} \mid \mathsf{a} = \mathsf{a_j})}, \tag{7.53}$$

where $\mathsf{p}(\mathbf{w_t} \mid \mathsf{a} = \mathsf{a_i})$ is computed according to (7.50).

At time $\mathbf{t}$, the robot's belief is used to select the sequence of barrier pairs that carry out the task of safely going to the estimated target region $\hat{\mathsf{a}}(t)$

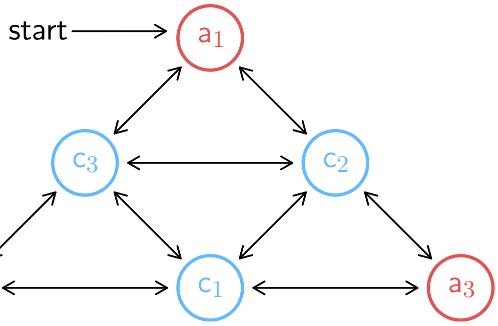

Figure 7.6: A finite state machine indicates the possible transitions between a_1, a_2, a_3, c_1, c_2, and c_3.

calculated as

$$\hat{a}(t) = \underset{i \in \{1,2,\ldots,n_o\}}{\arg\max}\ b_t(a_i), \tag{7.54}$$

which has the highest probability of being the human's intended goal.

7.3.2 Barrier Pair Synthesis

We use Algorithm 3 to build barrier pair sequences which connect between a_1, a_2, and a_3 (Fig. 7.7.a-c). Barrier pairs c_1, c_2, and c_3 are in the middle of the sequences from a_2 to a_3, from a_3 to a_1, and from a_1 to a_2, respectively. Sometimes, the inference of the human target region may change and result in the barrier pair sequence currently executed by the robot to be invalid. Therefore, we also use Algorithm 2 to connect between c_1, c_2, and c_3 (Fig. 7.7.d-f) such that the robot can freely switch between the correct barrier pair sequences without going through any undesired regions. Fig. 7.6 shows the transitions between a_1, a_2, a_3, c_1, c_2, and c_3.

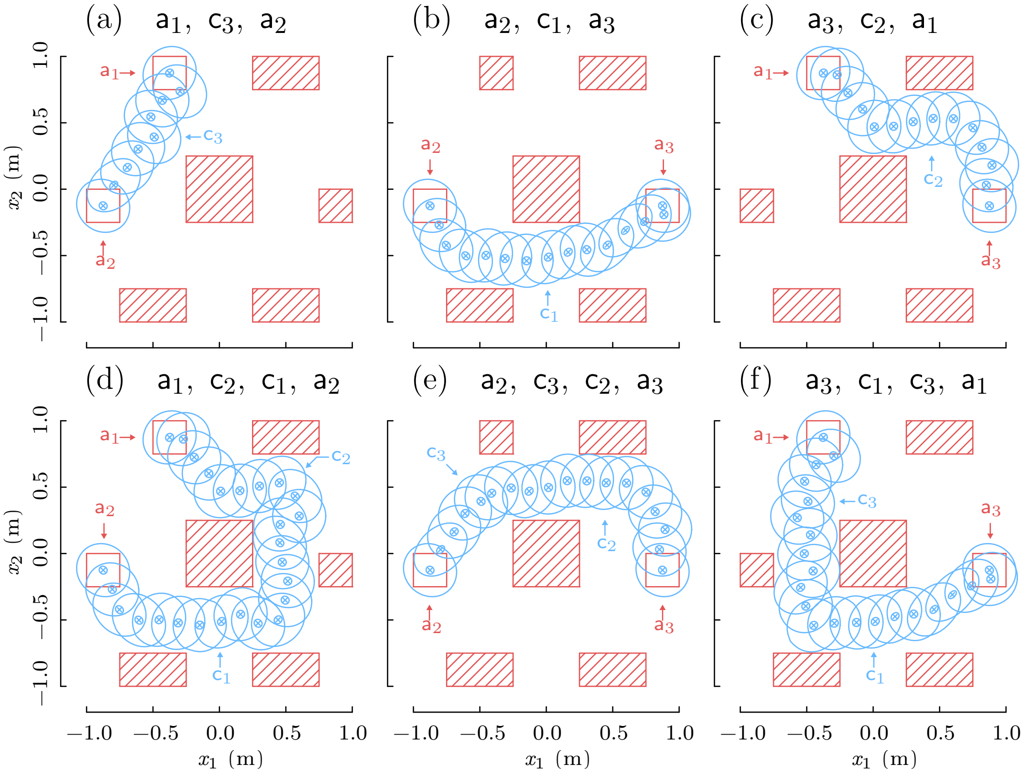
(a) $\mathsf{a}_1,\ \mathsf{c}_3,\ \mathsf{a}_2$
(b) $\mathsf{a}_2,\ \mathsf{c}_1,\ \mathsf{a}_3$
(c) $\mathsf{a}_3,\ \mathsf{c}_2,\ \mathsf{a}_1$
(d) $\mathsf{a}_1,\ \mathsf{c}_2,\ \mathsf{c}_1,\ \mathsf{a}_2$
(e) $\mathsf{a}_2,\ \mathsf{c}_3,\ \mathsf{c}_2,\ \mathsf{a}_3$
(f) $\mathsf{a}_3,\ \mathsf{c}_1,\ \mathsf{c}_3,\ \mathsf{a}_1$

Figure 7.7: Barrier pair sequences connect a_0 and a_f and avoid passing through the undesirable polytopic regions. The bigger and the smaller ellipsoids indicate the zero sub-level sets and the residue sets of the barrier pairs projected onto the x_1-x_2 space. The pointers indicate the locations of a_1, a_2, a_3, c_1, c_2, and c_3.

7.3.3 Simulation

The video of this simulation is available at https://youtu.be/xTprU0jMT8w. The simulated manipulator robot uses the measurement of the 1 N force to infer the human operator's desired goal region. As the video shows, the initial force input from the human operator is sometimes ambiguous because it can point to multiple potential goal regions. However, the proposed human intention inference method is able to successfully recover the intended goal fast enough such that the manipulator robot does not move its end-effector to an incorrect goal region.

Chapter 8

Concluding Remarks

8.1 Conclusions

Human-centered robots using human forces for feedback must be stable given the natural impedance displayed by human operators to avoid undesired vibrations. Chapter 3 presents a new model describing observed human impedances using an imaginary stiffness term to fill an energy-dissipation role. We also present experiments demonstrating that this new term is a more significant contributor to model accuracy than a linear damping term for cyclic motions of the human elbow. This was verified in a study that we performed involving a 10-subject cohort. Between the linear PI control method in Chapter 2 and the nonlinear fractional-order control method in Chapter 4, we can compare the control design problem with and without the use of the hysteretic adjustment in the human impedance model. The result is clear: without complex stiffness controllers must be designed to cross over (in a frequency domain sense) before the lowest natural frequency calculated using the human and exoskeleton inertias and the softest predicted human stiffness; with the hysteretic adjustment, the crossover frequency can exceed the above limits by implementing a fractional-order controller, thus improving bandwidth. Our loop shaping experiments demonstrate the stability and bandwidth of our controllers and highlight the importance of testing both maximum and minimum human stiffness values when tuning the fractional order controller.

In Chapter 5-7, we presented a method for synthesis of controllers that guarantee future satisfaction of state constraints, subject to input-limited dynamics. This method takes advantage of the guarantees provided through LMI-based controller synthesis. We introduced the concept of barrier pairs—which make it easier to reason about the satisfaction of input limits—and a min-quadratic barrier in particular as a simple means of combining the results of many LMI-synthesis problems. And we distinguish our work from others by addressing input constraints and synthesizing the barrier function and the controllers together so that the controller choices, which can significantly alter the shape of the invariant sets, are used to maximize their volume. In the presence of input constraints, our controller synthesis method will choose invariant ellipsoids to avoid the critical-point-terminating trajectories that represent dynamic limitations due to input limits. By incorporating the RRT method into our method for synthesizing barrier pairs, human-centered robots can provide safe motions in the presence of non-convex state-space constraints. We demonstrated that our sampling-based barrier pair method allows us to implement human-robot shared autonomy. In our control framework, a robot manipulator uses the inference of human target objectives to assist the human and prevent potential accidents.

8.2 Suggested Ideas for Future Research

In this dissertation, we discussed new human models and new control algorithms, which help to improve the responsiveness and safety of human-centered robots. Many types of human inputs can be measured using robot sensors and can be incorporated into feedback control policies. However, the responsiveness of human-centered robots can be further improved if we utilize additional hidden human inputs such as human desired trajectories and human impedances in our control loop. These hidden human inputs cannot be directly measured in real-time by robot sensors. Although various data-driven methods have attempted to estimate hidden human inputs, the randomness and time-varying nature of human behaviors make the estimation extremely difficult. While an aggressive control policy using an imperfect estimation of hidden human inputs brings safety and stability concerns, a conservative control policy that achieves more robustness to the variation of the human inputs will sacrifice the efficiency of controllers during human-robot interaction. Therefore, closing the gap between safety and responsiveness of human-centered robots is a challenging problem that we will continue investigating.

This dissertation introduced safety control algorithms using the concept of a barrier pair. Therefore, an idea to close the gap between safety and responsiveness is using a barrier pair, which consists of a barrier function and a tunable robot control policy. The barrier function quantifies the confidence of the hidden state estimation while the tunable robot control policy can provide aggressive or conservative behavior based on the run-time value of the barrier function. This kind of solution aims to simultaneously provide safety guarantees and real-time responsiveness of human-centered robots. Usually, safety requires control policies to be robust and conservative, while responsiveness requires control policies to be optimal and aggressive. Therefore, these two goals are difficult to satisfy at the same time. The idea is to resolve this conflict using a two-layer control framework. This framework includes a layer providing data-driven methods that estimate hidden human inputs and deal with real-time responsiveness and a layer providing barrier functions that quantify hidden state estimation confidence and guarantee safety constraint satisfaction.

Human-centered robots have the hallmark of a system with high potential in our industrial and service sectors. Instead of replacing the human capital in our workforce, they will assist us and cooperate with us to improve our productivity and quality of work and life. Considering the global pandemic of COVID-19 in 2020-2021, many types of close collaborations among humans became difficult to carry on because of social distancing requirements. However, human-centered robots are invulnerable to the spread of the virus. Thus they can take roles such as collecting biological samples for virus testing and helping humans to have their groceries delivered and sanitized in the supermarket or at home. The proposed ideas, if successful, will improve the safety and real-time responsiveness of human-centered robots for every day use. The achievements regarding these two goals will help our societies to improve our work and social lives and provide infrastructure for dealing with major events such as the current global pandemic.

Bibliography

R. J. Adams and B. Hannaford. Stable haptic interaction with virtual environments. *IEEE Transactions on Robotics and Automation*, 15(3):465–474, 1999.

G. Agarwal and C. Gottlieb. Compliance of the human ankle joint. *Journal of Biomechanical Engineering*, 99(3):166–170, 1977.

A. D. Ames, X. Xu, J. W. Grizzle, and P. Tabuada. Control barrier function based quadratic programs for safety critical systems. *IEEE Transactions on Automatic Control*, 62(8):3861–3876, 2016.

C. L. Baker, J. B. Tenenbaum, and R. R. Saxe. Goal inference as inverse planning. *Proceedings of the Annual Meeting of the Cognitive Science Society*, 29(29), 2007.

A. J. Barry, A. Majumdar, and R. Tedrake. Safety verification of reactive controllers for UAV flight in cluttered environments using barrier certificates. In *Robotics and Automation (ICRA), 2012 IEEE International Conference on*, pages 484–490. IEEE, 2012.

J. Becker and C. Mote. Identification of a frequency response model of joint rotation. *Journal of Biomechanical Engineering*, 112(1):1–8, 1990.

A. Bemporad. Reference governor for constrained nonlinear systems. *IEEE Transactions on Automatic Control*, 43(3):415–419, 1998.

D. Bennett, J. Hollerbach, Y. Xu, and I. Hunter. Time-varying stiffness of human elbow joint during cyclic voluntary movement. *Experimental Brain Research*, 88(2):433–442, 1992.

R. E. D. Bishop and D. C. Johnson. *The Mechanics of Vibration*. Cambridge University Press, 1960.

T. Boaventura and J. Buchli. Acceleration-based transparency control framework for wearable robots. In *Biomedical Robotics and Biomechatronics (BioRob), 2016 IEEE International Conference on*. ETH Zürich, 2016.

J. E. Bobrow, S. Dubowsky, and J. Gibson. Time-optimal control of robotic manipulators along specified paths. *The International Journal of Robotics Research*, 4(3):3–17, 1985.

S. Boyd, L. El Ghaoui, E. Feron, and V. Balakrishnan. *Linear matrix inequalities in system and control theory*, volume 15. Siam, 1994.

N. Brissonneau, B. He, G. C. Thomas, and L. Sentis. Biologically-inspired impedance control with hysteretic damping. *IEEE Control Systems Letters*, 5(5):1717–1722, 2021.

S. P. Buerger and N. Hogan. Complementary stability and loop shaping for improved human–robot interaction. *IEEE Transactions on Robotics*, 23(2):232–244, 2007.

R. R. Burridge, A. A. Rizzi, and D. E. Koditschek. Sequential composition of dynamically dexterous robot behaviors. *The International Journal of Robotics Research*, 18(6):534–555, 1999.

S. C. Cannon and G. I. Zahalak. The mechanical behavior of active human skeletal muscle in small oscillations. *Journal of Biomechanics*, 15(2):111–121, 1982.

T. Carlson and J. d. R. Millán. Brain-controlled wheelchairs: A robotic architecture. *IEEE Robotics & Automation Magazine*, 20(1):65–73, 2013.

S. Chen, Z. Chen, B. Yao, X. Zhu, S. Zhu, Q. Wang, and Y. Song. Adaptive robust cascade force control of 1-dof hydraulic exoskeleton for human performance augmentation. *IEEE/ASME Transactions on Mechatronics*, 22(2): 589–600, 2016.

E. Colgate, A. Bicchi, M. A. Peshkin, and J. E. Colgate. Safety for physical human-robot interaction. In *Springer handbook of robotics*, pages 1335–1348. Springer, 2008.

J. E. Colgate and J. M. Brown. Factors affecting the z-width of a haptic display. In *Robotics and Automation (ICRA), 1994 IEEE International Conference on*, pages 3205–3210. IEEE, 1994.

J. E. Colgate and N. Hogan. Robust control of dynamically interacting systems. *International Journal of Control*, 48(1):65–88, 1988.

M. Corless and J. Tu. State and input estimation for a class of uncertain systems. *Automatica*, 34(6):757–764, 1998.

J. A. DeCastro and H. Kress-Gazit. Synthesis of nonlinear continuous controllers for verifiably correct high-level, reactive behaviors. *The International Journal of Robotics Research*, 34(3):378–394, 2015.

A. M. Dollar and H. Herr. Lower extremity exoskeletons and active orthoses: challenges and state-of-the-art. *IEEE Transactions on Robotics*, 24(1):144–158, 2008.

D. M. Dudek and R. J. Full. Passive mechanical properties of legs from running insects. *Journal of Experimental Biology*, 209(8):1502–1515, 2006.

M. Fontana, R. Vertechy, S. Marcheschi, F. Salsedo, and M. Bergamasco. The body extender: A full-body exoskeleton for the transport and handling of heavy loads. *IEEE Robotics & Automation Magazine*, 21(4):34–44, 2014.

L. Fridman. Human-centered autonomous vehicle systems: Principles of effective shared autonomy. *arXiv preprint arXiv:1810.01835*, 2018.

E. Glassman, A. L. Desbiens, M. Tobenkin, M. Cutkosky, and R. Tedrake. Region of attraction estimation for a perching aircraft: A Lyapunov method exploiting barrier certificates. In *Robotics and Automation (ICRA), 2012 IEEE International Conference on*, pages 2235–2242. IEEE, 2012.

G. L. Gottlieb and G. C. Agarwal. Dependence of human ankle compliance on joint angle. *Journal of Biomechanics*, 11(4):177–181, 1978.

K. Gui, H. Liu, and D. Zhang. A practical and adaptive method to achieve emg-based torque estimation for a robotic exoskeleton. *IEEE/ASME Transactions on Mechatronics*, 24(2):483–494, 2019.

B. Hannaford and J.-H. Ryu. Time-domain passivity control of haptic interfaces. *IEEE Transactions on Robotics and Automation*, 18(1):1–10, 2002.

K. Hauser and Y. Zhou. Asymptotically optimal planning by feasible kinodynamic planning in a state–cost space. *IEEE Transactions on Robotics*, 32(6): 1431–1443, 2016.

B. He, H. Huang, G. C. Thomas, and L. Sentis. Complex stiffness model of physical human-robot interaction: Implications for control of performance augmentation exoskeletons. In *2019 IEEE/RSJ International Conference on Intelligent Robots and Systems (IROS)*, pages 6748–6755. IEEE, 2019.

B. He, G. C. Thomas, N. Paine, and L. Sentis. Modeling and loop shaping of single-joint amplification exoskeleton with contact sensing and series elastic actuation. In *2019 American Control Conference (ACC)*, pages 4580–4587. IEEE, 2019.

B. He, H. Huang, G. C. Thomas, and L. Sentis. A complex stiffness human impedance model with customizable exoskeleton control. *IEEE Transactions on Neural Systems and Rehabilitation Engineering*, 28(11):2468–2477, 2020a.

B. He, J. Lee, U. Topcu, and L. Sentis. BP-RRT: Barrier pair synthesis for temporal logic motion planning. In *IEEE Conference on Decision and Control (CDC)*, pages 1404–1409. IEEE, 2020b.

B. He, G. C. Thomas, and L. Sentis. Robust estimator-based safety verification: A vector norm approach. In *2020 American Control Conference (ACC)*. IEEE, 2020c.

B. He, M. Ghasemi, U. Topcu, and L. Sentis. A barrier pair method for safe human-robot shared autonomy. In *IEEE Conference on Decision and Control (CDC), in review*. IEEE, 2021.

H. Herr. Exoskeletons and orthoses: classification, design challenges and future directions. *Journal of Neuroengineering and Rehabilitation*, 6(1):21, 2009.

N. Hogan. Adaptive control of mechanical impedance by coactivation of antagonist muscles. *IEEE Transactions on Automatic Control*, 29(8):681–690, 1984.

N. Hogan. Controlling impedance at the man/machine interface. In *Robotics and Automation (ICRA), 1989 IEEE International Conference on*, pages 1626–1631. IEEE, 1989.

T. Hu and Z. Lin. Composite quadratic lyapunov functions for constrained control systems. *IEEE Transactions on Automatic Control*, 48(3):440–450, 2003.

T. Hu, L. Ma, and Z. Lin. On several composite quadratic Lyapunov functions for switched systems. In *Decision and Control, 2006 45th IEEE Conference on*, pages 113–118. IEEE, 2006.

H. Huang, H. F. Cappel, G. C. Thomas, B. He, and L. Sentis. Adaptive compliance shaping with human impedance estimation. In *2020 Annual American Control Conference (ACC)*. IEEE, 2020.

I. Hunter and R. Kearney. Dynamics of human ankle stiffness: Variation with mean ankle torque. *Journal of Biomechanics*, 15(10):747 – 752, 1982.

J. A. Inaudi and J. M. Kelly. Linear hysteretic damping and the hilbert transform. *J. Eng. Mechanics*, 121(5):626–632, 1995.

P. A. Ioannou and J. Sun. *Robust adaptive control*. Courier Corporation, 2012.

S. C. Jacobsen and M. X. Olivier. Contact displacement actuator system, Sept. 30 2014. US Patent 8,849,457.

S. Javdani, H. Admoni, S. Pellegrinelli, S. S. Srinivasa, and J. A. Bagnell. Shared autonomy via hindsight optimization for teleoperation and teaming. *The International Journal of Robotics Research*, 37(7):717–742, 2018.

S. Karaman and E. Frazzoli. Sampling-based algorithms for optimal motion planning. *The international journal of robotics research*, 30(7):846–894, 2011.

M. Kazemi, K. K. Gupta, and M. Mehrandezh. Randomized kinodynamic planning for robust visual servoing. *IEEE Transactions on Robotics*, 29(5): 1197–1211, 2013.

H. Kazerooni. Human-robot interaction via the transfer of power and information signals. *IEEE Transactions on Systems, Man, and Cybernetics*, 20(2): 450–463, 1990.

H. Kazerooni. Exoskeletons for human power augmentation. In *Intelligent Robots and Systems (IROS), 2005 IEEE/RSJ International Conference on*, pages 3459–3464. IEEE, 2005.

H. Kazerooni and J. Guo. Human extenders. *Journal of Dynamic Systems, Measurement, and Control*, 115(2B):281–290, 1993.

H. Kazerooni and T. J. Snyder. Case study on haptic devices: Human-induced instability in powered hand controllers. *Journal of Guidance, Control, and Dynamics*, 18(1):108–113, 1995.

H. Kazerooni, J.-L. Racine, L. Huang, and R. Steger. On the control of the berkeley lower extremity exoskeleton (bleex). In *Robotics and Automation (ICRA), 2005 IEEE International Conference on*, pages 4353–4360. IEEE, 2005.

A. Q. Keemink, H. van der Kooij, and A. H. Stienen. Admittance control for physical human–robot interaction. *The International Journal of Robotics Research*, 2017.

B. Kim and A. D. Deshpande. An upper-body rehabilitation exoskeleton harmony with an anatomical shoulder mechanism: Design, modeling, control, and performance evaluation. *The International Journal of Robotics Research*, 36(4):414–435, 2017.

S. Kitazaki and M. J. Griffin. Resonance behaviour of the seated human body and effects of posture. *Journal of Biomechanics*, 31(2):143 – 149, 1997. ISSN 0021-9290.

K. Kong and M. Tomizuka. Control of exoskeletons inspired by fictitious gain in human model. *IEEE/ASME Transactions on Mechatronics*, 14(6):689–698, 2009.

K. Kong, J. Bae, and M. Tomizuka. Control of rotary series elastic actuator for ideal force-mode actuation in human–robot interaction applications. *IEEE/ASME Transactions on Mechatronics*, 14(1):105–118, 2009.

K. Kong, H. Moon, D. Jeon, and M. Tomizuka. Control of an exoskeleton for realization of aquatic therapy effects. *IEEE/ASME Transactions on Mechatronics*, 15(2):191–200, 2010.

J. M. Lanman. *Movement and the mechanical properties of the intact human elbow joint.* PhD thesis, Massachusetts Institute of Technology, 1980.

S. M. Lavalle and J. J. Kuffner Jr. Rapidly-exploring random trees: Progress and prospects. In *Algorithmic and Computational Robotics: New Directions*, pages 293–308, 2000.

A. Lecours, B. M. St-Onge, and C. Gosselin. Variable admittance control of a four-degree-of-freedom intelligent assist device. In *Robotics and Automation*

(ICRA), 2012 IEEE International Conference on, pages 3903–3908. IEEE, 2012.

H.-D. Lee, B.-K. Lee, W.-S. Kim, J.-S. Han, K.-S. Shin, and C.-S. Han. Human–robot cooperation control based on a dynamic model of an upper limb exoskeleton for human power amplification. *Mechatronics*, 24(2):168–176, 2014.

S. Lee, J. Kim, L. Baker, A. Long, N. Karavas, N. Menard, I. Galiana, and C. J. Walsh. Autonomous multi-joint soft exosuit with augmentation-power-based control parameter tuning reduces energy cost of loaded walking. *Journal of Neuroengineering and Rehabilitation*, 15(1):66, 2018.

Y.-J. Liu and S. Tong. Barrier Lyapunov functions-based adaptive control for a class of nonlinear pure-feedback systems with full state constraints. *Automatica*, 64:70–75, 2016.

D. P. Losey, A. Erwin, C. G. McDonald, F. Sergi, and M. K. O'Malley. A time-domain approach to control of series elastic actuators: Adaptive torque and passivity-based impedance control. *IEEE/ASME Transactions on Mechatronics*, 21(4):2085–2096, 2016.

D. G. Luenberger. Observing the state of a linear system. *IEEE transactions on military electronics*, 8(2):74–80, 1964.

G. Lv and R. D. Gregg. Underactuated potential energy shaping with contact constraints: Application to a powered knee-ankle orthosis. *IEEE Transactions on Control Systems Technology*, 26(1):181–193, 2017.

M. Ma and H. Chen. LMI based H_∞ control for constrained linear systems with norm-bounded uncertainties. In *2006 6th World Congress on Intelligent Control and Automation*, volume 1, pages 2421–2425. IEEE, 2006.

J. B. Makinson, D. P. Bodine, and B. R. Fick. Machine augmentation of human strength and endurance Hardiman I prototype project. Technical report, Specialty Materials Handling Products Operation, General Electric Company, 1969.

D. Q. Mayne, J. B. Rawlings, C. V. Rao, and P. O. Scokaert. Constrained model predictive control: Stability and optimality. *Automatica*, 36(6):789–814, 2000.

T. E. Milner and C. Cloutier. Compensation for mechanically unstable loading in voluntary wrist movement. *Experimental Brain Research*, 94(3):522–532, 1993.

O. Morgenstern and J. Von Neumann. *Theory of games and economic behavior*. Princeton university press, 1953.

A. Morse. Representations and parameter identification of multi-output linear systems. In *1974 IEEE Conference on Decision and Control including the 13th Symposium on Adaptive Processes*, pages 301–306. IEEE, 1974.

A. Morse. Global stability of parameter-adaptive control systems. *IEEE Transactions on Automatic Control*, 25(3):433–439, 1980.

A. S. Morse. Supervisory control of families of linear set-point controllers-part i. exact matching. *IEEE transactions on Automatic Control*, 41(10):1413–1431, 1996.

Q. Nguyen and K. Sreenath. Exponential control barrier functions for enforcing high relative-degree safety-critical constraints. In *American Control Conference (ACC), 2016*, pages 322–328. IEEE, 2016a.

Q. Nguyen and K. Sreenath. Optimal robust safety-critical control for dynamic robotics. *International Journal of Robotics Research (IJRR), in review*, 2016b.

P. Nilsson and A. D. Ames. Barrier functions: Bridging the gap between planning from specifications and safety-critical control. In *2018 IEEE Conference on Decision and Control (CDC)*, pages 765–772. IEEE, 2018.

N. Paine, S. Oh, and L. Sentis. Design and control considerations for high-performance series elastic actuators. *IEEE/ASME Transactions on Mechatronics*, 19(3):1080–1091, 2014.

E. J. Perreault, R. F. Kirsch, and P. E. Crago. Multijoint dynamics and postural stability of the human arm. *Experimental Brain Research*, 157(4): 507–517, 2004.

Q.-C. Pham, S. Caron, and Y. Nakamura. Kinodynamic planning in the configuration space via admissible velocity propagation. In *Robotics: Science and Systems*, volume 32, 2013.

Q.-C. Pham, S. Caron, P. Lertkultanon, and Y. Nakamura. Admissible velocity propagation: Beyond quasi-static path planning for high-dimensional robots. *The International Journal of Robotics Research*, 36(1):44–67, 2017.

M. Pope, R. Crowninshield, R. Miller, and R. Johnson. The static and dynamic behavior of the human knee in vivo. *Journal of biomechanics*, 9(7):449–452, 1976.

R. Poppele and R. Bowman. Quantitative description of linear behavior of mammalian muscle spindles. *journal of Neurophysiology*, 33(1):59–72, 1970.

S. Prajna. Barrier certificates for nonlinear model validation. *Automatica*, 42 (1):117–126, 2006.

S. Prajna and A. Jadbabaie. Safety verification of hybrid systems using barrier certificates. In *International Workshop on Hybrid Systems: Computation and Control*, pages 477–492. Springer, 2004.

D. Pylorof and E. Bakolas. Analysis and synthesis of nonlinear controllers for input constrained systems using semidefinite programming optimization. In *2016 American Control Conference (ACC)*, pages 6959–6964. IEEE, 2016.

D. Pylorof, E. Bakolas, and K. S. Chan. Design of robust lyapunov-based observers for nonlinear systems with sum-of-squares programming. *IEEE Control Systems Letters*, 4(2):283–288, 2019.

T. Reid. Free vibration and hysteretic damping. *The Aeronautical Journal*, 60 (544):283–283, 1956.

P. Reist and R. Tedrake. Simulation-based LQR-trees with input and state constraints. In *Robotics and Automation (ICRA), 2010 IEEE International Conference on*, pages 5504–5510. IEEE, 2010.

P. Reist, P. Preiswerk, and R. Tedrake. Feedback-motion-planning with simulation-based lqr-trees. *The International Journal of Robotics Research*, 35(11):1393–1416, 2016.

M. Z. Romdlony and B. Jayawardhana. Stabilization with guaranteed safety using control lyapunov–barrier function. *Automatica*, 66:39–47, 2016.

J. Roy and L. L. Whitcomb. Adaptive force control of position/velocity controlled robots: theory and experiment. *IEEE Transactions on Robotics and Automation*, 18(2):121–137, 2002.

A. Shkolnik, M. Walter, and R. Tedrake. Reachability-guided sampling for planning under differential constraints. In *2009 IEEE International Conference on Robotics and Automation*, pages 2859–2865. IEEE, 2009.

E. D. Sontag. A 'universal'construction of artstein's theorem on nonlinear stabilization. *Systems & control letters*, 13(2):117–123, 1989.

G. Stein. Respect the unstable. *IEEE Control Systems*, 23(4):12–25, 2003.

R. Tedrake. LQR-trees: Feedback motion planning on sparse randomized trees. In *Robotics Science and Systems V*. MIT Press, 2009.

R. Tedrake, I. R. Manchester, M. Tobenkin, and J. W. Roberts. LQR-trees: Feedback motion planning via sums-of-squares verification. *The International Journal of Robotics Research*, 29(8):1038–1052, 2010.

K. P. Tee, S. S. Ge, and E. H. Tay. Barrier Lyapunov functions for the control of output-constrained nonlinear systems. *Automatica*, 45(4):918–927, 2009.

G. C. Thomas and L. Sentis. Towards computationally efficient planning of dynamic multi-contact locomotion. In *Intelligent Robots and Systems (IROS), 2016 IEEE/RSJ International Conference on*, pages 3879–3886. IEEE, 2016.

G. C. Thomas and L. Sentis. Quadric inclusion programs: An LMI approach to H_∞-model identification,. *IEEE Transactions on Automatic Control*, 64 (10):4229–4236, 2019.

G. C. Thomas, B. He, and L. Sentis. Safety control synthesis with input limits: a hybrid approach. In *2018 Annual American Control Conference (ACC)*, pages 792–797. IEEE, 2018.

G. C. Thomas, J. M. Coholich, and L. Sentis. Compliance shaping for control of strength amplification exoskeletons with elastic cuffs. In *Proceedings of the 2019 IEEE/ASME International Conference on Advanced Intelligent Mechatronics*, pages 1199–1206. IEEE and ASME, July 2019.

P. Weiss, I. Hunter, and R. Kearney. Human ankle joint stiffness over the full range of muscle activation levels. *Journal of Biomechanics*, 21(7):539–544, 1988.

N. Westerhof and A. Noordergraaf. Arterial viscoelasticity: a generalized model: effect on input impedance and wave travel in the systematic tree. *Journal of Biomechanics*, 3(3):357–379, 1970.

P. Wieland and F. Allgöwer. Constructive safety using control barrier functions. *IFAC Proceedings Volumes*, 40(12):462–467, 2007.

N. Yagn. Apparatus for facilitating walking, running, and jumping. *US patent*, 420179, 1890.

W. Yu and J. Rosen. Neural pid control of robot manipulators with application to an upper limb exoskeleton. *IEEE Transactions on Cybernetics*, 43(2): 673–684, 2013.

G. Zahalak and S. Heyman. A quantitative evaluation of the frequency-response characteristics of active human skeletal muscle in vivo. *Journal of Biomechanical Engineering*, 101:28–37, 1979.

D. Zanotto, Y. Akiyama, P. Stegall, and S. K. Agrawal. Knee joint misalignment in exoskeletons for the lower extremities: Effects on user's gait. *IEEE Transactions on Robotics*, 31(4):978–987, 2015.

M. Zeitz. The extended luenberger observer for nonlinear systems. *Systems & Control Letters*, 9(2):149–156, 1987.

J. Zhang, P. Fiers, K. A. Witte, R. W. Jackson, K. L. Poggensee, C. G. Atkeson, and S. H. Collins. Human-in-the-loop optimization of exoskeleton assistance during walking. *Science*, 356(6344):1280–1284, 2017.

Vita

Binghan He was born in China in 1991, the son of Dr. Guilong Zhu and Hong He. He received his B.S. degree in mechanical engineering from Purdue University, West Lafayette, IN, USA, in 2014 and his M.E. degree in mechanical engineering from Cornell University, Ithaca, NY, USA, in 2015. Since 2016, he has been pursuing his Ph.D. degree in mechanical engineering at the University of Texas at Austin, Austin, TX, USA. His research at the University of Texas at Austin includes control synthesis, human-robot interaction, and exoskeletons. He received the Kaiser Aluminum & Chemical Company Scholarship, in 2012 and 2014, the Purdue Industrial Roundtable Scholarship, in 2013, and the Kenneth Scudder Scholarship, in 2013.

Permanent address: he.binghan@hotmail.com

This dissertation was typeset with LaTeX[†] by the author.

[†] LaTeX is a document preparation system developed by Leslie Lamport as a special version of Donald Knuth's TeX Program.